

AD-A185 125

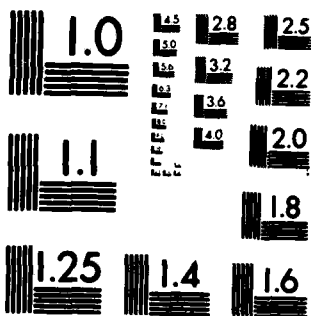
THEORETICAL ASPECTS OF TARGET CLASSIFICATION LECTURE
SERIES OF THE ELECTRIC (U) ADVISORY GROUP FOR AEROSPACE
RESEARCH AND DEVELOPMENT NEUILLY.. JUN 87 AGARD-13-152

1/3

UNCLASSIFIED

F/G 17/11

NL



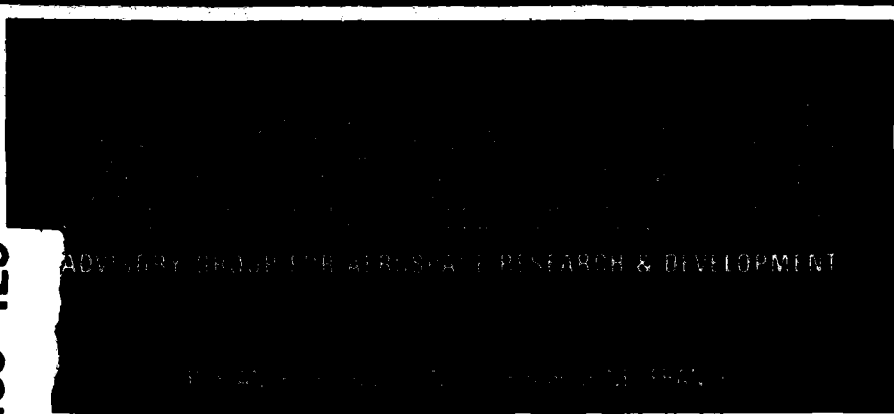
MICROCOPY RESOLUTION TEST CHART
NATIONAL BUREAU OF STANDARDS-1963-A

2

DTIC FILE COPY
AGARD-LS-152

AGARD-LS-152

AD-A185 125

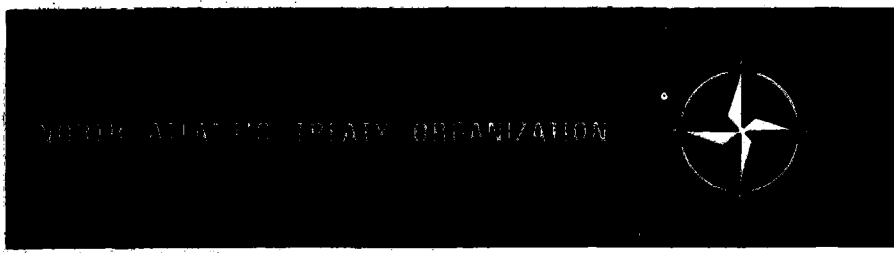


ADVISORY BOARD FOR AIRSPACE RESEARCH & DEVELOPMENT

AGARD LECTURE SERIES NO.152

Theoretical Aspects of Target Classification

DTIC
ELECTE
S AUG 17 1987 D
E



ATLANTIC TREATY ORGANIZATION



DISTRIBUTION AND AVAILABILITY
ON BACK COVER

This document has been approved
for public release and sale in
distribution is unlimited.

400049 CL

87 8 13 024

COMPONENT PART NOTICE

THIS PAPER IS A COMPONENT PART OF THE FOLLOWING COMPILATION REPORT:

TITLE: Theoretical Aspects of Target Classification. Lecture Series on Electromagnetic Wave Propagation Panel and the Consultant and Exchange Programme Held in Rome, Italy on 29-30 June 1987; Neubiberg, Germany on 2-3 July 1987 and Nonesund, Norway on 6-7 July 1987.

TO ORDER THE COMPLETE COMPILATION REPORT, USE AD-A185125.

THE COMPONENT PART IS PROVIDED HERE TO ALLOW USERS ACCESS TO INDIVIDUALLY AUTHORED SECTIONS OF PROCEEDING, ANNALS, SYMPOSIA, ETC. HOWEVER, THE COMPONENT SHOULD BE CONSIDERED WITHIN THE CONTEXT OF THE OVERALL COMPILATION REPORT AND NOT AS A STAND-ALONE TECHNICAL REPORT.

THE FOLLOWING COMPONENT PART NUMBERS COMPRISE THE COMPILATION REPORT:

AD#: P005644 through AD#: P005655

AD#: _____ AD#: _____

AD#: _____ AD#: _____

Accession For	
NTIS GRA&I	<input checked="" type="checkbox"/>
DTIC TAB	<input type="checkbox"/>
Unannounced	<input type="checkbox"/>
Justification	
By _____	
Distribution/	
Availability Codes	
Dist	Avail and/or Special
A-1	

S DTIC ELECTE **D**
OCT 26 1987
E

DTIC FORM 463
MAR 85

This document has been approved for public release and sale in distribution to unlimited.

OPI: DTIC-TID

AGARD-LS-152

NORTH ATLANTIC TREATY ORGANIZATION
ADVISORY GROUP FOR AEROSPACE RESEARCH AND DEVELOPMENT
(ORGANISATION DU TRAITE DE L'ATLANTIQUE NORD)

AGARD Lecture Series No.152
THEORETICAL ASPECTS OF TARGET CLASSIFICATION



Accession For	
NTIS GRA&I	<input checked="" type="checkbox"/>
DTIC TAB	<input type="checkbox"/>
Unannounced	<input type="checkbox"/>
Justification	
By _____	
Distribution/	
Availability Codes	
Dist	Avail and/or Special
A-1	

The material in this publication was assembled to support a Lecture Series under the sponsorship of the Electromagnetic Wave Propagation Panel and the Consultant and Exchange Programme of AGARD presented on 29-30 June 1987 in Rome, Italy, 2-3 July 1987 in Neubiberg, Germany and 6-7 July 1987 in Noresund, Norway.

THE MISSION OF AGARD

The mission of AGARD is to bring together the leading personalities of the NATO nations in the fields of science and technology relating to aerospace for the following purposes:

- Exchanging of scientific and technical information;
- Continuously stimulating advances in the aerospace sciences relevant to strengthening the common defence posture;
- Improving the co-operation among member nations in aerospace research and development;
- Providing scientific and technical advice and assistance to the Military Committee in the field of aerospace research and development (with particular regard to its military application);
- Rendering scientific and technical assistance, as requested, to other NATO bodies and to member nations in connection with research and development problems in the aerospace field;
- Providing assistance to member nations for the purpose of increasing their scientific and technical potential;
- Recommending effective ways for the member nations to use their research and development capabilities for the common benefit of the NATO community.

The highest authority within AGARD is the National Delegates Board consisting of officially appointed senior representatives from each member nation. The mission of AGARD is carried out through the Panels which are composed of experts appointed by the National Delegates, the Consultant and Exchange Programme and the Aerospace Applications Studies Programme. The results of AGARD work are reported to the member nations and the NATO Authorities through the AGARD series of publications of which this is one.

Participation in AGARD activities is by invitation only and is normally limited to citizens of the NATO nations.

The content of this publication has been reproduced directly from material supplied by AGARD or the authors.

Published June 1987

Copyright © AGARD 1987
All Rights Reserved

ISBN 92-835-1553-6



*Printed by Specialised Printing Services Limited
40 Chigwell Lane, Loughton, Essex IG10 3TZ.*

LIST OF SPEAKERS

Lecture Series Director: Prof. L.B.Felsen
Polytechnic University
Route 110
Farmingdale
New York 11735
USA

SPEAKERS

Prof. D.Dudley
University of Arizona
Department of Electrical Engineering
Tucson, Arizona 87721
USA

Dr E.Heyman
Tel Aviv University
Department of Electrical Engineering
Ramat Aviv 69978
Tel Aviv
Israel

Prof. K.J.Langenberg
University of Kassel
Department of Electrical Engineering
FB16
Wilhelmshohe Allee 73
D-3500 Kassel
Federal Republic of Germany

Dr M.Morgan
US Naval Postgraduate School
Electrical Engineering Dept.
Monterey, CA 92943
USA

Prof. Pathak
Ohio State University
Electrical Engineering Department
1320 Kinnear Road
Columbus, Ohio 43212
USA

Dr V.Stein
Institute for High Frequency Techniques
DFVLR
8031 Oberpfaffenhofen
Federal Republic of Germany

CONTENTS

	Page
LIST OF SPEAKERS	iii
	Reference
TARGET STRENGTH: AN OVERVIEW OF SOME RECENT THEORETICAL DEVELOPMENTS by L.B.Felsen	1
UNIFORM GEOMETRICAL THEORY OF DIFFRACTION by P.H.Pathak	2
SINGULARITY EXPANSION METHOD: TARGET RESONANCES by M.A.Morgan	3
THE HYBRID WAVEFRONT RESONANCE METHOD by E.Heyman	4
PHYSICAL OPTICS METHOD: PREDICTION OF RADAR SIGNATURES by V.Stein	5
THEORETICAL ASPECTS OF TARGET CLASSIFICATION: PHYSICAL OPTICS AND RADON TRANSFORM METHODS by K.J.Langenberg	6
PARAMETRIZATION IN SCATTERING MODELS by D.G.Dudley	7
INPUT SIGNAL SHAPING: K-PULSE by M.A.Morgan	8
NUMERICAL MODELING: FINITE METHODS by M.A.Morgan	9
NUMERICAL MODELING: INTEGRAL EQUATION METHOD by V.Stein	10
EXPERIMENTS: TEST RANGE FACILITIES (PART 1) by M.A.Morgan	11
EXPERIMENTS: TEST RANGE FACILITIES (PART 2) by D.G.Dudley	12
BIBLIOGRAPHY	B

Target Strength: An Overview of Some Recent Theoretical Developments

Leopold B. Felsen

Department of Electrical Engineering and Computer Science/Weber Research Institute
Polytechnic University, Route 110, Farmingdale, NY 11735 USA

AD-P005644

I. Introduction

With the increasing availability of short pulse sources of electromagnetic energy, targets can be subjected to broadband illumination, which gives rise in the returned signal to a rich variety of phenomena not encountered under time-harmonic or narrow-band conditions. Some recent theoretical developments that seek to cope with, and take advantage of, the resulting enhanced flexibility for target assessment and classification are summarized here. Basically, the techniques to be described seek to manipulate wave spectra in such a manner as to yield compact observable spectral objects with significant physical content. These compact spectral objects are then employed to interpret synthetic or real transient scattering returns and relate distinctive features in these returns to distinctive features of the target giving rise to them. Depending on whether the structural information content is local or global, the respective wave objects characterizing them are (progressing) wavefronts and (oscillatory) resonances, the transient analog of ray fields and modal fields under time-harmonic conditions. Evanescent spectra, which are transported along complex rays, are often found to be important in this process and should be included in the catalog of relevant spectral events. Having learned how to interpret, classify, and thereby parameterize, scattering data from known structures, one may attempt to use such a parameterization for reconstruction of unknown target features from given scattering data.

Emphasis will be on phenomena at high and moderate frequencies, for which the relevant wavelengths are much smaller than or comparable with, but not appreciably larger than, characteristic length scales in the scatterer. It is in these parametric regions where wave transport phenomena play an essential role. High frequency waves can be localized around the ray trajectories of the geometrical theory of diffraction (GTD), which thereby serves to chart and classify the progression of wavefronts. The reader is assumed to be familiar with GTD and its uniform refinements to account for transitional effects in various diffraction environments; a compilation of representative articles may be found in [1], and the techniques have been included in a number of texts [2] and handbooks [3] dealing with high frequency wave principles and applications. The oscillatory modal and resonance fields are global descriptors of a propagation or scattering environment, and thereby organize the overall wave process in an entirely different way. In the transient domain, the resonance formulation has become known within the framework of the Singularity Expansion Method (SEM) (for a representative set of articles see [4,5]). The connection between these two fundamental and physically meaningful building blocks for wave field synthesis in progressive or oscillatory form [6] has recently been elucidated in a bilateral and quantitative manner [7,8], thus granting insight into how these compact spectral objects are generated by alternative spectral contractions from a wave spectral continuum. These aspects will be covered in subsequent lectures in this series. The presentation below begins with the wavefront-resonance interplay, and then passes on to applications and examples illustrating various aspects of the theory.

II. Wavefront-Resonance Description

When the high-frequency methodology of GTD is transformed into the time domain [9], each ray describes the trajectory of a wavefront, and the time domain analog of the ray field yields the transient field at and near the wavefront arrival time. While these results are adequate for the transient response within a narrow time window surrounding each wavefront arrival, they fail when the received signal is monitored over a longer time interval that includes late observation times for early arrivals. Even if the field associated with each wavefront were described correctly for all subsequent times, the multiplicity of arrivals makes resolution of individual events nonfeasible, and thereby defeats the virtue of using these arrivals as identifiers of distinct scattering centers. It is then more appropriate to seek an alternative description that deals with the multiple wavefronts in a collective manner. This is provided by the target resonances of SEM which express the free oscillations of the entire structure. In fact, typical synthetic or actually measured broadband signatures of targets reveal fairly distinct replicas of the input pulse in the early time portion but more smoothed out oscillations at later times, indicative of the predominance of wavefronts and resonances, respectively.

The wavefront-resonance complementarity and duality has been expressed in a systematic and self-consistent format that provides flexibility of interpretation of direct scattering data [7] and efficient parameterization of such data for inversion to extract target characteristics [10,11]. A distinction is made between early (intrinsic) wavefront events that cannot be phenomenologically absorbed within the resonance structure (although a purely formal but physically awkward scheme of such incorporation can be implemented [12,13]), and subsequent (nonintrinsic) wavefront events that can be embedded within the resonances in a physically meaningful manner. The intrinsic events arise from the first scattered response before the incident signal has had time to traverse the entire scattering object; because these responses contain no knowledge of the actual total target shape, their incorporation into descriptors, like resonances, that do depend on the total shape is nonphysical and may lead to errors. Within the SEM format, the intrinsic wavefronts can be identified with the "intrinsic entire function" [7]. The nonintrinsic events correspond to subsequent arrivals after the entire object has been excited. While these wavefronts can be treated meaningfully in collective form, it may be more efficient and physically incisive to retain the first few intact and only convert into resonances those that remain [14,15]; see also [16]. Delaying the onset of the resonance description weakens the strength of the resonances and pushes their regime to lower frequencies, thereby limiting their significantly contributing number. Where to switch poses a tradeoff that is problem dependent but it is important to observe that by the self-consistent wavefront-resonance scheme [7,14,15], all combinations are correct although they may have different convergence properties. Typically, for low- σ scatterers, the resonances are highly damped and may actually be avoided altogether because all the essential signature features can be explained with a few wavefronts. For high- σ scatterers, especially those with penetrable low-loss interior, the resonances can be distinct, strong, and play

a major role at later times; here, it may even be desirable to revert to the resonance description after isolating the intrinsic wavefronts only.

To illustrate these observations, we consider electromagnetic plane pulse scattering by the perfectly conducting flat strip in Fig. 1(a) [17,18], which, even for H-polarization, represents a low-Q target. The GTD generated results for impulsive plane wave scattering are shown in Figs. 1(b)-1(d). Evidently, the failure of GTD at later times (low frequency spectral components) makes the method inapplicable for this type of input pulse but the results reveal nevertheless the internal consistency of the wavefront-resonance algorithm, including its hybrid form (Fig. 1(d)). When the chosen pulse spectrum is bandlimited with a low frequency cutoff, the high-frequency algorithm does become quantitatively accurate [18] (Fig. 1(e)). The resonances are now weakened substantially, and the entire "resonant" structure can, in fact, be duplicated by only a few wavefront events, as indicated. For E-polarization (acoustically soft case), the resonance contribution is so small in this case [18] as to mitigate altogether against its utility as a descriptor of target responses.

It has been mentioned earlier that GTD generated transient fields are applicable only for short time intervals after arrival of the wavefront transported along a particular ray. However, it is noteworthy that the complex resonance frequencies generated by collective treatment of the GTD arrivals (Fig. 1(f)) are remarkably accurate (Fig. 1(g)), even at the low frequency end, which is most relevant for late observation times. This feature has been confirmed in a number of other investigations of simple target shapes [19,20]. Thus, it is suggestive that the GTD machinery can be exploited to determine the resonance frequency map also for more complicated shapes, although the resonant fields may be strongly in error.

III. Concave-Convex Boundary Shapes: Complex Spectra

Ray fields incident on the concave portion of a convex-concave exterior boundary of a target are generally focused after reflection. When the scattered field is observed on the shadow side of the caustic confining this focused ray family, the corresponding evanescent fields have usually been ignored. Yet, numerical experiments on plane wave scattering from perfectly reflecting shapes of this kind have revealed certain features in the scattered signal shape that appear to originate near the concave-to-convex inflection point [21] and, yet, are neither conventional specularly reflected nor diffracted events (diffraction would require a point of non-analyticity on the surface contour but the postulated surface function is completely analytic). Analysis shows that the anomalous features can be attributed to specular reflection of complex incident ray fields from the complex analytic extension of the obstacle boundary [22] (Fig. 2). Thus, specular reflection, when generalized to include both real and complex rays, can explain signatures arising from the illuminated portion of smooth targets of arbitrary shape. Creeping waves, which account for contributions from the nonilluminated portion, may also undergo complex reflection when encountering convex-concave surface deviations [23] (Fig. 2).

IV. Exterior-Interior Coupling

When a target is penetrable or grants access through an opening to an interior that can trap energy, the reradiation from the enhanced interior fields at their resonance frequencies can strongly affect the scattered signal. For idealized models such as plane stratified layers and radially stratified dielectric cylinders and spheres, an exact analysis can be performed by separation of variables, and the solution cast in a form, from which one may extract the various ray-optical and resonant wave constituents that are useful for interpretation and classification in the high and mid-frequency range [24,24]. In some of these configurations, the layers may possess elastic properties [26,27]. Open-ended semi-infinite or terminated thin-walled waveguides in plane parallel, circular or elliptic geometry likewise form useful prototypes for testing hypotheses pertaining to edge diffraction coupling into, and subsequent radiation from, an elongated enclosure [28]. By expressing the results obtained from these canonical building blocks in invariant form tailored to a particular wave event, one may invoke the principle of locality, which is operative at high frequencies, to construct approximate theories applicable under more general conditions. In this endeavor, it is important to effect the modification in terms of wave phenomena that remain stable under perturbation from an idealized shape. For ray events, the analysis can be based on the general machinery of GTD and its uniformized modifications. For resonant and strongly guided fields, one may employ modal ray procedures [8], local (adiabatic) modes [29], intrinsic modes [30], boundary layer [31], parabolic equation [32], and perturbation methods to describe body modes and resonances occupying essentially the entire volume, whispering gallery modes and resonances confined to a layer near a concave boundary surface, or beam-type modes and resonances trapped by focusing between opposite concave boundary segments. Studies of configurations even with small perturbations from an idealized model are useful because wave type degeneracies that usually occur in strongly symmetric prototypes are broken thereby. Understanding wavefront and resonance behavior individually, one may then attempt to combine them within the hybrid format as for impenetrable structures. So far, this has been accomplished only for the simplest prototypes.

Perturbing structures in the interior of smooth enclosures cause coupling between the empty cavity wave fields, in addition to introducing signatures of their own. Here, hybrid approaches combining ray (wavefront) and mode (resonance) descriptions can be expected to be particularly useful to characterize the multiplicity of interaction mechanisms, which are predicted by numerical experiment as in [33]. In a physically transparent and numerically tractable manner. Numerical modeling for a compact interior scatterer, combined with a boundary integral equation approach, provides another type of hybrid option for coupling the wavefields due to a confined structure to the global configuration of the enclosing shell. Evidently, the "best" approach is problem dependent, and much carefully posed analytical and numerical modeling is required to sort out even the dominant effects that influence the signal scattered from a composite target with interior structure. When certain parts of an interior are highly disorganized, they may be better treated as a statistical ensemble. This requires combining statistical measures (averages) of a random wave field with deterministic guiding and scattering events [34,35], a discipline that is only beginning to be explored at present. For an interior of moderate complexity that permits construction of numerical programs for multiple reflected, refracted and diffracted ray trajectories, ray shooting algorithms, which cover the interior with rays, can provide much insight concerning the strong field (dense rays near caustics) and weak field domains. Ray shooting is widely used in seismic exploration [36] and, by

associating it with dynamic ray tracing and Gaussian beam methods [37], can provide some quantitative information about field strengths, although much remains to be done to render these methods truly predictive. Some attempts have already been made to transfer this approach to electromagnetics and underwater acoustics [34,35].

Figure 3 provides a numerical generated set of data [33] that illustrate how the interior of a high- Q -cavity backed aperture influences the target signature. For analytical modeling, one may employ conventional (including edge diffracted) ray tracing or ray-mode coupling introduced by the edge discontinuities. The ray-to-mode coupling can be calculated either by collective treatment of multiple reflected and diffracted rays, or (often more conveniently) by establishing on the obstacle surface or cavity aperture an initial physical optics distribution determined from the incident signal, and evaluating the modal excitation coefficients from this prescribed excitation. This requires knowledge of the complete mode structure, i.e., the Green's function, of the interior. Examples may be found in [40,41]. Typically, the most strongly excited modes or resonances in a highly overmoded system are those whose modal ray congruences have directions near the ones produced by the incident ray family. Radiation due to the resonant modal fields, or modal fields reflected from the cavity end and/or interior structures, can be treated by considerations of reciprocity. These considerations may also help toward an understanding of anomalous phenomena exhibited by the computed data in Fig. 3.

V. Matching the Interrogating Signal to the Target

Having gained an understanding of the wave mechanisms that are instrumental in producing the scattered field from a target of given size, shape and composition, an important question is whether input signals can be constructed that interrogate this target in such a manner as to produce a unique response for classification and identification. Evidently, such a scheme will have to depend on the manner in which the target signature is parametrized, i.e., on the basic waveforms that are assumed to synthesize the response. One approach, based on the resonance spectrum, seeks to shape an input pulse so as to eliminate several or all of the complex resonances from the late time response [42,43]. Since each target has, in principle, a unique aspect-independent set of resonances, illumination by its own matched input signal will produce predetermined features in the response that distinguish it from a "wrong" target. Some model analytical, numerical and physical experiments, which have been conducted, reveal that this scheme may merit further exploration. The late-time restriction is imposed to assure that the resonances (and not the wavefronts) do indeed dominate the scattered response, and that the number of resonances is not excessively large. However, the delayed onset of observations reduces the excitation strengths of the resonances, thereby leaving inadequate information content for low- Q structures. This limitation is removed for high- Q structures if the incident signal level is sufficiently high to produce a distinctive response. The late time regime also deemphasizes the high-frequency resonances, thereby blurring local target features in favor of global structural effects. Local features are best identified by wavefronts whose arrival times, if they can be resolved, give a firm indication of where on the scatterer the response originates. This is the early time regime which, generally, also contains most of the pulse energy. It may be conjectured that the most effective interrogation will utilize both the early and late time returns parametrized, respectively, in terms of wavefronts and resonances, which may be embodied self-consistently, in any combination, via the hybrid wavefront-resonance formalism.

VI. Summary

This brief review, has focused on some recent developments and trends in the theory of target scattering and classification, with the intent of setting the tone for the presentations that follow. Subsequent talks deal with foundations of the theory and with applications.

References

1. R.C. Hansen, ed., Geometric Theory of Diffraction, IEEE Press, New York, 1981.
2. Greame L. James, Geometrical Theory of Diffraction for Electromagnetic Waves, Peter Peregrinus Ltd., London, England.
3. A.W. Rudge, K. Milne, A.D. Olver and P. Knight, The Handbook of Antenna Design, Peter Peregrinus Ltd., London, England, 1982.
4. Electromagnetics, 1, No. 4(1984), Special Issue on "Singularity Expansion Method".
5. C.E. Baum, "The Singularity Expansion Method", in Transient Electromagnetic Fields (L.B. Felsen, ed.), Springer, New York, 1976.
6. J.B. Keller and J.S. Papadakis (ed.), Wave Propagation in Underwater Acoustics, Springer, New York, 1977, Ch. II.
7. E. Heyman and L.B. Felsen, "A Wavefront Interpretation of the Singularity Expansion Method", IEEE Trans. on Antennas and Propagation, AP-33 (1985), pp. 706-718.
8. L.B. Felsen, "Progressing and Oscillatory Waves for Hybrid Synthesis of Source Excited Propagation and Diffraction", Invited Paper, IEEE Trans. on Antennas and Propagation, AP-33 (1984), pp. 775-796.
9. M. Kline and I. Kay, Electromagnetic Theory and Geometrical Optics, Interscience, New York, 1965.

10. D.G. Dudley, "Comments on SEM and the Parametric Inverse Problem", IEEE Trans. Antennas and Propagation, AP-33 (1985), pp. 119-120.
11. K.J. Langenberg, M. Berger, K. Mayer, G. Weinfuter and P. Zanger, "Inverse Scattering and Identification with Initial Arrival Wavefronts", paper presented at URSI International Symposium on Electromagnetic Theory, Budapest, Hungary, August 1984.
12. L.W. Pearson, "A Note on the Representation of Scattered Fields as a Singularity Expansion", IEEE Trans. on Antennas and Propagation, AP-32 (1984), pp. 520-524.
13. M.A. Morgan, "Singularity Expansion Representations of Fields and Currents in Transient Scattering", IEEE Trans. on Antennas and Propagation, AP-32 (1984), pp. 466-473.
14. E. Heyman and L.B. Felsen, "Creeping Waves and Resonances in Transient Scattering by Smooth Convex Objects", IEEE Trans. on Antennas and Propagation AP-31 (1983), pp. 426-437.
15. E. Heyman and L.B. Felsen, "Traveling Wave and SEM Representations for Transient Scattering by a Circular Cylinder", J. Acoust. Soc. Am. 79 (1986), pp. 230-240.
16. G.C. Gaunaurd and H. Uberall, "Relation Between Creeping-Wave Acoustic Transients and the Complex-Frequency Poles of the Singularity Expansion Method", J. Acoust. Soc. Am. 78 (1985), pp. 234-243. Earlier related references are cited in this paper.
17. H. Shirai and L.B. Felsen, "Wavefront and Resonance Analysis of Scattering by a Perfectly Conducting Flat Strip", IEEE Trans. Antennas and Propagation, AP-34(1986), pp. 1196-1207.
18. H. Shirai, "De-emphasizing Low Frequency Defects in GTD Analysis of Pulsed Signal Scattering by a Perfectly Conducting Flat Strip", IEEE Trans. on Antennas and Propagation, AP-34(1986), pp. 1261-1266.
19. R.M. Jones, A.W. Howard, Jr., and J.I. Simon, "Creeping Ray Analysis of Resonance for Prolate Spheroid", to be published in IEEE Trans. on Antennas and Propagation.
20. R. Naishadham and L.W. Pearson, "Numerical Evaluation of Complex Resonances of an Elliptic Cylinder", IEEE Trans. on Antennas and Propagation AP-33 (1985), pp. 674-676.
21. H. Ikuno, "Transient Scattering from Periodic Deformed Cylinders", Radio Sci., 19 (1984), pp. 1327-1332.
22. H. Ikuno and L.B. Felsen, "Complex Ray Interpretation of Reflection from Concave-Convex Surfaces", to be published in IEEE Trans. on Antennas and Propagation.
23. H. Ikuno and L.B. Felsen, "Complex Rays in Transient Scattering from Smooth Targets with Inflection Points", to be published in IEEE Trans. on Antennas and Propagation.
24. G. Maze, J.L. Izbicki, J. Ripoché, A. Nagl, H. Uberall and K.B. Yoo, "Transient Acoustic Scattering from Layers and Plates", J. Acoust. Soc. Am. 80(1986), pp. 295-301.
25. A.G. Tuijthuis, "Angularly Propagating Waves in a Radially Inhomogeneous, Lossy Dielectric Cylinder and their Connection with the Natural Modes", IEEE Trans. on Antennas and Propagation AP-34 (1986), pp. 813-824.
26. G.C. Gaunaurd and D. Brill, "Acoustic Spectrogram and Complex-Frequency Poles of a Resonantly Excited Elastic Tube", J. Acoust. Soc. Am. 75 (1984), pp. 1680-1693.
27. G.C. Gaunaurd and M.F. Werby, "Resonance Response of Submerged, Acoustically Excited Thick and Thin Shells", J. Acoust. Soc. Am. 77 (1985), pp. 2081-2093.
28. J.J. Bowman, T.B.A. Senior and P.L.E. Uslenghi (editors), Electromagnetic and Acoustic Scattering from Simple Shapes, North Holland, Amsterdam, 1969.
29. A.D. Pierce, "Extension of the Method of Normal Modes to Sound Propagation in an Almost Stratified Ocean", J. Acoust. Soc. Am. 37 (1965), pp. 19-27.
30. J.M. Arnold and L.B. Felsen, "Local Intrinsic Modes--Layer with Nonplanar Interface", Wave Motion 8 (1986), pp. 1-14.
31. V.M. Babich and N.Y. Kirpichnikova, The Boundary-Layer Method in Diffraction Problems, Springer, New York, 1979.
32. V.M. Babich and V.S. Buldrev, Asymptotic Methods in Short Wave Diffraction Theory, Nauka, Moscow, 1972.
33. R.W. Ziolkowski, "New Electromagnetic Resonance Effects Associated with Cavity-Baked Apertures", Lawrence Livermore National Laboratory, Livermore, California, Preprint UCRL-94517, May 1986.
34. R.N. Bear, D.H. Berman, J.S. Perkin and E.B. Wright, "A Three-Dimensional Model of Scattering from Rough Ocean Bathymetry", Computers and Mathematics, 11, (1985) pp. 863-872.
35. R. Mazar and L.B. Felsen, "Evaluation of the Two-Point High Frequency Coherence Function Along Ray Paths in the Inhomogeneous Background of a Weakly Random Medium", to be published in J. Acoust. Soc. Am.
36. V. Cerveny, "Ray Synthetic Seismograms for Complex Two-Dimensional and Three-Dimensional Structures", J. Geophysics 58 (1985), pp. 2-26.

37. V. Cerveny, "Gaussian Beam Synthetic Seismograms", *J. Geophysics* 58 (1985), pp. 44-72.
38. M.B. Porter and H.P. Bucker, "Calculation of Underwater Acoustic Fields by Gaussian Beam Tracing", *J. Acoust. Soc. Am. Suppl. 1*, 78 (1985), p. S22.
39. E. Niver, M.S. Vogas, C.J. Ruiz, and L.B. Felsen, "Correcting Ray Field Failures Caused by Focusing and Shadowing in an Inhomogeneous Duct" presented at NATO/AGARD Symposium on Terrestrial Propagation Characteristics in Modern Systems of Communication, Surveillance, Guidance and Control, Ottawa, Canada, Oct. 1986.
40. P.H. Pathak, C.W. Chuang, M.C. Liang, N. Wang and H.T. Kim, "RAM and Inlet Modeling Studies", Electroscience Lab., Ohio State Univ., Report 7164495-2, 1985.
41. L.B. Felsen and H. Shirai, "Hybrid Ray-Mode Analysis of High-Frequency Wave Coupling into Large Waveguides and Cavities", submitted to *Wave Motion*.
42. F. Fok, D. Moffatt and N. Wang, "K-Pulse Estimation from the Impulse Response of a Target", Digest of 1986 National Radio Science Meeting, Philadelphia, Pa., June, 1986.
43. K.M. Chen, D.P. Nyquist, E.J. Rothwell, L.L. Webb and R. Drachman, "Radar Target Discrimination by Convolution of Radar Return with Extinction Pulses and Single-Mode Extraction Signals", *IEEE Transactions Antennas Propagat.* AP-34 (1986), pp. 896-904.
44. P. Fellinger, et al., "Zur Modellierung der Ultraschallstreuung an Rissen: Vergleiche von Analytisch-Numerischen mit PO- und GTD-Ergebnissen für den skalaren Fall", Technical Report, University of Kassel, 1984 (in German).
45. H. Shirai and L.B. Felsen, "Modified GTD for Generating Complex Resonances for Flat Strips and Disks", *IEEE Transactions Antennas Propagat.*, AP-34 (1986), pp. 779-790.
46. S.V. Hsu and L.W. Pearson, "Numerically Determined Natural Resonances for an Infinitely Long Perfectly Conducting Strip", presented at 1984 International IEEE/AP-S Symposium, National Radio Science Meeting, Boston, Massachusetts.

Fig. 1 Far zone transient plane wave scattering by a perfectly reflecting flat strip of width d [17, 18]. All numerical results are for electromagnetic H-polarization (acoustically rigid), incidence angle $\theta_0 = 45^\circ$, observation angle $\theta = -45^\circ$, $d = 20m$, observation distance $\sim 3km$.

- Physical configuration, ray trajectories, and ray species. ρ and θ are cylindrical coordinates centered at an edge. Relevant rays are specularly reflected (ρ_R , shaded region) and edge diffracted ($\rho_{A,B}$, existing everywhere). SBI, r are incident and reflected ray shadow boundaries. Ray species $j=1$ to 4 group diffracted wave processes according to their excitation (downgoing ray) and emission (upgoing ray) points.
- Diffracted wave front contributions $U_{1,n}(t)$ in ray species $j=1$ (excitation and departure at edge A), for impulsive plane wave incidence. N denotes the number of edge interactions as depicted below each arrow, which locates the diffracted wavefront arrival time at the observer. Other ray species behave similarly. --: individual GTD diffracted wave fields; —: sum of all diffracted wave fields (note the predominance of the $n=1$ contribution and the successive weakening of the others); Δ : sum of SEM resonances (for this low- Q structure, the resonances furnish only a small slowly convergent correction whose inclusion, however, restores complete agreement with the ray field sum); \ast : continuous spectrum (arises for two-dimensional (infinitely extended) scatterers, but not for three-dimensional spatially confined targets; this spectrum is almost entirely equivalent to the diffracted ray sum); x : ($\ast + \Delta$). The numbers next to Δ show how many resonances had to be included to stabilize their sum to within 1% error. Due to the low-frequency inadequacy of GTD, the results diverge at later times. Nevertheless, the formulations by either wavefronts or resonances plus continuous spectrum agree.
- Total scattered field (all species $j=1$ to 4 plus primary diffracted (intrinsic) contributions $U_{1,3}$ arising from single scattering at edges A and B, respectively). Same low frequency defects as in Fig. 1(b). Legend as in Fig. 1(b). Crosses denote sum of resonances plus continuous spectrum.
- Hybrid wavefront-resonance formulation (species $j=1$), where $U_{1,1}$ is kept intact and where the collective treatment is initiated at $n=2$ with $U_{1,2}$. Legend as in Fig. 1(b) and 1(c). SEM contributions are now much weaker but more rapidly convergent.
- Incident plane wave with band-limited raised cosine time dependence instead of the impulse. All other parameters and notations as in Fig. 1(b) except that diffracted wave fields are denoted by $U_{1,n}^b$ and $U_{1,n}^c$, and the observation distance is 1km. Low frequency cutoff of pulse spectrum now repairs defects of GTD analysis, and the total GTD results shown [18] agree completely with the solution from an exact eigenfunction expansion [44]. The resonances are weakened substantially, and the entire "resonant" structure can, in fact, be duplicated by only a few wavefront events, as indicated. For E-polarization, the resonance contribution is so small as to mitigate altogether against its utility as a descriptor of target response.
- Resonance generation mechanism by self-consistent closure of multiple edge diffracted fields [45]. Resonance condition requires equality of fully established diffracted fields after each full cycle around the object. Ray closure condition: $P_1 D_B P_2 D_A P_0 = 1 (P_3 D_B P_2 D_A)$ where $P_{i,j} = \theta - 5$, are propagation functions, and D_A, D_B signify edge diffraction; C is an arbitrary reference point. Possible partial closure paths: $P_2 P_4; P_2 P_3; P_4 P_5; P_3 P_5$. Each such path generates a corresponding partial resonance condition. For a strip, there is multiple degeneracy, and $P_2 P_4 = P_3 P_5; P_3 P_4 = P_2 P_5$, with $D_A = D_B = D$. For example, $P_2 P_4$ accounts for partial resonances due to the lower surface contour between the edges [7].
- Dominant (first layer) complex resonance frequencies (SEM poles) γ_m in complex $\gamma = kd$ plane. A symmetrical set in the third quadrant is not shown. x : GTD construction [45]. \ast : numerical, by method of moments [46]. Agreement is excellent, even for the lowest frequency resonance γ_2 . For higher order layers, see [45]. There is also a continuous spectrum along the negative imaginary axis, due to the two-dimensionality of the problem. The corresponding branch cut is not shown.

Fig. 2 Plane wave far field back-scattering by a perfectly reflecting deformed cylinder with surface sinusoidal contour $\rho(\theta) = a(1 - 0.2\cos 3\theta)$, where ρ and θ are cylindrical coordinates. Incidence and observation angle $\alpha = \theta = \pi/3$. Numerical results are for electromagnetic H-polarization [21,22].

- Physical configuration, ray trajectories and reflection points for backscattering. SR and (SR) $_c$ denote real and complex specular reflection points, respectively, for the incident field. They can be found either from direct complex ray tracing or from a physical optics analysis with subsequent stationary phase evaluation of the surface integral containing the physical optics induced surface fields over the directly illuminated portion. Real and complex stationary phase points locate real and complex ray reflection points, respectively. Real incident and reflected ray trajectories are shown solid, while complex ray trajectories are shown shaded. The complex rays are reflected specularly from the complex extension of the scatterer surface. The depiction of the complex ray trajectories and reflection points should be regarded as symbolic, located in a complex coordinate space. Diffraction effects are described by creeping waves which circumnavigate the obstacle along trajectories marked C. Like the incident rays, creeping rays can be reflected from complex reflection points RC. The creeping rays progress in both directions around the obstacle. Only the counterclockwise creeping ray C is shown; the clockwise arrow accounts for the reflection from RC.
- Real incident rays reflected specularly from the concave portion between inflections points. A two-branched caustic is formed by these rays which do not reach the observer in the back-scatterer direction of Fig. 2(a). Such an observer, who is situated in the shadow region of this system, is reached by an evanescent wave "tunneled" across the caustic. The tunneled ray can alternatively be regarded as a complex ray reflected specularly from the complex extension of the obstacle. Its contribution as in Fig. 2(a) becomes weaker as the observer moves further into the shadow.

- c) Time-harmonic transfer function (normalized back-scattering cross section) $H(ka)$ contributed by directly illuminated portion of the scatterer, as a function of frequency [22]. $k = \omega/c$ is the incident wavenumber, $\exp(-i\omega t)$ is the suppressed time dependence, and c is the wave propagation speed in the medium. Dashed curve: numerical integration of physical optics (PO) integral over illuminated portion; this serves as the reference solution. Solid curve: ray solution with real and complex contributions from the specular points (SR) and $(SR)_c$, given by

$$H(ka) \Big|_{SR} = 0.741 \exp(-12.21 ka)$$

$$H(ka) \Big|_{(SR)_c} = 0.608 - 10.250 \exp(-11.24 ka - 0.125 ka)$$

Their sum, through interference, generates the oscillations in the transfer function. The transfer function for the unperturbed cylinder $c = a$ is constant. The ray solution is seen to agree well with the reference solution for $ka \geq 2$.

- d) Pulsed plane wave used for transient calculation. Pulse shape: $g(t) = D d^3 f(t) / dt^3$, $f(t) = (6t/\tau\pi)^{1/2} \exp[-(6t/\tau)^2]$, $\tau = 2a/c$. D is a normalization constant. The pulse spectrum deemphasizes low frequencies, thereby making ray theory applicable.
- e) Back-scattered transient response obtained by frequency inversion of time-harmonic solution in Fig. 2(c) convolved with the pulse spectrum in Fig. 2(d), with inclusion of creeping wave effects [23]. Arrival times of various ray field contributions along the trajectories depicted in Fig. 2(a) have been identified by arrows, with $(t/\tau) = 0$ for the SR (central zero crossing) chosen as a reference. Each arrival is seen to contribute an identifiable feature (zero or maximum) to the signal shape. The insert shows a fourfold magnification of the weak C and RC portion. Dashed curve: reference solution by numerical integration of coupled mode code. Solid curve: real and complex ray contributions.

Fig. 3

Time-harmonic normalized electromagnetic back-scattering cross section for perfectly reflecting thin-walled open sphere with radius $a = 1$ perforated by a circular aperture with polar angle $\theta_{ap} = 10^\circ$, without and with interior loading by a concentric dielectric sphere having dielectric constant $\epsilon = 3$ and radius $b = 0.3$ [33]. The incident field is a plane wave along the axis of symmetry. The closed sphere exterior resonance response (not shown) is a smooth curve with decreasing oscillations around $ka = 1$. For $ka \leq 3$, the solid curve for the perforated sphere, as plotted in the figure, agrees essentially with that for the closed sphere. At higher (ka) values, access to the interior produces some background distortion and superimposes a series of spikes, whose (ka) locations are slightly lower than those corresponding to the interior resonances of the closed empty sphere. Adding the concentric dielectric sphere (dashed curve) does not substantially affect the empty sphere response over the plotted (ka) interval but shifts the resonance spikes. Thus, the spikes contain information about the interior configuration.

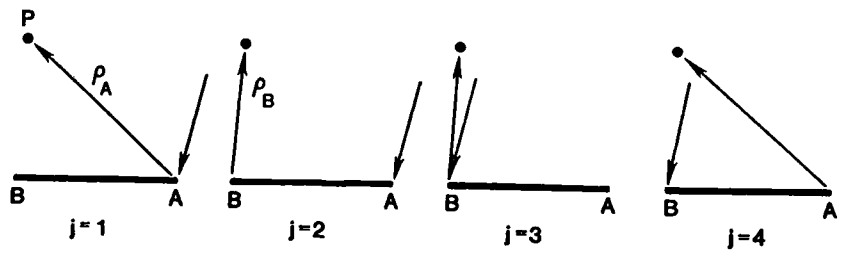
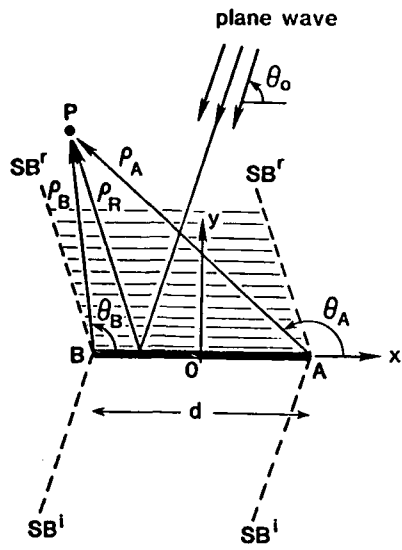


Fig. 1 (a)

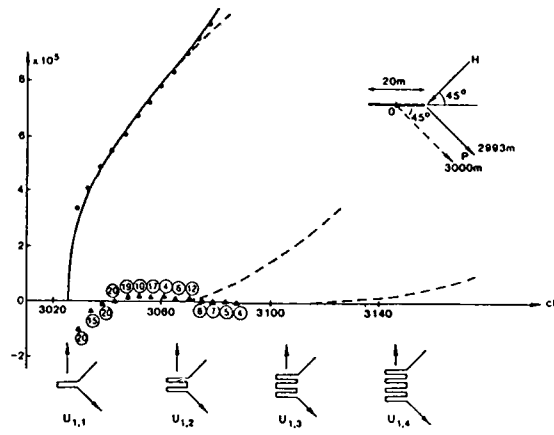


Fig. 1(b)

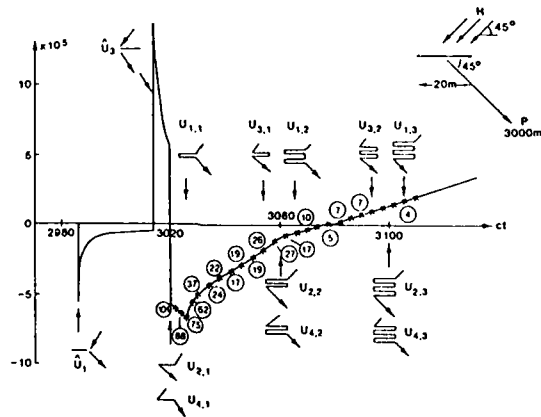


Fig. 1(c)

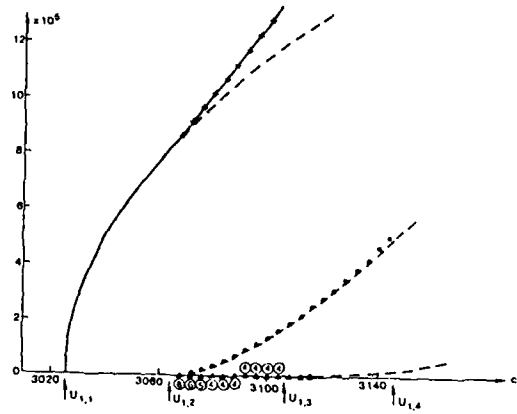
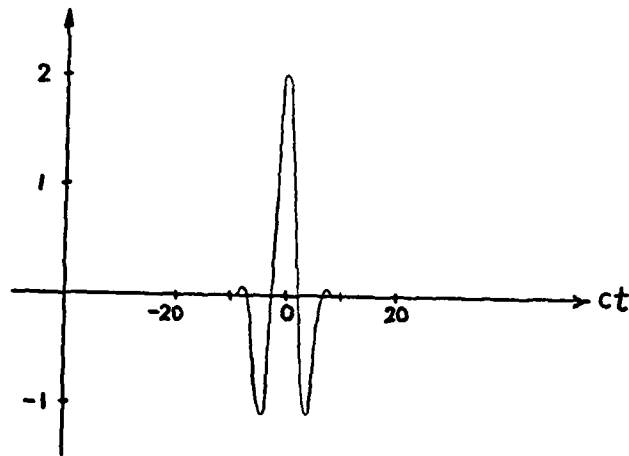
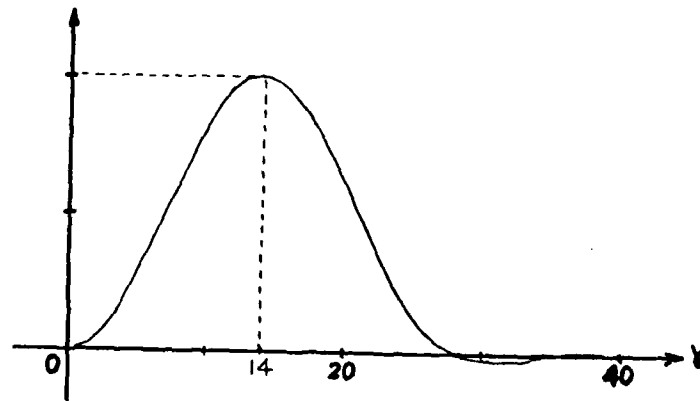


Fig. 1(d)



Input Pulse Shape



Input Pulse Spectrum
Fig. 1(e)

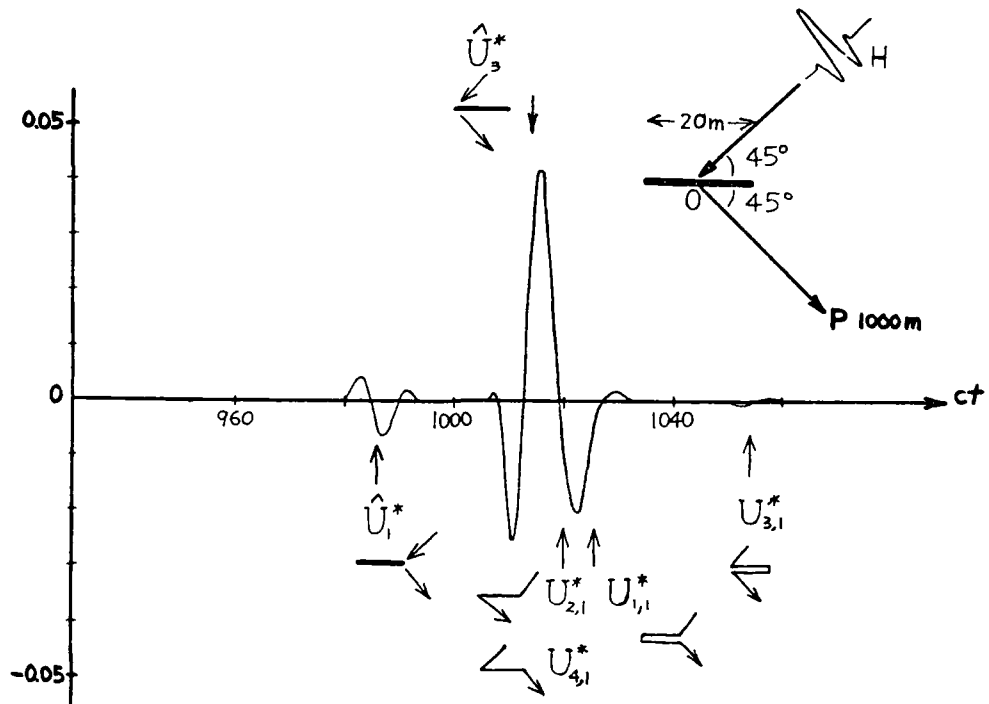


Fig. 1(e), cont'd.

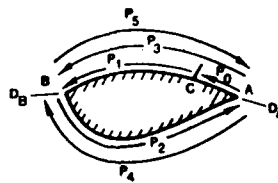


Fig. 1(f)

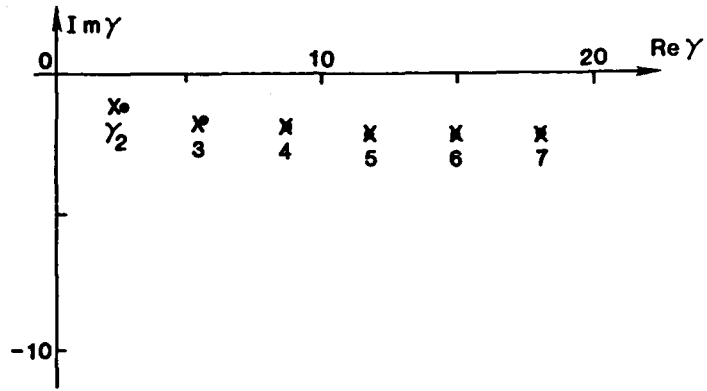


Fig. 1 (g)

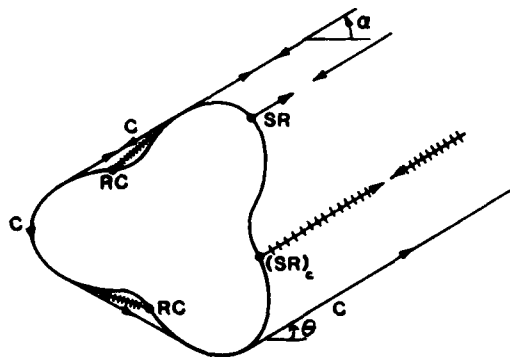


Fig. 2 (a)

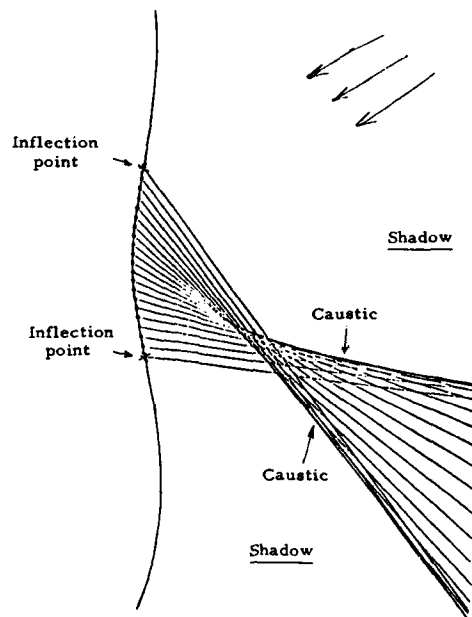


Fig. 2(b)

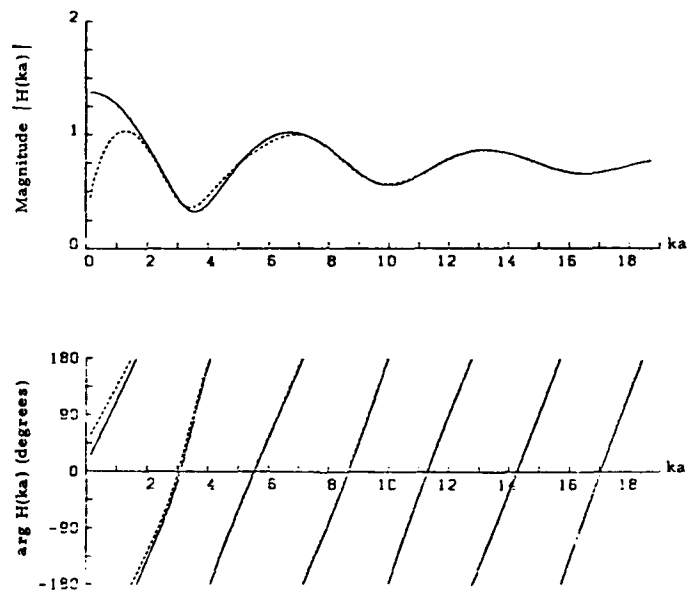
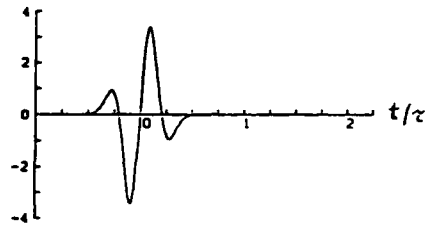
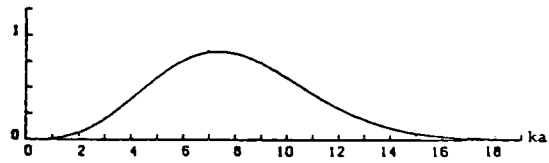


Fig. 2(c)



Incident Pulse Shape



Incident Pulse Spectrum

Fig. 2(d)

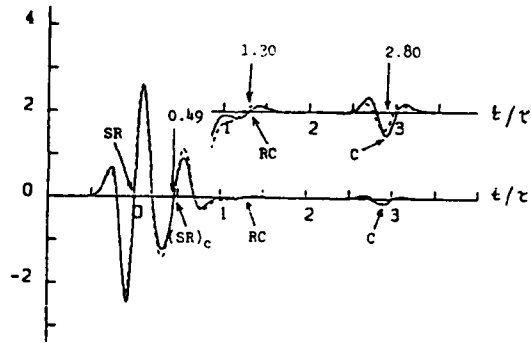


Fig. 2(e)

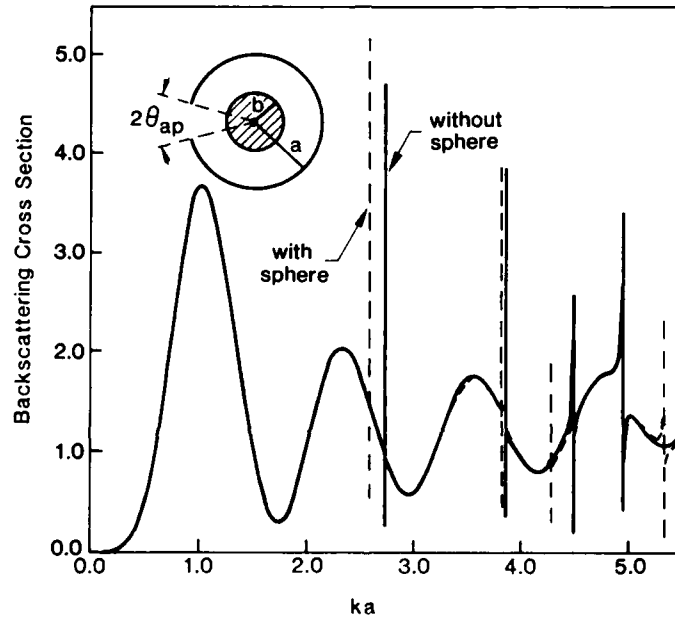


Fig. 3

UNIFORM GEOMETRICAL THEORY OF DIFFRACTION

by
P.H. Pathak
The Ohio State University ElectroScience Laboratory
1320 Kinnear Road
Columbus, Ohio 43212

SUMMARY

Keller's geometrical theory of diffraction (GTD) represents a major breakthrough in solving a wide variety of electromagnetic (EM) radiation and scattering problems at high frequencies. In particular, the GTD is an extension of geometrical optics to include a class of diffracted rays via a generalization of Fermat's principle. These diffracted rays are initiated, for example, from geometrical and electrical discontinuities in a scatterer, or from points of grazing incidence on smooth convex parts of the scattering surface. However, being a purely ray optical theory, the original GTD fails within the transition regions adjacent to geometric optical shadow boundaries where the diffracted field generally assumes its largest value. This limitation of the GTD is overcome via the uniform version of the GTD (i.e., UTD) which requires the diffracted field to make the total high frequency field continuous across the optical shadow boundaries. The UTD solutions for the diffraction by edges and smooth convex surfaces are reviewed in detail after introducing the basic concepts of GTD. Results based on a few additional UTD solutions are also presented together with a few selected applications of these UTD solutions to predict the EM radiation and scattering from complex structures.

I. INTRODUCTION

An efficient analysis of the radiation and scattering of waves by objects which are large in terms of the wavelength can be performed via high frequency techniques. One of the most versatile and useful high frequency (HF) techniques is Keller's geometrical theory of diffraction (GTD) [1,2,3] which was developed in the early 1950s. The GTD constitutes a significant extension of geometrical optics (GO) in which a class of diffracted rays are introduced to exist in addition to the usual rays of GO. These diffracted rays are postulated via a generalization of Fermat's principle with the knowledge that at high frequencies diffraction, like reflection, is a highly local phenomenon. Just as reflected rays originate from points of specular reflection on an illuminated surface, the diffracted rays likewise originate from certain localized parts on the surface; e.g., from geometrical and electrical discontinuities, and from points of grazing incidence on a smooth convex surface as shown in Figure 1.

The shadow boundaries divide the space surrounding an illuminated body into a lit region where the GO incident, reflected and refracted rays are present, and into a shadow region where these GO rays are absent. Thus, the GO approach is seriously in error within the shadow region where it predicts a zero field; this limitation of GO is overcome by the GTD since the diffracted rays penetrate into the GO shadow zone to entirely account for the field therein. Furthermore, the diffracted rays can also enter into the lit region and thereby provide an improvement to GO in the lit region. The total GTD field is a superposition of the field of all the GO incident, reflected and refracted rays together with the field of all the diffracted rays which pass through the observation point. The initial values of the diffracted ray fields are given in terms of the diffraction coefficients just as the initial amplitudes of the GO reflected and refracted rays are given in terms of the reflection and transmission coefficients.

Due to the local nature of diffraction at high frequencies, the diffraction coefficients can be found from the appropriate solutions to simpler canonical problems which model the geometrical and electrical properties in the neighborhood of the point of diffraction as in the original problem. Consequently, the GTD provides an efficient high frequency solution to problems that cannot be solved rigorously. Thus, a GTD analysis of the radiation/scattering from complex shapes can be developed by simulating these structures with simpler shapes that locally provide a sufficiently accurate description of the dominant reflection and diffraction effects. The GTD can also be useful in providing information on ways to control the radiation/scattering from different parts of the structure. It is interesting that even though GTD is a high frequency method, it is often found to work for objects nearly as small as a wavelength in size. Although GTD is not a rigorous method, it generally yields the leading terms in the asymptotic high frequency solutions of diffraction problems.

Since the GTD is a purely ray optical theory, it fails within the transition regions adjacent to the GO shadow boundaries where the HF field generally undergoes a rapid transition across the shadow boundary from one ray optical form in the lit region to another ray optical form in the shadow region. Consequently, the HF field departs from a strictly ray optical character within the GO shadow boundary transition regions. This failure of the original GTD can be overcome by uniform versions of the GTD such as the UTD [4,5] and the UAT [6]. In the present development, the focus will be on the UTD. Basically, the UTD remains valid within the GO shadow boundary transition regions where the ordinary GTD fails, and secondly, it reduces to the GTD outside these transition regions where the latter is indeed valid.

The GTD and its uniform versions (UTD/UAT) fail within the regions of GO and diffracted ray caustics. Ray caustics or foci occur whenever a family of rays (i.e., ray congruences) merge or intersect to form a focal surface, or a focal line or a focal point. The field near diffracted ray caustics can be described with the help of the equivalent current method (ECM) [7,8,9] in which the GTD indirectly provides the strengths of these equivalent currents that radiate fields at and near the caustics. Away from the boundaries and caustics do not overlap. In the latter situation, ECM could in some cases still be used but only after significant modification; alternatively, the physical theory of diffraction (PTD) can be employed. The PTD was introduced by Ufimtsev [10] in the Soviet Union at about the same time as Keller's GTD was introduced in the U.S. The PTD requires an integration of the asymptotic HF currents on the radiating/scattering body. If the PTD integrals can be evaluated asymptotically outside the confluence of GO shadow boundary and caustic regions, then it generally reduces to the GTD. However, in some special instances, the GTD can be made to work without resorting to ECM or PTD despite a presence of a confluence

AD-P005 645

of caustic and GO shadow boundary transition regions. Away from the special regions where it may be necessary to use ECM or PTG, it is natural to employ the more efficient GTD/UTD which unlike the ECM and PTG requires no integration [11].

These notes will deal mostly with the diffraction by perfectly-conducting surfaces in free space. The GTD formulation is presented after briefly introducing the concept of wavefronts, rays and GO in Section II. Next, the UTD is discussed and UTD expressions are given for the two main diffraction mechanisms; namely, for edge diffraction and diffraction at a smooth convex surface. Other UTD solutions are not included due to space limitations. Finally, a few examples illustrating the utility of UTD to analyze radiation and scattering problems are given in Section III. An $e^{j\omega t}$ time dependence is assumed and suppressed in the following development.

II. THE GTD AND ITS UNIFORM VERSION -- THE UTD

The basic ideas of wavefronts, rays and GO are briefly reviewed at first. Diffracted rays which exist in addition to the GO rays are discussed subsequently.

A. Wavefronts and Rays

A wavefront is an equiphase surface. The connection between wavefronts and rays can be made in several ways. One such procedure which is based on the method of stationary phase is described below. Let $\vec{E}(\vec{r}')$ and $\vec{H}(\vec{r}')$ refer to the electric and magnetic field intensities at any point \vec{r}' on an equiphase (or wavefront) surface S . The electric field $\vec{E}(\vec{r})$ at a point P ahead of the wavefront is provided by the equivalence theorem as:

$$\vec{E}(\vec{r}) = \iint_S ds' \left(\frac{jkZ_0}{4\pi} \right) [\hat{R} \times \hat{R} \times \vec{J}_s(\vec{r}') + Y_0 \hat{R} \times \vec{M}_s(\vec{r}')] \frac{e^{-jkR}}{R} \quad (1)$$

in which the equivalent electric and magnetic surface current sources \vec{J}_s and \vec{M}_s , respectively on S are

$$\vec{J}_s(\vec{r}') = \hat{n}' \times \vec{H}(\vec{r}'); \quad \vec{M}_s(\vec{r}') = \vec{E}(\vec{r}') \times \hat{n}' \quad (2a, 2b)$$

The quantity Z_0 denotes the impedance of free space, and $Y_0 = (Z_0)^{-1}$. Also, k represents the wave number of free space. The vector \vec{R} and the unit normal vector \hat{n}' to the surface S at \vec{r}' are shown in Figure 2.

Consider a rectangular coordinate system chosen for convenience so that the x and y axes are tangent to the wavefront at O , and $\vec{OP} = \hat{z}|\vec{OP}|$ as in Figure 2. It is noted that $\hat{n}' = \hat{z}$ at O . It is generally true that there is at least one point O on S so that $\vec{OP} = \hat{n}'|\vec{OP}|$; however, for the present development it is assumed that there is only one such point O . If there are more points on S with the above property such that the \hat{n}' directions from those points intersect at P , then P is said to be a focal or caustic point.

From the principle of stationary phase as described for example by Silver [12], the e^{-jkR} within the integrand of (1) oscillates rapidly for large k to produce a cancellation (destructive interference) between each of the spherical wave contributions to P which arise from the different elemental sources on

ds' over S that do not lie in the immediate neighborhood of O ; whereas, e^{-jkR} changes slowly for the spherical wave contributions to P arising from the elemental sources on ds' that are in the immediate neighborhood of O and thereby provide a constructive interference to P . Thus, at high frequencies (or large k), the dominant field contribution to P comes from O on S ; this point O is called the "stationary point." Without details (which can be found in [12]), the stationary phase evaluation of (1) yields the following contribution from the stationary point:

$$\vec{E}(P) = \vec{E}(O) \sqrt{\frac{\rho_1}{(\rho_1+s)} \frac{\rho_2}{(\rho_2+s)}} e^{-jks}; \quad |\vec{OP}| = s \quad (3)$$

The expression in (3) describes the continuation of the field at O to the field at P along the highly localized or "ray" path \vec{OP} ; the field $\vec{E}(P)$ in (3) is thus referred to as a ray optical field. Figure 3 shows a ray tube interpretation of the energy transport along the central ray \vec{OP} as indicated by (3). The ρ_1 and ρ_2 in (3) refer to the principal wavefront radii of curvatures at O . From Figure 3 one notes that the energy flux crossing the area dA_0 of the wavefront at O is given by $|\vec{E}(O)|^2 dA_0$, and likewise, the energy flux crossing the area dA_P of the same ray tube is $|\vec{E}(P)|^2 dA_P$. Since $dA_0 = (\rho_1 d\psi_1)(\rho_2 d\psi_2)$ and $dA_P = [(\rho_1+s)d\psi_1][(\rho_2+s)d\psi_2]$, it is then clear that conservation of energy in a ray tube, which in turn requires that $|\vec{E}(O)|^2 dA_0 = |\vec{E}(P)|^2 dA_P$, leads to

$$|\vec{E}(P)|^2 = |\vec{E}(O)|^2 \left(\frac{\rho_1 \rho_2}{(\rho_1+s)(\rho_2+s)} \right) \quad (4)$$

which is automatically implied in (3). The field $\vec{E}(P)$ at P has the same polarization as the field $\vec{E}(O)$ at O because the ray path is straight in a homogeneous medium. The field intensity in (3) becomes singular when $s = -\rho_1$ or $s = -\rho_2$; these points on the ray path are marked (3-4) and (1-2) in Figure 3, and they are referred to as ray caustics. The actual field is not singular at the caustics; clearly the simple expression in (3) is therefore not valid at and near the caustics even though it is asymptotically accurate away from the caustics. The distances ρ_1 and ρ_2 are also referred to as caustic distances. The distance s is measured positive in the direction of ray propagation. The caustic distances ρ_1 and ρ_2 are

positive if the caustics occur before the reference point 0 as one propagates along the ray; otherwise, they are negative. If ρ_1 and ρ_2 are positive, the wavefront is convex; if they are negative, the wavefront is concave. If one of the radii (ρ_1 or ρ_2) is positive while the other is negative then the wavefront is saddle-shaped. If ρ_1 and ρ_2 are negative, and if $s > -|\rho_1|$, or $s > -|\rho_2|$, then a caustic is crossed at (3-4) or (1-2) in Figure 3, respectively so that $\{(\rho_1)/(\rho_1+s)\}$ or $\{(\rho_2)/(\rho_2+s)\}$ changes sign within the square root of (3). The positive branch of the square root is chosen in (3) so that

$$\sqrt{\frac{\rho}{\rho+s}} = \left| \sqrt{\frac{\rho}{\rho+s}} \right| e^{j(\pi/2)} \quad , \quad \text{if } \left(\frac{\rho}{\rho+s}\right) \leq 0 \quad (5)$$

and $\rho = \rho_1$ or ρ_2 . Thus, a phase jump of $\pi/2$ occurs at each caustic crossing.

The field in (3) is sometimes also referred to as an "arbitrary" ray optical field since ρ_1 and ρ_2 can be "arbitrary." The geometry in Figure 3 is referred to as an astigmatic ray tube or a quadratic ray pencil because of the quadratic wavefront surface approximation at 0 that is used in the stationary phase approach leading to (3). It is noted that if ρ_1 and ρ_2 become infinite, then the field in (3) is that of a plane wave. If ρ_1 or ρ_2 become infinite then (3) is a cylindrical wave field. Also, if $\rho_1 = \rho_2$ (finite value), then (3) is a spherical wave field. Thus, plane, cylindrical, spherical and even conical wave fields are special cases of an arbitrary ray optical field; clearly, it follows that each of these fields is also ray optical.

Since the wavefront surface S in Figure 3 can be associated with either an incident, reflected or diffracted wave, the field expression in (3) therefore applies equally to incident, reflected or diffracted rays. The field is polarized transverse to the ray and the wavefront at P is "locally" plane if ks is sufficiently large (as is assumed to be true in the stationary phase evaluation leading to (3)); also, the local plane wave relation between \vec{E} and \vec{H} holds, namely:

$$\vec{H}(P) = Y_0 \hat{s} \times \vec{E}(P) \quad (6)$$

or

$$\vec{E}(P) = -Z_0 \hat{s} \times \vec{H}(P) \quad (7)$$

in which $\hat{s} = \vec{OP}/|\vec{OP}|$ is the ray direction.

8. The GO Field

The GO field is a ray optical field. The incident GO field is associated with rays directly radiated from the source to the field point. When such an incident ray congruence strikes an object, it is transformed into a reflected ray congruence. Since the present notes deal mostly with scattering by impenetrable objects, there are no transmitted or refracted rays produced in this case. The incident and reflected GO rays satisfy Fermat's principle which makes the incident and reflected ray paths an extremal. Consider a plane wave incident on a perfectly-conducting wedge or a smooth convex surface as shown in Figures 4(a) or 4(b). The incident rays are partly blocked by these surfaces creating the so-called shadow zone where the incident ray optical field vanishes. The incident shadow boundary ISR in Figure 4(a) and the surface shadow boundary SSR in Figure 4(b) divide the region of space surrounding the wedge and the convex surface into a lit zone and a shadow zone.

It is important to note that unlike the conventional incident field which is defined to exist in the absence of any scattering objects, the GO incident ray field exists in the presence of any objects that it might illuminate. It is for this reason that the GO incident field becomes discontinuous across the shadow boundaries ISR and SSR in Figures 4(a) and 4(b). On the other hand, the conventional incident field would not be discontinuous anywhere outside the source region which produced that field. Henceforth, the GO incident electric and magnetic fields will be denoted by \vec{E}^i and \vec{H}^i , respectively.

The field of the GO reflected rays that are produced by the illuminated wedge in Figure 4(a) is also discontinuous. In particular, the reflection shadow boundary (RSR) delineates the regions of existence and shadow for the reflected rays in Figure 4(a); whereas, the incident and reflection shadow boundaries ISR and RSR merge into the SSR for the convex surface in Figure 4(b).

Consider a general problem of reflection where an arbitrary GO incident ray optical field illuminates a smooth, perfectly-conducting curved surface. The astigmatic incident ray tube associated with the incident ray in the direction \hat{s}^i is shown in Figure 5. This incident ray strikes the surface at Ω_R to produce a reflected ray in the direction \hat{s}^r . The astigmatic reflected ray tube associated with the reflected ray from Ω_R is also shown in Figure 5. The field $\vec{E}^r(P)$ at P which is reflected from Ω_R can be written via (3) as:

$$\vec{E}^r(P) = \vec{E}^r(\Omega_R) \sqrt{\frac{\rho_1^r \rho_2^r}{(\rho_1^r + s^r)(\rho_2^r + s^r)}} e^{-jks^r} \quad (8)$$

It is noted that $\vec{E}^r(P)$ in (8) is given in terms of $\vec{E}^r(\Omega_R)$ at the point of reflection Ω_R . Thus, the reference point 0 in (3) corresponds to the point Ω_R in (8). The caustic distances ρ_1^r and ρ_2^r associated with the reflected wavefront are shown in Figure 5 along with the reflected ray distance s^r from Ω_R to P . The value of $\vec{E}^r(\Omega_R)$ is related to the incident field $\vec{E}^i(\Omega_R)$ via the boundary condition

$$\hat{n} \times (\vec{E}^i(Q_R) + \vec{E}^r(Q_R)) = 0 \quad (9)$$

Here, \hat{n} is the unit normal vector to the surface at Q_R . It follows from (9) that

$$\vec{E}^r(Q_R) = \bar{R} \cdot \vec{E}^i(Q_R) \quad (10)$$

where \bar{R} is the dyadic reflection coefficient of the surface at Q_R . Incorporating (9) into (8) yields

$$\vec{E}^r(P) = \vec{E}^i(Q_R) \cdot \bar{R} \sqrt{\frac{\rho_1^r}{\rho_1^r + s^r} \cdot \frac{\rho_2^r}{\rho_2^r + s^r}} e^{-jks^r} \quad (11)$$

The reflected magnetic field $\vec{H}^r(P)$ is found easily from (11) via

$$\vec{H}^r(P) \sim Y_0 \hat{s}^r \times \vec{E}^r(P) \quad (12)$$

It is convenient to express $\vec{E}^i(Q_R)$ and $\vec{E}^r(P)$ in terms of the unit vectors $(\hat{e}_i^i, \hat{e}_\perp^i)$ and $(\hat{e}_i^r, \hat{e}_\perp^r)$ which are fixed in the incident and reflected rays, respectively, as shown in Figure 6. The $\hat{e}_i^i, \hat{e}_\perp^i$ and \hat{s}^i are mutually orthogonal; likewise, $\hat{e}_i^r, \hat{e}_\perp^r$ and \hat{s}^r are also a mutually orthogonal set. Furthermore, \hat{e}_i^i and \hat{e}_i^r lie in the plane of incidence defined by \hat{s}^i and \hat{n} at Q_R . As a result of Fermat's principle, \hat{s}^r also lies in the plane of incidence and $\theta^i = \theta^r$ in Figure 6. Thus, if

$$\vec{E}^i(Q_R) = E_i^i(Q_R) \hat{e}_i^i + E_\perp^i(Q_R) \hat{e}_\perp^i \quad (13)$$

and

$$\vec{E}^r(P) = E_i^r(P) \hat{e}_i^r + E_\perp^r(P) \hat{e}_\perp^r \quad (14)$$

where $\hat{e}_\perp^r = \hat{s}^i \times \hat{e}_i^r$, then \bar{R} in (10) subject to the boundary condition (9) becomes

$$\bar{R} = \hat{e}_i^i \hat{e}_i^r R_h + \hat{e}_\perp^i \hat{e}_\perp^r R_s \quad ; \quad R_h = \pm 1 \quad (15)$$

In matrix notation, the above \bar{R} can be written as

$$\begin{bmatrix} R_h & 0 \\ 0 & R_s \end{bmatrix} = \begin{bmatrix} 1 & 0 \\ 0 & -1 \end{bmatrix} \quad (16)$$

Therefore, in matrix notation, (11) becomes

$$\begin{bmatrix} E_i^r(P) \\ E_\perp^r(P) \end{bmatrix} = \begin{bmatrix} 1 & 0 \\ 0 & -1 \end{bmatrix} \begin{bmatrix} E_i^i(Q_R) \\ E_\perp^i(Q_R) \end{bmatrix} \sqrt{\frac{\rho_1^r \rho_2^r}{(\rho_1^r + s^r)(\rho_2^r + s^r)}} e^{-jks^r} \quad (17)$$

The caustic distances or the principal radii of curvature of the incident and reflected wavefronts which are denoted by (ρ_1^i, ρ_2^i) and (ρ_1^r, ρ_2^r) , as well as their principal wavefront directions are given in [13].

It is clear that the GO representation of (11) fails at caustics which are the intersection of the paraxial rays (associated with the ray tube or pencil) at the lines 1-2 and 3-4 as shown in Figure 3.

Upon crossing a caustic in the direction of propagation, $(\rho_1^i + s^i, \rho_2^i + s^i)$ changes sign under the radical in and a phase jump of $\pm\pi/2$ results as explained earlier. Furthermore, the reflected field \vec{E}^r of (11) fails in the transition region adjacent to SSR of Figure 4(h). It is important to note that near the SSR (i.e., as $\theta^i \rightarrow \pi/2$), ρ_1^r and ρ_2^r approach the following limiting values:

$$\rho_2^r = \frac{\rho_g(0_R) \cos \theta^i}{2} + 0 \quad \text{for } \theta^i \rightarrow \pi/2 \quad (18a)$$

$$\rho_1^r = \rho_h^i, \quad (18b)$$

where $\rho_g(0_R)$ is the surface radius of curvature in the plane of incidence at 0_R , and ρ_h^i is the radius of curvature of the incident wavefront in the (\hat{t}, \hat{h}) plane (i.e., in the plane tangent to the surface) at 0_R for $\theta^i \rightarrow \pi/2$. Furthermore, the principal directions $\hat{\lambda}_1^r$ and $\hat{\lambda}_2^r$ of the reflected wavefront approach the following values for grazing incidence:

$$\hat{\lambda}_1^r = \hat{h} \quad (\text{at } 0_R) \quad (19)$$

$$\hat{\lambda}_2^r = (-\hat{s}^r \times \hat{\lambda}_1^r) + \hat{n} \quad (\text{at } 0_R) \quad (20)$$

where \hat{t} is the direction of grazing incidence at 0_R and $\hat{h} = \hat{t} \times \hat{n}$ at 0_R . The total GO electric field E^{GO} at P_L in the lit region is the sum of the incident and reflected ray optical fields; hence,

$$\bar{E}^{GO}(P_L) \sim \bar{E}^i(P_L) + \bar{E}^r(0_R) \cdot \bar{R} \sqrt{\frac{\rho_1^r \rho_2^r}{(\rho_1^r + s^r)(\rho_2^r + s^r)}} e^{-jks^r} \quad (21)$$

In summary, it is noted that the GO incident and reflected fields are discontinuous across their associated shadow boundaries such as ISB, RSB, and SSB in Figures 4(a) and 4(b). The failure of GO to account for a proper non-zero field within the shadow region behind an impenetrable obstacle can be overcome through the GTD and its uniform versions. Nevertheless, GO generally yields the dominant contribution to the total high frequency fields, and it constitutes the leading term in the GTD solution.

The reflected GO field $E^r(P_L)$ for the two-dimensional (2-D) case can be deduced directly from the 3-D case by allowing ρ_1^r to approach infinity. Thus, one may let $\rho_2^r \equiv \rho^r$ and $\rho_1^r \rightarrow \infty$ in (11) to arrive at the 2-D reflected GO field $\bar{E}^r(P_L)$ as

$$\bar{E}^r(P_L) = \bar{E}^i(0_R) \cdot \bar{R} \sqrt{\frac{\rho^r}{\rho^r + s^r}} e^{-jks^r} \quad (22)$$

in which the incident ray optical field $\bar{E}^i(0_R)$ is now a cylindrical wave at 0_R , and the caustic distance ρ^r in (22) for the 2-D case is given by

$$\frac{1}{\rho^r} = \frac{1}{s^i} + \frac{2\cos^{-1}\theta^i}{\rho_g(0_R)} \quad (23)$$

where θ^i has the same meaning as before, and s^i is the radius of curvature of the incident cylindrical wavefront at 0_R . If the cylindrical wave is produced by a 2-D line source, then s^i in (22) can be chosen to be the distance from that line source to the point of reflection 0_R on the 2-D boundary. The quantity $\rho_g(0_R)$ in (23) denotes the radius of curvature of the 2-D boundary at the point of reflection 0_R .

C. The Diffracted Ray Fields

The diffracted rays are introduced in the GTD via a generalization of Fermat's principle as stated previously. Away from the point of diffraction, the diffracted rays behave according to the laws of GO. The initial value of the diffracted ray field is given in terms of a diffraction coefficient. The phenomenon of edge diffraction will be discussed first, and it will be followed by a discussion on the phenomenon of diffraction at a smooth convex surface. The latter phenomenon is more complicated than the first.

(i) Edge Diffraction

When an incident ray strikes an edge in an otherwise smooth surface, it produces diffracted rays which lie on a cone about the tangent to the edge at the point of diffraction such that the angle β_0 between the incident ray and the edge tangent equals the half angle of the diffracted ray cone as shown in Figure 1(a). This cone of diffracted rays is sometimes referred to as the "Keller cone," and it results from the generalization of Fermat's principle to describe rays diffracted by an edge.

Let an arbitrary ray optical field be incident on a perfectly-conducting curved wedge as shown in Figure 7. The resultant total HF electric field $\vec{E}(P)$ at any point P exterior to the wedge is given by

$$\vec{E}(P) = \vec{E}^{GO}(P) + \vec{E}^d(P) \quad (24)$$

where the GO field component $\vec{E}^{GO}(P)$ is given as

$$\vec{E}^{GO}(P) = \vec{E}^i(P)U_i + \vec{E}^r(P)U_r \quad (25)$$

The domains of existence of the incident and reflected ray optical fields $\vec{E}^i(P)$ and $\vec{E}^r(P)$ are indicated by the step functions U_i and U_r , respectively, which are defined as follows:

$$U_i = \begin{cases} 1, & \text{if } 0 < \phi < \pi + \phi' \\ 0, & \text{if } \pi + \phi' < \phi < n\pi \end{cases} \quad (26)$$

and

$$U_r = \begin{cases} 1, & \text{if } 0 < \phi < \pi - \phi' \\ 0, & \text{if } \pi - \phi' < \phi < n\pi \end{cases} \quad (27)$$

The azimuthal angles ϕ and ϕ' are made by the projections of the directions of incidence and observation on a plane perpendicular to the edge at the point of diffraction O_E . These angles are measured from a plane tangent to the "0" face of the wedge at O_E as shown in Figure 8. The plane tangent to the other face of the wedge at O_E is denoted by " $n\pi$;" it is also shown in Figure 8.

The interior wedge angle is therefore given by $(2-n)\pi$. The expressions for the GO incident and reflected fields have been discussed previously. The diffracted field \vec{E}^d exists exterior to the wedge (i.e., for $0 < \phi < n\pi$). From (2), one may write the general field expression for the ray diffracted in the direction \hat{s}^d from O_E as:

$$\vec{E}^d(P) \sim \vec{E}^d(P_0) \sqrt{\frac{\rho_1^d \rho_2^d}{(\rho_1^d + s_0^d)(\rho_2^d + s_0^d)}} e^{-jks_0^d} \quad (28)$$

The diffracted ray tube corresponding to (28) is shown in Figure 7. The superscript "d" on ρ_1^d, ρ_2^d , and s_0^d denotes that these quantities are associated with the diffracted ray field component. In order to relate $\vec{E}^d(P)$ to the incident field at the point of edge diffraction O_E , one moves the reference P_0 in Figure 7 to the point of diffraction O_E on the edge by letting $\rho_1^d \rightarrow 0$ so that

$$\vec{E}^d(P) = \lim_{\rho_1^d \rightarrow 0} [\sqrt{\rho_1^d} \vec{E}^d(P_0)] \sqrt{\frac{\rho_2^d}{(\rho_1^d + s_0^d)(\rho_2^d + s_0^d)}} e^{-jks_0^d} \quad (29)$$

Since $\vec{E}^d(P)$ is independent of the reference point P_0 , the above limit exists and it is defined as

$$\lim_{\rho_1^d \rightarrow 0} \sqrt{\rho_1^d} \vec{E}^d(P_0) \equiv \vec{E}^i(O_E) \cdot \vec{D}_e^k \quad (30)$$

where $\vec{D}_e^k = \vec{D}_e^k(\phi, \phi', \beta_0; k)$ is Keller's "dyadic edge diffraction coefficient" which indicates how the energy is distributed in the diffracted field as a function of the angles ϕ , ϕ' , and β_0 ; \vec{D}_e^k also depends on n and the wavenumber k . From (29) and (30), it is clear that

$$\vec{E}^d(P) \sim \vec{E}^i(O_E) \cdot \vec{D}_e^k(\phi, \phi', \beta_0; k) \sqrt{\frac{\rho_e}{s^d(\rho_e + s^d)}} e^{-jks^d} \quad (31)$$

where $\lim_{\rho_1^d \rightarrow 0} \rho_2^d \equiv \rho_e$ (edge diffracted ray caustic distance), and likewise $\lim_{\rho_1^d \rightarrow 0} s_0^d \equiv s^d$, as shown in Figure

7. $\vec{E}^d(P)$ is polarized transverse to the diffracted ray direction \hat{s}^d since the field $\vec{E}^d(P)$ is ray optical; thus, the associated magnetic field can be expressed as

$$\vec{H}^d(P) \sim Y_0 \hat{s}^d \times \vec{E}^d(P) \quad (32)$$

If the incident field $\vec{E}^i(Q_E)$ exhibits a rapid spatial variation at Q_E then an additional term referred to as a slope diffracted field must be included in (31) to describe the diffraction effects accurately; however, that slope diffracted field will not be described here. An expression for finding the diffracted ray caustic distance ρ_e is given later in (43b).

It is convenient to express the dyadic edge diffraction coefficient \vec{D}_e^k in terms of unit vectors fixed in the incident and diffracted rays as follows. Let \hat{s}^i and \hat{e} define an edge fixed plane of incidence where \hat{e} is the edge tangent at Q_E . Likewise, let \hat{s}^d and \hat{e} define the edge fixed plane of diffraction. The law of edge diffraction which defines the Keller cone is $\hat{s}^i \cdot \hat{e} = \hat{s}^d \cdot \hat{e}$. Let $\hat{\beta}_0^i$ and $\hat{\beta}_0^d$ be parallel to the edge fixed planes of incidence and diffraction, respectively as in Figure 8, and let⁹

$$\hat{\beta}_0^i = \hat{s}^i \times \hat{\phi}^i \quad ; \quad \hat{\beta}_0^d = \hat{s}^d \times \hat{\phi}^d \quad (33a; 33b)$$

Here, $\hat{\phi}$ and $\hat{\phi}^i$ point in the direction of increasing angles ϕ and ϕ^i , respectively. The incident field $\vec{E}^i(Q_E)$ can then be expressed in terms of the triad of unit vectors $(\hat{s}^i, \hat{\beta}_0^i, \hat{\phi}^i)$ fixed in the incident ray; likewise, the edge diffracted field $\vec{E}^d(P)$ can be expressed in terms of $(\hat{s}^d, \hat{\beta}_0^d, \hat{\phi}^d)$ fixed in the diffracted ray. Thus,

$$\vec{E}^i(Q_E) = \hat{\beta}_0^i E_{\beta_0^i}^i + \hat{\phi}^i E_{\phi^i}^i \quad (34a)$$

and

$$\vec{E}^d(P) = \hat{\beta}_0^d E_{\beta_0^d}^d + \hat{\phi}^d E_{\phi^d}^d \quad (34b)$$

Then

$$\vec{D}_e^k = -\hat{\beta}_0^i \hat{\beta}_0^d D_{es}^k - \hat{\phi}^i \hat{\phi}^d D_{eh}^k \quad (34c)$$

The D_{es}^k and D_{eh}^k can be found from the asymptotic solutions of appropriate canonical wedge diffraction problems; they are given by:

$$D_{\hat{e}\hat{R}}^k(\phi, \phi^i; \beta_0) = \frac{e^{-j\frac{\pi}{4}} \sin \frac{\pi}{n}}{n\sqrt{2\pi k} \sin \beta_0} \cdot \left[\frac{1}{\cos \frac{\pi}{n} - \cos \left(\frac{\phi - \phi^i}{n} \right)} + \frac{1}{\cos \frac{\pi}{n} - \cos \left(\frac{\phi + \phi^i}{n} \right)} \right] \quad (35)$$

It is noted that the Keller edge diffraction coefficient in (35) becomes singular at the incident shadow boundary (ISR) and the reflection shadow boundary (RSR) which occur when $\phi = \pi + \phi^i$ and $\phi = \pi - \phi^i$, respectively. Thus, the result in (31) together with (34c) and (35) is not valid at and near the GO incident and reflection shadow boundaries. This deficiency of the GTD can be overcome via the use of uniform geometrical theory of diffraction (UTD). According to the UTD [4,5], the total HF field exterior to the wedge is still given by (24) as in Keller's original GTD; however, the \vec{E}^d in (24) and (31) is now modified so that \vec{D}_e^k of (31) is replaced by the UTD edge diffraction coefficient \vec{D}_e^k so that:

$$\vec{E}^d(P) = \vec{E}^i(Q_E) \cdot \vec{D}_e(\phi, \phi^i; \beta_0; k) \sqrt{\frac{\rho_e}{s^d(\rho_e + s^d)}} e^{-jks^d} \quad (36a)$$

The \vec{D}_e in (36a) can also be expressed as

$$\vec{D}_e = -\hat{\beta}_0^i \hat{\beta}_0^d D_{es} - \hat{\phi}^i \hat{\phi}^d D_{eh} \quad (36b)$$

In matrix notation, (36a) becomes

$$\begin{bmatrix} E_{\beta_0^d}^d \\ E_{\phi^d}^d \end{bmatrix} = \begin{bmatrix} -D_{es} & 0 \\ 0 & -D_{eh} \end{bmatrix} \begin{bmatrix} E_{\beta_0^i}^i \\ E_{\phi^i}^i \end{bmatrix} \sqrt{\frac{\rho_e}{s^d(\rho_e + s^d)}} e^{-jks^d} \quad (37)$$

in which the D_{es} and D_{eh} are [13]:

$$D_{\text{EIR}}(\phi, \phi'; \beta_0) = \frac{-e^{-j\frac{\pi}{4}}}{2n\sqrt{2\pi k} \sin \beta_0} \left[\cot\left(\frac{\pi+(\phi-\phi')}{2n}\right) F[kL^i a^+(\phi-\phi')] + \cot\left(\frac{\pi-(\phi-\phi')}{2n}\right) F[kL^i a^-(\phi-\phi')] \right] \\ + \left[\cot\left(\frac{\pi+(\phi+\phi')}{2n}\right) F[kL^{rn} a^+(\phi+\phi')] + \cot\left(\frac{\pi-(\phi+\phi')}{2n}\right) F[kL^{ro} a^-(\phi+\phi')] \right] \quad (3A)$$

where the asymptotic large parameter kL (with the superscripts i , rn , ro on L omitted for convenience) is required to be sufficiently large (generally greater than 3) and

$$a^\pm(\beta) = 2 \cos^2\left(\frac{2n\pi N^\pm - \beta}{2}\right) \quad (39a)$$

The N^\pm are the integers which most nearly satisfy the equation:

$$2n\pi N^\pm - \beta = \pm\pi \quad (39b)$$

with

$$\beta = \phi \pm \phi' \quad (39c)$$

Note that $n=2$ for a half plane or a semi-infinite curved screen. Also, $n=3/2$ for an exterior right angled wedge, etc.

For exterior edge diffraction $N^+ = 0$ or 1, and $N^- = -1, 0$, or 1. The values of N^\pm at the shadow and reflection boundaries as well as their associated transition regions are given in Table I for exterior wedge angles ($1 < n < 2$):

TABLE I

	The cotangent is singular when	value of N at the boundary
$\cot\left(\frac{\pi+(\phi-\phi')}{2n}\right)$	$\phi = \phi' - \pi$, an ISR surface $\phi=0$ is shadowed	$N^+ = 0$
$\cot\left(\frac{\pi-(\phi-\phi')}{2n}\right)$	$\phi = \phi' + \pi$, an ISR surface $\phi=n\pi$ is shadowed	$N^- = 0$
$\cot\left(\frac{\pi+(\phi+\phi')}{2n}\right)$	$\phi = (2n-1)\pi - \phi'$, an RSR reflection from surface $\phi=n\pi$	$N^+ = 1$
$\cot\left(\frac{\pi-(\phi+\phi')}{2n}\right)$	$\phi = \pi - \phi'$, an RSR reflection from surface $\phi=0$	$N^- = 0$

For a point source (or spherical wave) type illumination, the distance parameter L^i is:

$$L^i = \frac{s^i s^d}{s^i + s^d} \sin^2 \beta_0 \quad (40)$$

in which s^i and s^d are the distances from the point of edge diffraction at O_c to the source and observation points, respectively. Only for a straight wedge with planar faces that is illuminated by a point source,

$$L^{ro} = L^{rn} = L^i = \frac{s^i s^d}{s^i + s^d} \sin^2 \beta_0 \quad (41)$$

as in (40). For an arbitrary ray optical illumination which is characterized by two distinct principal wavefront radii of curvature, ρ_1^i and ρ_2^i , the above L^i must be modified as shown below in the general expressions for L^{ro} and L^{rn} pertaining to a curved wedge; thus,

$$L^i = \left[\frac{s^d(\rho_1^i + s^d)\rho_2^i \sin^2 \beta_0}{\rho_1^i(\rho_1^i + s^d)(\rho_2^i + s^d)} \right] \text{ at ISR} \quad (42a)$$

$$L^r = \left[\frac{s^d (\rho_e^r + s^d) \rho_1^r \rho_2^r \sin^2 \beta_0}{\rho_e^r (\rho_1^r + s^d) (\rho_2^r + s^d)} \right] \text{ at RSB} \quad (42b)$$

Here, L^{r0} and L^{rn} are the values of L^r associated with the "0" and "n" faces of the wedge, respectively. Furthermore, ρ_e^r is given by:

$$\frac{1}{\rho_e^r} = \frac{1}{\rho_e^i} - \frac{2(\hat{n} \cdot \hat{n}_e)(\hat{s}^i \cdot \hat{n})}{a \sin^2 \beta_0} \quad (43a)$$

Also ρ_e in (36) is given by:

$$\frac{1}{\rho_e} = \frac{1}{\rho_e^i} - \frac{\hat{n}_e \cdot (\hat{s}^i - \hat{s}^d)}{a \sin^2 \beta_0} \quad (43b)$$

The unit vector \hat{n} is defined in Figure 8(b); whereas, \hat{n}_e is a unit vector normal to the edge which is directed away from the center of edge curvature at O_e . The radius of edge curvature is denoted by "a" in (43). ρ_e^i is the radius of curvature of the incident wavefront at O_e which lies in the edge fixed plane of incidence. In the far zone when $s^d \gg \rho_{1,2}^i$, $s^d \gg \rho_{1,2}^r$, and $s^d \gg \rho_e$ then the L^i and L^r in (42a) and (42b) simplify to $L = \frac{\rho_1 \rho_2 \sin^2 \beta_0}{\rho_e}$ in which the appropriate superscripts on L, ρ_1 and ρ_2 are omitted for convenience. It is noted that L^i and L^r in (42a) and (42b) are calculated on the appropriate shadow boundaries. The transition function, F which appears in (38) contains a Fresnel integral; it is defined by

$$F(x) = 2j\sqrt{x} e^{jx} \int_{\sqrt{x}}^{\infty} dt e^{-jt^2} \quad (44)$$

A plot of the above $F(x)$ is illustrated in Figure 13. In (44), $\sqrt{x} = |\sqrt{x}|$ if $x > 0$ and $\sqrt{x} = -j|\sqrt{x}|$ if $x < 0$. If $x < 0$, then $F(x) \Big|_{x < 0} = F^*(|x|)$ where * denotes the complex conjugate. Exterior to the (ISR, RSB) transition regions x becomes large and $F(x) \rightarrow 1$ so that the uniform D_{eh} in (38) then reduces to Keller's form as it should; namely,

$$\vec{D}_e = \vec{D}_e^k, \text{ outside the transition region.} \quad (45)$$

Near the (ISR and RSB) boundaries, the small argument approximation for $F(x)$ may be employed (since $x = 0$ on ISR and RSB); namely, one can incorporate

$$F(x) \underset{x \rightarrow 0}{\approx} \sqrt{\pi x} e^{j\left(\frac{\pi}{4} + x\right)} \quad (46)$$

into (38) to arrive at the following result for the diffracted field \vec{E}^d at ISR or RSB:

$$\vec{E}^d \Big|_{\text{ISR;RSB}} = \left[\frac{1}{2} \vec{E}^i; r + \begin{array}{l} \text{continuous} \\ \text{(higher order)} \\ \text{terms} \end{array} \right] \quad (47)$$

if $\left\{ \begin{array}{l} \text{on lit side of ISR;RSB} \\ \text{on shadow side of ISR;RSB} \end{array} \right\}$

The above result in (47) ensures the continuity of the total HF field in (24) at ISR and RSB. The field contribution arising from the edge excited "surface diffracted rays" is not included in (24); it may be important for observation points close to the surface shadow boundaries (SSB) associated with the tangent to the "0" and "n" faces of a curved wedge at O_e if the "0" and "n" faces are convex boundaries. The result in (36a) and (36b) along with (38) is valid away from any diffracted ray caustics and away from the edge caustic at O_e .

For grazing angles of incidence on a wedge with planar faces, $D_{es} = 0$, and D_{eh} must be replaced by $(1/2) D_{eh}$. The reason for the $1/2$ factor in the latter case is explained as follows. The incident and reflected GO fields tend to combine into a single "total incident field" as one approaches grazing angles of incidence; consequently, only half of this "total field" illuminating the edge at grazing constitutes the incident GO field while the other half constitutes the reflected GO field. The case of grazing angles of incidence at an edge in a curved surface cannot be handled as easily as the case of a wedge with planar faces. Presently, one can only treat angles of incidence that are greater than $\left[\frac{2}{k \rho_g(\eta_e)} \right]^{1/3}$ where $\rho_g(\eta_e)$ is the radius of curvature of the surface in the direction of the incident ray at the point of edge diffraction O_e .

Under the above restrictions, the result in (38) for D_{eh}^{ns} simplifies in the case of a plane or curved screen ($n=2$ case) to

$$D_{eh}^{ns}(\beta, \phi', \beta_0) = \frac{e^{-j\frac{\pi}{4}}}{2\sqrt{2\pi k} \sin\beta_0} \left[\sec\left(\frac{\beta-\beta'}{2}\right) F[kL^i a(\beta-\beta')] + \sec\left(\frac{\beta+\beta'}{2}\right) F[kL^r a(\beta+\beta')] \right] \quad (48)$$

where $a(\beta) = 2 \cos^2(\beta/2)$ and L^i, r are in (42a,b) with the understanding that L^r is evaluated at the RSR corresponding to the face which is illuminated; hence the superscripts "o" and "n" in L^r are dropped for this $n=2$ case.

The edge diffracted field $\bar{E}^d(P)$ for the 2-D situation can be obtained from (36a) by allowing ρ_a to approach infinity and by requiring $\beta_0 = \pi/2$; thus, for the 2-D case,

$$\bar{E}^d(P) = \bar{E}^i(0_E) \cdot \bar{D}_e^d(\beta, \phi', \pi/2; k) \frac{e^{-jks^d}}{\sqrt{s^d}} \quad (49)$$

The \bar{D}_e^d in (49) for the 2-D case is available from (36a) and (36b) with $\beta_0 = \pi/2$ (or $\sin\beta_0 = 1$). Also, L^i for the 2-D case is given by (41) with $\beta_0 = \pi/2$; in particular,

$$L^i = \frac{s^i s^d}{s^i + s^d} \quad (50)$$

Likewise, L^r is obtained from (42b) with $\beta_0 = \pi/2$, $\rho_1^r = \infty$, $\rho_2^r = \rho^r$ (as in (22)), and $\rho_a^r = \infty$; therefore, in the 2-D case,

$$L^r = \frac{\rho^r s^d}{\rho^r + s^d} \quad (51)$$

Note that ρ^r in (51) is the same as the one in (23); however, ρ^r is in general different for the "o" and "n" faces of the wedge, with L^{ro} and L^{rn} denoting the values of L^r for these two different faces. While the expression for L^r in (42b) is fixed to its value on the RSR for convenience, the one in (51) can be evaluated as a function of the observation point with almost the same ease as if one had approximated the value of L^r by its value at the RSR. The values of L^i and L^r for the 3-D case involve various caustic distances as is evident from (42a) and (42b). These distances are generally slowly varying within the ISR and RSR transition regions and it is therefore convenient to approximate L^i and L^r throughout the transition regions by their values at the ISR and RSR as done in (42a) and (42b). Outside the respective transition regions, the F functions containing L^i and L^r approach unity anyway unaffected by the above approximation.

It is noted that the comment below (47) in regard to grazing incidence is also valid for the 2-D case.

It is further noted that the essential difference between \bar{D}_e^k and \bar{D}_e^k is that the former is range dependent whereas the latter is not. As a result, (36a) is not ray optical within the ISR and RSR transition regions;

exterior to these regions, $\bar{D}_e^k + \bar{D}_e^k$ as indicated before. Figure 9 illustrates the diffraction of a plane wave by a perfectly-conducting half-plane. It is noted that the geometrical optics field is discontinuous; however, the UTD diffracted field cancels the GO discontinuity to yield a total UTD field which is continuous.

(ii) Diffraction at a Smooth Convex Surface

The geometry for this problem of the diffraction by a smooth convex surface is shown in Figure 10. The total high frequency field $\bar{E}(P)$ for the situation in Figure 10 can be written as

$$\bar{E}(P) = \begin{cases} \bar{E}^i(P_L)U + \bar{E}^r(P_L)U + \bar{E}^d(P_L) & , \text{ if } P = P_L \text{ in the lit zone.} \\ \bar{E}^d(P_S) [1 - U] & , \text{ if } P = P_S \text{ in the shadow zone.} \end{cases} \quad (52)$$

The incident and reflected fields \bar{E}^i and \bar{E}^r are associated with the incident and reflected GO rays shown in Figure 11. The step function U in (52) is defined below with respect to the surface shadow boundary (SSB) as:

$$U = \begin{cases} 1, & \text{in the lit region which lies above the SSB} \\ 0, & \text{in the shadow region which lies below the SSB.} \end{cases} \quad (53)$$

The surface diffracted field $\bar{E}^d(P_S)$ follows the surface diffracted ray path into the shadow region, as in Figure 11; whereas, the field $\bar{E}^d(P_L)$ which is diffracted into the lit region follows the reflected ray path (of \bar{E}^r) in this solution. Therefore, it is convenient in this problem to combine the GO reflected field $\bar{E}^r(P_L)U$ and the diffracted field $\bar{E}^d(P_L)$ into a single "generalized reflected field", $\bar{E}^{gr}(P_L)U$ in the lit region so that (52) becomes

$$\bar{E}(P) = \begin{cases} \bar{E}^i(P_L)U + \bar{E}^{gr}(P_L)U & , \text{ if } P = P_L \text{ in the lit zone.} \\ \bar{E}^d(P_S) [1 - U] & , \text{ if } P = P_S \text{ in the shadow zone.} \end{cases} \quad (54)$$

The fields $\bar{E}^{gr}(P_L)$ and $\bar{E}^d(P_S)$ are given symbolically by

$$\bar{E}^{gr}(P_L) \sim E^i(O_R) \cdot [\mathcal{R}_{se} \hat{e}_L + \mathcal{R}_{he} \hat{e}_L^r] \sqrt{\frac{\rho_s \rho_s^r}{(\rho_s^r + s^r)(\rho_s + s^r)}} e^{-jks^r} \quad (55)$$

$$\bar{E}^d(P_S) \sim E^i(O_1) \cdot [\mathcal{D}_{sh} \hat{h}_2 + \mathcal{D}_{hn} \hat{h}_2] \sqrt{\frac{\rho_s}{s^d(\rho_s + s^d)}} e^{-jks^d} \quad (56)$$

where the points O_R and O_1 , and the distances s^r and s^d are indicated in Figure 10. The surface diffracted ray caustic distance ρ_s is shown in Figure 11. The quantities within brackets involving $\mathcal{R}_{s,h}$ and $\mathcal{D}_{s,h}$ in (55) and

(56) may be viewed as generalized dyadic coefficients for surface reflection and diffraction, respectively. It is noted that (55) and (56) are expressed invariantly in terms of the unit vectors fixed in the reflected and surface diffracted ray coordinates. The unit vectors \hat{e}_L^i , \hat{e}_L^r , and \hat{e}_L in (55) have been defined earlier in connection with the reflected field. It can be shown that cross terms actually exist in the above generalized dyadic reflection coefficient; but, in general their effect is seen to be weak within the SSR transition region. Also these terms vanish in the deep lit region and on the SSR, hence they have been ignored in (55).

At O_1 , let \hat{t}_1 be the unit vector in the direction of incidence, \hat{n}_1 be the unit outward normal vector to the surface, and $\hat{h}_1 = \hat{t}_1 \times \hat{n}_1$; likewise at O_2 , let a similar set of unit vectors (\hat{t}_2 , \hat{n}_2 , \hat{h}_2) be defined with \hat{t}_2 in the direction of the diffracted ray as in Figure 12. In the case of surface rays with zero torsion, $\hat{h}_1 = \hat{h}_2$. It is clear from Figure 11 that ρ_s in (56) is the wave-front radius of curvature of the surface

diffracted ray evaluated in the \hat{h}_2 direction at O_2 . First, the UTD expressions for $\mathcal{R}_{s,h}$ and $\mathcal{D}_{s,h}$ in (55) and (56) will be given below; it will be shown that these expressions are valid within the transition region adjacent to the SSR. Subsequently, it will be shown how these expressions automatically simplify outside the SSR transition region to reduce to those obtained by Keller in his GTD representation. The $\mathcal{R}_{s,h}$ and $\mathcal{D}_{s,h}$ in (55) and (56) are [14,15]:

$$\mathcal{R}_{s,h} = - \left[\sqrt{\frac{4}{\epsilon^L}} e^{-j(\epsilon^L)} \right]_{12} \left[\frac{e^{-j\pi/4}}{2\sqrt{\pi} \epsilon^L} [1 - F(x^L)] + \tilde{p}_{s,h}(\epsilon^L) \right] \quad , \text{ for the lit region} \quad (57)$$

and

$$\mathcal{D}_{s,h} = - \left[\sqrt{m(O_1)m(O_2)} \sqrt{\frac{2}{k}} \frac{e^{-j\pi/4}}{2\sqrt{\pi} \epsilon} [1 - F(x^d)] + \tilde{p}_{s,h}(\epsilon) \right] \cdot \sqrt{\frac{dn(O_1)}{dn(O_2)}} e^{-jkt} \quad , \text{ for the shadow region} \quad (58)$$

TABLE II

Zeros of the Airy Function	Zeros of the Derivative of the Airy Function
$At(-q_p) = 0$	$At'(-\tilde{q}_p) = 0$
$q_1 = 2.33811$	$\tilde{q}_1 = 1.01879$
$q_2 = 4.08795$	$\tilde{q}_2 = 3.24820$
$At'(-q_1) = 0.70121$	$At(-\tilde{q}_1) = 0.53566$
$At'(-q_2) = -0.80311$	$At(-\tilde{q}_2) = -0.41902$

The function F appearing above has been defined earlier in (44). The Fock type surface reflection function $\tilde{p}_{s,h}$ is related to the ^{soft}(hard) Pekeris function (q^*) by

$$\tilde{p}_h(\delta) = \begin{cases} p^*(\delta) \\ q^*(\delta) \end{cases} e^{-j\frac{\pi}{4}} - \frac{e^{-j\frac{\pi}{4}}}{2\sqrt{\pi\delta}} \quad (59a)$$

$$, \quad (\text{Note that } \delta=0 \text{ at SSR}) \quad (59b)$$

where p^* and q^* are finite and well behaved even when $\delta=0$; these universal functions are plotted in Figures 13, 14 and 15. Also,

$$\tilde{p}_h(\delta) = \frac{e^{-j\frac{\pi}{4}}}{\sqrt{\pi}} \int_{-\infty}^{\infty} dt \frac{\tilde{V}(t)}{\tilde{W}_2(t)} e^{-j\delta t} ; \quad \tilde{\eta} = \begin{cases} 1 & , \text{ soft case} \\ \frac{3}{3\tau} & , \text{ hard case} \end{cases} \quad (60a)$$

in which the Fock type Airy functions $V(t)$ and $W_2(t)$ are

$$2jV(t) = W_1(t) - W_2(t) ; \quad W_1(t) = \frac{1}{\sqrt{\pi}} \int_{-\infty}^{\infty} dt e^{it-t^3/3} ; \quad (61a;61b)$$

$$W_2(t) = \frac{1}{\sqrt{\pi}} \int_{-\infty}^{\infty} j2\pi/3 dt e^{it-t^3/3} . \quad (61c)$$

The rest of the quantities occurring in (57) and (58) are:

$$\xi^L = -2m(\rho_R) \cos \theta^i ; \quad \xi = \int_{\rho_1}^{\rho_2} dt' \frac{m(\xi')}{\rho_g(\xi')} ; \quad m(\cdot) = \left[\frac{k \rho_g(\cdot)}{2} \right]^{1/3} \quad (62;63;64)$$

$$t = \int_{\rho_1}^{\rho_2} dt' ; \quad x^L = 2kL \cos^2 \theta^i ; \quad x^d = \frac{kL (\xi^L)^2}{2m(\rho_1)m(\rho_2)} . \quad (65;66;67)$$

The quantity $\rho_g(\rho_R)$ in $m(\rho_R)$ denotes the surface radius of curvature at ρ_R in the plane of incidence;

whereas, $\rho_g(\rho_1)$ is the surface radius of curvature at ρ_1 in the \hat{t}_1 direction. The dt' in (63) and (65) is an incremental arc length along the surface ray path. The angle of incidence θ^i is shown in Figure 6. Also, the $dn(\rho_1)$ and $dn(\rho_2)$ in (58) denote the widths of the surface ray tube at ρ_1 and ρ_2 , respectively; the surface ray tube is formed by considering a pair of rays adjacent to the central ray as in Figure 11. The geodesic surface ray paths are easy to find on cylinders, spheres, and cones. For example, the geodesic paths on a convex cylinder are helical; whereas, they are great circle paths on a sphere. For more general convex surfaces, the geodesic surface ray paths must be found numerically. The distance parameter L in (66) and (67) is given by

$$L = \frac{\rho_1^i(\rho_1) \rho_2^i(\rho_1)}{(\rho_1^i(\rho_1)+s)(\rho_2^i(\rho_1)+s)} \cdot \frac{s(\rho_h^i(\rho_1)+s)}{\rho_h^i(\rho_1)} , \quad (68)$$

where:

$$s \equiv \left. \begin{matrix} s^r \\ \text{SSR} \end{matrix} \right|_{\text{SSR}} = \left. \begin{matrix} s^d \\ \text{SSR} \end{matrix} \right|_{\text{SSR}} ; \quad \rho_h^i(\rho_1) = \begin{cases} \text{incident wavefront radius of curvature} \\ \text{in the } \hat{h}_1 \text{ direction at } \rho_1. \end{cases} \quad (69;70)$$

The distance s in (68) may be obtained by projecting $(\xi^L)^r$ on the SSR if the observation point within the (lit/shadow) side of the SSR transition region does not move in a predetermined manner. If the observation point moves across the SSR in a predetermined fashion then it is clear that s in (68;69) can be found unambiguously.

The $\rho_1^i(\rho_1)$ and $\rho_2^i(\rho_1)$ in (68) denote the principal radii of curvature of the incident wavefront at ρ_1 , and ρ_h^i , which is defined in (70), has been introduced earlier in (18b). For the special case of point source or spherical wave illumination, the L in (66) and (67) simplifies to:

$$L = \frac{s's}{s'+s} , \quad \text{for spherical wave illumination,} \quad (71)$$

where:

$$s' \equiv (\rho_1^i(\rho_1) = \rho_2^i(\rho_1) = \rho_h^i(\rho_1)) = \begin{cases} \text{distance from the point source to the} \\ \text{point of grazing incidence at } \rho_1. \end{cases} \quad (72)$$

In the case of plane wave illumination, $s' = \infty$ and hence (71) above simplifies to:

$L = s$, for plane wave illumination.

(73)

If the incident wavefront is of the converging $\rho_1, \rho_2 < 0$, or converging-diverging ($\rho_1 < 0; \rho_2 > 0$) type, then the parameter L in (68) can become negative. It has not been fully investigated how the general solution can be completed if L becomes negative. On the other hand, if one of the principal directions of the incident wavefront coincides with one of the principal planes of the surface at grazing, then one can treat a converging, or converging-diverging (saddle) type wavefront for which $L < 0$, by replacing $F(x^{L,d})$ with $F^*(|x^{L,d}|)$. Note that the asterisk on F^* denotes the complex conjugate operator. The use of $F^*(|x^{L,d}|)$ when $L < 0$ leads to a continuous total field at SSR in this case.

The above UTD result remains accurate outside the paraxial (i.e. near axial) regions of quasi-cylindrical or elongated convex surfaces; a different solution is required in these regions and it has not yet been completed. It is assumed that the source and observation points are not too close to the surface. Also, it is assumed that any caustics of the incident ray system are not too close to the surface. Furthermore, the amplitude of the incident field is assumed to be slowly varying at Ω_0 and Ω_1 ; otherwise, it is necessary to add a slope diffraction contribution. The UTD solution described above remains accurate if kl and m are sufficiently large. Typically kl should be larger than 3 although in some cases kl can be made smaller. Also m should be such that $2m^2 > 5$ or so; however, the results generally lose their accuracy slowly as $2m^2$ becomes smaller. It is noted that the angular extent of the SSR transition region is of order m^{-1} radians.

A surface diffracted field of the type $\bar{E}_s^d(p_s)$ can also be present in the lit zone if the surface is closed; this may be seen by noting that the field of the type \bar{E}^d can propagate around the closed surface.

Also, additional contributions to $\bar{E}^d(p_s)$ can be present in the shadow zone for a closed surface because surface diffracted rays can be initiated at all points of grazing incidence on that closed surface; furthermore, these surface rays can undergo multiple encirclements around the closed body. However, these

additional surface diffracted ray contributions are generally quite weak in comparison to the \bar{E}^{GR} contribution within the lit zone for surfaces which are quite large in terms of the wavelength; hence their contribution may be neglected in such cases.

The parameters $\epsilon^1, \epsilon, x^1$ and x^d become small as one approaches the surface shadow boundary, SSR, from both the lit and shadow regions. As one approaches the SSR, the small argument limiting form of the transition function $F(x)$ which has been introduced previously in (44) becomes helpful for verifying the continuity of the total high frequency field at the SSR. On the other hand, the above parameters become large as one moves outside the SSR transition region; in this case $F(x) \rightarrow 1$ for large x , and likewise,

$$\left. \frac{\bar{p}_s(\delta)}{h} \right|_{\delta < 0} \sim \pm \sqrt{\frac{-\delta}{4}} e^{j\delta^3/12} \quad (74)$$

$$\left. \frac{\bar{p}_s(\delta)}{h} \right|_{\delta > 0} = \begin{cases} -\frac{e^{-j\pi/4}}{\sqrt{\pi}} \sum_{n=1}^N \frac{e^{j\pi/6} \delta q_n e^{-j5\pi/6}}{2[Ai^2(-q_n)]^2} \\ -\frac{e^{-j\pi/4}}{\sqrt{\pi}} \sum_{n=1}^N \frac{e^{j\pi/6} \delta \bar{q}_n e^{-j5\pi/6}}{2[\bar{q}_n Ai(-\bar{q}_n)]^2} \end{cases} \quad (75)$$

where $N = 2$ is generally sufficient to compute $\bar{p}_s(\delta)$ accurately for $\delta > 0$ in (75). In (75) and Table II, the Miller type Airy function $Ai(\tau) = V(\tau)/\sqrt{\pi}$, and $Ai^h(\tau) = \frac{d}{d\tau} Ai(\tau)$. Thus, upon incorporating the limiting values of (74) and (75), which are valid outside the SSR transition region, into (57) and (58) and replacing $F(x)$ by its asymptotic value of unity, it is clear that \bar{R}_s reduces to $R_s = \pm 1$ outside the SSR transition region so that $\bar{E}^{GR}(p_L) + \bar{E}^r(p_L)$ of (60), and likewise $\bar{E}^d(p_s) + \bar{E}_k^d(p_s)$ therein, respectively, in which the Keller surfaced diffracted ray field $\bar{E}_k^d(p_s)$ is given by [3]

$$\bar{E}_k^d(s) \sim \bar{E}^i(\Omega_1) \cdot \bar{T}^k(\Omega_1, \Omega_2) e^{-jkt} \sqrt{\frac{dn(\Omega_1)}{dn(\Omega_2)}} \sqrt{\frac{\rho_s}{s^d(\rho_s + s^d)}} e^{-jks^d} \quad (76)$$

$$\bar{T}^k(\Omega_1, \Omega_2) = \left[\hat{h}_1 \hat{h}_2 T_s + \hat{n}_1 \hat{n}_2 T_h \right] \quad (77)$$

where

$$T_h = \sum_{n=1}^N \frac{\bar{q}_n^h}{n}(\Omega_1) e^{-\int_{\Omega_1}^{\Omega_2} \bar{q}_n^h(t') dt'} \quad \bar{q}_n^h(\Omega_2) \quad (78)$$

The $D_n^{\hat{h}}$ and $= \hat{h}_n$ are the Keller's GTD diffraction coefficients and attenuation constants for the n^{th} soft (s) or hard (h) surface ray mode. Thus, in the GTD, the surface ray field consists of surface ray modes which propagate independently of one another. Also, this surface ray field is not the true field on the surface; it is a boundary layer field. The $D_n^{\hat{h}}$ and $= \hat{h}_n$ are given by:

$$[D_n^s(n)]^2 = \sqrt{\frac{1}{2\pi k}} m(Q) \frac{e^{-j(\pi/12)}}{[A_1'(-q_n)]^2} \quad (79a)$$

$$[D_n^h(n)]^2 = \sqrt{\frac{1}{2\pi k}} m(Q) \frac{e^{-j(\pi/12)}}{q_n [A_1'(-q_n)]^2} \quad (79b)$$

and

$$= \frac{s}{n}(Q) = \frac{q_n}{\rho_g(Q)} m(Q) e^{j(\pi/6)} \quad ; \quad = \frac{h}{n} = \frac{\hat{q}_n}{\rho_g(Q)} m(Q) e^{j(\pi/6)} \quad (80a; 80b)$$

In (79) - (80), Q is any point on the geodesic surface ray path. The GTD result of (76) in terms of (77) and (78) is not valid within the SSA transition region.

The UTD result for the 3-D configuration can be simply modified to recover the corresponding UTD result for the 2-D case by allowing the caustic distances ρ_1^r and ρ_s in (55) and (56) to recede to infinity. Then, let

$$\rho_2^r = \rho_1^r, \text{ if } \rho_1^r \rightarrow \infty \text{ and } \rho_s \rightarrow \infty \quad (81)$$

so that

$$E^r(P_L) \sim E^i(Q_R), [\mathcal{R}_s \hat{e}_1 \hat{e}_1 + \mathcal{R}_h \hat{e}_{//} \hat{e}_{//}] \sqrt{\frac{\rho_1^r}{\rho_1^r + s^r}} e^{-jks^r} \quad (82)$$

in which ρ^r is as in (23), and

$$E^d(P_S) \sim E^i(Q_L), [\mathcal{D}_s \hat{b} \hat{b} + \mathcal{D}_h \hat{n}_1 \hat{n}_2] \frac{e^{-jks^d}}{\sqrt{s^d}} \quad (83)$$

since $\hat{b}_1 = \hat{b}_2 = \hat{b}$ for the 2-D case (note: $\hat{b} = \hat{e}_1$). The \mathcal{R}_s and \mathcal{D}_s in (82) and (83) are as defined earlier, respectively; only the L appearing in (66) and (67) is given by

$$L = \frac{s^1 s^d}{s^1 + s^d} \quad , \text{ for the 2-D case,} \quad (84)$$

where s^1 is the distance from the 2-D line source to the point of grazing incidence at Q_1 and $s = s^d \Big|_{SSR}$ as before. A comparison of the UTD and GTD solutions for a 2-D circular cylinder illuminated by a nearby line source is illustrated in Figures 16(a) and 16(b); those UTD solutions are then compared with the corresponding exact (Eigenfunction) solutions in Figures 17(a) and 17(b).

III. A FEW ADDITIONAL UTD SOLUTIONS AND SOME APPLICATIONS

In addition to the basic UTD edge and convex surface diffraction solutions described above, UTD solutions for some other canonical shapes also exist; however, the latter are not described here because of space limitations. UTD type solutions for the radiation and mutual coupling associated with antennas on a smooth convex surface are given in [16-19]; also, an approximate vertex diffraction solution may be found in [5,11,20]. A result based on a recently obtained approximate UTD solution for the field scattered by a fully illuminated, semi-infinite, right-circular perfectly-conducting cone [21] is shown in Figure 18. Also, UTD results for the 3-D diffraction by a penetrable dielectric/ferrite strip in Figure 19 based on the work in [22] are shown in Figures 20 and 21, for parallel and perpendicular polarization of the incident field, respectively. It is noted therein that even though the incident fields are TE_z or TM_z , the scattered fields are not simply TE_z or TM_z due to a coupling between the two which is introduced by the dielectric edge when $\theta' \neq \pi/2$. Finally, Figures 22 and 23 show the application of UTD to deal with more realistic shapes [23,24]. The ogival shape in Figure 22 has a circular duct on it. In Figure 23, the aircraft fuselage is modeled by a best fit prolate spheroid near the antenna location, a more recent calculation employs a composite ellipsoid fuselage model [25].

Acknowledgment

This work was sponsored by the Joint Services Electronics Program under Contract No. N00014-78-C-0049 with the Ohio State University Research Foundation.

REFERENCES

- [1] J.R. Keller, "Geometrical Theory of Diffraction," *J. Opt. Soc. Am.*, Vol. 52, pp. 116-130, 1962.
- [2] J.R. Keller, "A Geometrical Theory of Diffraction," in *Calculus of Variations and Its Applications*, L.M. Graves, Ed., New York, McGraw-Hill, pp. 27-52, 1958.
- [3] R.R. Levy and J.R. Keller, "Diffraction by a smooth Object," *Comm. Pure and Appl. Math.*, Vol. 12, pp. 159-209, 1959.
- [4] R.G. Kouyoumjian, "The Geometrical Theory of Diffraction and Its Applications," in *Numerical and Asymptotic Techniques in Electromagnetics*, R. Mittra, ed., New York, Springer-Verlag, 1975.
- [5] R.G. Kouyoumjian, P.H. Pathak, and W.D. Burnside, "A Uniform GTD for the Diffraction by Edges, Vertices, and Convex Surfaces," in *Theoretical Methods for Determining the Interaction of Electromagnetic Waves with Structures*, J.K. Skwirzynski, ed., Netherlands, Stijhoff and Noordhoff, [1981].
- [6] S.W. Lee and G.A. Deschamps, "A Uniform Asymptotic Theory of EM Diffraction by a Curved Wedge," *IEEE Trans. AP-24*, pp. 25-34, January 1976. Also see D.S. Ahluwalia, R.M. Lewis, and J. Roersna, "Uniform asymptotic theory of diffraction by a plane screen," *SIAM J. Appl. Math.*, Vol. 16, pp. 783-907, 1968.
- [7] C.F. Ryan Jr. and L. Peters, Jr., "Evaluation Edge Diffracted Fields including Equivalent Currents for Caustic Regions," *IEEE Trans. AP-7*, pp. 292-299, 1969.
- [8] W.D. Burnside and L. Peters, Jr., "Axial RCS of Finite Cones by the Equivalent Current Concept with Higher Order Diffraction," *Radio Sci.*, Vol. 7, #10, pp. 943-948, Oct. 1972.
- [9] E.F. Knott and T.R.A. Senior, "Comparison of Three High-Frequency Diffraction Techniques," *Proc. IEEE*, Vol. 62, pp. 146A-147A, 1974.
- [10] P. Ya. Ufimtsev, "Method of edge waves in the physical theory of diffraction," (from the Russian "Metod Krayevykh voln v fizicheskoy teorii difraktsii," *Izd-Vo Sov. Radio*, pp. 1-243 (1962), translation prepared by the U.S. Air Force Foreign Technology Division, Wright-Patterson AFB, Ohio; released for public distribution Sept. 7, 1971.
- [11] P.H. Pathak, "Techniques for High Frequency Problems," chapter in *Handbook of Antenna Theory and Design*, (eds., Y.T. Lo and S.W. Lee), to be published in 1987 by Van Nostrand (Cat. No. 27054).
- [12] S. Silver, *Microwave Antenna Theory and Design*, Boston Technical Publishers, Inc., 1964.
- [13] R.G. Kouyoumjian and P.H. Pathak, "A Uniform Geometrical Theory of Diffraction for an Edge in A Perfectly Conductin Surface," *Proc. IEEE*, Vol. 62, pp. 1448-1461, November 1974.
- [14] P.H. Pathak, "An Asymptotic Result for the Scattering of a Plane Wave by a Smooth Convex Cylinder," *J. Radio Science*, Vol. 14, No. 3, pp. 419-435, May-June 1979.
- [15] P.H. Pathak, W.D. Burnside and R.J. Marhefka, "A Uniform GTD Analysis of the Diffraction of Electromagnetic Waves by a Smooth Convex Surface," *IEEE Trans. Antennas and Propagation*, Vol. AP-29, No. 5, pp. 631-642, September 1980.
- [16] P.H. Pathak, N. Wang, W.D. Burnside and R.G. Kouyoumjian, "Uniform GTD Solution for the Radiation from Sources on a Smooth Convex Surface," *IEEE Trans. Antennas and Propagation*, Vol. AP-29, No. 4, pp. 609-621, July 1981.
- [17] P.H. Pathak and N.W. Wang, "Ray Analysis of Mutual Coupling Between Antennas on A Convex Surface," *IEEE Trans. Antennas and Propagation*, Vol. AP-29, No. 6, pp. 911-922, November 1981.
- [18] S.W. Lee, "Mutual Admittance of Slots on a Cone: Solution by Ray Technique," *IEEE Trans. Antennas Propagat.*, Vol. AP-26, no. 6, pp. 768-773, Nov. 1978.
- [19] K.K. Chan, L.R. Felsen, A. Hessel and J. Shmoys, "Creeping Waves on a Perfectly-Conducting Cone," *IEEE Trans. AP-26*, pp. 661-670, Sept. 1977.
- [20] F.A. Sikta, W.D. Burnside, T.T. Chu and L. Peters, Jr., "First-order equivalent current and corner diffraction scattering from flat plate structures," *IEEE Trans. Antennas and Prop.*, Vol. 31, No. 4, pp. 584-589, July 1983.
- [21] K.D. Trott, "A High Frequency Analysis of Electromagnetic Plane Wave Scattering by a Fully Illuminated Perfectly-Conducting Semi-Infinite Cone," Ph.D. dissertation, The Ohio State University, Department of Electrical Engineering, Columbus, Ohio, Summary 1986.
- [22] R.G. Rojas, "A Uniform GTD Analysis of the EM Diffraction by a Thin Dielectric/Ferrite Half-Plane and Related Configurations," Ph.D. dissertation, The Ohio State University, Department of Electrical Engineering, Columbus, Ohio, Winter 1985.
- [23] J. Volakis, "EM Scattering from Inlets and Plates Mounted on Arbitrary Smooth Surfaces," Ph.D. dissertation, The Ohio State University, Department of Electrical Engineering, Columbus, Ohio, Summer 1982. Also, see Volakis et al., *IEEE Trans. Antennas and Prop.*, Vol. AP-33, No. 7, pp. 736-743, July 1985.
- [24] H.H. Chung and W.D. Burnside, "General 3-D Airborne Antenna Radiation Pattern Code User's Manual," The Ohio State University ElectroScience Laboratory, Report 711679-10, Columbus, Ohio, July 1982.
- [25] J.J. Kim and W.D. Burnside, "Simulation and Analysis of Antennas Radiating in a Complex Environment," *IEEE Trans. on Antennas and Propagation*, AP-34, No. 4, pp. 554-562, April 1986.
- [26] L.R. Felsen, "Plane Wave Scattering by Small Angle Cones," *IRE Trans.*, AP-5, pp. 121-129, January 1957.

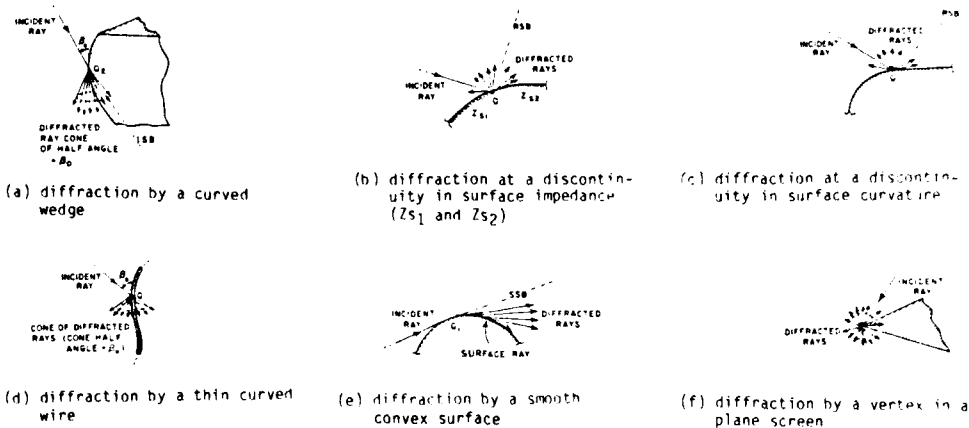


Figure 1. Examples of diffracted rays

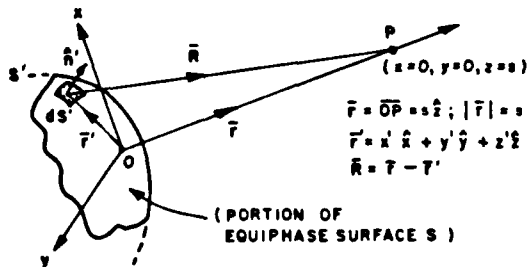


Figure 2. Equiphas (or wavefront) surface

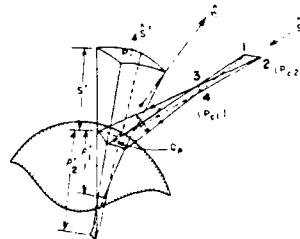


Figure 5. Reflected wavefront geometry

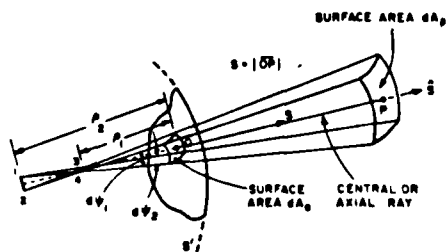


Figure 3. Ray tube geometry associated with the ray path OP



Figure 6. Unit vectors fixed in the incident and reflected rays

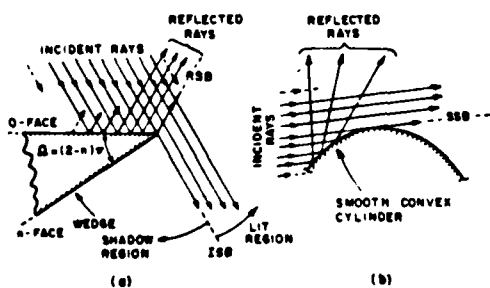


Figure 4. Examples of shadow and reflection boundaries

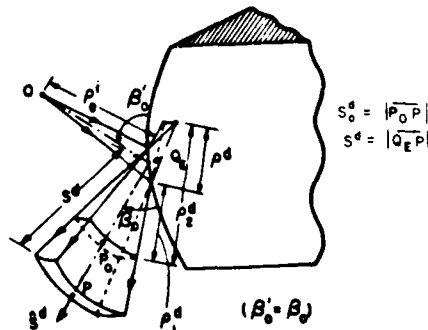


Figure 7. Edge diffracted ray tube

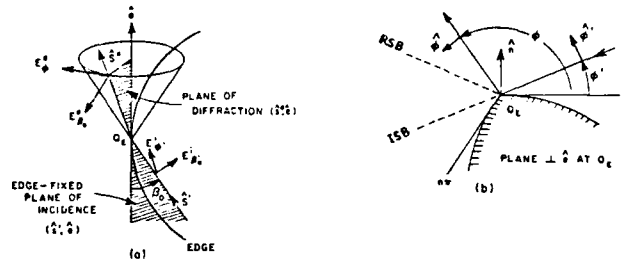


Figure 8. Edge fixed planes of incidence and diffraction

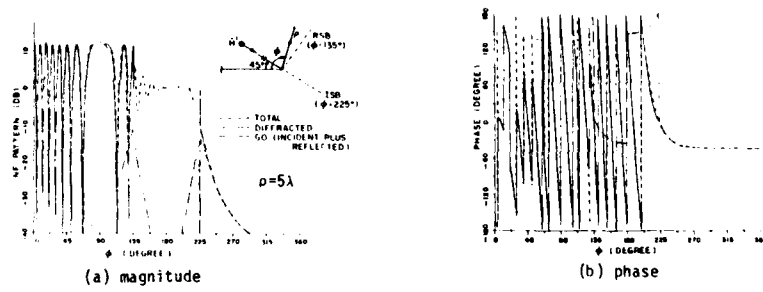


Figure 9. Continuity of the total IITD field surrounding a perfectly-conducting half plane excited by a plane wave

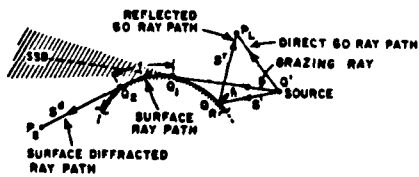


Figure 10. Diffraction at a convex surface

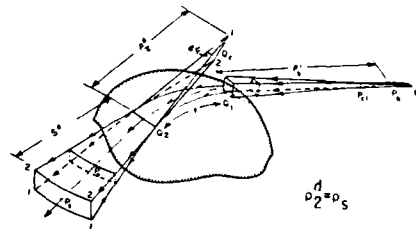


Figure 11. Surface diffracted ray path

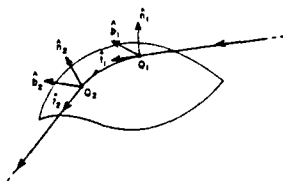


Figure 12. Unit vectors fixed in the surface ray

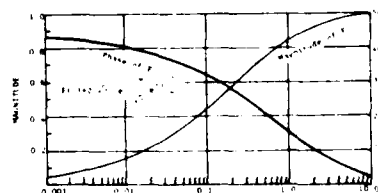


Figure 13. Plot of $F(a)$ versus a

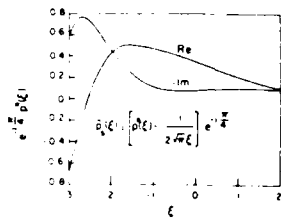


Figure 14. Plot of $e^{-j\pi/4} p^*(\xi)$ versus ξ .

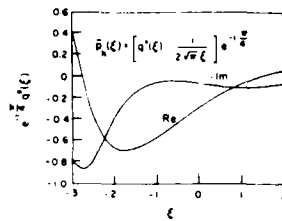


Figure 15. Plot of $e^{-j\pi/4} q^*(\xi)$ versus ξ .

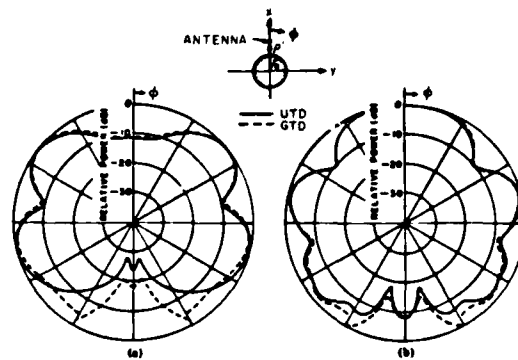


Figure 16. Comparison between GTD and UTD solutions for the radiation by electric (a) and magnetic (b) line sources in the presence of a circular cylinder. Here $a=\lambda$ and $\rho'=2\lambda$.

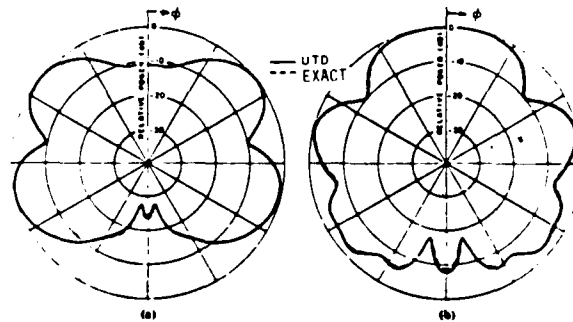


Figure 17. Comparison of UTD solutions of Fig. 16 with exact (eigenfunction) solutions

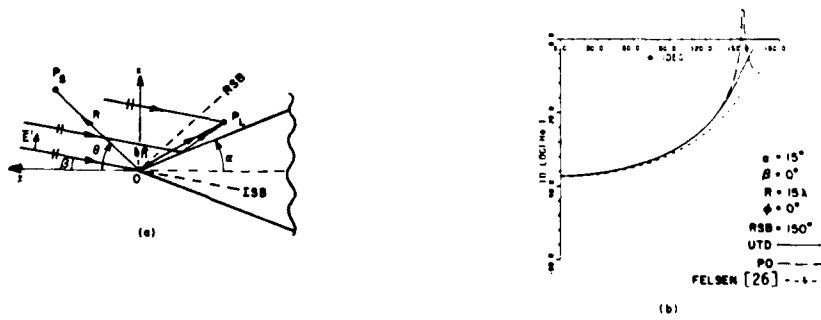


Figure 18. Magnetic field H_0 scattered by a semi-infinite, perfectly-conducting right circular cone when illuminated with a plane wave E_0^i

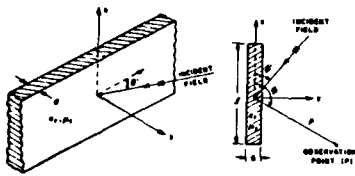


Figure 19. Plane wave incident on a dielectric/ferrite strip

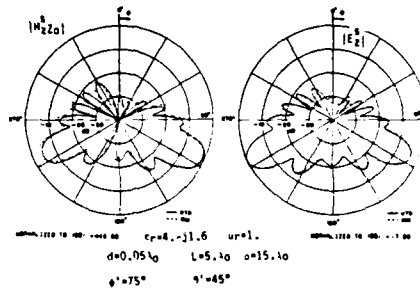


Figure 20. Magnitude of the scattered E_z^S and H_z^S fields for a E_0^i -polarized incident plane wave

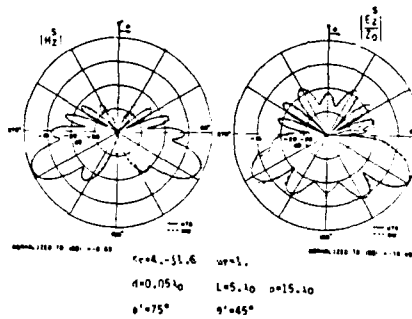


Figure 21. Magnitude of the scattered E_z^S and H_z^S fields for a H_0^i (or E_0^i)-polarized incident plane wave

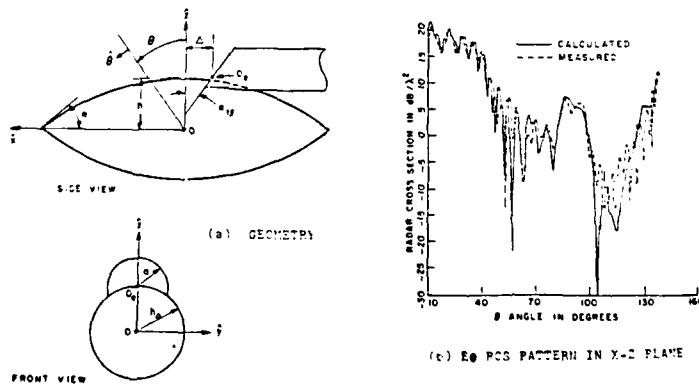


Figure 22. Radar cross section of an ogive with a circular duct

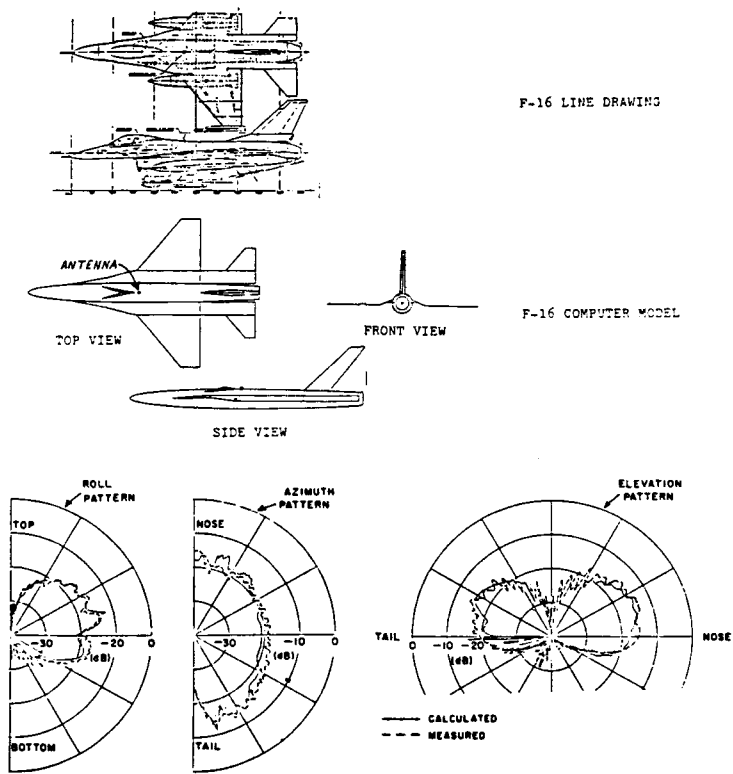


Figure 23. Radiation patterns of a monopole on an F-16 aircraft

SINGULARITY EXPANSION METHOD: TARGET RESONANCES

Michael A. Morgan, Associate Professor, (Code 62 Mo),
Naval Postgraduate School, Monterey, CA 93943 USA

AD-P005646

SUMMARY

A unified treatment of the natural mode representations for induced currents and scattered fields is described using elementary concepts of causality and superposition. The transient back-scattered field is shown to have the form of a constant coefficient exponential series only in the "late-time", after the last directly driven response is received from the scatterer. Prior to this, the "early-time" response is found to be due to both the direct physical optics fields as well as a sum of modulated natural modes. Practical implications of this result, regarding aspect-invariant target classification using natural resonances, are discussed.

INTRODUCTION

A major impetus behind the development of the singularity expansion method (SEM) by Baum in 1971, [1], was the need to predict electromagnetic pulse (EMP) excitation of complex electronic systems. Efforts since then have, for the most part, considered the numerical solutions for induced current natural modes and their associated coupling coefficients for systems of increasing complexity. Very little quantitative analysis was performed with EMP related efforts in extending the SEM description to the scattered fields. It was conjectured by Baum [2], and others, that the scattered field could be described by the usual exponential series plus a *possible* complex plane "entire" (fully analytic) function. Until recently, even the SEM description for induced currents has been a controversial and often confusing topic. Articles by Michalski [3], and others have clarified the alternate SEM representations for induced currents. Heyman and Felsen [4], have even developed a hybrid representation for induced currents and scattered fields using both geometrical diffraction theory and natural modes.

The natural mode representation of the SEM has been more recently employed in the framework of electromagnetic system identification, particularly in the context of non-cooperative target recognition (NCTR). The complex values of the natural resonance frequencies of the current distributions which can be induced on the scatterer are dependent upon its physical composition and geometry, while being *independent of the aspect and polarization* of the incident field. This has led many researchers to believe that a viable NCTR technique could be based upon the identification of the natural resonance frequencies contained in the scattered field echo signature. Having no comprehensive guide as to the exact SEM description of transient scattered fields, early proponents of natural resonance NCTR usually assumed a simple complex exponential sum model for the echo signature. Several methods exist for extracting the complex natural resonances from this model. Most of these techniques are variations of the classic Prony's method (circa 1795), which has been resurrected and improved upon by Van Blaricum [5] and several others.

As will be shown, the simple exponential series model, which is known as a "class 1" SEM representation, does not provide a complete description of the transient scattered field. In particular, the scattered field can be separated into two time segments: that due to the driven current distribution, known as the "early-time" field, and that due to the undriven natural mode current distribution, known as the "late time" field. Only the late-time field can be accurately represented by the class 1 SEM form.

If it were not for the noise and clutter pollution of the received echo signal, it would be a simple matter to base NCTR only upon the late-time portion of the scattered field. Unfortunately, in many cases of practical concern, only a small percentage of the total scattered signal energy remains in the late time portion. This condition may thus result in a much reduced signal to noise ratio (SNR) in the class 1 portion of the signal. Compounding this problem is the well documented intolerance of established natural resonance extraction methods to low SNR. Typical SNR requirements for even moderately accurate pole extraction is in the range of 15 to 20 dB, [6]. These practical concerns motivated the work to now be described, where a complete signal model is presented for use in developing efficient natural resonance NCTR signal processing strategies. The theoretical development, whose major results are presented in this paper, is more completely described, with derivations, in a previous publication by this author, [7].

THE NATURAL MODE CONCEPT

Consider the transient electromagnetic scattering problem as depicted in Figure 1, wherein a perfectly conducting finite-sized object is being illuminated by a generalized incident field, (not necessarily a plane wave) in free space. The induced current on the surface of the object will satisfy the magnetic field integral equation (MFIE), [8],

$$J(r, t) = 2 \hat{n} \times H^i(r, t) + \iint_{S_{ov}} K(r, r') \cdot J(r', t - |r - r'|/c) dS \quad (1)$$

where \hat{n} is the outward (to the surface) unit normal vector, J is the surface current density, H^i is the incident magnetic field at the surface, K is a dyadic Green's function kernel and the principal-value (PV) type integral excludes the surface point $r = r'$. The cross product of \hat{n} and the incident magnetic field forms the "physical optics" portion of the induced current while the surface integral term provides the "feedback" current to each point on the scatterer due to all other induced current values.

With no incident field, the solutions of Eq.(1) are termed the natural modes of the scattering problem. These source free solutions each have the form of a product of a spatial (on the surface) current distribution, $J_n(r)$, and a complex exponential term,

$$J_n(r,t) = J_n(r) \exp(s_n t) \quad (2)$$

Each of these surface current distributions will generate a scattered field mode. These natural mode fields can be found through Green's function type surface integrations of the respective current modes. For example the natural mode magnetic field is given by

$$H_n^s(r,t) = \iint_S G(r,r') \cdot J_n(r,t) \cdot |r-r'|/c \, dS = H_n^s(r) \exp(s_n t) \quad (3)$$

where it should be understood that the spatial position vectors r and r' represent points on the scatterer when used in reference to the surface current distribution, while for the case of the field quantities the r -vector represents all spatial positions both on and outside of the surface.

Since the currents and fields in Eqs.(2) and (3) are assumed to exist at times when no incident field is illuminating the object, the complex natural frequencies,

$$s_n = \sigma_n + j\omega_n \quad (4)$$

are functions only of the geometry and physical composition of the scatterer. These complex natural resonances may thus have the potential for use in aspect and polarization independent identification of scatterers. Some additional properties of the natural resonances are:

- (1) The s_n 's appear in complex conjugate pairs as a result of the "real" nature of source-free induced currents in physical problems
- (2) The real part of each s_n is less than zero to produce exponential decay of the magnitude of each mode, corresponding to power being radiated away from the scatterer (radiation loss)
- (3) The index "n" is an integer for the case of finite-sized conducting bodies, as has been shown by Marin, [9]. There are also an infinite number of natural resonances, even for the simplest scattering shape. In practice, however, only a finite number of resonances will be significantly excited by an incident signal of particular frequency bandwidth.

Assuming that the incident field had previously illuminated the scatterer and then had identically vanished for $t > t_0$, the source free current distribution on the surface of the object and the corresponding scattered field will each be a weighted superposition of their respective natural modes

$$J(r,t) = \text{Re} \left\{ \sum_{n=1}^{\infty} A_n J_n(r,t) \right\} = \sum_{n=1}^{\infty} |A_n| J_n \exp(\sigma_n t) \cos(\omega_n t + \phi_n) \quad (5)$$

$$H(r,t) = \text{Re} \left\{ \sum_{n=1}^{\infty} A_n H_n(r,t) \right\} = \sum_{n=1}^{\infty} |A_n| H_n \exp(\sigma_n t) \cos(\omega_n t + \phi_n) \quad (6)$$

The exponentially decaying sinusoidal series results from the complex conjugate nature of the pole-pairs, while the phase offset, ϕ_n , is the phase of the complex amplitude, A_n .

The natural mode currents and fields are thus seen to be akin to generalized source-free "steady-state" solutions which, although decaying due to outbound radiation, are self-sustaining in the absence of any further excitation from that which provided their genesis. Furthermore, one can view the integral equation in Eq. (1) as a continuous "feedback system" equation where the undriven modes are space-time distributions whose feedback to each surface point from all other points exactly sustains the form of the distribution, both in magnitude and phase.

PLANE WAVE IMPULSE SCATTERING

Having introduced the concept of source-free natural modes, let us now investigate the form of the scattered field due to an incident plane wave impulse. The situation is depicted in Figure 2. The impulsive plane wave is moving with the velocity of light in the direction indicated by the unit vector, \hat{p} . To provide generalized results, let us define the origin of our coordinate system to be located at the initial "impact" point of

the incident plane wave on the scatterer. In addition, assume that $t=0$ when this event occurs. By considering a delta function plane wave, we can then use convolution to obtain the scattered field which is due to any form of transient plane wave illumination. This is directly analogous to the concept of impulse response in circuit theory or Green's functions in mathematical physics.

As was initially discussed, the scattered field response to the plane wave will be composed of two parts: an early-time driven response and a late-time natural mode response. To see why this is true, let us look at Figure 2 and reconsider Eq.(1). Note that the impulsive plane wave incident field will be identically zero everywhere on the surface of the scatterer *except* on the conformal ring which circumscribes the surface at the intersection with the plane wavefront. The plane wavefront is indicated by the dashed line in Figure 2. This conforming source ring on the scatterer's surface changes shape and position as the wavefront moves over the scatterer at the velocity of light. From Eq.(2), the surface current at points on the wavefront ring will be composed of both the direct "Physical Optics" term, $2 \hat{n} \times H^i$ and a contribution from all previously illuminated points on the scatterer. These points, which reside in the "wake" of the incident field, are dot-shaded in Figure 2. Because of causality, there is no induced current on the remainder of the scatterer, at points "ahead" of the incident wavefront.

Let us now consider the resultant back-scattered far-field (in the direction $-\hat{p}$ at a very large distance) due to the surface current distribution. This "echo" field will be due to a surface integration of the same form as in Eq.(3), but where the Green's function can be simplified because of the far-field assumption, [8],

$$H^S(-\hat{r}\hat{p}, t) = \frac{1}{4\pi cr} \frac{\partial}{\partial t} \iint_S \hat{p} \times J(r', t - |r-r'|/c) \, ds' \quad (7)$$

Upon substituting Eq.(1) into Eq.(7), two distinct terms result: the "physical optics" scattered field generated by the $2 \hat{n} \times H^i$ driven current and the scattered field produced by the source-free "wake" current behind the moving wavefront,

$$H^S(-\hat{r}\hat{p}, t) = H_{po}(-\hat{r}\hat{p}, t) + H_w(-\hat{r}\hat{p}, t) \quad (8)$$

The physical optics current can be shown to be directly proportional to the second time derivative of the silhouette area of the scatterer [10]. This fact provides the basis for an alternate means of NCTR, based upon ramp response imaging, [11]. The second component of the scattered field is due to a *source free* current distribution on a time-varying portion of the surface of the scatterer. It is shown in [7] that this wake current can be represented by a class 1 SEM expansion, with constant coefficients, as in Eq.(5). However, because the surface area is changing in Eq.(7), wherein the wake current integration takes place, the resultant H_w will contain the same exponential resonance terms as the source free current, but with time-varying coefficients until such time as the field results from a complete surface integration. This form of the SEM expansion is termed "Class 2". The backscattered far field can be represented by the following generic equation:

$$H^S(-\hat{r}\hat{p}, t) = u(t-r/c) \{ H_{po}(-\hat{r}\hat{p}, t) + \sum_{n=1}^{\infty} C_n(-\hat{r}\hat{p}, t) \exp(s_n t) \} \quad (9)$$

where the time-varying expansion coefficients become constant coefficients after a delay of $2D/c$ from the initial field turn on at $t = r/c$. D is the length of the scattering object in the direction parallel to \hat{p} . At this same transition instant, in going from the class 1 to the class 2 SEM forms, the physical optics field vanishes and there remains only the constant coefficient expansion. This "early time" scattered field is thus composed of both a physical optics term and a class 2 SEM expansion, with time-varying coefficients, while the "late time" field can be represented by a simple class 1 expansion which contains aspect independent natural resonant frequencies, s_n .

The general case of bistatic scattering at arbitrary distance (not necessarily in the far field) has been considered in [7]. If r is used to represent a particular scattered field point and r' is used to denote points on the surface of the scatterer, then the time at which the physical optics field reaches r from r' will be

$$t_{po} = (\hat{p} \cdot r' + |r - r'|) / c \quad (10)$$

By allowing r' to vary over the surface, one can define the minimum and maximum of t_{po} . The early-time field at r begins at $t = \min[t_{po}]$ and ends, with transition to the late-time when $t = \max[t_{po}]$. Two special far-field cases result from this analysis: (1) the backscattered case, wherein the early-time duration is $2D/c$ and (2) the forward scattering case where the early-time duration is of measure zero when illumination is due to a plane wave impulse. These two cases represent the extrema in possible early time durations.

Consider now the forms of the natural resonance representations for the general case

of an incident plane wave which has time modulation $f(t)$, instead of a delta function. This $f(t)$ can represent such radar waveshapes as AM pulsed CW or FM chirp-type waveforms. Assuming that $f(t)$ is time-limited, with duration T then the resultant time before transition to the late time in the scattered field will, at all observation points, be lengthened by T vis-a-vis that for the impulse illumination.

DISCUSSION

The motivation behind this original effort at quantifying the SEM form for the scattered field was the need for proper signal processing models on which to base NCTR using natural resonances. This was quite important in light of the fact that many researchers (the author included) had met with failure in attempting to "extract" the natural resonances from experimental and numerical scattering signatures while assuming a class 1 SEM signal model for the entire time signature.

With the discovery of the impropriety of the class 1 SEM model as a complete signal description, a new and quite serious problem became apparent in regards to the practical implementation of aspect independent NCTR based upon natural resonances. For the case of typical convex "low-Q" metallic targets, having rapidly decaying natural resonances, only a very small percentage of the total signal energy will remain in the late time signature. As previously mentioned, class 1 pole extraction methods require relatively high-fidelity signals which may be difficult to attain in even a friendly radar environment.

It thus becomes of paramount importance, in implementing natural resonance NCTR in the real world, to investigate methods for either scattered field signature to enhance the recognition process and/or circumventing the sensitivity of natural resonance processing methods to low SNR in the late-time signature. Blending the concepts of physical optics imaging with natural resonance NCTR may be the key to the first approach while employing non-extraction type processing, such as the K-pulse (to be considered in a separate paper by this author) will follow the second technique.

REFERENCES

- [1] C.E. Baum, "On the singularity expansion method for the solution of electromagnetic interaction problems," Air Force Weapons Laboratory Interaction Notes, No. 88, Dec. 1971.
- [2] C.E. Baum, "Singularity expansion of electromagnetic fields and potentials radiated from antennas or scattered from objects in space," Air Force Laboratory Interaction Notes No. 179, May 1973.
- [3] K.A. Michalski, "On the class 1 coupling coefficient performance in the SEM expansions for current density on a scattering object," *Electromagnetics*, vol. 2, no.3, pp.201-210, July 1982.
- [4] E. Heyman and L.B. Felsen, "Creeping waves and resonances in transient scattering by smooth convex objects," *IEEE Trans. Antennas & Propagation*, vol. 31, pp. 426-437, May 1983.
- [5] M.L. Van Blaricum and R. Mittra, "A technique for extracting the poles and residues of a system directly from its transient response," *IEEE Trans. Antennas & Propagation*, vol. 23, pp. 777-781, Nov. 1975.
- [6] A. Poggio, M.L. Van Blaricum, E.K. Miller and R. Mittra, "Evaluation of a processing technique for transient data," *IEEE Trans. Antennas & Propagation*, vol. 26, pp 165-173, Jan. 1978.
- [7] M.A. Morgan, "Singularity expansion representations of fields and currents in transient scattering," *IEEE Trans. Antennas & Propagation*, vol. 32, pp. 466-473, May 1984.
- [8] R. Mittra, "Integral equations for transient scattering," in *Transient Electromagnetic Scattering*, L. Felsen, Editor, New York: Springer-Verlag, 1976, pp. 74-127.
- [9] L. Marin, "Representation of transient scattered fields in terms of free oscillations of bodies," *Proc. IEEE*, vol. 60, pp. 640-641, May 1972.
- [10] E.M. Kennaugh and R.L. Cosgriff, "The use of impulse response in electromagnetic scattering problems," *Proceedings 1958 IRE National Convention Record*, Part I, pp. 72-77.
- [11] J.D. Young, "Radar imaging from ramp response signatures," *IEEE Trans. Antennas & Propagation*, vol. 24, pp. 276-282, May 1976.

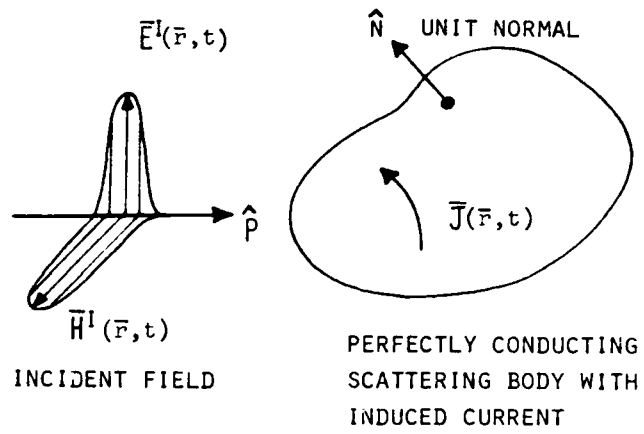


FIGURE 1 TRANSIENT SCATTERING PROBLEM

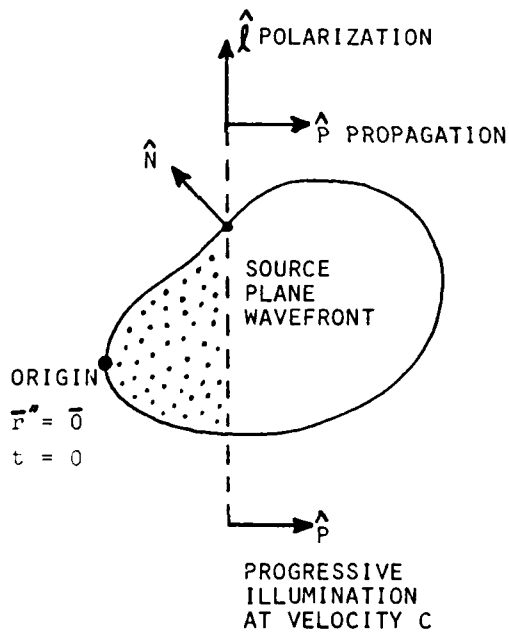


FIGURE 2 PLANE WAVE IMPULSE ILLUMINATION

AD- P005647

THE HYBRID WAVEFRONT RESONANCE METHOD

by

Ehud Heyman

Department of Electrical Engineering,
Tel-Aviv University,
Tel-Aviv 69978, Israel

Summary

When observed over long periods, scattered returns from targets illuminated by broad band signals reveal distinctive features in the early and late time regimes. The features can be explained in terms of the different wave phenomena, progressive and oscillatory, that are dominant during these respective intervals. The former represent wavefront arrivals, and the latter full body resonances. A recently developed hybrid theory has formalized the connection between them and has provided new interpretations that did not emerge in earlier treatments. These interpretations can clarify issues which have arisen within the singularity expansion method (SEM), in particular, the adequacy of the expansion at early times. Here the hybrid wavefront resonance theory is reviewed, first within the rigorous context of scattering by a circular cylinder, and then via a ray analysis of scattering by a general (composite) object.

I. INTRODUCTION

With the present trend toward short pulse excitation and the consequent broad frequency spectrum, analytical models for these propagation and scattering problems must be able to accommodate early time (high frequency) as well as late time (low frequency) characteristics. Two essentially different, but complementary, approaches involve a description of the propagation or scattering process in terms of traveling waves (wavefronts) or oscillatory waves (resonances) [1]. In a traveling wave formulation [2,3], a **causal wavefront** is tracked from the source to the scatterer, where it undergoes an interactive process that is conveyed to the observer by successive wavefront arrivals corresponding to multiple circumnavigations of the object and (or) multiple diffractions from scattering centers located on the object (Fig. 1). This description, which is sensitive to **local** features encountered along the wavefront trajectory, becomes cumbersome at late observation times when many wavefronts (transient ray fields) have had time to reach the observer. Moreover, monitoring of the field at late times where low frequency spectral contributions predominate also causes difficulties because high frequency methods, such as the **Geometrical Theory of Diffraction (GTD)**, are not applicable there.

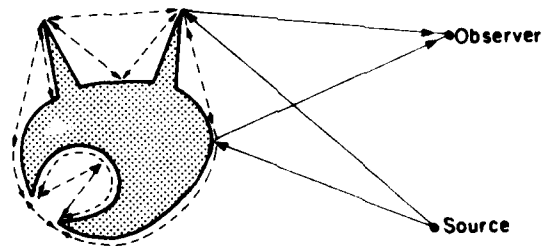


Fig. 1 Interaction mechanisms for scattering by a typical composite object. Full and dashed lines represent direct and multiple interactions, respectively.

The oscillatory representation, formalized by the **Singularity Expansion Method (SEM)** [4,5], emphasizes **global** features of the scatterer by expressing the field in terms of **resonant modes** which are **damped** in time. Therefore, this formulation is most convenient for late observations times and the lower frequency spectral components relevant there. However, the resonance expansion is deficient at early times where damping is negligible and many resonances are needed to synthesize the abruptly changing local high-frequency field near a (causal) wavefront. These convergence difficulties at early times are manifested in the formal structure of the SEM, which evolves from the treatment of an integral equation for the surface field, by the need to add to the SEM resonance series an **entire function** in the complex frequency plane. A certain arbitrariness in the choice of this function and therefore of the excitation

coefficients (usually referred to as "coupling coefficients") of the resonances has caused problems which have, however, been clarified in recent studies [6-8].

By incorporating self-consistently the well-behaved portions of wavefronts at early times and of resonances at later times, the recently developed **hybrid representation** [9-15], provides a description applicable and convenient for **all** times. Its foundation is a bilateral equivalence between wavefronts and resonances as cumulative phenomena of the one in terms of the other, which was first demonstrated numerically and qualitatively in references [16] and [17], but which has been put in [9] on a rigorous theoretical basis, utilizing the concepts of the GTD. Thereby a penetrating physical interpretation that has remained hidden within the conventional integral equation format of SEM has been furnished. The wavefront analysis establishes the evolution of the resonances as a cumulative effect of the multiple wavefront interactions and the role of the entire function which represents the contributions of the direct interactions of the incident field with the scattering object (see Fig. 1). We call this function **intrinsic** or **non-removable** entire function [10,11]. By selective cumulative wavefront treatment, there also emerge alternative choice for the SEM resonance excitation coefficients, and for the corresponding turn-on times of the SEM expansion, as well as the related definition of **removable** (non-intrinsic) entire functions. A remarkable feature of the resonance construction by wavefront summation is the accuracy of the complex resonances, even including those at the lower frequency end, when high-frequency asymptotic (ray) methods are used to approximate the scattering process [9,13,14,18].

The preceding discussion makes evident the systemization achieved by placing the constituents and concepts of SEM, as derived from the integral equation approach, within the framework of wavefront representation and GTD. By retaining certain wavefront fields intact while treating the remaining ones collectively to yield resonances, one may obtain alternative expressions that highlight different aspects of the scattering process and resonance formation. Success in this endeavour depends critically on a **systematic ordering** of the multiplicity of wavefront events. For simple structures with few ray species, this ordering is straightforward [9,10,13-15], but for more complicated configurations with multiple scattering centers and/or multiple reflection points, the number of ray species proliferates. Here, use of flow diagrams as in systems theory [19] can provide an overview that places in evidence the **totality** of multiple interactions and therefore their collective role in establishing each of the **full-body** resonances. For targets comprising composite substructures (e.g. Fig. 1), one may also consider **partial** resonances characteristic of each substructure in isolation, and then explore the perturbation of these isolated resonances when the substructures are assembled to form the composite object. By this approach, it is possible to explore the effect on the resonance map caused by changes in a substructure, thereby providing insight into the scattering mechanisms that establish a compound resonance. If the coupling between subsystems is weak, the resulting full-body resonances are expected to be only weakly perturbed from those of the isolated subsystems. This feature may facilitate a **parametric identification** of certain class of scatterers which have distinct groups of partial resonance. A special class of such scatterers are those containing resonance mechanisms with relatively low radiation loss, i.e., with high Q, such as open resonators, open pipes, dielectric scatterers, etc. In such cases some of the full-body resonances are located near the high Q (partial) resonances.

It should be noted that the general scheme in this paper addresses multiple interaction and resonance phenomena in a broad sense, with ray terminology employed to identify wave transport and interaction trajectories. Along these trajectories, the time harmonic field may be expressed by the ray approximation and is then subject to the rules and constraints of GTD. However, the field may be expressed more generally by a "better" wave function, for example a **ray integral** spanning a spectrum of local plane waves whose stationary phase approximation yields GTD but which, when kept intact, is uniformly valid in transition regions where GTD fails [1]. Moreover, such spectral integrals, when inverted into the time domain via the **Spectral Theory of Transients (STT)** [20,21], yield expressions valid for longer observation times that the wavefront approximation corresponding to GTD. Although not emphasized throughout the discussion, the foregoing general features should be kept in mind. In a similar vein, the presentation here is slanted toward obstacle scattering, but the concepts and techniques apply equally to categorization and collective treatment of multiple ray events caused by reflection and (or) refraction in layered media.

In what follows, the traditional SEM formulation is reviewed in Section II, but within the perspectives noted above. In Section III we examine the hybrid wavefront resonance theory within the rigorous context

of diffraction by a circular cylinder where the traveling waves basis functions are known for all frequencies, with ray terminology employed only to identify wave transport and interaction events. The rigorously derived results of Section III are generalized in Section IV, within the framework of high frequency ray theory to scattering by a general (composite) object. Here diagrammatic methods are introduced for systematic ordering and subsequently "collectivizing" the multiplicity of wavefront interactions. In both sections the discussion is pursued so as to highlight the wavefront interpretation of the various SEM constituents, the removable and the intrinsic entire functions, SEM turn-on-times, full body resonances, coupled partial resonances, etc. The concept of the weakly coupled partial resonances is examined in Section V and concluding remarks are made in Section VI.

II. SEM FORMULATION

As formulated by Baum [4,5] and established rigorously by Marin [22] the SEM describes the transient field for a perfectly conducting object of finite extent as a superposition of the natural mode-solutions of the scattering integral equation, which relates the field incident on a scatterer to the induced current and thereby to the scattered field. The eigenmodes represent damped oscillations of standing wave solutions which, for an implied $\exp(-i\omega t)$ dependence, occur at resonant frequencies ω_ν , $\nu=1,2,\dots$, in the lower half of the complex frequency plane, and generate poles in the resolvent kernel of the integral equation. The induced current or the scattered field in the frequency domain may therefore be written in the form

$$\hat{u}(\underline{r};\omega) = \sum_{\nu} n_{\nu}^{(1)}(\underline{r}) \frac{1}{\omega - \omega_{\nu}} + \hat{f}(\underline{r};\omega) \quad (1)$$

The field in the time domain results from the Fourier inversion

$$u(\underline{r};t) = \frac{1}{2\pi} \int_B d\omega e^{-i\omega t} \hat{u}(\underline{r};\omega) \quad (2)$$

with causality ensured by having the Bromwich integration contour B pass above all singularities in the complex ω -plane. Here and henceforth, a caret indicates a frequency domain constituent while its time domain counterpart is written without this symbol.

By closing the integration contour in (2) about the lower half of the ω -plane, permissible only for $t > t_0$ where the turn on time t_0 is determined by the asymptotic properties of \hat{u} , one obtains the time domain resonance series representation of the field. The resonance excitation coefficients $n_{\nu}^{(1)}$ in (1), the residues at the complex frequency poles, are designated in the SEM literature somewhat inappropriately (since no intermode coupling is involved) as "class 1 coupling coefficients" [4-8]. Class 1 coefficients, in contrast with class 2, are frequency (or time) independent. In the integral equation procedure of SEM, they arise from surface current integrations over the **entire** obstacle surface. In what follows, we shall construct the scattered field explicitly by asymptotic diffraction theory without recourse to the integral equation. It is thereby implied that the interpretation of our results in terms of SEM coupling coefficients involves only "class 1" since integrations over portions of the scatterer, as required for "class 2" [6-8], have no counterpart in our treatment.

As shown, the pole series in (1) must generally be augmented by an **entire function** $\hat{f}(\underline{r};\omega)$ in the frequency domain [4,5] which, in the time domain, corresponds to a **finite duration signal at early times**. The role of the entire function, and whether or when to include it, has caused confusion and controversy, but has recently been partially clarified [6-8] by linking it to the time of initiation (turn-on times) of the resonance series. Referring to the class 1 coupling coefficients only (as in (1)), it has been shown [6-8] that there is a degree of flexibility in choosing the turn-on time of the resonance series, and that the series converged formally in a time interval **before** the arrival of the causal excitation (see also [9]). However, in that interval, numerical convergence difficulties arise for the required synthesis of a null field [23,24]. Accordingly it has been conjectured in [24] that the turn-on time for the class 1 coupling coefficients should be the arrival time of the incident wavefront along a straight line path to the observer. If, on the other hand, the resonance series is turned on thereafter, one should compensate for the early time field in the deleted time interval by an entire function in the frequency domain. In fact, the pole series in (1) may be modified via the formal identity [6]

$$\sum_{\nu} n_{\nu}^{(1)} \frac{1}{\omega - \omega_{\nu}} - e^{i\omega t'} \sum_{\nu} n_{\nu}^{(1)} \frac{e^{-i\omega_{\nu} t'}}{\omega - \omega_{\nu}} + \sum_{\nu} n_{\nu}^{(1)} \frac{1 - e^{i(\omega - \omega_{\nu})t'}}{\omega - \omega_{\nu}} \quad (3)$$

to express turn-on of the first sum at any time $t=t'$. The second sum on the right-hand side of (3), which has been generated solely by a shift in the turn-on time of the pole series, has no pole singularities and thus is an entire function that contributes the field between $t=0$ and $t=t'$. In [10-12] it has been shown that there is, however, another type of entire function which is *intrinsic* to the scattering process. This will emerge in the discussion to follow.

The above mentioned convergence difficulties at early times in the class 1 representation are alleviated in the class 2 representation wherein a time varying region of integration covers only that part of the object surface which has already been illuminated [6-8] (the region of integration may even be smaller, extending only over part of the illuminated domain which has had time to contribute at the current observation point). Accordingly, the class 2 coefficients are time dependent at early times, but after the incident wavefront has transversed the entire structure and the domain of integration spans the entire object, the two types of coupling coefficients are the same. The greater computational stability with class 2 coefficients comes at the expense of certain complexities in the computation of these coefficients, as well as in their use for interpretation of measured transient data.

The role and interpretation of these constituents in the SEM may be clarified by recourse to the hybrid wavefront resonance theory wherein the wavefront play a crucial role that remains submerged in the conventional SEM approach. These aspects are examined below within the rigorous context of diffraction by a circular cylinder, and then are generalized, via GTD construction of the field, to more complicated scattering objects.

III. TRANSIENT SCATTERING BY A CIRCULAR CYLINDER

A. Formulation

Referring to Fig. 2, in a conventional cylindrical coordinate frame, an impulsive line source is located at $\rho'=(\rho', \phi')$ exterior to a cylinder with radius "a" embedded in a homogeneous medium with wave velocity "v". The exterior observer is at $\rho=(\rho, \phi)$. Without loss of generality, it is assumed that $\phi'=0$ and that $0 < \phi < \pi$. The transient field $G(t)$ (transient Green's function) is assumed to satisfy on the cylinder the acoustically hard boundary condition

$$\partial G / \partial n = 0 \quad (4)$$

where "n" is the normal to the boundary. We shall construct $G(t)$ from the time harmonic Green's function $\hat{G}(\omega)$ corresponding to $\exp(-i\omega t)$ by the Fourier inversion (2).

B. Conventional Construction of SEM Representation

In general, the singularity expansion of the field is obtained by solving the scattering integral equations for the induced current. In the present example, one may employ the cylindrical symmetry to expand the current and the field into a series of angular harmonics as basis functions, and then solve the boundary value problem for the coefficient of that series. The time harmonic Green's function obtained via this procedure may be expressed as

$$\hat{G}(\rho, \rho') = \hat{G}^i(\rho, \rho') + \hat{G}^s(\rho, \rho') \quad (5)$$

where

$$\hat{G}^i(\rho, \rho') = \frac{1}{4} H_0^{(1)}(k|\rho - \rho'|) = \sum_{m=-\infty}^{\infty} \frac{1}{4} J_m(k\rho_c) H_m^{(1)}(k\rho_s) e^{im\phi} \quad (6a,b)$$

is the incident field (free space Green's function),

$$\hat{G}^s(\rho, \rho') = \sum_{m=-\infty}^{\infty} \frac{1}{8} e^{im\phi} S_m(\gamma) H_m^{(1)}(k\rho) H_m^{(1)}(k\rho') \quad (7)$$

is the scattered field and, for the boundary conditions in (4)

$$S_m(\gamma) = -2 J_m'(\gamma) / H_m^{(1)}(\gamma), \quad \gamma = ka = \omega a / v \quad (8)$$

Here, ρ_c and ρ_s are, respectively, the smaller and larger of the variables ρ and ρ' and a prime indicates a derivative of a function with respect to its argument.

The singularities of \hat{G}^s in the complex frequency plane comprise a branch point at $\omega=0$ and simple poles ω_{mp} , $p = 1, 2, \dots$ for the m -th term in the series (7) (Fig. 3). The branch cut is chosen along the

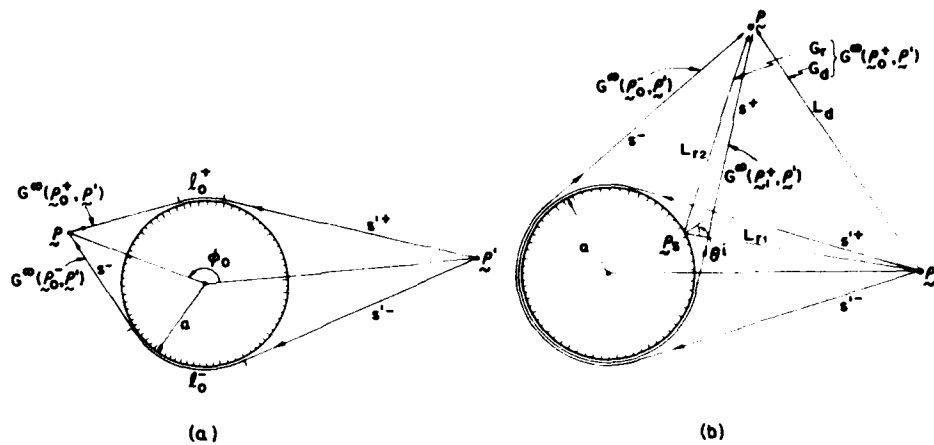


Fig. 2 Wavefront contributions to cylindrical wave scattering by a circular cylinder.
(a) Observation point in shadow region. The field comprises diffracted wavefronts only; the earliest to arrive are $G^{\pm}(P_0^{\pm}, P')$ and $G^{\pm}(P_0^{\pm}, P')$. By incorporating these into the collective term (34), the field is described entirely by SEM resonances.
(b) Observation point in lit region. The geometrical optics direct and reflected rays L_1 and L_2 , respectively, are represented by $G^{\pm}(P_0^{\pm}, P')$. The earliest diffracted (propagating) wavefront arrivals are $G^{\pm}(P_0^{\pm}, P')$ and $G^{\pm}(P_0^{\pm}, P')$. They are the first which may be treated collectively as in (34), thereby leaving $G^{\pm}(P_0^{\pm}, P')$ as a free term (entire function).

negative imaginary axis to ensure symmetry on the entire top Riemann sheet (see Appendix in [10]). The pole singularities (the SEM resonances) are the roots of the equation

$$H_m^{(1)}(\gamma_{\pm m, p}) = 0, \quad m = 0, 1, 2, \dots$$

on the top sheet $-\pi/2 < \arg \omega < 3\pi/2$. For a given m , the index p assumes the values [10, Fig. 7]

$$p = 1, 2, \dots \left[\frac{|m|+1}{2} \right] \quad (34)$$

where $[a]$ denotes the largest integer less than a . The poles are located in the lower half of the $(\text{Re } \gamma, \text{Im } \gamma)$ plane, symmetrically with respect to the imaginary axis, i.e. in pairs such that

$$\omega_{m, p}^* = -\omega_{m, p}^* \quad (35)$$

where the asterisk denotes the complex conjugate $\omega^* = |\omega| \exp(-i \arg \omega)$. This definition of the indices facilitates the physical interpretation of the wave processes shown in Sec. II.D.

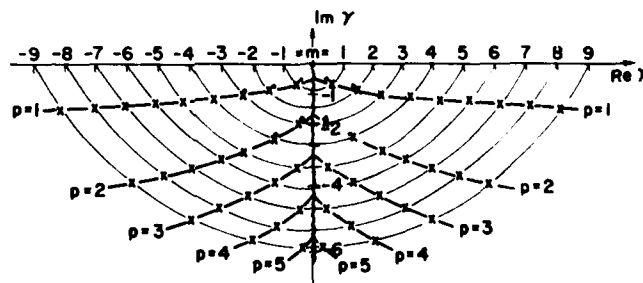


Fig. 3 Singularities of \bar{G} in complex $\gamma = ka$ plane: ~ branch cut, x x x poles $\gamma_{m, p}$. Asymptotic solutions for $\gamma_{m, p}$ are shown by dots when they deviate from the exact solutions within the scale of the drawing.

The SEM representation of the time-domain field may be obtained by closing the integration contour in (2) at infinity about either the upper or the lower half plane. The time intervals legitimizing these

closures depends on the asymptotic properties of the integrand in the complex ω -plane. From (7) and (8), one finds that for $t < \rho + \rho' - 2a$, the integration contour may be closed at infinity about the upper half-plane, giving a null contribution. For $t > \rho + \rho'$, the integration contour may be closed about the singularities in the lower half-plane, giving

$$G^{\pm}(\rho, \rho'; t) = \sum_{m=-\infty}^{\infty} \sum_p (G_{m,p}^+ + G_{m,p}^-) + \sum_{m=-\infty}^{\infty} I_m \quad (11)$$

where Σ' excludes the $m=0$ term (which has no poles), and p assumes values according to (9a). $G_{m,p}^{\pm}$ is the contribution from the pole $\omega_{\pm m, p}$, respectively, to the m -th term in the angular harmonics series (7)

$$G_{m,p}^{\pm} = -\frac{1}{4} \frac{J_m'(\gamma)}{H_m^{(1)}(\gamma)} H_m^{(1)}(k\rho') H_m^{(1)}(k\rho) e^{im\phi - i\omega t} \Big|_{\omega_{\pm m, p}} \quad (12)$$

The branch cut integral, taken along the contour C_b surrounding the branch cut in Fig. 3, is given by

$$I_m = e^{im\phi} \frac{1}{2\pi} \int_{C_b} d\omega e^{-i\omega t} \frac{1}{8} S_m(\gamma) H_m^{(1)}(k\rho') H_m^{(1)}(k\rho) \quad (13)$$

Using (10) and the symmetry relation of the Bessel functions in the complex argument plane (when the branch cut is taken as in Fig. 3) one may verify that $(G_{m,p}^+ + G_{m,p}^-)$ is a real function; the same is true for the residue contributions with negative superscripts and for $(I_m + I_{-m})$.

The time intervals that legitimize the evaluation of the Fourier transform (2) by upper and lower half plane closure do not overlap (see discussion before (11)) and there is a time interval $\rho + \rho' - 2a < t < \rho + \rho'$ where the field does not necessarily vanish, yet (11) is not valid. In fact, it may be verified that depending on the observation point, the arrival time of the specularly reflected wave occurs somewhere in this time interval. Thus, in order to obtain a valid SEM expansion in that time interval, one has to extract this early time entire function contribution from the total scattered field in (7). The SEM representation in (11) will then have to be changed accordingly; clearly the residue contributions will not change yet the branch cut integrals and the turn-on times will be modified. This procedure is described in its most natural and physically transparent way by the collective treatment of the travelling wave representation via the hybrid wavefront resonance approach, as described in Section II.D below.

C. Travelling Wave Representation

1. Frequency domain solution

To construct a travelling wave (wavefront) representation, one utilizes a Green's function $\hat{G}^{\pm}(\rho, \rho')$ representing an angularly propagating waves in an infinitely extended (non-periodic) angular coordinate space [25]. Accordingly, the field is separated into contributions \hat{G}^+ and \hat{G}^- from positively and negatively travelling waves,

$$\hat{G}(\rho, \rho') = \hat{G}^+(\rho, \rho') + \hat{G}^-(\rho, \rho') \quad (14)$$

where

$$\hat{G}^{\pm}(\rho, \rho') = \sum_{j=0}^{\infty} \hat{G}^{\pm}(\rho_j^{\pm}, \rho') \quad (15)$$

and

$$\rho_j^{\pm} = (\rho, \phi_j^{\pm}), \quad \phi_j^+ = \phi + 2\pi j, \quad \phi_j^- = \phi - 2\pi(j+1) \quad (16)$$

are the images of ρ in the infinitely extended ϕ domain $-\infty < \phi < \infty$. The j -th term in (15) represents the contribution due to the $(j+1)$ th positive or negative progression of the wave \hat{G}^{\pm} travelling around the cylinder in the unbounded angular space. The travelling wave \hat{G}^{\pm} may be represented by a spectral integral [25]

$$\hat{G}^{\pm}(\rho, \rho') = \frac{1}{2\pi} \int_{-\infty}^{\infty} \hat{g}_{\rho}^{\pm}(\rho, \rho'; \mu; \omega) e^{i\mu|\phi|} d\mu \quad (17)$$

with the radial Green's function given by

$$\hat{g}_{\rho}^{\pm}(\rho, \rho'; \mu; \omega) = \frac{\pi i}{4} \left[2J_{\mu}(k\rho_c) + S_{\mu}(\gamma) H_{\mu}^{(1)}(k\rho_c) \right] H_{\mu}^{(1)}(k\rho_s) \quad (18)$$

Here ρ_c and ρ_s are defined in (6) and for the boundary condition in (4) (c.f. (8))

$$S_{\mu}(\gamma) = -2J_{\mu}'(\gamma)/H_{\mu}^{(1)}(\gamma), \quad \gamma = ka \quad (19)$$

Alternatively, by closing the integration contour in (17) about the poles of \hat{g}_{ρ}^{\pm} in the upper half of the complex μ -plane, \hat{G}^{\pm} may be expanded in terms of radial eigenfunctions ψ_{ρ} and their adjoints $\bar{\psi}_{\rho}$.

$p=1,2,\dots$ giving

$$\hat{G}^{\omega}(\rho, \rho') = \sum_{p=1}^{\infty} \hat{G}_p^{\omega}(\rho, \rho') \quad (20)$$

with

$$\hat{G}_p^{\omega}(\rho, \rho') = \psi_p(\rho; \omega) \bar{\psi}_p(\rho'; \omega) \frac{1}{2\mu_p} e^{i\mu_p |\phi|} = \frac{H_{\mu_p}^{(1)}(k\rho) H_{\mu_p}^{(1)}(k\rho')}{1\gamma H_{\mu_p}^{(1)}(\gamma) H_{\mu_p}^{(1)}(\gamma)} e^{i\mu_p |\phi|} \quad (21)$$

and

$$H_{\mu}^{(1)'}(\gamma) = 0 \quad \text{at} \quad \mu = \mu_p(\gamma). \quad (22)$$

A prime or an overdot denote differentiation with respect to the order or argument of the Hankel function, respectively.

In the complex frequency plane, the wave functions \hat{G}_p^{ω} of (21) are analytic except for a branch point singularity at $\omega=0$. For symmetry, it is convenient to choose the branch cut along the negative imaginary axis (Fig. 3), thereby defining the top Riemann sheet in the complex ω -plane by $-\pi/2 < \arg \omega < 3\pi/2$. With this cut, $\mu_p(\gamma)$ satisfies the symmetry relation

$$\mu_p(\gamma) = -\mu_p^*(\gamma^* e^{i\pi}) \quad (23)$$

Accordingly, \hat{G}_p^{ω} possesses similar symmetries which ensure that the transient response of each wave species is a real function.

At high frequencies, such that $\gamma \gg 1$, one finds that

$$\mu_p(\gamma) = \gamma + \bar{\alpha}_p' (\gamma/2)^{1/3} + O(\gamma^{-2/3}), \quad \bar{\alpha}_p' = \alpha_p' e^{i\pi/3} \quad (24)$$

where α_p' is the p -th zero of $\text{Ai}(-\alpha_p') = 0$. Accordingly, the asymptotic approximation of (21) is interpreted in terms of the GTD **creeping rays** which propagate around the cylinder and shed energy along tangents into the surrounding medium. For various source-observer configurations, either near or far from the boundary, one may extract from (21) the appropriate ray diffraction, attachment or launching coefficients [26]. Here, we choose source and observer far enough from the boundary to permit formation of well-defined illuminated and shadow zones. It then follows from (21) that use of the Debye asymptotic form of the Hankel functions when the argument is $k\rho$ or $k\rho'$, and of the Airy function approximation when the argument is γ [25], leads to the reduction

$$\hat{G}_p^{\omega}(\rho, \rho') = \frac{-(\gamma/2)^{1/3} e^{i\kappa(s+s')}}{\bar{\alpha}_p' w_1(\bar{\alpha}_p') \kappa \sqrt{ss'}} e^{i\kappa p \ell} \quad (25)$$

where $\kappa_p = (\mu_p/a)$ is the wavenumber of the creeping wave along the boundary, and $w_1(a) = \sqrt{\pi} [\text{Bi}(a) - i \text{Ai}(a)]$. Referring to Fig. 2.

$$s = \sqrt{\rho^2 - a^2}, \quad s' = \sqrt{\rho'^2 - a^2} \quad (26)$$

are the lengths of the tangent rays from the source and the observer to the boundary, respectively, and

$$\ell = |\phi| - \sin^{-1}\left(\frac{s}{\rho}\right) - \sin^{-1}\left(\frac{s'}{\rho}\right) \quad (27)$$

is the path length along the surface between the points of tangency. From their definition, $\ell < 0$ and $\ell > 0$ define the shadow and lit regions, respectively. Referring to (16), all the images ρ_j^{\pm} are in the shadow except possibly for the $j^{\pm}=0$ term which is in the lit region if ρ is in the lit region (since we have assumed that $0 \leq \phi \leq \pi$, the $j^{\pm}=0$ term is always in the shadow).

Since the roots α_p' in (24) are well approximated by $[(p-3/4)3\pi/2]^{2/3}$, then for $\text{Im } \mu \geq 0$, the wave functions in (25) decay in the shadow region $\ell > 0$, and furnish there an efficient approximation for the field in terms of creeping waves. In the illuminated region $\ell < 0$, the initial terms with $p=O(\gamma)$ in the wave series (20), contributed by (25), grow although the total series of **exact** eigenfunctions (21) converges [25]. The growth of this part of the series implies that **convergence is not uniform** in the frequency domain. Accordingly the representation in (20) is inappropriate in the illuminated region for the high frequency range and also for determination of the time-dependent Green's function since the Fourier inversion of the series cannot be performed term by term. Therefore, the field in the illuminated region must be treated in another fashion.

Recalling that only $\rho_0^{\pm} = \rho$ is located in the illuminated region, we express its contribution by the spectral integral (17) which yields asymptotically the direct and reflected ray fields of geometrical optics [25]

$$\hat{G}_d(\rho, \rho') = \frac{e^{ikL_d + i\pi/4}}{\sqrt{8\pi k L_d}}, \quad \hat{G}_r(\rho, \rho') = \frac{e^{ikL_{s1} + i\pi/4}}{\sqrt{8\pi k L_{r1}}} R_s \frac{e^{ikL_{sr}}}{\sqrt{1 + L_{r2}/\rho_r}} \quad (28a, b)$$

respectively. Here, L_d is the length of the direct ray from ρ' to ρ , while L_{r1} and L_{r2} are the lengths along the reflected ray from ρ' to the specular reflection point ρ_s on the cylinder, and from ρ_s to ρ , respectively (see Fig. 2(b)). Also, $R_s=1$ is the boundary reflection coefficient at the specular point, and ρ_r is the radius of curvature of the reflected wavefront which depends on the angle of incidence θ_i and on the local radii of curvature of the incident wavefront ($\rho_i=L_{r1}$) and of the boundary,

$$\frac{1}{\rho_r} = \frac{1}{\rho_i} + \frac{2}{a \cos \theta_i} \quad (29)$$

2. Time domain solution

The transient fields are obtained by Fourier transforming the time harmonic wave species discussed above. For observation points in the shadow region, where the time harmonic series converge uniformly as discussed after (27), the various wave fields are described term by term by the transient counterpart of the series in (14), (15) and (20). The same representation applies for observation points in the lit region except for the contribution from $\hat{G}^{\infty}(\rho, \rho')$ which is described by the spectral integral (17) because of the convergence difficulties noted above. We begin with the evaluation of (17), which represents in the lit region the dominant and earliest field contribution as expressed by the geometrical optics field.

a. Geometrical optics field

For observation points in the lit region, $\hat{G}^{\infty}(\rho, \rho')$ of (17) is given asymptotically by the sum of the direct and reflected ray fields in (28a,b). The Fourier transforms of these expressions are, respectively,

$$G_d(\rho, \rho') = \frac{1}{2\pi} \frac{v}{\sqrt{2L_d}} \frac{H(vt-L_d)}{\sqrt{vt-L_d}}, \quad G_r(\rho, \rho') = \frac{1}{2\pi} \frac{v}{\sqrt{2L_{r1}}} \frac{1}{\sqrt{1+L_{r2}/\rho_r}} \frac{H(vt-L_r)}{\sqrt{vt-L_r}}, \quad L_r=L_{r1}+L_{r2} \quad (30a, b)$$

where the Heaviside function H equals zero or unity for negative or positive arguments, respectively, and v is the wave velocity in the medium. These signals turn on at $t=L_d/v$ and at $t=L_r/v$, the arrival times of the direct and reflected rays, respectively. Resulting from saddle point evaluation of (17), expressions (30a,b) represent constructive interference of a very narrow spectrum of plane waves around the central geometrical ray. Therefore, these waveforms are limited to a short time interval behind the wavefront (after turn-on), and are called therefore **wavefront approximations**.

A representation valid for longer time may be obtained by utilizing a wider spectral range around the geometrical ray. This can be done by utilizing a non-dispersive plane wave (WKB) approximation of the integrand in (17), with subsequent **closed form** evaluation of the integral via the **Spectral Theory of Transients (STT)** [20,21], which is a generalization of the Cagniard-deHoop technique [27]. The STT derivation of these transient waveforms for the present example of transient scattering by a circular cylinder is given in [12].

b. Creeping Waves

Except for the lit region, where the $\hat{G}(\rho, \rho')$ integral describes the the geometrical optics field, all other terms in (14) and (15) are expressed by the radial eigenfunction expansion in (20), with (21). For a typical term $\hat{G}_j(\rho, \rho')$, one observes from (24) and (25) that

$$\hat{G}_j(\rho, \rho') \sim O(e^{-kL_j}), \quad L = s + s' + l \quad (31)$$

where l is the total diffracted ray path from ρ' to ρ . Accordingly, $G_j^{\infty}(\rho, \rho')$ vanishes before $t = L/v$ so that the j -th term in (15), which represents the contribution from the j -th circumnavigation of the composite travelling wave, turns on at $t = L_j^{\dagger}/v$, where L_j^{\dagger} is the ray path of that wave, (obtained from (31) and (27) with ϕ replaced by ϕ_j^{\dagger} in (16) (see Fig. 4).

After turn-on, G_j^{∞} is resolved into the creeping waves given by the Fourier transform of (21), which cannot be found explicitly. However, near the wavefront ($t \geq L/v$) the main contribution to the integral comes from high frequencies, whence G_p^{∞} may be approximated by Fourier transforming the asymptotic creeping ray field (25), yielding the result

$$\hat{G}_p^{\infty}(\rho, \rho') \sim \frac{2^{1/3}}{8\pi\alpha_p A_1(-\alpha_p)} \frac{av}{t^{3/2} \sqrt{3s'}} \delta A_1(\delta) H(vt-L), \quad \delta = \delta(t, L) = \alpha_p' [6(vt-L)/a]^{1/3} \quad (32)$$

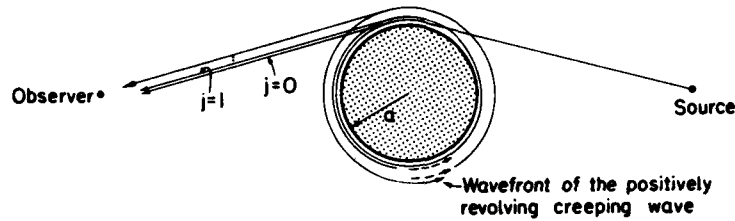


Fig. 4 Wavefront contributions from positively revolving creeping wave. Only wavefronts with small index j such that $L_j < vt$ contribute at time t .

Equation (32) is an exact evaluation of the Fourier integral of the asymptotically approximated creeping wave field (25). Accordingly, its range of validity may be estimated by requiring that the approximation (25) of the integrand will be valid in the vicinity of the stationary point of the phase of the integrand which yields the main contribution to the integral (see Fig. 5). Accordingly, (32) applies as long as

$$|Y_s| = |i\alpha_p^3 \delta^{-3/2}| \gg \rho, \quad (33)$$

where $Y_s = \omega_s a/v$ is the stationary point and δ is given in (32). Since this condition imposes a restriction on the observation time after the arrival of the wavefront of the creeping wave, (32) may be used to describe only the contributions from the **latest passes** (see Fig. 4). Contributions from the earlier passes (fewer revolutions or small j) are dominated by low frequency components not accommodated by (32). However, by the hybrid representation of [9], the contribution from the earlier passes can be combined into low frequency SEM resonances.

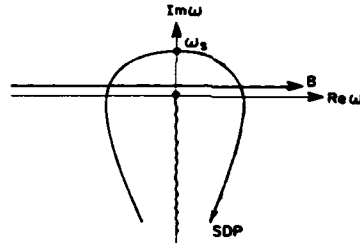


Fig. 5 Complex w -plane for the Fourier evaluation of the creeping wave result in (32). The range of validity of (32) is estimated by requiring that the integrand in (25) will be valid along the steepest descent path (SDP) which pass through the saddle point ω_s . B is the original integration contour in (2).

D. Collective Summation of Wavefronts: SEM Representation

1. Frequency domain solution

The series of arrivals in (15) can be readily summed in closed form since, as follows from (16) and (21), the index j appears only in the angular phase term. When the observer is in the **shadow region**, all terms $j \geq 0$ can be treated collectively to yield

$$\hat{G}^{\pm}(\rho, \rho') = \sum_{p=1}^{\infty} \frac{\hat{G}_p^{\pm}(\rho_0^{\pm}, \rho')}{1 - e^{i2\pi p}} \quad (34)$$

with ρ_0^{\pm} given in (16). However, for observation points in the **lit region**, since the $j^+ = 0$ term in \hat{G}^+ is represented by the spectral integral (17) (see discussion after (27)) and **cannot** be included in the collective treatment, the sum starts at $j^+ = 1$, giving

$$\hat{G}^+(\rho, \rho') = \hat{G}^-(\rho, \rho') + \sum_{p=1}^{\infty} \frac{\hat{G}_p^-(\rho_1^+, \rho')}{1 - e^{i2\pi p}} \quad (35)$$

The summation for \hat{G}^- starts at $j^- = 0$ as in (34). The field representations in (34) and (35) consists of a

collective term that give rise to the SEM resonances in terms of the roots of the denominator, plus a possible free term (in (35), for observation point in the lit region) which does not have the SEM pole singularities and may be interpreted as the SEM entire function. We shall consider these terms in sequence.

2. The resonances

The collective terms in (34) and (35) generate a field representation in terms of SEM resonances. The numerators represent the field \hat{G}_p^m of the first creeping wave included in the collective sum: $j^+ = 0$ in the shadow, and $j^+ = 1$ for \hat{G}^+ , $j^- = 0$ for \hat{G}^- in the lit region, respectively (see Fig. 2). The denominator represents the **collective effect** due to all subsequent revolutions. The roots of the denominator, in the lower half of the complex ω -plane, define the poles $\omega_{p,m}$ of the scattered field via

$$u_p(\gamma_{p,m}) = m, m = \pm(2p-1), \pm 2p, \dots \quad (36)$$

which states that for a resonance, the phase accumulation in a complete revolution must be an integer multiple of 2π . From their definition in (36) and (22) one may readily verify that the resonances are identical with those defined by (9). Moreover, it follows from (36) that for a given p , the resonances lie on the p -th layer in the complex ω -plane (Fig. 3) which generates the singularity expansion of the angularly progressing p -th creeping wave. For given m , the resonances lie on arcs in the complex ω -plane, and define by this grouping the conventional angular harmonics that are **oscillatory** in the angular domain (c.f. (7)). The value m of u_p at the resonances is in agreement with (9) and (9a). The resonances defined by the indices (m,p) in (36) are located on the upper Riemann sheet $-\pi/2 < \arg \omega < 3\pi/2$. Other poles with other values of (m,p) are located on the lower sheet (e.g. poles with $m = 1, \dots, 2(p-1)$ are located on the continuation of the p -layer in Fig. 3 from the forth quadrant $-\pi/2 < \arg \omega < 0$ to the third quadrant $-\pi < \arg \omega < -\pi/2$ in the lower sheet)

3. Time domain resonance series

The SEM resonance series (including the branch point contribution) is generated by evaluation of the inversion integral (2) through contour deformation at infinity around the lower half plane frequency in the complex frequency plane. The ability to deform the contour in the upper or lower halves depends on the convergence properties of the integrand. From (24) and (25), one may infer the dominant behavior as follows:

$$\text{collective term} = \begin{cases} \exp[ikL] & , \text{Im } \omega \geq 0 \\ \exp[ik(L-2\pi a)] & , \text{Im } \omega < 0 \end{cases} \quad \begin{matrix} (37a) \\ (37b) \end{matrix}$$

where, L defined in (31) represents the length of the surface ray paths associated with the wavefronts in the numerator of the collective term, i.e., $L = L_0^+$ and $L = L_1^+$ for the collective terms of (34) and of (35), respectively. Thus, the field vanishes for $t < L/v$ since, in view of (37), the integration contour of (2) may be closed at infinity in the upper half plane. After that time, the integration contour may be closed about the singularities in the lower half plane to yield for g in the shadow region two real series

$$G^\pm(g, g') = H(vt - L_0^\pm) \sum_{p=1}^{\infty} \left\{ \sum_m G_{p,m}^\pm(g, g') + G_{p,c}^\pm(g, g') \right\} \quad (38)$$

with residue contributions that are real for pairwise (symmetrical) m and $(-m)$,

$$G_{p,m}^\pm(g, g') = \hat{G}_p^\pm(g_0^\pm, g'; \omega) \frac{ve^{-i\omega t}}{2\pi a u_p'(\gamma)} \Big|_{\omega=\omega_{p,m}} = \frac{\omega}{2\pi i} \frac{H_m^{(1)}(k\rho) H_m^{(1)}(k\rho')}{[\gamma^2 - m^2][H_n^{(1)}(\gamma)]^2} e^{i\pi m \phi_0 - i\omega t} \Big|_{\omega_{p,m}} \quad (39)$$

and (real) branch cut contributions from the p -th term in (34),

$$G_{p,c}^\pm(g, g') = \frac{1}{2\pi} \int_0^{\infty} \frac{d\omega}{\omega} e^{-i\omega t} 2\text{Re}(\omega \hat{G}_p^\pm(g_0^\pm, g')) \quad (40)$$

In view of the relation

$$u_p'(\gamma) H_{2p}^{(1)}(\gamma) = H_{2p}^{(1)'}(\gamma)$$

the pole contributions may be shown to be identical with those in (12). Thus, (38) defines two real SEM transient series, one for the positively, and the other for the negatively, revolving travelling waves. Each "turns on" at the "physically correct" arrival time of the first wavefront of the corresponding wave

species. Note also that the p -th term in (34) and (38) may be considered as the SEM representation for the field of the positively or negatively revolving p -th creeping wave. The m -summation in this case, with p constant, goes along layers in the SEM pole map in Fig.3 (see results of numerical summation in [16]).

4. The intrinsic entire function

For observation points in the **lit region**, the SEM representation of G^- is unchanged whereas the one of G^+ follows from (35) and contains, in addition to the collective term, the GO field as expressed by $\hat{G}^{\infty}(\rho, \rho')$ (cf. Sec. III.C). This term, a spectral integral, does not have the SEM pole singularities and, except for the branch point at $\omega = 0$ (attributable to the two-dimensional problem here), is analytic in the complex frequency plane. It can therefore be interpreted as the SEM intrinsic (non removable) entire function. In the time domain, it yields a short duration signal, as discussed in Sec. II.5.2.a, which turns on at the arrival time of the GO rays, i.e. **before** turn-on of the diffracted wavefronts expressed either by the travelling wave expansion (15), with (32), or by the collective term in (35). This latter term yields, in the time domain, the resonance series (38)-(40), with $\rho_0^+ + \rho_1^+$. Note that since $\phi_1 = \phi_0 + 2\pi$ and $\nu_p = m$ at $\omega_{p,m}^+$, the residue contribution is the same as in (39), but the turn-on time of this expansion is now the arrival time $t = L_1^+/v$ of the first positively revolving creeping wave and is later than that of the geometrical optics field (see Fig. 2(b)).

5. The removable entire function

As explained in the Introduction, one may generate another type of entire function by switching the resonance series on at some time **after** the physical turn-on time. Since this entire function may be absorbed into the SEM representation by turning on at the physically correct time, it is **non-intrinsic (removable)**. This function appears if the collective summation of travelling waves in (15) is started not at the first possible revolution (lowest j , e.g. $j^+ = 0$ for (34) and $j^+ = 1$ for (35)) but after any given number of revolutions, say J (see Fig. 6). Thus

$$\hat{G}^+(\rho, \rho') = \sum_{j=0}^{J-1} \hat{G}^{\infty}(\rho_j^+, \rho') + \sum_{p=1}^{\infty} \frac{\hat{G}_p^{\infty}(\rho_J^+, \rho')}{1 - e^{i2\pi\nu_p}} \quad (41)$$

where the **singularity-free** explicit contributions from the first J revolutions in the first sum can also be written **collectively** in the form

$$\sum_{j=0}^{J-1} \hat{G}^{\infty}(\rho_j^+, \rho') = \sum_{p=1}^{\infty} \hat{G}_p^{\infty}(\rho_0^+, \rho') \frac{1 - e^{iJ2\pi\nu_p}}{1 - e^{i2\pi\nu_p}} \quad (42)$$

Clearly, in view of (36), the poles in the collective expression on the right hand side of (42) are cancelled by the zeroes of the numerator. Thus, the wavefronts on the left-hand side of (42) are seen to provide an interpretation for the removable entire function on the right-hand side, and thereby for the entire function on the left hand side of (3), which has been constructed (as in [6]) by formal rearrangement of the full resonance series with delayed turn-on times. The collective term in (41) (second term on the right hand side) is equal to (34) multiplied by $\exp(i2\pi J\nu_p)$ (see (16) and (21)), whence after Fourier transforming into the time domain, it yields an expression similar to (38) with the **same resonances** as in (39), but turn-on time $t = L_1^+/v$, the arrival time of the **first** (the J -th) wavefront included in the collective treatment.

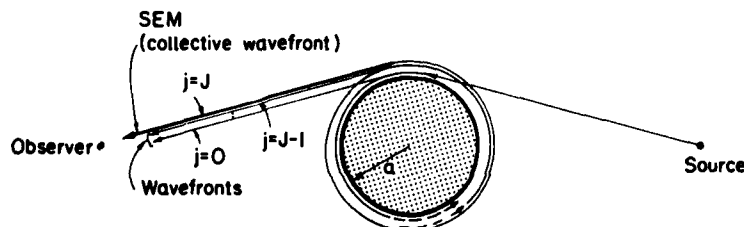


Fig. 6 A hybrid representation of the scattered field wherein the first J wavefronts are kept intact whereas the remainder are expressed collectively via SEM (cf. (41)).

E. Hybrid Formulation

To circumvent the various analytical, conceptual and computational problems associated with either the wavefront or the resonance expansion schemes in certain time intervals, one may explore hybrid formulations that combine wavefronts and resonances (usually with a remainder term) in uniquely defined proportion, so chosen as to minimize the source of difficulty. The strategies for constructing these forms, and the resulting expressions for the transient field, have been given in [9]. We shall therefore not pursue this matter further.

However, one may note that utilization of the removable entire function in Sec. IV.D.5 also generates a hybrid representation as schematized in Fig. 6, where an arbitrarily selected number of creeping wave fields is kept intact, and the remainder is expressed in terms of resonances (plus a branch cut integral). As seen from (41) and (42), and the discussion thereafter, **all** of the resonances contribute here with the same excitation (coupling) coefficients, but with delayed turn-on which diminishes the dominant excitation amplitude from the $j = 0$ creeping wave to that of the first creeping wave $j = J$ included in the collective treatment. Since delaying the turn-on time implies reduction of the high-frequency spectral components in the response, this procedure improves the convergence properties of the resonance series as well as reducing its overall importance.

IV. WAVEFRONT ANALYSIS OF SCATTERING BY A GENERAL OBJECT

The basic observations derived in Sec. III regarding the wavefront resonance interplay, may be generalized to more complicated targets comprising composite substructures. Here, the target response may be described by wavefront interactions between identifiable scattering centers on the scatterer, and the totality of multiple interactions can be "collecterized" in many alternative forms. This approach however requires a systematic ordering of the multiplicity of wavefronts corresponding to successive scattering events on the target as provided by the system flow diagram.

A. Ray Formulation of the Scattering Process

1. Ray expansion

The response generated by a field incident on a complicated configuration may be analyzed in terms of simpler (canonical) **scattering events** and the interaction between these events. The choice of the canonical constituents is not unique but is influenced by the ease, or not, of treating each in isolation and then accounting for the mutual interaction. Within the framework of ray theory, a scattering event is taken to designate any process that converts an incoming ray into an outgoing ray. Scattering events therefore include processes of reflection and refraction at a boundary, refraction by medium inhomogeneity, diffraction at an edge, etc. The interaction process between (isolated) scattering events is described by the propagation function, the ray optical amplitude and phase, that connects successive **scattering centers**. The scattering centers, which identify where the scattering process takes place, may be at a fixed location, as at an edge, or they may correspond to different points on a surface, as for reflections from smooth boundaries (see Fig. 1).

To construct the hierarchy of scattering processes caused by direct scattering of the incident field and by subsequent successive scattering events, we shall assume N scattering centers and identify by the index $p = 1, \dots, N$ and their locations by the coordinate vector \vec{r}_p . We also define a **scattering function** $\hat{S}(\vec{r}, \vec{r}_p; \vec{r})$ which expresses the field at a point \vec{r} caused by scattering at \vec{r}_p of a ray field with unit amplitude arriving from a point \vec{r} . Thus $\hat{S}(\vec{r}, \vec{r}_p; \vec{r})$ includes the scattering process at \vec{r}_p (normalized with respect to a unit amplitude incident field from the direction of \vec{r}) and the propagation function between \vec{r}_p and \vec{r} . For time-harmonic ray field, it has the local plane wave form

$$\hat{S}(\vec{r}, \vec{r}_p; \vec{r}) \sim A(\vec{r}, \vec{r}_p; \vec{r}) \exp[ik\psi(\vec{r}, \vec{r}_p)] \quad (43)$$

where A is slowly varying amplitude function, which may be proportional to an inverse fractional power of the reference wavenumber k , and $k\psi$ is a rapidly varying phase. The function ψ is independent of k to the leading asymptotic order, and equals to

$$\psi(\vec{r}, \vec{r}_p) \sim L(\vec{r}, \vec{r}_p) \quad (44)$$

where $L(\vec{r}, \vec{r}_p)$ is the (optical) length of the ray trajectory from \vec{r}_p to \vec{r} . The higher order correction terms are such that they have a positive imaginary part for $\text{Im } \omega \geq 0$. Finally, for vector fields, the scattering function is a vector function that depends also on polarization (a dyad).

The total field $\hat{u}(\underline{r})$ is given by

$$\hat{u}(\underline{r}) = \sum_{j=1}^{\infty} \hat{u}^{(j)}(\underline{r}) \quad (45)$$

with the contributions $\hat{u}^{(j)}(\underline{r})$ ordered according to the number j of interactions that have taken place before reaching the observer at \underline{r} and $j=1$ accounting for the direct scattering of the incident field \hat{u}^i at the scattering center \underline{r}_p . Thus, if the source located at \underline{r}' establishes at \underline{r}_p the incident field $\hat{u}^i(\underline{r}_p; \underline{r}') = \hat{u}^i(\underline{r}_p)$, one may write

$$\hat{u}^{(1)}(\underline{r}) = \sum_p \hat{u}^i(\underline{r}_p) \hat{S}(\underline{r}, \underline{r}_p; \underline{r}') \quad (46a)$$

and express the field $\hat{u}^{(j)}(\underline{r})$ by iteration as

$$\hat{u}^{(j)}(\underline{r}) = \sum_{p,q} \hat{u}^{(j-1)}(\underline{r}_p; \underline{r}_q) \hat{S}(\underline{r}, \underline{r}_p; \underline{r}_q), \quad j \geq 2 \quad (46b)$$

With the indices p, q and i extending over the N scattering centers, $\hat{u}^{(j)}(\underline{r}_p; \underline{r}_q)$, the ray field incident on \underline{r}_p from \underline{r}_q after j interactions can be found recursively as

$$\hat{u}^{(j)}(\underline{r}_p; \underline{r}_q) = \sum_i \hat{u}^{(j-1)}(\underline{r}_q; \underline{r}_i) \hat{S}(\underline{r}_p, \underline{r}_q; \underline{r}_i), \quad j \geq 2 \quad (47a)$$

$$\hat{u}^{(1)}(\underline{r}_p; \underline{r}_q) = \hat{u}^i(\underline{r}_q) \hat{S}(\underline{r}_p, \underline{r}_q; \underline{r}') \quad (47b)$$

In most time-harmonic applications the scattering amplitudes associated with A in (43) are reduced by successive scattering events, thereby permitting truncation of the interaction series (45). This is not the case however in certain applications, in particular those involving high Q resonances, where the implementation of (45)-(47) in its stated form is clearly nonfeasible. One must therefore attempt to sum these multiple interactions collectively to synthesize the high frequency field. In the time domain, truncation is automatic, due to causality. The wavefront fields are ordered according to their arrival times along paths corresponding to the phase ψ in (43), and constituents with long composite travel paths are eliminated at early times, thereby making the recursive approach a workable option. As time goes on, not only does the number of arrivals increase, but the high-frequency ray model as in (43) fails to describe the fields of the early arrivals, far behind their wavefronts. Therefore, alternative methods, based on collective treatment of many wavefront fields, must be considered also at later times in the transient domain. In this collective treatment, limitations imposed by GTD approximations (if these have been used) must be kept in mind.

2. Implicit collective representation via matrix formulation

To proceed, it is desirable to reformulate the iterative equations (45)-(47) in matrix form. Summing over j we obtain

$$\hat{u}(\underline{r}_p; \underline{r}_q) = \sum_i \hat{u}(\underline{r}_q; \underline{r}_i) \hat{S}(\underline{r}_p, \underline{r}_q; \underline{r}_i) + \hat{u}^i(\underline{r}_q) \hat{S}(\underline{r}_p, \underline{r}_q; \underline{r}') \quad (48a)$$

$$\hat{u}(\underline{r}) = \sum_q \hat{u}^i(\underline{r}_q) \hat{S}(\underline{r}, \underline{r}_q; \underline{r}') + \sum_{p,q} \hat{u}(\underline{r}_p, \underline{r}_q) \hat{S}(\underline{r}, \underline{r}_p; \underline{r}_q), \quad (48b)$$

where $i, p, q = 1 \dots N$. This represents a system of N^2 equations for the unknown total fields $\hat{u}(\underline{r}_p; \underline{r}_q)$ at \underline{r}_p due to all ray fields coming from \underline{r}_q . Equations (45)-(47) may be regarded as an iterative solution of (48). To affect a collective representation, (48a) will be solved alternatively in terms of the inverse of the matrix $(\underline{I} - \underline{S})$, wherein \underline{I} is the identity matrix and \underline{S} is the $(N^2 \times N^2)$ matrix of the scattering functions $\hat{S}(\underline{r}_p, \underline{r}_q; \underline{r}_i)$ on the right hand side of (48a). In the frequency domain, the zeros of the determinant of $(\underline{I} - \underline{S})$, which appears in the denominator of its inverse, are the SEM poles of the frequency response of the scatterer (their accuracy will depend on the approximation, if any, incorporated into the scattering function). Fourier transforming into the time domain, the transient response may then be expressed in terms of the residues of the inverted matrix at the poles, thereby generating the SEM resonance series representation. Physically, the collective representation accounts for multiple interactions which occur along any closed ray path encompassing some (or all) of the scattering centers in

a certain order. Resonances are consequences of self-consistent closure of the ray fields along such a path. Due to coupling between various closed paths (each scattering center may interact not only with one other but with many centers), the **partial resonances** for a single closed path are perturbed, and the resulting mechanism for generating the composite resonances is not easily discerned from the matrix treatment of (48). Moreover, the asymptotic properties of the inverted matrix, of importance for determination of turn-on times and convergence of the resonance series in the time domain, are not explicit, but hidden within the formal treatment. For clarification of these features, it is suggestive to resort to a graphical representation of (45)-(47) in terms of a signal flow graph, which yields the determinant and the inverse of the matrix **explicitly** in terms of the scattering function along the ray paths.

B. Flow Graph Representation

1. Construction of the graph

A signal flow graph is an operational diagram, in which weighted directed branches indicate the operational relation between nodes that correspond to a set of variables describing the state of the system. The "flow" incorporates the **causal relationship** among the variables and the graph as a whole but permits insight into the dynamical properties of the system. These features have been exploited for engineering analysis of complicated system configurations [19].

In a signal flow graph for the problem stated in (45)-(48) a typical node as shown in Fig. 7 is taken to represent the field $\hat{u}(r_p; r_q)$ at r_p due to rays originating at r_q , the latter in turn being excited by rays originating at r_l , $l = 1 \dots N$. These rays are represented by the branches which have weights (transmittance ratios) given by scattering functions $\hat{S}(r_p, r_q; r_l)$. They are the graphical equivalent of terms in the sum in (48a) or (47a). Other branches shown on the graph depict the direct ray from the source at r' to r_q [node $\hat{u}^i(r_q)$] and from there to the observer [node $\hat{u}(r)$; terms of the first sum in (48b) or (46a)] as well as to the various scattering centers r_p [node $\hat{u}(r_p; r_q)$; second terms on the right hand side of (48a) or (47b)]. The contributions from $\hat{u}(r_p; r_q)$ to $\hat{u}(r)$ are also shown [terms in the second sum in (48b) or (46b)]. To distinguish branches which are associated with multiple interaction process from those which are not, the former are depicted by solid lines and the latter by dashed or dotted lines in Fig. 7 and thereafter. The complete flow graph is obtained by drawing simultaneously all possible (p,q) nodes and their branch interactions. The graph then consists of a **main graph** (solid branches), describing the multiple interactions, and of **coupling branches**, connecting the main graph to the source and observer nodes.

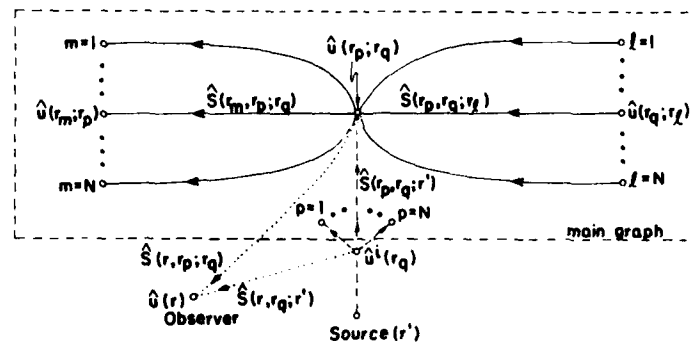


Fig. 7 Typical unit cell in a flow graph. The node $\hat{u}^i(r_q)$ is excited by the source and radiates in turn to the observer and to the node $\hat{u}(r_p; r_q)$, $p=1, \dots, N$. The field $\hat{u}(r_p; r_q)$ is also generated by $\hat{u}(r_q; r_l)$, $l=1, \dots, N$, and radiate to $\hat{u}(r_m; r_p)$, $m=1, \dots, N$. Excitation of the graph by the source, and radiation to the observer are denoted by dashed and dotted lines, respectively. The main part of the graph, along which multiple interactions occur, is represented by solid lines. The total graph is obtained by connecting all the (p,q) unit cells.

2. Cumulative treatment and entire function

The iterative approach to reading the flow diagram yields the ray expansion in (45)-(47). Here, one tracks the signal as it evolves along the branches of the graph from one node to another. Alternatively, the cumulative approach is based upon describing multiple interactions as repetitive events occurring along closed ray paths, closed loops in the main part of graph, that include some or all of the scattering centers in any order. In general, there are infinitely many such loops but for a finite graph there exists a finite set of **linearly independent loops** in terms of which one may represent all others. This set consists of **all non-repeating closed loops on the graph**, i.e., those which may be drawn without encountering the same node twice. Having found all the closed loops, one may write the cumulative body response (the total graph transmittance) in closed form by using Mason's formula [19]

$$\hat{u} = \frac{1}{\Delta} \sum_n \hat{u}_n \bar{\Delta}_n \quad (49)$$

where the **graph determinant** Δ is given by

$$\Delta = 1 - \sum_i \hat{P}_{i,1} + \sum_i \hat{P}_{i,2} - \sum_i \hat{P}_{i,3} + \dots \quad (50)$$

Here

\hat{u}_n is the **path gain** (product of branch transmittances) of the n -th **direct path** (without loops) from the source to the observer node;

$\bar{\Delta}_n$ is the **complementary graph determinant**, i.e., determinant of the n -th **nontouching-subgraph** (which has no common node with the n -th direct path);

$\hat{P}_{i,1}$ is the **loop gain** (product of branch transmittances along the loop) of the i -th loop;

$\hat{P}_{i,2}$ is the product of loop gains of the i -th **pair of nontouching loops**;

$\hat{P}_{i,j}$ is the product of loop gains of the i -th group of j nontouching loops.

The index n in (49) may be taken to identify different ray species which we distinguish from one another by the number and types of encounters between source and observer. When applying (49) to the graph of equation (48) and of Fig.7, one may note first, that the path depicting the **direct interaction** of the incident field with the scatterer (the dashed path from r' to r via node $\hat{u}^1(r_q)$) does not touch **any** of the (solid line) closed loops which describe the multiple interactions. Accordingly the determinants $\bar{\Delta}_n$ of the non touching subgraphs for these direct paths are equal to Δ . Extracting these terms, one may write instead of (49)

$$\hat{u}(r) = \sum_q \hat{u}_q^d(r) + \sum_n \hat{u}_n^w(r) (\bar{\Delta}_n / \Delta) \quad (51)$$

This expression has the same functional form as (1) (cf. (35)). The first term in (51) contains contributions at r from **direct** interaction of the incident field with each of the scattering centers at r_q

$$\hat{u}_q^d(r) = \hat{u}^1(r_q) \hat{S}(r, r_q; r') \quad (52)$$

and may be recognized as the first term in (48b) or the $j=1$ iteration in (46a). The summation over q in (51) only includes points r_q in the region illuminated by the source. Points in the shadow are reached by diffracted wavefronts, which have undergone at least two interactions with the scatterer and are therefore in the main part of the graph (the non-dashed part) and also in the second term in (51).

The second sum in (51) accounts **cumulatively** for **all** the higher order interactions j in (47), taking place in the main part of the graph. The term \hat{u}_n^w represents the wavefront or ray field contribution along paths going from source to observer via successive (more than one but without repetition) single scattering events. Calling such a path the n -th direct path and denoting by p_1, p_2, \dots, p_u the indexes of the scattering centers along it, one has for the direct path transmittance

$$\hat{u}_n^w(r) = \hat{u}^1(r_{-p_1}) \hat{S}(r_{-p_2}, r_{-p_1}; r') \hat{S}(r_{-p_3}, r_{-p_2}; r_{-p_1}) \dots \hat{S}(r_{-p_u}, r_{-p_{u-1}}) \quad (53)$$

Cumulative effects of multiple interactions along loops of the graph are included in $(\bar{\Delta}_n / \Delta)$. This expression will be seen to give rise to the **SEM resonances** located at the complex poles generated by the roots of Δ :

$$\Delta = 0 \quad \text{at } \omega = \omega_v \quad (54)$$

The first term in (51), which does not contain these pole singularities, will be identified in Sec. IV.C.4 as the **SEM intrinsic entire function**. It should be noted that Δ and thereby the SEM resonances, are generated by the **main part** of the graph only and are therefore **independent** of the source or the observer locations.

C. SEM Representation

1. SEM resonances

When the direct path in (53) is modified to include multiple interactions (closed loops) between scattering centers, the cumulative effect of the wavefronts transversing these loops is to the SEM resonances of the scatterer. Consider first a direct path perturbed by a simple closed loop. The direct wavefront or ray path field \hat{u}_n^w in ray species n is now weighted by the multiple interaction series (c.f. (34))

$$\hat{u}_n^w(r) \sum_{j=0}^{\infty} (\hat{P}_n)^j = \hat{u}_n^w(r)/\Delta, \quad \Delta = 1 - \hat{P}_n \quad (55)$$

where \hat{P}_n , the closed loop transmittance (gain), expresses the ray field modification after one complete round trip. The collective effect of that species, written in closed form on the right hand side, exhibits (SEM) resonances whenever the closed loop gain \hat{P}_n equals unity (ray closure condition). These resonances are indicative of **global** features pertaining to the physical environment along the closed loop. In general, there are many such loops, and there is coupling (either direct or indirect) between them. Accordingly, the simple model pertaining to an **isolated** ray species as in (55) has to be modified. We shall define the n -th **ray species** as the group of **all** wavefronts associated with the n -th direct path, including those which, **in addition** to travelling along the direct path, traverse also various closed loops. From the topological considerations leading to (49) and (51), it follows that the collective effect of the closed loops, which are associated with the n -th direct path, is given by $(\bar{\Delta}_n/\Delta)$, where $\bar{\Delta}_n$ is the complementary (or nontouching) subgraph determinant while Δ is the determinant of the **total** graph. Accordingly, the collective field of the n -th wave species is given by the n -th term in (51),

$$\hat{u}_n^w(r) = \hat{u}_n^w(r) (\bar{\Delta}_n/\Delta) \quad (56)$$

Since Δ and $\bar{\Delta}_n$ generally have no common zeros in the complex frequency plane, the SEM pole map of the n -th species (56) is generated by **all** of the zeros ω_v of Δ (possible poles introduced by the signal spectrum of \hat{u}_n^w are not considered here). Thus, **each** wave species, in principle, excite **all** of the **full-body** resonances, thereby expressing the effect of **all** of the **closed loops** in the graph. However, the excitation amplitudes differ from one species to the next because of their dependence on $\bar{\Delta}_n$ and \hat{u}_n^w at $\omega = \omega_v$. The former will be discussed in Sec. V, and will be shown to influence essentially the strength of the coupling coefficients and the possibilities of resolving individual wave species from their SEM pole map. On the other hand, \hat{u}_n^w is associated essentially with the turn on times of the wave species as will be discussed in section IV.C.2.

Considering the locations of the SEM poles in the complex ω -plane one may infer from the functional form of Δ and of $\bar{\Delta}_n$ in (50), that both have their **zeros** in the **lower half plane**. This observation is based on the fact that since the closed loop gains $\hat{P}_{i,j}$ appearing in (50) consist of multiplication of branch transmittances, they behaviour with frequency is essentially as was discussed in (43) and thereafter. It follows that the algebraic part of the $\hat{P}_{i,j}$ is small, and that their exponential dependence is one of decay and growth, respectively, in the upper and lower halves of the complex frequency plane. Thus, (56) can be satisfied only in the lower half. Moreover, again from the functional form of (50), the location of the dominant SEM poles, those near the real frequency axis, is determined by loops whose gains $\hat{P}_{i,1}$ are dominant near the real axis; these closed loop interactions are associated with low radiation loss (high Q) (see Sec. V).

2. Resonance series, turn-on and switch-on

The SEM expansion for the transient field associated with a particular ray species follows on inversion of (56) into the time domain. The evaluation of the transform depends on the asymptotic properties of the integrand which may be inferred from (43) and the discussion thereafter. Via (53) and (43), the dominant asymptotic behaviour of the wavefront field in the frequency domain is

$$\hat{u}_n^w(r) \sim k^{-\gamma_n} \exp(ikL_n) \quad (58)$$

where γ_n is some positive constant, L_n is the (optical) length of the ray along the n -th direct path, and k is the reference wavenumber. Considering the structure of Δ and $\bar{\Delta}_n$ in (50), with the observation that the closed loop gains $\hat{P}_{i,j}$ in (50) have essentially the same asymptotic exponential form $\exp(ikL_{i,j})$ as in (58), it follows that $\bar{\Delta}_n/\Delta \sim 1$ and $-\exp[ikc_n]$ in the upper and lower half planes, respectively, with c_n a positive constant. Accordingly, the asymptotic behavior of the n -th wave species in (56), expressed only by its exponential dependence, is

$$\hat{u}_n(r) \begin{cases} \exp[ikL_n] , & \text{Im } \omega \geq 0 \\ \exp[ik(L_n - \epsilon_n)] , & \text{Im } \omega < 0 \end{cases} \quad (59a)$$

$$(59b)$$

From (59a) and from the fact that all pole singularities ω_v of \hat{u}_n in (56) lie in the lower half of the complex frequency one concludes that the Fourier transform of (56) vanishes before the **turn on time of the n-th ray species** defined by

$$t_{0,n} = L_n/v \quad (60)$$

which is recognized as the arrival time of the wavefront $u_n^w(r;t)$ - the **first wavefront** in the n-th species. For $t > t_{0,n}$, the transient field in that species is obtained by closing the integration contour with a large semicircle in the lower half plane, yielding the residue contributions from the SEM poles and possible branch cut integrals $I_{b,n}$ in the lower half of the frequency plane

$$u_n(r;t) = H(t - t_{0,n}) \left\{ \sum_v \hat{u}_n^w(r) \frac{-i\Delta_n}{\partial\Delta/\partial\omega} e^{-i\omega t} \Big|_{\omega_v} + I_{b,n} \right\} \quad (61)$$

where H is the Heaviside unit function. The factors multiplying the exponential term in (61) represent the previously referred to excitation, or class 1 coupling, coefficients. Their properties in relation to the flow will be discussed in Section V. They are seen to be proportional to the ray species field $u_n^w(r)$, which provides the mechanism of excitation, and to Δ_n . In view of the meromorphicity of the resolvent kernel for **three-dimensional** scatterers [22], it is expected that the total contribution from **all** of the branch cut integrals will cancel in the overall result given by the second term in (51). For two-dimensional scatters of infinite extent, however, there is an intrinsic branch point singularity at $\omega = 0$ as was discussed in Sec. III. Finally, since the poles ω_v are distributed symmetrically with respect to the imaginary ω axis, and utilizing a similar symmetry relation for the wave function in (56), it follows that the contribution from any pair of symmetrical poles in (61) yields a real field.

Finally, one may observe from (59b) that the lower half plane closing may be performed even before $t_{0,n}$ and that (61) may be modified by replacing the turn-on time $t_{0,n}$ in (60) with a **switch-on time** $t_{s,n}$ bounded by:

$$(t_{0,n} - \epsilon_n/v) < t_{s,n} \leq t_{0,n} \quad (62)$$

Thus, the SEM time domain expression in (61) is valid **formally** even before the actual turn on time [6,7,9], even though many terms are needed to synthesize the null field required there.

3. Delayed turn-on and removable entire function

In arriving at (56) and (61), **all** of the wavefronts associated with the ray species have been treated collectively. This description can be modified into a **hybrid** form by retaining some of the earliest wavefronts (small j) intact and accounting collectively for the remaining ones (cf. (41)). There is a systematic procedure for extracting successive wavefronts from the collective ensemble involving partial summation in (55) or in its generalized form in (56). Since the basic principle is illustrated adequately by applying it to the first wavefront, we restrict our considerations to this special case. Accordingly, instead of (56), we shall express the field of the n-th ray species, which is the one to be modified, by the following identity:

$$\hat{u}_n = \hat{u}_n^w + \hat{u}_n^w(\Delta_n - \Delta)/\Delta \quad (63)$$

where the isolated first term represents the first wavefront which follows the direct path for that species (cf. (53)). The second term in (63) expresses the collective effect of all remaining wavefronts. The manipulation leading from (56) to (63) can evidently be continued for retention of subsequent wavefronts.

Alternatively, one may arrive at (63) by modifying the flow diagram to account for the individual monitoring of \hat{u}_n^w . We illustrate this for a typical unit cell in the flow graph shown in Fig. 8, where wavefronts with two scattering events are kept explicitly; here the wavefront in question passes from the source at r' to r_q and to r_p before reaching the observer at r . Accordingly, a new node $\hat{u}^{(1)}(r_p; r_q)$ is added to identify this event (c.f. (47b)). This node contributes to the field at r as well as to nodes $\hat{u}(r_m; r_p)$, $m=1, \dots, N$, in the main part of the graph. Note that the node $\hat{u}(r_p; r_q)$ in the main graph now represents the incident field at r_q due to the field at r_p , **excluding the first wavefront** which has already been accounted for in $\hat{u}^{(1)}(r_p; r_q)$. By calculating, via (49), the graph response, one may verify that the field of the wave species associated with the direct path $r' \rightarrow r_q \rightarrow r_p \rightarrow r$ is modified according to (63).

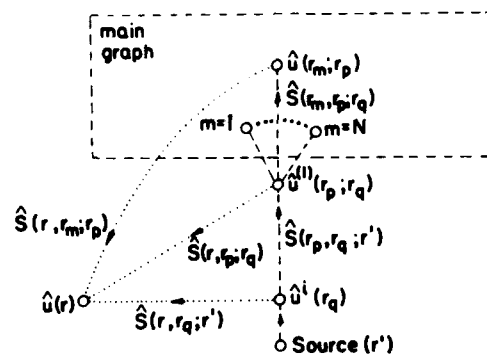


Fig. 8 Modification of typical unit cell in the flow graph of Fig. 7, exhibiting explicitly the field of the wavefront $u^{(1)}(r_p, r_q)$ and the corresponding contribution $u^{(2)}(r)$ which reach the observer after two scattering events.

The collective part in (63) has the **same** resonance denominator as (56). Moreover, the coupling coefficients in (61) (i.e. the residues at the resonances) are **unchanged** for (63) since $\Delta=0$ at resonance. However, these alternative collective expressions have different asymptotic properties in the complex frequency plane. In (56), the numerator consists of $\bar{\Delta}_n$ which, like Δ , is $O(1)$ in the upper half plane (see discussion after (58)). In contrast, considering the definition of $\bar{\Delta}_n$, the numerator $(\bar{\Delta}_n - \Delta)$ in (63) consists only of loop gains of those loops which **touch** the n -th direct path, whence the dominant term in the upper half plane is $O[\exp(ikL_{n,1})]$ where $L_{n,1}$ is the **shortest** closed ray path which belongs to the n -th species. Thus, the collective part of (63) behaves essentially like (59) except that L_n is replaced by $(L_n + L_{n,1})$, the ray path of the **first** wavefront of the n -th species which arrives at the observer after the direct wavefront u_n^w . Accordingly, the second term in (63) contributes a resonance series which is identical with (61) except that it turns on at the arrival time of the **first** wavefront which arrives after u_n^w but is included in the collective sum.

Generalizing this observation, we may state that if some of the earlier wavefronts in a ray species are monitored individually, the collective response of the remainder is described by the **same** resonance series as in (61) except that its turn-on is **delayed** to the arrival time of the first wavefront included in the collective treatment. Since the first term in (63) or its generalization as described above has no pole singularities, we shall call it a "**removable entire function**" (cf. (42)). In the time domain, the removable entire function turns on at $t_{o,n}$ of (60) and contributes primarily at early times. The representation in (63) is equivalent to, and gives a wavefront interpretation of, the formal decomposition in (3).

4. Intrinsic entire function

Unlike the removable entire function in the first term of (63), which could be incorporated into the resonance series as in (56), the first term in (51) **cannot** be treated in this manner. Therefore, we call it the **intrinsic** entire function. Physically, this term represents the field at r due to **direct** interaction of the incident field with individual scattering centers, without any interaction between these centers. Since each scattering center in isolation provides no input about the scatterer as a whole, the global information essential for developing the body resonances is lacking. As noted after (52), only those scattering centers, which are directly visible from source **and** observation points, contribute here. In the transient domain, the turn-on time at r of the intrinsic entire function is **generally** earlier than that of the resonance series (61), as follows from the observation that at least one of the direct ray paths in the first term in (51) will be shorter than the shortest path included in the second term.

Unlike the collective term in (51) which has a long time transient representation in terms of the SEM resonances, the intrinsic entire function in (51) usually contributes only at early times but even there, its GTD form, which yields only a transient wavefront approximation is not enough to represent its full transient waveform [2,3] (cf. (30)). However, the expressions for the intrinsic entire function in the first term of (51) may be represented by "better" wave functions, such as ray integrals, spanning a spectrum of local plane waves whose stationary phase approximations yields the GTD fields but which, when kept intact, are uniformly valid in transition regions where GTD fails [1]. Moreover, such spectral integrals, when inverted into the time domain yield closed-form spectral expressions for the transient field, that is valid for longer observation times than the wave front approximations corresponding to GTD [20,21]. Alternatively, recognizing that intrinsic entire function represents the contribution from the direct interaction of the incident field with the scatterer, it may be represented by the Physical Optics (PO) field [7], which has a closed-form finite duration expression for the transient scattered field in terms of the scatterer's geometry [28,29].

D. An Example: Scattering by a Flat Strip

To illustrate the ideas presented above, we apply the flow graph procedure to a simple obstacle with two scattering centers for diffracted fields: a perfectly conducting flat strip. This configuration can actually be handled without the flow graph [13-15] but, as will be shown below, the flow graph analysis handles systematically the 4-fold multiplicity of diffracted wave species which arises due to the fact that diffractions occur on both faces of the strip.

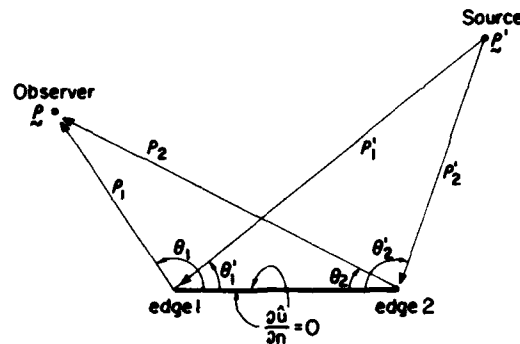


Fig. 9 Scattering by a strip.

Referring to Fig. 9, a harmonic line source at g' emits an H-polarized field whose strength at a distance L from the source is

$$\hat{G}(L) = (8\pi kL)^{-1/2} \exp(ikL + i\pi/4) \quad (64)$$

By GTD, the diffracted H field \hat{u}^d at a distance ρ from the edge is given by

$$\hat{u}^d = \hat{u}^i D(\theta, \theta') \hat{G}_0(\rho) \quad (65)$$

where \hat{u}^i is the strength of the incident field at the edge which arrives from the direction θ' , θ is the angle of observation and D is the soft edge diffraction coefficient

$$D(\theta, \theta') = -\sec\left(\frac{\theta - \theta'}{2}\right) - \sec\left(\frac{\theta + \theta'}{2}\right) \quad (66)$$

For grazing incidence $\theta' = 0$, \hat{u}^i is replaced by $\hat{u}^i/2$.

If the observer is located so that there is no specular point contribution, the field scattered from the strip is generated by single and multiple diffraction at edges 1 and 2 in Fig. 9. Introducing source and observer coordinates $g' = (\rho_p', \theta_p')$ and $g = (\rho_p, \theta_p)$, respectively, in coordinate systems centered at edge p ($p=1,2$), one is led to the flow graph in Fig. 10(a). The incident field at the edges is represented by nodes $\hat{u}^i(p)$, $p = 1,2$, given by (64) with $L = \rho_p'$, and the singly diffracted ray contributions by the dotted branches $A_p = D(\theta_p, \theta_p') \hat{G}_0(\rho_p)$ leading from these nodes to the observer. In addition, each edge also sends two diffracted rays towards the other edge, one along the upper surface of the strip and the other along the lower surface. Accordingly, nodes $\hat{u}(p, \pm)$ denote the field incident on edge p along the upper and lower surfaces, respectively, and the transmittances of the corresponding branches are $\pm B_p$, $B_p = D(0, \theta_p') \hat{G}_0(\rho)$ (note

that $D(0, \theta') = -D(2\pi, \theta')$. Similarly, recalling the remark after (66), the branch transmittances between nodes $\hat{u}(p, z)$, which represent interaction between the edges, are $\pm C$, $C = 1/2D(0, 0)\hat{G}_0(d)$, and the branch transmittances from $\hat{u}(p, z)$ to the observer are $\pm E_p$, $E_p = 1/2D(\theta_p, 0)\hat{G}_0(\rho_p)$, respectively.

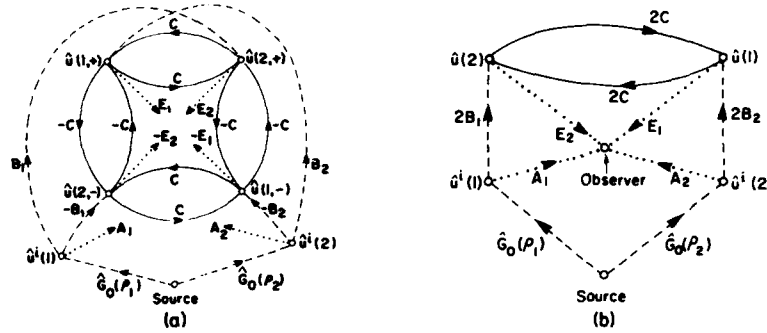


Fig. 10 Flow graph for strip scatterer.

(a) Full graph. Nodes $\hat{u}(p, z)$ are the fields incident on edge p along the upper or lower surfaces of the strip, respectively. As in Fig. 7, the dashed, full, and dotted branches represent excitation, multiple interaction, and radiation, respectively. The branch transmittances for $p = 1, 2$ are defined in the text. For clarity, the observer node is suppressed.
(b) Graph reduced by symmetry.

The graph of Fig. 10(a) has four two-branch loops, two four-branch loops and as many as 32 direct paths through the main graph. However, due to symmetries it can be reduced to the simple graph in Fig. 10(b), which yields the simple expression for the graph determinant

$$\Delta = 1 - 4C^2 = 1 - [\hat{G}_0(d) D(0, 0)]^2 \quad (67)$$

Similarly, equation (51) yields

$$\hat{u} = \sum_{p=1}^2 \hat{u}_p^d + \sum_{p=1}^2 \sum_{q=1}^2 \hat{u}_{p,q} \quad (68)$$

where the direct contributions \hat{u}_p^d are the singly diffracted ray fields

$$\hat{u}_p^d = \hat{G}_0(\rho_p) D(\theta_p, \theta_p) \hat{G}_0(\rho_p) \quad (69)$$

and $\hat{u}_{p,q}$ represent multiple interactions corresponding to wave species (56) along direct paths through the main graph, and account for all combinations of wave fields incident on edge p and radiating from edge q (4 species). From (56), (53) and Fig. 10(b), one obtains by inspection

$$\hat{u}_{p,q} = 2\hat{G}_0(\rho_p) B_p E_q / \Delta = \hat{G}_0(\rho_p) D(0, \theta_p) \hat{G}_0(d) D(\theta_q, 0) \hat{G}_0(\rho_q) / \Delta, \quad q \neq p \quad (70a)$$

$$\hat{u}_{p,p} = 4\hat{G}_0(\rho_p) B_p C E_p / \Delta = \hat{G}_0(\rho_p) D(0, \theta_p) \hat{G}_0^2(d) D(0, 0) D(\theta_p, 0) \hat{G}_0(\rho_p) / \Delta \quad (70b)$$

With Δ given in (67), (70) represents the collective field of the wave species (cf. (56)). Alternatively, the wavefront expansion is obtained by using in (70)

$$1/\Delta = \sum_{j=0}^{\infty} [\hat{G}_0(d) D(0, 0)]^{2j} \quad (71)$$

One may verify that none of the direct interactions in (69) can be incorporated **collectively** into the sum of multiple interactions in (70) and (71). The collective sum gives rise to the SEM resonances, the roots of Δ , whose GTD approximation ω_m is given by

$$[\hat{G}_0(d) D(0, 0)]^2 = e^{i2m\pi}, \quad m = \text{integer}. \quad (72)$$

These poles in the lower half of the complex frequency plane, and refinements obtained by retaining higher order terms in the edge diffracted fields, have been calculated in [14] while the corresponding scattered field due to an incident impulsive plane wave have been calculated in [15]. The resonance implied by (72) are located along a layer that goes parallel to the real ω -axis in the lower half of the ω -plane. Moreover, the simple diffraction model used in (65) has been improved in [13] by incorporating high order slope diffracted rays within the multiple interaction scheme, with a subsequent generation of additional layers of resonances which are located deeper into the lower half of the complex ω -plane. The GTD

approximated resonances agree remarkably well, even at the lower frequency end, with the resonances calculated by applying the method of moments to the integral equation for the induced current on the strip.

V. COMPOSITE SCATTERERS AND PARTIAL RESONANCES

As was described in Sec. IV.C the resonance equation and thereby the SEM poles takes into account the collective effect of **all** the closed loop interactions, including coupling between the loops. In general, for targets comprising composite substructures (Fig. 1) the flow graph consist of subgraphs that correspond to the substructures, with branches that couple between them. For such targets, one may consider **partial resonances** characteristic of each substructure in isolation, and then explore the perturbation of these isolated resonances when the substructures are assembled to form the composite object. By this approach, it is possible to explore the effect on the resonance map caused by changes in substructures or in their relative location in the composite object, thereby providing insight into the scattering mechanisms that establish a compound resonance. Accordingly, the determinant of a scatterer comprising M subscatterers with determinants Δ_m , $m = 1, \dots, M$, will be written in the form

$$\Delta = \prod_{m=1}^M \Delta_m + C \quad (73)$$

where, in view of (50), the coupling term C consists of product of loop gains of the loops that are involved in the coupling between the substructures (cf. (74)).

Assuming first that the scatterer is composed of completely isolated subgraphs, then there is no coupling term in (73) and the resonances of the composite object consists of the **partial resonances**, the resonances of each substructure in isolation, as implied by the roots of Δ_m in (73). Depending on the subgraph within which the n -th ray species is defined, the corresponding complementary graph determinant $\bar{\Delta}_n$ has factors in common with Δ in (73) (without the term C) thereby removing the poles generated by the common factors from the field in (56). Accordingly, the poles from each isolated subgraph appear **only** in the SEM pole map of a ray species which pass through this subgraph.

In general, the graph of a typical scatterer does not consist of completely isolated subgraphs. However, there might be scatterers with weak coupling between subgraphs of an overall flow graph (e.g., those which contain resonance mechanisms with relatively low radiation loss - or high Q - such as open resonators, open pipes, dielectric scatterers, etc.). In such cases, the factorization described above is no longer possible but furnishes a good first approximation. The zeroes of Δ will still cluster in groups defined essentially by the **dominant** unperturbed zeros of the Δ_m in (73). This feature provides insight into the physical mechanisms responsible for the various resonances. It therefore follows that ray species with direct paths which do not pass through an almost isolated subgraph, provide weak excitation of the SEM resonances for that subgraph, since the determinant of that subgraph is almost a common factor of Δ and $\bar{\Delta}_n$ is (56) (cf. (79) and (80) below).

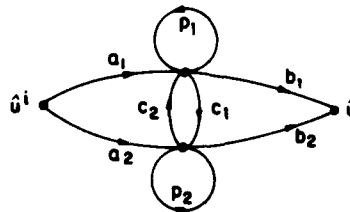


Fig. 11 A flow graph for a scatterer comprising two coupled substructures.

We shall demonstrate the observations above by considering a simple flow graph model of a scatterer comprising two weakly coupled substructures (Fig. 11). Here, the wave interaction in each substructure is modeled by a single closed loop p_m , $m=1,2$ and the coupling is modeled by two branches c_1 and c_2 . The scattered field \hat{u} due to the incident field \hat{u}^i is given now by

$$\hat{u} = \hat{u}^i [a_1 b_1 (1-p_2) + a_2 b_2 (1-p_1) + a_1 c_2 b_2 + a_2 c_1 b_1] / \Delta \quad (74)$$

where the graph determinant is given by (cf. 73))

$$\Delta = (1-p_1)(1-p_2) - c_1c_2 \quad (75)$$

and the various branch transmittances are defined in Fig. 11. Recalling that the branch transmittance has the form (43), one may readily verify that the partial resonances, the roots of the uncoupled loops are located in the lower half of the ω -plane along layers whereon $|p_m|=1$, $m=1,2$, with p_m being exponentially small or large for ω located above or below these layers, respectively. Similarly, the coupling term is also either exponentially small or large for ω above or below a "layer" whereon $|c_1c_2|=1$. Supposing now that one of the closed loop interactions, say p_1 , is of high Q type, then the corresponding layer lies close to the real ω -axis so that $|c_1c_2| \ll 1$ along that layer. The global resonances, the roots of (75), are therefore located near the partial resonances ω_{v_1} of p_1 and may be approximated by

$$\omega_v = \omega_{v_1} - \frac{c_1c_2}{p_1(1-p_2)} \Big|_{\omega_{v_1}}, \quad v = 1,2,\dots \quad (76)$$

where c_1c_2 is a small parameter and ω_{v_m} , $m = 1,2$, are the roots of

$$p_m = 1 \quad (77)$$

Regarding the partial resonances of p_2 , one may consider two cases in which p_2 represents either high Q or low Q interactions (e.g., in the first case p_1 and p_2 represent weakly coupled resonators whereas in the second case p_1 and p_2 represent, respectively, internal and external closed loop interactions of an open resonator). In the first case, the coupling term is again negligible and there is another group of high Q resonances related to the partial resonances ω_{v_2} as in (76). On the other hand, in the second case, one usually has $c_1c_2 = O(p)$ so that the coupling term is non-negligible along the layer of the partial resonances of p_2 . However, since $|p_1| \gg 1$ on that layer (recall that p_1 represents high Q interactions), one finds that Δ also has roots near ω_{v_2} , given approximately by (cf. (76))

$$\omega_v = \omega_{v_2} - \frac{c_1c_2}{(1-p_1)p_2} \Big|_{\omega_{v_2}}, \quad v = 1,2,\dots \quad (78)$$

where here, p_1 is a large parameter.

When the above approximations are substituted into (74) one finds for the field of a high Q resonance of (76)

$$u_v(t) = iu^{s_1} [a_1b_1/p_1 + O(c_1c_2)] \Big|_{\omega_{v_1}} e^{-i\omega_v t} \quad (79)$$

while the contribution of a low Q resonance of (78) is

$$u_v(t) = iu^{s_1} [a_2b_2/p_2 + O(1/p_1)] \Big|_{\omega_{v_2}} e^{-i\omega_v t} \quad (80)$$

It therefore follows that both the high Q and the low Q resonances are excited and monitored, to the leading order, by the corresponding partial resonance mechanisms, i.e. through the direct paths a_1b_1 and a_2b_2 , respectively (see Fig. 11).

VI. CONCLUSIONS

Transient fields scattered by an object may be synthesized in terms of traveling waves (wavefronts) or oscillatory waves (resonances). Traveling waves sample the propagation or scattering environment locally along their trajectories while oscillatory waves convey global information about the environment, with the former and latter being convenient (rapidly convergent) at early and late times. The two schemes have generally been employed independently, but together, these local and global samples yield effective discriminants for classification and identification of environmental features. The hybrid wavefront resonance method, reviewed in this presentation, not only clarifies the connection between the two schemes but also permits their combination within a self-consistent systematic format that draws upon the advantages of each. The hybrid approach has also been utilized for classification of the SEM resonances and the corresponding class 1 coupling coefficients and turn-on times, and for identification and interpretation of the entire function, whether intrinsic (non-removable) or removable. The main properties of these constituents of the SEM are summarized and discussed in Sections IV.C.1, 2, 3 and 4, respectively (for the circular cylinder problem, analog discussions are given in Sections III.D.2, 3, 4 and 5, respectively).

For targets comprising composite substructures, we have considered **partial resonance** characteristics, obtained by wavefront interactions within each substructure in isolation. The global resonance fields may in turn be regarded as a synthesis of interacting partial resonances due to ray coupling between the substructures. When a partial resonance process is only weakly coupled (e.g., when it is of high-Q type), it will identify approximately a subgroup of global resonances in the SEM pole map of the full body, and thereby clarify its origin. This feature may facilitate a parametric identification of certain class of targets. Conversely, this selective sampling by rays can be used for an approximate calculation of the full-body resonances.

The hybrid wavefront resonance theory has been demonstrated first within the **rigorous** context of transient scattering by a perfectly conducting circular cylinder (Sec. III), and has been generalized latter within the high frequency framework of ray theory (Sec. IV). In the analysis of Sec. III, we have treated the **exact** traveling wave solutions collectively (cf. Sec. III.D), and ray notations have been employed only to interpret wave transport and interactions mechanisms. In the general high frequency analysis of Sec. IV on the other hand, emphasis has been put on methods of systematic ordering and "collectivizing" the multiplicity of wavefront events. Accordingly, the matrix representations in (45)-(48) has been introduced to assort the wavefront interactions, whereas the flow graph representation has been used to collectivize them in terms of wave species. The field of these wave species depends **explicitly** on the scattering functions along the ray paths (cf. (51), (56)), yielding the ray interpretation of the SEM.

The preceding discussion has been based on the assumption that the propagation or scattering environment can be decomposed into scattering centers and interaction functions between the centers. Although ray terminology has been employed throughout, the model applies not only to GTD ray fields **per se** but to any other more general wave description (such as spectral integrals, modal rays, complex rays, beams, etc.) whose transport properties are associated with the ray trajectories. By using ray spectral integrals, for example, one may uniformize GTD in transition regions and also obtain long-time expressions for the ray fields [20,21]. However, the assignment of scattering centers and interaction regions in a complicated environment may be difficult. The choice of the one influences the choice of the other. Here, one may be guided by a combination of numerical and analytical techniques. Numerical methods are effective, for calculation of low frequency resonances and the SEM series converges well at the later observation times corresponding to that regime. At early times, wavefronts are few, initial ray paths can be traced, and wavefront representations (via GTD, or even better, via STT) legitimized in this high frequency regime. The wavefront treatment at early times **must** include the intrinsic entire function but it may also include some of the earliest wavefront interactions. Thereby, one can postpone turn-on of the resonance series until the low frequency resonances generated **numerically** provide an adequate description. These analytical-numerical tradeoffs, when built into the hybrid wavefront resonance scheme, may lead to an effective means for attacking a broad class of forward and inverse transient propagation and scattering problems.

REFERENCES

1. L.B. Felsen, "Progressing and oscillatory waves for hybrid synthesis of source excited propagation and diffraction", IEEE Trans. Antennas Propagat., Vol. AP-32, pp. 775-796, 1984.
2. M. and I.W. Kay, **Electromagnetic Theory and Geometrical Optics**, Wiley, N.Y. 1965.
3. L.B. Felsen, "Propagation and diffraction of transient fields in non-dispersive and dispersive media" in **Transient Electromagnetic Fields**, L.B. Felsen ed., Springer Verlag, N.Y. 1976.
4. C.E. Baum "The singularity expansion method", in **Transient Electromagnetic Fields**, L.B. Felsen ed., Springer Verlag, N.Y. 1976.
5. C.E. Baum, "The singularity expansion method: background and developmen's" *Electromagnetics*, Vol.1, No.4 (special issue on the SEM), pp.351-361, 1981.
6. L.W. Pearson, D.R. Wilton and R. Mittra "Some implication of the Laplace transform inversion on SEM coupling coefficients in the time domain", *Electromagnetics*, Vol.2, pp.184-200, 1982.
7. M.A. Morgan, "Singularity expansion representation of fields and currents in transient scattering", IEEE Trans. Antennas Propagat., Vol. AP-32, 466-473, 1984.
8. L.W. Pearson, "A note on the representation of scattered fields as a singularity expansion", IEEE Trans. Antennas Propagat., Vol. AP-32, pp. 520-524, 1984.

9. E. Heyman and L. B. Felsen "Creeping Waves and resonances in transient scattering by smooth convex objects", IEEE Trans. Antennas Propagat., Vol. AP-31, pp. 426-437, 1983.
10. E. Heyman and L.B. Felsen, "Wavefront interpretation of SEM resonances, turn-on times and entire functions", in **Hybrid Formulation of Wave Propagation and Scattering**, L.B. Felsen ed., Nijhoff Pub., North Holland, The Netherlands, 1984.
11. E. Heyman and L.B. Felsen, "A wavefront interpretation of the singularity expansion method", IEEE Trans. Antennas Propagat., Vol AP-33, pp. 706-718, 1985.
12. E. Heyman and L.B. Felsen, "Travelling waves and SEM representation for transient scattering by a circular cylinder", J. Acoust. Soc. Am., Vol. 79, pp. 230-238, 1986.
13. H. Shirai and L.B. Felsen, "Modified GTD for generating complex resonances for flat strips and disks", IEEE Trans. Antennas Propagat., Vol. AP-34, pp. 779-790, 1986.
14. H. Shirai and L.B. Felsen, "High frequency multiple diffraction by a flat strip: Higher order asymptotics", IEEE Trans. Antennas Propagat. Vol. AP-34, pp. 1106-1112, 1986.
15. H. Shirai and L.B. Felsen, "Wavefront and resonance analysis of scattering by a perfectly conducting flat strip", IEEE Trans. Antennas Propagat., Vol. AP-34, pp. 1196-1207, 1986.
16. H. Uberall and G.C. Gaunaurd, "The physical content of the singularity expansion method", Appl. Phys. Lett., Vol. 39, pp. 362-364, 1981.
17. K.M. Chen and D. Westmorland, "Impulse response of a conducting sphere based on the singularity expansion method", Proc. IEEE, Vol. 69, pp. 747-750, 1981.
18. R. Naishadham and L.W. Pearson, "Numerical evaluation of complex resonances of an elliptic cylinder", IEEE Trans. Antennas Propagat., Vol. AP-33, pp. 674-676, 1985.
19. S.J. Mason and H.J. Zimmerman, **Electronic Circuits, Signals and Systems**, Wiley, N.Y. 1960.
20. E. Heyman and L.B. Felsen, "Non dispersive closed form approximations for transient propagation and scattering of ray fields", Wave Motion, Vol. 7, pp. 335-358, 1985.
21. H. Heyman and L.B. Felsen, "Weakly dispersive spectral theory of transients: Part I - Formulation and Interpretation; Part II - Evaluation of the spectral integral; Part III - Applications", IEEE Trans. Antennas Propagat., (to be published).
22. L. Marin "Natural-mode representation of transient scattered fields", IEEE Trans. Antennas Propagat., Vol AP-21, pp.809-818, 1973.
23. C.E. Baum and L.W. Pearson, "On the convergence and numerical sensitivity of the SEM pole series in early time scattering response", Electromagnetics, Vol.1, pp.209-228, 1981.
24. K.A. Michalski, "On the class 1 coupling coefficient performance in the SEM expansion for current density on a scattering object", Electromagnetics, Vol.2, pp.201-210, 1982.
25. L.B. Felsen and N. Marcuvitz, **Radiation and Scattering of Waves**, Prentice-Hall, Englewood Cliffs, NJ, 1973, Chap. 6, Sec. 7.
26. R.G. Kouyoumjian, "The geometrical theory of diffraction and its applications", in **Numerical and Asymptotic Techniques in Electromagnetics**, R. Mittra ed., Springer Verlag, NY, 1975.
27. A.T. DeHoop, "A modification of Cagniard's method for solving seismic pulse problems", Quart. Appl. Math., Vol. 23, pp. 151-169, 1965.
28. E.M. Kennaugh and D.L. Moffatt, "Transient and impulse response approximations". Proc. IEEE. Vol. 53, pp. 893-901, 1965.
29. W.M. Boerner, C.M. Ho and B.Y. Foo, "Use of Radon's projection theory in electromagnetic inverse scattering", IEEE Trans. Antennas Propagat., Vol. AP-29, pp. 336-341, 1981.

ACKNOWLEDGEMENT

This work has been sponsored in part by the Office of Naval Research, Electronics Branch, under Contract No. 00014-83-K-0214. The author would like to acknowledge support by the Bat-Sheva De Rothschild Foundation.

PHYSICAL OPTICS METHOD: PREDICTION OF RADAR SIGNATURES

V. Stein

Deutsche Forschungs- und Versuchsanstalt für Luft- und Raumfahrt e.V.
 Institut für Hochfrequenztechnik
 8031 Oberpfaffenhofen
 Germany

AD-P005648

SUMMARY

The physical optics method finds increasing interest in the computation of radar signatures of complicated objects, which are large compared to the wavelength. A series of ideal conducting structures for which the physical optics method has been successfully applied to compute the back-scattered field is presented at first. The basic idea of physical optics following the Huygens-Helmholtz principle is evaluated. The surface integrals for the electromagnetic scattered field are presented and discussed. Some details of the physical optics method, when applied to complicated structures, are considered in the form of a short survey. This includes the hidden surface problem, the ability to predict depolarization effects for certain situations, the evaluation of the phase integral, the extension of physical optics to treat double reflections, the accuracy of the geometrical model and an estimation of the computer time. In the conclusion some steps for further extension and improvement of the physical optics method are summarized.

1. INTRODUCTION

The physical optics method (PO) is used since long time to predict bistatic scattering processes when applied to the computation of reflector antennas [1, 2]. There are numerous measurements to validate the PO-results for the copolar and crosspolar cases. The reflector systems under investigations may consist of a single reflector in the symmetric or offset [3] arrangement. In recent times also more complicated structures like dual- and four-reflector antennas [4, 5] were successfully treated with PO.

The progress in radar technology concerning the classification, identification and discrimination of targets has stimulated the interest in predicting the monostatic scattering process for application oriented objects like an airplane or a sea surface, see Fig. 1.1. Various methods, among these the PO method come into consideration for this purpose [6]. The scattering objects as the reflector antennas are large compared to the wavelength. They are in general very complicated structures with partially or completely shadowed surface regions. In a variety of practical cases also non ideally conducting subregions must be taken into account. For this category of objects rigorous methods like the integral equation method fail because of the high effort in computer time and capacity. One tries to use approximate methods, and since PO

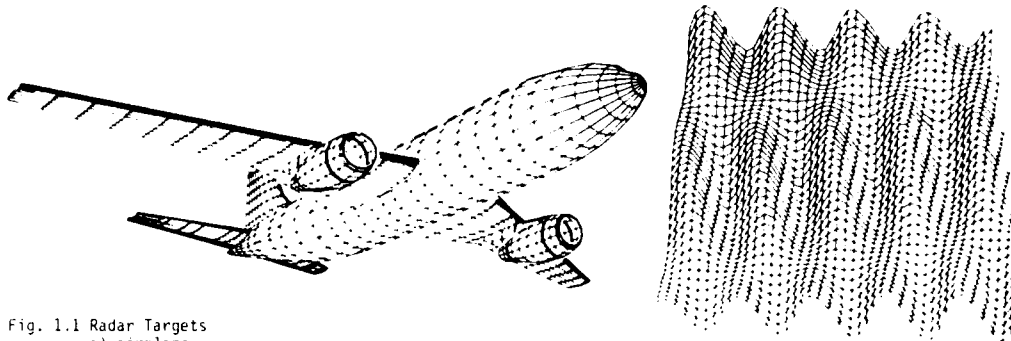


Fig. 1.1 Radar Targets
 a) airplane
 b) moving sea surface.

has proved its advantage in analyzing reflector antennas, one could think, that also in the radar back scatter case the method would work with an accuracy, which is sufficient for most practical problems. If one considers the structures of Fig. 1.1 one realizes that they can be constructed from a series of simpler structures like a flat plate, a sphere a.s.o. Several work has been done till now to test the physical optics method in the scattering case against measurements or other independent theories. Some of these structures are listed in the following and depicted in Fig. 1.2:

- flat plate (panel) [7],
- sphere [8, 9],
- circular disk [9],
- cylinder [9],
- cylinder with sphere and cone [8, 9],
- cube [8, 9],
- cube with additional shadowing surfaces [9, 10],
- trihedral corner reflector [11].

In the following the PO procedure is developed parallel to the geometrical optics (GO) concept, which forms the basis of PO. Since a lot of references, which deal with the validation of PO in the antenna and in the

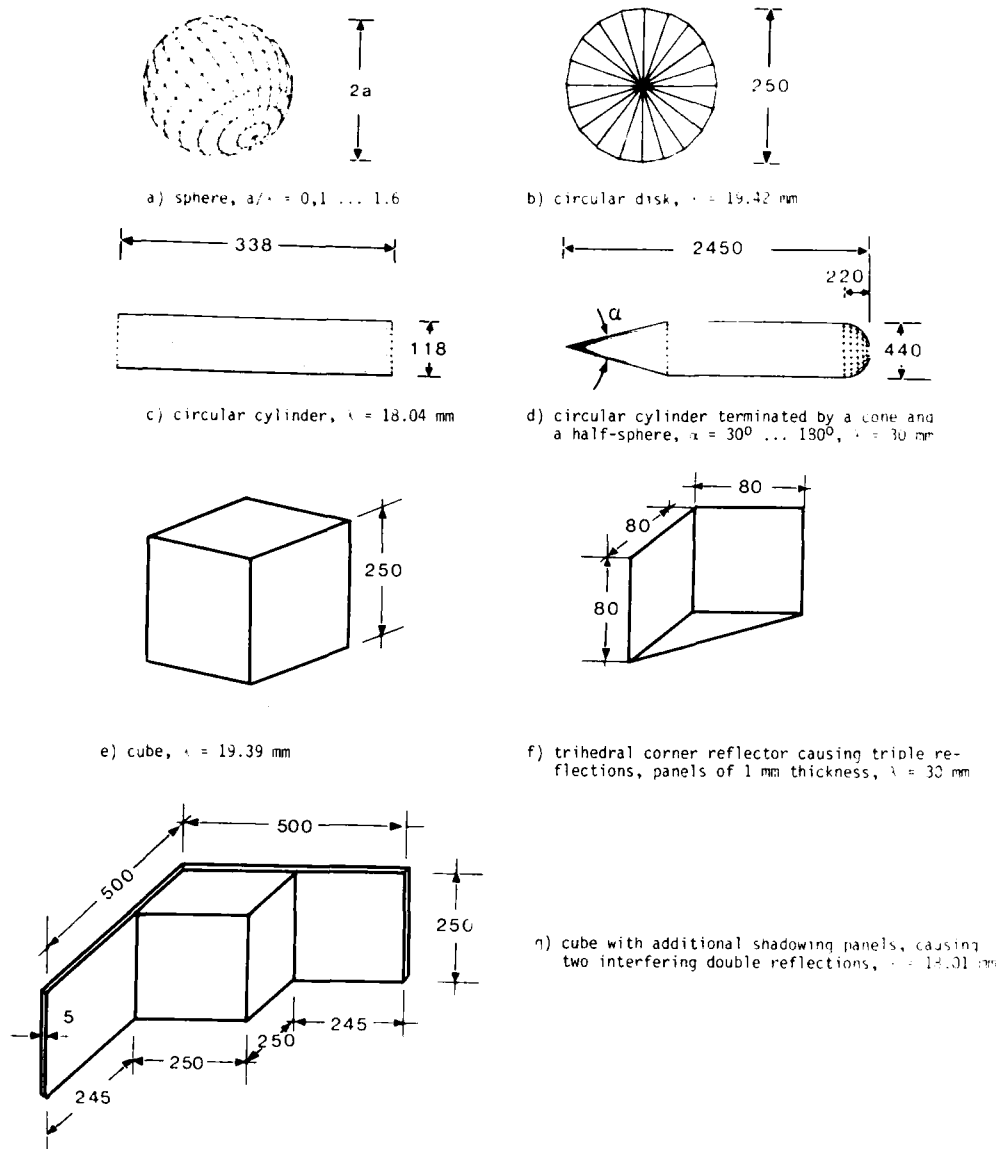


Fig. 1.2 Test objects, dimensions in mm.

scattering case is given above, the paper is restricted to some details of PO like the hidden surface problem, depolarization effects, double reflections and some other problems concerning the evaluation of the phase integral, modeling accuracy, and computer time.

2. THE HUYGENS-HELMHOLTZ PRINCIPLE FOR SCALARS AND THE ELECTROMAGNETIC VECTOR FORMULAS

The name "physical optics" is often used synonymously with the terms "Kirchhoff approximation", "tangent plane approximation" and "Huygens' principle". This is due to historical evaluation and individual preferences [12 - 16].

The diffraction theory of light, developed by Fresnel (1818) is based on the Huygens' principle (1690) of the construction of envelopes and the Young's principle (1801) of the interference [17]. The Huygens' principle states, that every point of a wave-front may be considered as a center of a secondary disturban-

ce, which gives rise to spherical wavelets, and the wave-front at any later instant may be regarded as the envelope of these wavelets [18, 19]. So Huygens' principle was first formulated long before Maxwell's equations (1873) showed the true vector nature of electromagnetic waves. According to the principle of Young the distribution of light behind a black screen is due to the direct incident wave and a wave, which propagates from the edges of the screen, the diffracted wave. The diffraction phenomena are explained by the interference of the several diffracted waves under each other, mainly however, by interference with the direct wave [20].

The Huygens-Fresnel principle extends the Huygens' principle by taking into consideration the interference of waves and states, that the wave excitation in an observer point is obtained by the superposition of all wavelets, which propagate from different points taking into account their phase [19]. An exact formulation of the Huygens' principle by an integral formula was the merit of Helmholtz (1859). This integral formula allows the computation of the field $v(\vec{r})$ at an observer point $P(\vec{r})$ from the values $v(\vec{r}')$ of the field and its normal derivatives $\partial v(\vec{r}')/\partial n'$, both given in the points $Q(\vec{r}')$ of a closed surface:

$$v(\vec{r}) = -\frac{1}{4\pi} \oint_F \left(\frac{\partial v(\vec{r}')}{\partial n'} \phi - v(\vec{r}') \frac{\partial \phi}{\partial n'} \right) d\vec{r}' \quad (2.1)$$

$\phi = \phi(\vec{r}, \vec{r}') = \exp(-jk|\vec{r}-\vec{r}'|)/|\vec{r}-\vec{r}'|$ = scalar Green's function,
 $\vec{n}' = \vec{n}(\vec{r}')$ = unit normal vector, directed in the interior of the surface, see Fig. 2.1,
 $|\vec{r}-\vec{r}'|$ = distance between observer and integration point, later $R = |\vec{r}-\vec{r}'|$ is introduced.

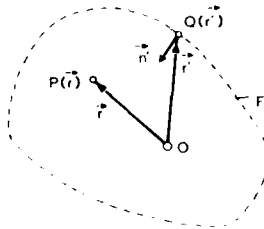


Fig. 2.1 The Huygens' principle for a source free finite space, bounded toward the exterior by the closed surface F .

The function $v(\vec{r})$ is solution of the inhomogeneous wave equation

$$\Delta v + k^2 v = 0 \quad (2.2)$$

and satisfies the radiation condition. The values $v(\vec{r}')$ and $\partial v(\vec{r}')/\partial n'$ are denoted as boundary values of the field $v(\vec{r})$.

The integral formula above is known in the literature as the Huygens-Helmholtz principle. The names Huygens-Kirchhoff principle or Kirchhoff formula, which also sometimes are found in the literature are unhistorical.

Eq. (2.1) expresses that each wave field $v(\vec{r})$ can be generated by a superposition of spherical waves $\exp(-jkR)/R$ with "density distribution" $-\partial v(\vec{r}')/\partial n'$ and dipole waves $v(\vec{r}')/\partial n' \exp(-jkR)/R$ with density distribution $v(\vec{r}')$. The waves propagate from a closed surface, which encloses the observer point [17, 20, 21].

The choice of F is arbitrarily. Of special interest is the division of F into two closed surfaces F_i and F_a , where F_a encloses F_i , see Fig. 2.2. F_i may enclose all sources E and scattering bodies. A further special case of high practical interest is given, if there are no sources within F_i , and F_i coincides with F_s , the surface of the scattering body.

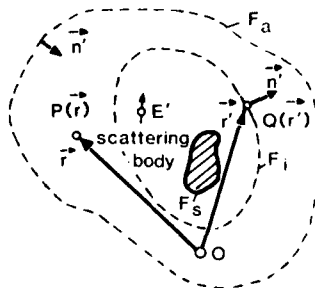


Fig. 2.2 The surface F is divided into an inner surface F_i and an outer surface F_a .

If F_a tends to infinity, see Fig. 2.3, one gets no contribution from F_a , since v satisfies the radiation condition. In this case equation (2.1) is also valid in the exterior. The unit normal vector now is directed outwards of F_i , which we denote again as F in the following.

If the boundary values $v(\vec{r}')$ and $\partial v(\vec{r}')/\partial n'$ of the field would be known on the surface F , e.g. by measurements or by estimations, the field at any observer point could be computed according Eq. (2.1). The rigorous treatment of Eq. (2.1), however, leads to the formulation of two independent integral equations and their solution for the unknown density distributions. Thereby one has to take into account that a relation be-

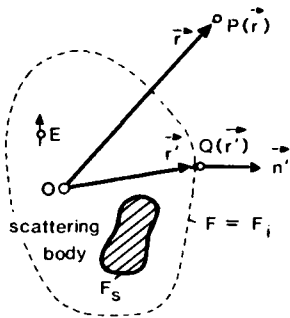


Fig. 2.3 The Huygens' principle for a source free infinite space, bounded towards the interior by the closed surface $F = F_i$.

tween the two boundary values exists. That is the solution $v(\vec{r})$ can be determined uniquely if either $v(\vec{r}')$ or $\partial v(\vec{r}')/\partial n'$ is defined on the surface F [17].

For completeness the Huygens-Kirchhoff principle should be mentioned. It can be evaluated from the Huygens-Helmholtz principle by a Fourier transformation [20]. Kirchhoff (1882) received the following expression for the function f describing the wave propagation in space and time:

$$f(\vec{r}, t) = -\frac{1}{4\pi} \int_F \left(\frac{1}{R} \frac{\partial}{\partial n'} f(\vec{r}', t - \frac{R}{c}) - \frac{\partial}{\partial n} \frac{1}{R} f(\vec{r}', t - \frac{R}{c}) \right) df' \quad (2.3)$$

$\partial/\partial n'$ = normal derivative if \vec{r}' is variable, $\partial/\partial n$ = normal derivative if \vec{r} is variable.

Therewith the motion of the wave at the observer point P can be computed for the time t , if it is known at the points Q on a surface F at times, which are retarded by the times R/c .

The Huygens-Helmholtz principle originally was formulated for scalars. There are several vector formulations for the electromagnetic field, which are derived from different starting points but also can be transferred into each other [17, 22, 23]. In the following the expressions only for the electric field are given, since the magnetic field expressions may be constructed by applying the duality principle.

Using the second Green's formula for the scalar components one receives [1]

$$\vec{E}(\vec{r}) = -\frac{1}{4\pi} \int_F \left(\frac{\partial \vec{E}(\vec{r}')}{\partial n'} \phi - \vec{E}(\vec{r}') \frac{\partial \phi}{\partial n'} \right) df' \quad (2.4)$$

In applying the vectorial Green's formula with the vector potential of a point source one can derive [21, 22, 24]:

$$\vec{E}(\vec{r}) = -\frac{1}{4\pi} \int_F \left(j\omega\mu(\vec{n}' \times \vec{H}(\vec{r}')) \phi - (\vec{n}' \times \vec{E}(\vec{r}')) \times \nabla' \phi - (\vec{n}' \cdot \vec{E}(\vec{r}')) \nabla' \phi \right) df' \quad (2.5)$$

$\omega = 2\pi f$ = angular frequency,

f = frequency,

μ_0 = permeability of the vacuum,

μ_r = complex relative permeability,

$\mu = \mu_0 \mu_r$ = absolute complex permeability of the propagation medium,

$\vec{n}' \times \vec{H}(\vec{r}') =$ } component of the { magnetic } field tangential to the surface F ,

$\vec{n}' \times \vec{E}(\vec{r}') =$ } component of the { electric } field tangential to the surface F .

$\vec{n}' \cdot \vec{H}(\vec{r}') =$ } component of the { magnetic } field normal to the surface F .

$\vec{n}' \cdot \vec{E}(\vec{r}') =$ } component of the { electric } field normal to the surface F .

Using the classical theory of vector potentials and the equivalence theorem one immediately receives [22]

$$\vec{E}(\vec{r}) = -\frac{1}{4\pi} \nabla \times \int_F (\vec{n}' \times \vec{E}(\vec{r}')) \phi df' + \frac{1}{j\omega\epsilon} \nabla \times \int_F (\vec{n}' \times \vec{H}(\vec{r}')) \phi df' \quad (2.6)$$

$\epsilon = \epsilon_0 \epsilon_r$ = absolute complex dielectric constant,

ϵ_0 = permittivity of the vacuum,

$\epsilon_r = \epsilon_r' + j\epsilon_r''$ = complex relative permittivity (dielectric constant).

Starting with the reciprocity theorem or with the vectorial Green's formula, now with the vector potential of a point source, one arrives with the expression [2, 22, 25]:

$$\vec{E}(\vec{r}) = -\frac{1}{4\pi} \int_F \left(j\omega\mu(\vec{n}' \times \vec{H}(\vec{r}')) \phi - (\vec{n}' \times \vec{E}(\vec{r}')) \times \nabla' \phi - \frac{1}{j\omega\epsilon} ((\vec{n}' \times \vec{H}(\vec{r}')) \cdot \nabla') \nabla' \phi \right) df' \quad (2.7)$$

Equations (2.6) and (2.7) have the advantage, that only field components tangential to the surface F are under the integrand.

It should be mentioned, that the derivation of the field equations with the aid of the vectorial Green's theorem or the reciprocity theorem represents the field \vec{E} as a sum of a volume integral and the above given surface integrals. The volume integral is extended over the known primary sources and thus represents the incident field \vec{E}_e . The surface integral is extended over the tangential components of the total field and represents the scattered field \vec{E}_s , so that the equation holds

$$\vec{E}(\vec{r}) = \vec{E}_e(\vec{r}) + \vec{E}_s(\vec{r}). \quad (2.8)$$

The extension of the surface integral over the components of the total field can lead to some confusion, since there is no difference in the function inside and outside of the integral of the Huygens' principle. This confusion can be explained by the proof, that it is possible to express the scattered field \vec{E}_s in terms of \vec{E}_e as well as in terms of $\vec{E}_e + \vec{E}_s$, that is in terms of the total field [15, 26]. This means that the expressions given above are suited to compute the scattered field by inserting for \vec{E} , \vec{H} under the integral either \vec{E}_s , \vec{H}_s or $\vec{E}_e + \vec{E}_s$, $\vec{H}_e + \vec{H}_s$. From Sec. 4 on the scattered field will be denoted by \vec{E}_s , \vec{H}_s .

3. THE KIRCHHOFF INTEGRAL FOR SCALARS AND THE PROPERTIES OF THE VECTOR FORMULATIONS

In general it is very difficult to construct a solution of the Huygens-Helmholtz formula Eq. (2.1). That is, why Kirchhoff (1882, 1891) tried to find an approximate solution. He had the opinion, that one receives good results, if one uses instead of the unknown exact boundary values $v(\vec{r}')$, $\partial v(\vec{r}')/\partial n'$ approximate boundary values $v_a(\vec{r}')$, $\partial v_a(\vec{r}')/\partial n'$, which follow from geometrical optics laws. This idea forms the basis of the physical optics method.

If one inserts the approximate values $v_a(\vec{r}')$ and $\partial v_a(\vec{r}')/\partial n'$ in the Huygens-Helmholtz formula, one receives the so-called Kirchhoff integral

$$v(\vec{r}) = -\frac{1}{4\pi} \int_F \left(\frac{\partial v_a(\vec{r}')}{\partial n'} \psi - v_a(\vec{r}') \frac{\partial \psi}{\partial n'} \right) df'. \quad (3.1)$$

With this step one has to deal no longer with a boundary value problem but with a discontinuity problem. In this case the surface F may be an arbitrary non closed surface. As before, $v(\vec{r})$ satisfies the scalar homogeneous wave equation. How behave the vector formulations in the case, that the surface is not closed?

Equations (2.4) and (2.5) no longer satisfy Maxwell's equations and would become therewith not applicable for a lot of practical problems like reflector antennas. The satisfaction of Maxwell's equations can be achieved in adding correction terms in form of line integrals to the surface integrals [1, 24]. The line integrals were extended over the rim of the open surface. One gets instead of Eq. (2.4):

$$\vec{E}(\vec{r}) = -\frac{1}{4\pi} \int_F \left(\frac{\partial \vec{E}_a(\vec{r}')}{\partial n'} \psi - \vec{E}_a(\vec{r}') \frac{\partial \psi}{\partial n'} \right) df' - \frac{1}{4\pi} \oint_C (\vec{E}_a(\vec{r}') \times \vec{t}') \psi ds' - \frac{1}{4\pi j\omega\epsilon} \oint_C (\vec{H}_a(\vec{r}') \cdot \vec{t}') \psi ds', \quad (3.2)$$

and instead of Eq. (2.5):

$$\vec{E}(\vec{r}) = -\frac{1}{4\pi} \int_F (j\omega\mu(\vec{n}' \times \vec{H}_a(\vec{r}')) \psi - (\vec{n}' \times \vec{E}_a(\vec{r}')) \nabla' \psi - (\vec{n}' \cdot \vec{E}_a(\vec{r}')) \nabla' \psi) df' - \frac{1}{4\pi j\omega\epsilon} \oint_C (\vec{H}_a(\vec{r}') \cdot \vec{t}') \psi ds'. \quad (3.3)$$

$\vec{t}' = \vec{t}(\vec{r}')$ - unit tangent vector, C = curve of the rim of the open surface. The geometrical situation is depicted in Fig. 3.1.

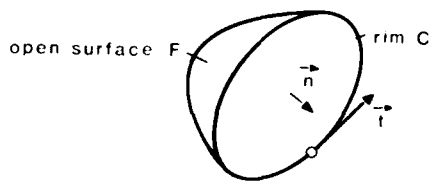


Fig. 3.1 Geometry of a nonclosed surface.

Eqs. (2.6) and (2.7) have the remarkable property that even in the case of an open surface they will satisfy Maxwell's equations, so in general one would prefer to work with these. One receives:

$$\vec{E}(\vec{r}) = -\frac{1}{4\pi} \nabla \times \int_F (\vec{n}' \times \vec{E}_a(\vec{r}')) \psi df' + \frac{1}{j\omega\epsilon} \nabla \times (\nabla \times \int_F (\vec{n}' \times \vec{H}_a(\vec{r}')) \psi df'), \quad (3.4)$$

or alternatively

$$\vec{E}(\vec{r}) = -\frac{1}{4\pi} \int_F (j\omega\mu(\vec{n}' \times \vec{H}_a(\vec{r}')) \psi - (\vec{n}' \times \vec{E}_a(\vec{r}')) \times \nabla' \psi - \frac{1}{j\omega\epsilon} ((\vec{n}' \times \vec{H}_a(\vec{r}')) \cdot \nabla') \nabla' \psi) df'. \quad (3.5)$$

In the following the second equation is preferred, since there the differentiations can be evaluated under the integral. One receives:

$$\vec{E}(\vec{r}) = \frac{1}{4\pi j\omega\epsilon} \int_F \left(\frac{-1-jkR+k^2R^2}{R^2} (\vec{n}' \times \vec{H}_a(\vec{r}')) + j\omega\epsilon \frac{1+jkR}{R} ((\vec{n}' \times \vec{E}_a(\vec{r}')) \times \vec{e}_R) + \right. \\ \left. + \frac{3+3jkR-k^2R^2}{R^2} ((\vec{n}' \times \vec{H}_a(\vec{r}')) \cdot \vec{e}_R) \vec{e}_R \right) \frac{e^{-jkR}}{R} df' \quad (3.6)$$

$\vec{e}_R = (\vec{r}-\vec{r}')/|\vec{r}-\vec{r}'| = \vec{R}/R =$ unit vector, which points from the integration point toward the observer point, see Fig. 3.2.

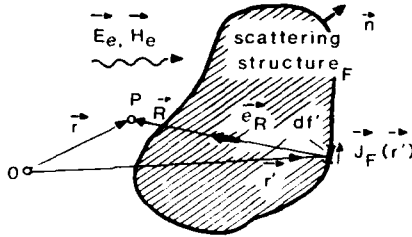


Fig. 3.2 Geometry for equation (3.6).

For the computation of the bistatic or monostatic scatter cross-section, only the far field approximation of Eq. (3.6) is of interest:

$$\vec{E}(\vec{r}) = \frac{j\omega\epsilon}{4\pi} \frac{e^{-jkr}}{r} \vec{e}_r \times \int_F \left(\vec{e}_r \times (\vec{n}' \times \vec{H}_a(\vec{r}')) - \frac{\vec{e}_r}{\epsilon} (\vec{n}' \times \vec{E}_a(\vec{r}')) \right) e^{jk\vec{e}_r \cdot \vec{r}'} df' \quad (3.7)$$

$r =$ distance between the coordinate origin, which is situated within or in the neighbourhood of the surface F , see Fig. 3.3.

$\vec{e}_r =$ unit vector, which points from the coordinate origin toward the observer point.

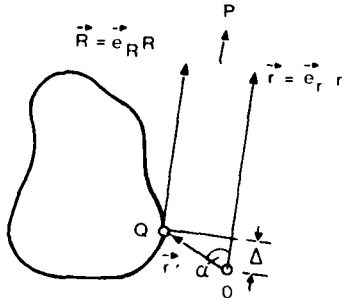


Fig. 3.3 Geometry for the far field formula Eq. (3.7).

The magnetic field in this case is given explicitly:

$$\vec{H}(\vec{r}) = -\frac{j\omega\epsilon}{4\pi} \frac{e^{-jkr}}{r} \vec{e}_r \times \int_F \left(\vec{e}_r \times (\vec{n}' \times \vec{E}_a(\vec{r}')) + \sqrt{\frac{\mu}{\epsilon}} (\vec{n}' \times \vec{H}_a(\vec{r}')) \right) e^{jk\vec{e}_r \cdot \vec{r}'} df' \quad (3.8)$$

4. THE KIRCHHOFF ANSATZ AND THE ANSATZ OF PHYSICAL OPTICS

The ansatz, which Kirchhoff made for the functions $v_a(\vec{r}')$ and $\partial v_a(\vec{r}')/\partial n$ is explained in hand of Fig. 4.1 [17]. We consider a scattering (Fig. 4.1a) and a diffracting (Fig. 4.1b) body in the field of a point source of light E . Both types of bodies are to be dark. This means that the incident light is absorbed and no light is reflected. The shadow boundary S_g in the GO sense touches the bodies in a shadow line C . This line can be regarded as a rim of an arbitrary surface L , which should close behind the source. The surface L forms together with the shadow part S'' of the body a closed surface $S'+L$, dividing the space into a source free space T^+ and in a space T^- , which contains the source. According GO the following situation exists in T^+ : within the frustum T_g bounded by L and S_g the field distribution v_e of the source is undisturbed, outside of T_g the field disappears. This GO field distribution can be represented according the Huygens' principle by an integral over the boundary lines of the frustum:

$$v_g(\vec{r}) = \begin{cases} v_e(\vec{r}) \\ 0 \end{cases} = -\frac{1}{4\pi} \int_{S_g+L} \left(\frac{\partial v_e(\vec{r}')}{\partial n'} \phi - v_e(\vec{r}') \frac{\partial \phi}{\partial n'} \right) df' \quad \text{for } \begin{cases} \vec{r} \in T_g \\ \vec{r} \notin T_g \end{cases} \quad (4.1)$$

By transversing the shadow boundary S_g from the positive towards the negative area, field discontinui-

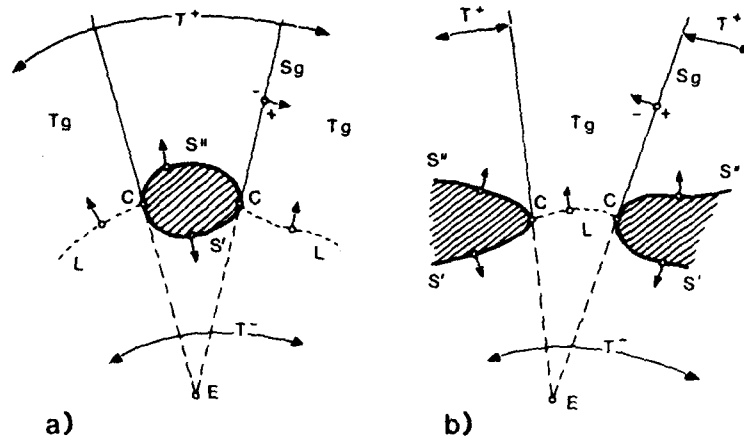


Fig. 4.1 Illustration of Kirchhoff's procedure
a) scattering at a structure, b) diffraction at a screen.

ties arise with magnitude

$$(v_g)_+ - (v_g)_- = v_e, \quad \left(\frac{\partial v}{\partial n}\right)_+ - \left(\frac{\partial v}{\partial n}\right)_- = \frac{\partial v_e}{\partial n}. \quad (4.2)$$

These discontinuities, however, which can be due to fictive surface source distributions, are in contradiction to the homogeneous wave equation. We construct now in T^+ a solution, which satisfies the wave equation. For this purpose we add on the right hand side a term, which shows exactly the same discontinuities, however, with the opposite sign. This term is given by

$$+ \frac{1}{4\pi} \int_{S_g} \left(\frac{\partial v_e(\vec{r}')}{\partial n'} \phi - v_e(\vec{r}') \frac{\partial \phi}{\partial n'} \right) df'.$$

Therewith one receives the following solution, valid for the total space T^+ :

$$\begin{aligned} v(\vec{r}) &= v_g(\vec{r}) + \frac{1}{4\pi} \int_{S_g} \left(\frac{\partial v_e(\vec{r}')}{\partial n'} \phi - v_e(\vec{r}') \frac{\partial \phi}{\partial n'} \right) df' = \\ &= - \frac{1}{4\pi} \int_L \left(\frac{\partial v_e(\vec{r}')}{\partial n'} \phi - v_e(\vec{r}') \frac{\partial \phi}{\partial n'} \right) df', \quad \vec{r} \in T^+. \end{aligned} \quad (4.3)$$

This is the Kirchhoff solution, which expresses, that the wave field in space is generated by the superposition of wavelets, which propagate from the points of the aperture L . Kirchhoff originally has derived this formula by choosing the surface $S''+L$ for the application of the Huygens' principle and inserting in Eq. (3.1) the more or less plausible boundary values

$$v_a = v_e, \quad \frac{\partial v_a}{\partial n} = \frac{\partial v_e}{\partial n} \quad \text{on } L; \quad v_a = 0, \quad \frac{\partial v_a}{\partial n} = 0 \quad \text{on } S''. \quad (4.4)$$

These are the values of the GO field at the surfaces L and S'' .

Specially in the scattering case we are interested in a solution, which is valid in the total space. This can be reached by deforming the surface L in Fig. 4.1 in such a way that it borders the illuminated surface S' of the scattering object. Then, however, the source singularity in E is to be taken into account. The contribution of this singularity results in the undisturbed field v_e . Therewith we now can write the previous equation in the form

$$v(\vec{r}) = v_e(\vec{r}) - \frac{1}{4\pi} \int_{S'} \left(\frac{\partial v_e(\vec{r}')}{\partial n'} \phi - v_e(\vec{r}') \frac{\partial \phi}{\partial n'} \right) df', \quad \vec{r} \in T^+. \quad (4.5)$$

Since with this special choice of the surface L the total space is described by T^+ , the solution Eq. (4.5) is valid everywhere with exception of the scattering body and the source. For this formula Kirchhoff has assumed that on the illuminated side of the body or the screen the values v_a and $\partial v_a / \partial n$ are given by the incident field v_e , where on the shadowed side these values disappear:

$$v_a = v_e, \quad \frac{\partial v_a}{\partial n} = \frac{\partial v_e}{\partial n} \quad \text{on } S'; \quad v_a = 0, \quad \frac{\partial v_a}{\partial n} = 0 \quad \text{on } S''. \quad (4.6)$$

These assumptions become obvious, if one assumes that the screen is completely absorbing the light. Since then on the illuminated side no reflection occurs, the light movement is given by the incident light approximately. Further a black screen is opaque for the light and, therefore, in first approximation there is no wave movement in the shadowed parts [20].

The subdivision of a body into its illuminated and shadowed parts is a purely geometrical problem, which in the case of a complex body needs a considerable computer effort, see Sec. 5.

In the electromagnetics we are used to construct the total field \vec{E} as the sum of the incident field \vec{E}_e and the scattered field \vec{E}_s . In this way we can write

$$\vec{v}(\vec{r}) = \vec{v}_e(\vec{r}) + \vec{v}_s(\vec{r}) \quad (4.7)$$

with the scattered field

$$\vec{v}_s(\vec{r}) = -\frac{1}{4\pi} \int_S \left(\frac{\partial v_e(\vec{r}')}{\partial n'} \phi - v_e(\vec{r}') \frac{\partial \phi}{\partial n'} \right) d\vec{r}' \quad (4.8)$$

The Kirchhoff idea for the ansatz of approximate boundary conditions for a black scattering or diffracting structure following GO principles may be used accordingly in electromagnetics for the estimation of the tangential components $\vec{n} \times \vec{H}_a$ and $\vec{n} \times \vec{E}_a$.

In the case of an ideally conducting structure we know some boundary conditions exactly, while other boundary conditions may be constructed in the Kirchhoff sense. The following Table 4.1 gives a survey over the known and unknown boundary conditions in the scattering and diffracting case.

		boundary conditions		
		exact	approximate	
scattering body	on the scatterer	$\vec{n} \times \vec{E} = 0$	$\vec{n} \times \vec{H}_a = 0$	shadow region
			$\vec{n} \times \vec{H}_a = 2\vec{n} \times \vec{H}_e$	illuminated region
	outside the scatterer	$\vec{n} \times \vec{H} = \vec{n} \times \vec{H}_e$	$\vec{n} \times \vec{E}_a = \vec{n} \times \vec{E}_e$	
diffracting body	in the aperture	$\vec{n} \times \vec{H} = \vec{n} \times \vec{H}_e$	$\vec{n} \times \vec{E}_a = \vec{n} \times \vec{E}_e$	
	on the screen	$\vec{n} \times \vec{E} = 0$	$\vec{n} \times \vec{H}_a = 0$	shadow region
			$\vec{n} \times \vec{H}_a = 2\vec{n} \times \vec{H}_e$	illuminated region

Table 4.1 Exact and approximate boundary conditions of the total fields in the scattering and diffracting case if the bodies are ideally conducting.

The approximate boundary condition

$$\vec{n} \times \vec{H}_a = \vec{n} \times \vec{H}_e + \vec{n} \times \vec{H}_r = 2\vec{n} \times \vec{H}_e$$

would be exact, if the scatterer could be represented by an infinitely extended ideally conducting plane, where $\vec{H}_r = \vec{H}_e$ holds. In practice this means that a scatterer should be modeled by local tangent planes. \vec{E}_r, \vec{H}_r denote the reflected field in the GO sense.

Of special interest within this lecture is the scattering case with the boundary conditions given on a scatterer. From Table 4.1 we receive

$$\vec{n} \times \vec{E}_a = \vec{n} \times \vec{E} = 0 \quad \text{for the total scatterer,} \quad (4.9a)$$

$$\vec{n} \times \vec{H}_a = 0 \quad \text{in the shadow region of the scatterer,} \quad (4.9b)$$

and

$$\vec{n} \times \vec{H}_a = \vec{n} \times \vec{H}_e + \vec{n} \times \vec{H}_r = 2\vec{n} \times \vec{H}_e \quad \text{in the illuminated region} \quad (4.9c)$$

of the scatterer. Using Eqs. (3.7) and (3.8) we receive for the case of an ideally conducting scatterer the PO solution of the scattered field:

$$\vec{E}_s(\vec{r}) = \frac{j\omega\mu}{2\pi} \frac{e^{-jk r}}{r} \vec{e}_r \times \int_F (\vec{n}' \times \vec{H}_e(\vec{r}')) e^{jk \vec{e}_r \cdot \vec{r}'} d\vec{r}' \quad (4.10)$$

$$\vec{H}_s(\vec{r}) = -\frac{j\omega \sqrt{\mu\epsilon}}{2\pi} \frac{e^{-jk r}}{r} \vec{e}_r \times \int_F (\vec{n}' \times \vec{H}_e(\vec{r}')) e^{jk \vec{e}_r \cdot \vec{r}'} d\vec{r}' \quad (4.11)$$

If the scatterer is nonideally conducting, we cannot define any exact boundary condition. The approximate boundary conditions may be formulated as follows:

$$\vec{n} \times \vec{E}_a = 0 ; \quad \vec{n} \times \vec{H}_a = 0 \quad \text{in the shadow region,} \quad (4.12a)$$

$$\vec{n} \times \vec{E}_a = \vec{n} \times \vec{E}_e + \vec{n} \times \vec{E}_r; \quad \vec{n} \times \vec{H}_a = \vec{n} \times \vec{H}_e + \vec{n} \times \vec{H}_r \quad \text{in the illuminated region of the scatterer.} \quad (4.12b)$$

Again, these boundary conditions would be exact if the scatterer could be represented by an infinite extended nonideally conducting plane. Using the Fresnel reflection coefficients R_E and R_H for a plane multi-layered medium, Fig. 4.2, the boundary conditions (4.12b) above can be formulated in the following way:

$$\vec{n} \times \vec{E}_a = \vec{n} \times (E_{e\perp} \vec{e}_\perp + E_{e\parallel} \vec{e}_\parallel + R_E E_{e\perp} \vec{e}_\perp + R_H E_{e\parallel} \vec{s}_\parallel) \quad (4.13a)$$

$$\vec{n} \times \vec{H}_a = \vec{n} \times (-E_{e\parallel} \vec{e}_\perp + E_{e\perp} \vec{e}_\parallel - R_H E_{e\parallel} \vec{e}_\perp + R_E E_{e\perp} \vec{s}_\parallel) / Z_0 \quad (4.13b)$$

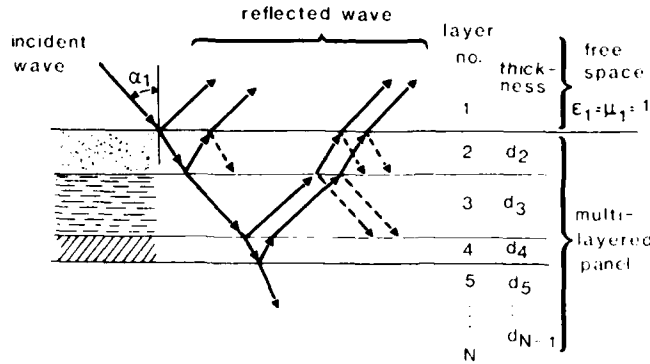


Fig. 4.2 Geometry of a multi-layered panel.

R_H = reflection coefficient for the case, that the incident magnetic field vector is vertical to the plane of incidence (H-polarization),
 R_E = reflection coefficient, if the incident electric field vector is vertical to the plane of incidence (E-polarization).
 The reflection coefficients have to be determined at the interface between free space and multi-layered panel.
 \vec{e}_\perp = unit vector vertical to the plane of incidence,
 \vec{e}_\parallel = unit vector vertical to \vec{e}_\perp and vertical to the incident ray $-\vec{e}_2$ and therewith parallel to the plane of incidence, so that $\vec{e}_\parallel = \vec{e}_\perp \times \vec{e}_2$ holds,
 \vec{s}_\parallel = unit vector vertical to \vec{e}_\perp and vertical to the reflected ray with direction \vec{s} and therewith parallel to the plane of incidence, so that $\vec{s}_\parallel = \vec{s} \times \vec{e}_\perp$ holds.

$E_{e\perp}$ resp. $E_{e\parallel}$ = component of the electric field in the direction of \vec{e}_\perp resp. in the direction of \vec{e}_\parallel . For details see [10, 26-30]. The geometrical situation is depicted in Fig. 4.3.

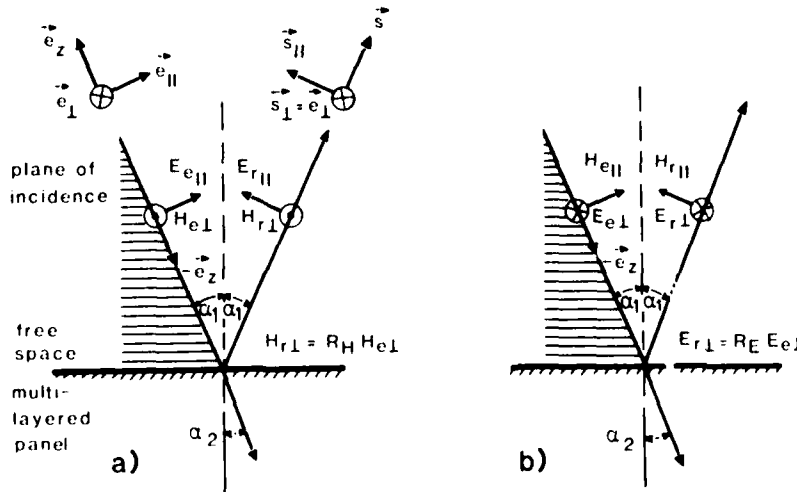


Fig. 4.3 Definition of polarizations
 a) H-polarization, b) E-polarization.

5. SOME DETAILS OF PHYSICAL OPTICS

5.1 GEOMETRICAL MODEL AND HIDDEN SURFACES

The GO concept of using Fresnel reflection coefficients, which rigorously are valid for infinitely extended plane layers, proposes to model the structure by panels (flat plates); the structure should be large compared to the wave length. For this kind of modeling the so-called hidden surface problem, that is the discrimination between the illuminated and shadowed surface regions, has to be solved by a computer program. At this time there are two computer programs in use. The first computer program [31] has been applied for the solution of all hidden surface and double reflection problems, cited in this and previous reports [9, 10]. The computer time increases almost linearly with the number of panels. The second computer program [32] is a basis version, which is foreseen to be extended to treat multiple reflections. A rough description of the procedure, which is illustrated by Fig. 5.1, is given in [10].

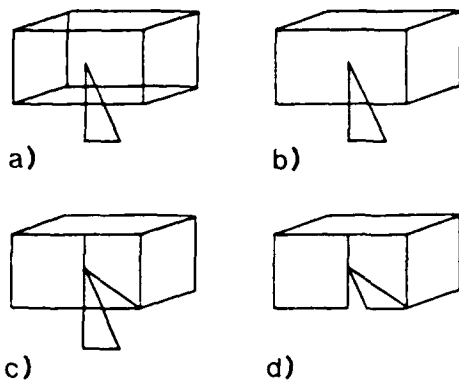


Fig. 5.1 Illustration of the hidden surface procedure at hand of a rectangular box modeled by triangles or quadrangles. A triangle is positioned in front of it

- original situation
- elimination of all surfaces with normal vectors including more than 90° with the observer direction
- splitting of the box panel, which is partially hidden by the triangle, the invisible part of the box can now be removed
- remaining elements of the box only.

One also could think to use curved panels in order to model the structure. This may have some advantages in modeling certain structure like a wing of an airplane or a bow of a ship. The solution of the hidden surface problem, however, will increase in complexity. The PO solution for a curved panel, described by the two principal radii of curvature is evaluated in [33, 34].

A further modeling technique is described in [35]. The body is considered to be an ensemble of components, each of which can be geometrically approximated by a simple shape. For these simple shapes, the so-called basis structures (sphere, flat plate, cylinder, cone, etc.), the radar cross-section is known by exact solutions, approximation method or measurements. By proper combining the component cross-sections one can estimate the cross-section of the entire body. Hidden surface and multiple reflection problems must also be solved within this procedure. The correct treatment of the phase of the component scattered field is a very difficult task. That is why one often uses a random-phase method, which yields the average radar cross-section and the amount of probable deviation from this average.

5.2 PREDICTION OF POLARIZATION EFFECTS

PO predicts zero cross-polarization in the monostatic case, when the scattering structure is ideally conducting and no doubly or multiply reflecting panels occur. This is not in agreement with the actual situation. Also in all other cases the predicted cross-polarization effects are erroneous. Therefore, tests are in progress to decide, if the PO results in this case satisfy practical accuracy requirements.

Fig. 5.2 shows as an example for the bistatic case the computed and the measured radiation pattern of an offset reflector antenna [3] with a corrugated horn as primary feed. The reflector was assumed to be ideally conducting. No double reflections occur. Experimental and theoretical results are in fair agreement.

The components of the backscattered field (monostatic case) of a multi-layered panel [10, 26, 30], may be represented by

$$\begin{bmatrix} E_{sx} \\ E_{sy} \end{bmatrix} = [T] \begin{bmatrix} E_{ex} \\ E_{ey} \end{bmatrix}, \quad (5.1)$$

where the scattering matrix [T], computed by PO, is given by

$$[T] = -\frac{jk}{2\pi r(1-n_z^2)} \int_P e^{2jkz'} dx' dy' \begin{bmatrix} R_H n_x^2 - R_E n_y^2 & (R_H + R_E) n_x n_y \\ (R_H + R_E) n_x n_y & R_H n_y^2 - R_E n_x^2 \end{bmatrix} \begin{bmatrix} E_{ex} \\ E_{ey} \end{bmatrix} \quad (5.2)$$

n_x, n_y, n_z = cartesian components of the unit normal vector of the panel,
 F_p = area of the panel.

The geometrical situation is illustrated in Fig. 5.3.

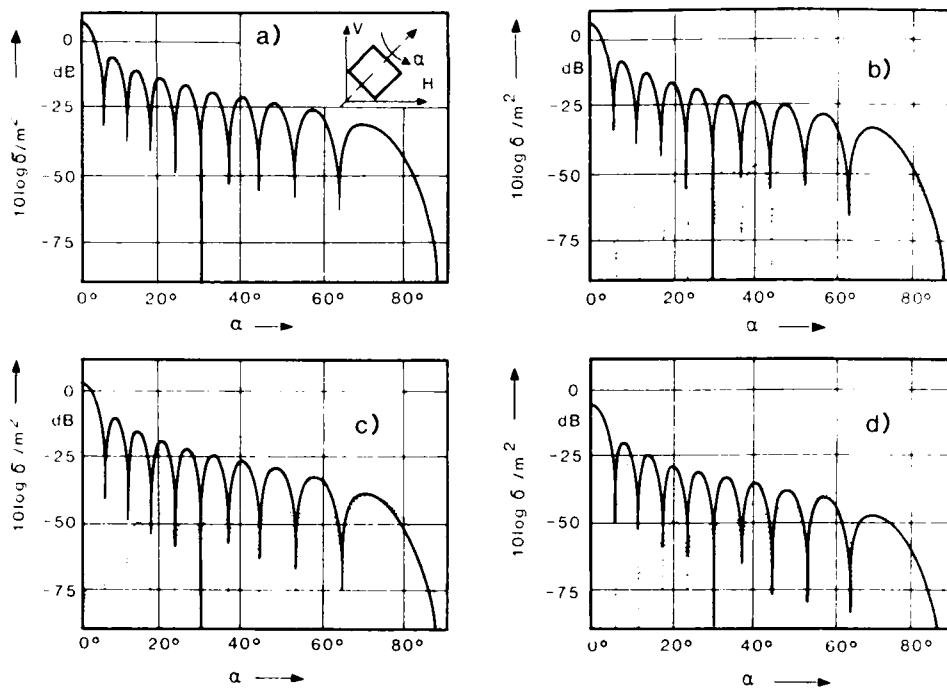


Fig. 5.4 Backscatter cross section of nonideally conducting panels, size of the panels: $150 \times 150 \text{ cm}^2$, frequency: $f = 10 \text{ GHz}$, solid line: copolar RCS, dotted line: crosspolar RCS, $\sigma_p = \sigma_{\parallel} + j\sigma_{\perp}$,
 a) iron: $\epsilon_r = 1.8 \cdot 10^7$, $\mu_r = 1$,
 b) sea-water: $\epsilon_r = 62$, $\mu_r = 1$,
 c) plastic: $\epsilon_r = 9$, $\mu_r = 10^{-5}$,
 d) teflon: $\epsilon_r = 2$, $\mu_r = 0$.

5.3 EVALUATION OF THE PHASE INTEGRAL

The phase integral in Eq. (5.2) can be evaluated numerically in any case. If triangular or quadrangular panels are chosen, the phase integral can be evaluated analytically [10, 37]. If the object to be modeled has such a shape, that large panels can be used, the analytic solution has some advantage in accuracy and computer effort.

In the literature one finds very often an approximate evaluation of the phase integral by the stationary phase principle [12, 19]. It is a well-known phenomenon that waves, which are short compared with objects dimensions, are scattered almost entirely from those surface points, which are specularly oriented. When applying the stationary phase principle on the phase integral one can show, that most of the scattering does indeed come from these specular points and the small neighbourhood surrounding them. The evaluation of the phase integral by the stationary phase principle has the advantage that analytical expressions for the scattered field are available. On the other side very incorrect results can arise for directions far away from the main lobe of scattered energy. Since the stationary phase principle is not inherent to the Kirchnoff method one should emphasize a precise evaluation of the phase integral by numerical or in special cases by analytical techniques.

5.4 DOUBLE REFLECTIONS

In order to treat double reflections the GO concept for the construction of the surface fields is applied in a logical extension [9, 10]. Fig. 5.5 shows the geometry of two back scattering panels, which are oriented in such a way, that double reflections can occur. In order to describe double reflections in the GO sense, the angle ψ is set to zero. ψ takes into account that the PO field of panel B propagates not only in the GO direction. The proper value of the angle ψ depends on the desired accuracy and is subject of current investigations. Values of $0^\circ \leq \psi \leq 50^\circ$ seem to be realistic.

The back scattering of each panel is described by Eqs. (5.1) and (5.2). Additionally each panel generates a reflected field at the surface of the other panel, which is scattered toward the receiver. This

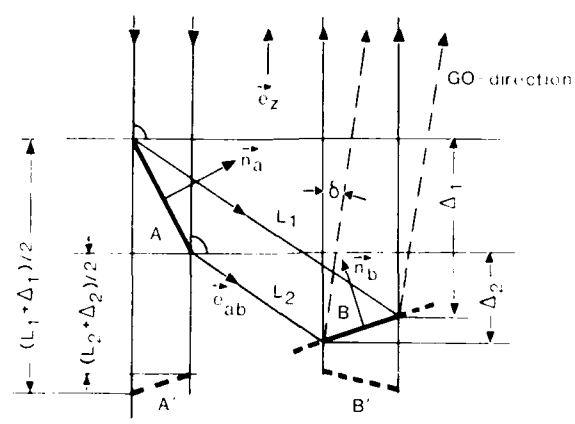


Fig. 5.5 Geometry for double reflections.

reflected field, which is constructed according GO principles, represents the incident field in the PO sense.

In the case of ideally conducting doubly reflecting panels the polarization vector \vec{p}_s of the backscattered field is given by the following formula:

$$\vec{p}_s = (\hat{n}_b \times ((\hat{n}_a \times \vec{p}_e) \times \vec{e}_{ab})) \times \vec{e}_z \quad (5.3)$$

- \vec{p}_e = polarization vector of the incident field \vec{E}_e ,
- \vec{e}_{ab} = unit vector in the direction of the GO reflection of panel A,
- \hat{n}_a = unit normal vector of panel A,
- \hat{n}_b = unit normal vector of panel B,

$$\vec{e}_{ab} = \lambda(\vec{e}_z \cdot \hat{n}_a) \hat{n}_a - \vec{e}_z \quad (5.4)$$

This means that in the case of ideally conducting surfaces, the PO concept is able to predict cross polarizations also in the back scatter case, if double reflections occur. The same is valid, if multiple reflections arise. On the basis of this concept a computer program was developed [8 - 10]. The geometrical problems arising with double reflections are treated in [38].

Fig. 5.7 shows the computed and measured depolarization effects for an ideally conducting cube with additional snadowing surfaces, which give rise to double reflections. The dimensions of the object are given in Fig. 1.2g. The position of the object for the rotation angles 0° , 15° , 30° and 45° is illustrated in Fig. 5.6. The results show the actual state of the work in the field of double reflections. The differences between experimental and theoretical results are subject of current discussions.

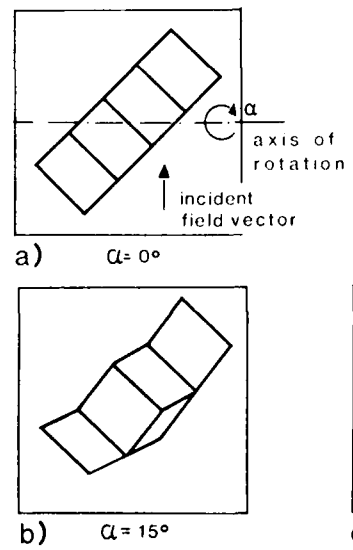


Fig. 5.6 Position of the depolarizing structure for the rotation angles 0° , 15° , 30° , 45° .

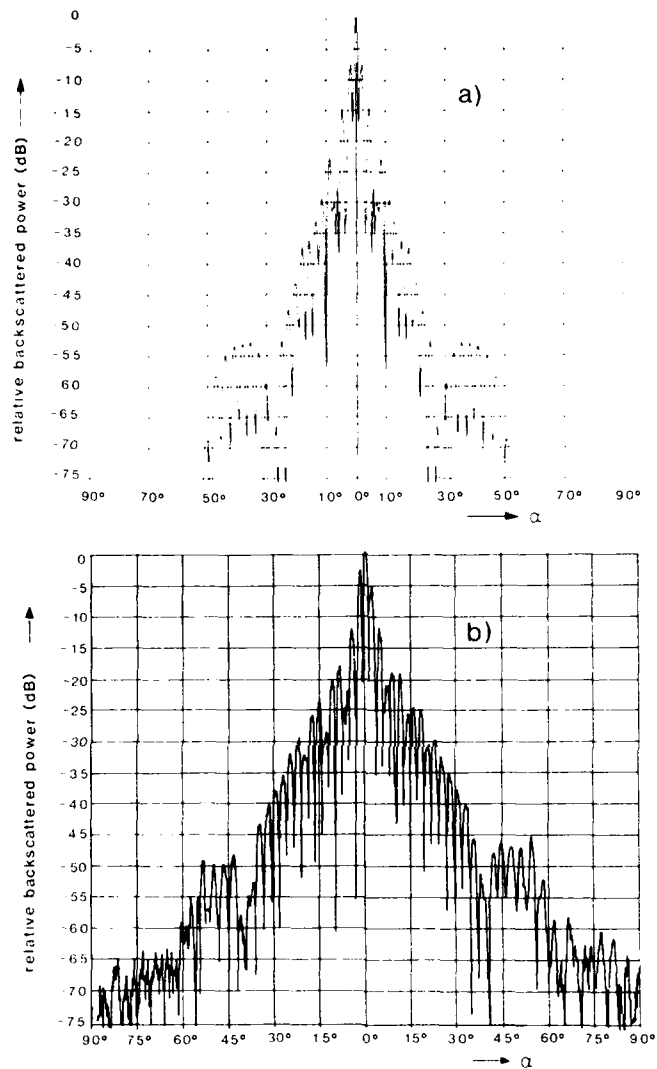


Fig. 5.7 Depolarization effects of the ideally conducting doubly reflecting structure, see Fig. 1.2g and Fig. 5.6;
 a) theoretical results,
 b) experimental results.

5.5 MODELING ACCURACY

In modeling a structure by panels the question arises according to which criterium the size of the panels has to be determined. On the one side one would like to choose the panel size as large as possible in order to save computer time. On the other side the difference between the true surface and the model surface is not allowed to exceed a certain value. A series of tests has shown that the deviation between the true surface and the modeled surface should not exceed a value of about $\lambda/16$. This is illustrated in Fig. 5.8.

This criterium is well known from antenna measuring technique. If the admissible phase error over the aperture with diameter D of the antenna under test is assumed to be 22.5° ($\lambda/16$), then the far field distance R must be chosen in such a way that $R > 2D^2/\lambda$. The true far field pattern for the distance $R \rightarrow \infty$ then will differ only in a negligible amount from the measured one.

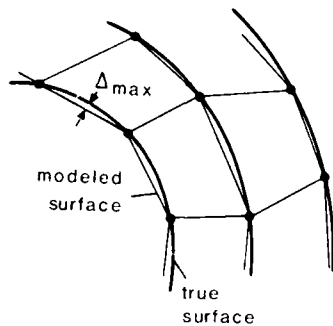


Fig. 5.8 Admissible deviation between the true and the modeled surface.

5.6 COMPUTER TIME

The major portion of the computer time is needed to carry out purely geometrical computations like the elimination of the shadowed subsurfaces and the search procedure for doubly reflecting panels. The actual version of the computer program takes about 0.01 s per field contribution of one panel and per one aspect angle on a computer of the type IBM 3081. The cylinder with a hemisphere at one end and a cone at the other end (see Fig. 1.2d) is modeled by 140 panels. This means that the computation of the scattered field for 180 aspect angles takes a time of about 250 s.

6. CONCLUSION

The PO method has proved its qualification in the prediction of the radiation pattern of symmetric and off-set reflector antennas with single-, dual- and four-reflector systems. A series of test objects with increasing complexity has been used to validate PO also in the monostatic radar case. For the accuracy checks numerous comparisons with measurements and/or the results of independent theories were made. The test objects were assumed to be ideally conducting. The computations were carried out for the far field.

Though the used test objects can be identified as substructures of more complicated objects, a validation of PO for application oriented objects should be provided for. Exact backscatter measurements, however, of an object like an airplane require a high effort, and a comparison with the theory is a comprehensive task. Further PO should be validated for the case of nonideally conducting multi-layered structures. This affords a precise knowledge of the constituent parameters of the materials. In the field of double reflections more measurements are needed to discuss the preliminary PO results presented.

Since the quasi-near field of a scattering structure is of practical interest one should study the qualification of PO in predicting the scattering process in this event. Further it seems of high practical interest to extend the PO method to treat multiple reflections for ideally and non ideally conducting complex structures and to solve the ray tracing problem for this general case. A further point of investigation could be the correction of the PO field by an additional field term, which takes into account edge diffraction effects. This correction term has to be evaluated for an edge of finite length.

7. REFERENCES

- [1] R. Kunn, "Mikrowellenantennen", Berlin: VEB Verlag Technik, 1964, S. 117-118, 235, 252-254, 261-265.
- [2] W.V.T. Rusch and P.D. Potter, "Analysis of Reflector Antennas", New York, London: Academic Press, 1970, pp. 33-51, 169-172.
- [3] D. Klement, V. Stein and H.-J. Steiner, "Offset-Reflector Antennas, Design, Computation, Construction and Pattern Measurement", ESA-TT-770, European Space Agency, 1982, Translation of DFVLR-Mitt. 81-33.
- [4] S.A. Skyttenyr, "Cross Polarization in Dual Reflector Antennas - A PO and PTD Analysis", IEEE Transactions on Antennas and Propagation, Vol. AP-34, No. 6, June 1986, pp. 849-853.
- [5] A.J. Cha, "Physical Optics Analysis of a Four-Reflector Antenna", IEEE Transactions on Antennas and Propagation, Vol. AP-34, no. 8, August 1986, pp. 992-996.
- [6] E.F. Knott, "A Progression of High-Frequency RCS Prediction Techniques", Proceedings of the IEEE, Vol. 73, no. 2, February 1985, pp. 252-264.
- [7] G.F. Koch, "Die verschiedenen Ansätze des Kirchhoffschen Prinzips und ihre Anwendung auf die Beugungsdiagramme bei elektromagnetischen Wellen", A.E.O., Band 14, 1960, Heft 2, S. 77-98 und Heft 3, S. 132-153.

- [16] D. Klement "Scattering by Complicated Structures: Calculation of the Radar Properties of Metallic Targets by Means of Physical Optics", ESA-TI 946, Translation of DFVLR-FB 85-22, 1985.
- [19] D. Klement, J. Preißner and V. Stein, "Computation of the Scattering Matrix of Radar Targets: Concept of the Method and First Results", AGARD Conference Print No. 364, 1984, pp. 20-1 to 20-23.
- [10] D. Klement, J. Preißner and V. Stein, "Special Problems in Applying the Physical Optics Method for Backscatter Computations of Complicated Objects", to be published in IEEE Transactions on Antennas and Propagation, 1987.
- [11] W.C. Anderson, "Polarisation Dependent Scattering Properties of Trinedral Corner Reflectors", J. of Electrical and Electronics Engineering, Australia, IE Aust. and IREE Aust., Vol. 5, No. 3, September 1985, pp. 198-200.
- [12] G.T. Ruck, D.E. Barrick and W.D. Stuart, Chapter 2 in Radar Cross Section Handbook, edited by G.T. Ruck, D.E. Barrick, W.D. Stuart, C.K. Krichbaum, pp. 50-63, New York, London: Plenum Press, 1970.
- [13] J.J. Bowman, T.B.A. Senior and P.L.E. Uslenghi, Chapter Introduction in Electromagnetic and Acoustic Scattering by Simple Shapes, edited by J.J. Bowman, T.B.A. Senior and P.L.E. Uslenghi, pp. 29-31, Amsterdam: North-Holland Publishing Company, 1969.
- [14] A.J. Poggio and E.K. Miller, "Integral Equation Solutions of Three-Dimensional Scattering Problems", in Computer Techniques for Electromagnetics, edited by R. Mittra, pp. 192-193, Oxford, New York, Toronto, Sydney, Braunschweig: Pergamon Press, 1973.
- [15] F.T. Ulaby, K.K. Moore and A.K. Fung, "Microwave Remote Sensing, Active and Passive, Vol. II, Radar Remote Sensing and Surface Scattering and Emission Theory", London, Amsterdam, Don Mills/Ontario, Sydney, Tokyo: Addison-Wesley Publishing Company, 1982, pp. 925-933, 1019-1020.
- [16] P. Beckmann and A. Spizzichino, "The Scattering of Electromagnetic Waves from Rough Surfaces", Oxford, London, New York, Paris: Pergamon Press, 1963, pp. 17-32 and 178-181.
- [17] H. Honl, A.W. Maue, K. Westpfahl, "Theorie der Beugung", Handbuch der Physik, edited by S. Flügge, Berlin, Göttingen, Heidelberg: Springer-Verlag, 1961, S. 216-219, 233, 236, 238-245, 266-289.
- [18] H. Born and E. Wolf, "Principles of Optics", Oxford, London, Edinburgh, New York, Paris, Frankfurt: Pergamon Press, 1964, pp. 370-375.
- [19] Chr. Gerthsen, "Physik", Berlin, Göttingen, Heidelberg: Springer-Verlag, 1958, S. 124.
- [20] A. Rubinowicz, "Die Beugungswelle in der Kirchhoffschen Theorie der Beugung", Berlin, Heidelberg, New York: Springer-Verlag, Warszawa: Polnischer Verlag der Wissenschaften, 1966, S. 1-58.
- [21] J.A. Stratton, "Electromagnetic Theory", New York, London: McGraw-Hill Book Company, 1941, pp. 187-193, 464-468.
- [22] A. Schroth and V. Stein, "Moderne numerische Verfahren zur Lösung von Antennen- und Streuproblemen", München, Wien: R. Oldenbourg Verlag, 1985, S. 33-37, 45, 48, 50-55.
- [23] V. Stein, "Die Integraldarstellungen des elektromagnetischen Felds", Institut für Hochfrequenztechnik, DFVLR, Oberpfaffenhofen, IB 501-05/7, 1985.
- [24] S. Silver, "Microwave Antenna Theory and Design", New York, Toronto, London: McGraw-Hill Book Company, Inc., 1949, pp. 80-83, 164-166.
- [25] A.Z. Fradin, "Microwave Antennas", Oxford, London, New York, Paris: Pergamon Press, 1961, pp. 45-48.
- [26] V. Stein, "Zur Berechnung des Streufelds bei nicht ideal leitenden ebenen Flächen mit Hilfe des physikalisch-optischen Ansatzes", Institut für Hochfrequenztechnik, DFVLR, Oberpfaffenhofen, to be published in 1987.
- [27] L.M. Brekhovskikh, "Waves in Layered Media", New York, London: Academic Press Publishers, 1960, pp. 1-134.
- [28] J. Preissner, "Reflexions- und Transmissionseigenschaften ebener, inhomogener und unbegrenzter Medien unter besonderer Berücksichtigung von glatten See- und Meeresoberflächen", Institut für Hochfrequenztechnik, DFVLR, Oberpfaffenhofen, IB 551-84/3, 1984.
- [29] J. Preissner, "Reflexion an mehrschichtigen Medien unter besonderer Berücksichtigung des Mikrowellenbereichs", Institut für Hochfrequenztechnik, DFVLR, Oberpfaffenhofen, to be published in 1987.
- [30] D.E. Barrick, "A More Exact Theory for the Scattering of Electromagnetic Waves from Statistically Rough Surfaces", Dissertation, The Ohio State University, 1965.
- [31] G. Böye, a publication concerning the solution of the hidden surface problem will be prepared.
- [32] R. Schwemmer, "Ein Algorithmus zur Ermittlung der sichtbaren Teile von Strukturen, die durch Dreiecke und Vierecke modelliert sind", Institut für Hochfrequenztechnik, DFVLR, Oberpfaffenhofen, to be published in 1987.

- [133] H. Ansoerge, "Reflexion und Brechung elektromagnetischer Wellen an der gekrümmten Trennfläche zweier Dielektrika", Kleinheubacher Berichte, Band Nr. 29, 1986, S. 151-160.
- [134] H. Chaloupka and H.-J. Meckelburg, "Improved High-Frequency Current Approximation for Curved Conducting Surfaces", A.E.U., Band 39, 1985, Heft 4, S. 245-250.
- [135] J.W. Crispin and K.M. Siegel, "Methods of Radar Cross-Section Analysis", New York: Academic Press, 1968, pp. 281-297.
- [136] D.M. Le Vine, "The Radar Cross Section of Dielectric Disks", IEEE Transactions on Antennas and Propagation, Vol. AP-32, No. 1, January 1984, pp. 6-12.
- [137] W.B. Gordon, "Far Field Approximations to the Kirchhoff-Helmholtz Representations of Scattered Fields", IEEE Transactions on Antennas and Propagation, Vol. AP-23, No. 4, pp. 590-592.
- [138] H. Mosebach, "Das Softwarepaket RAMSES, Radar Modelling and Signature Evaluation Software zur Berechnung und Bewertung von Radarzielsignaturen", IABG, B-TU 2564/01, 1985.

8. ACKNOWLEDGEMENT

The author wishes to thank his colleagues D. Klement and J. Preissner for the cooperation in applying and extending of the PO theory and the development of computer programs. Dr. B. Röde and K.H. Bethke carried out the precise backscatter measurements of most of the cited test objects. The computer program used for the solution of the hidden surface problem was developed by Professor Dr. G. Böge, Universität der Bundeswehr, Neubiberg, the computer program for the geometry of double reflections was developed by Dr. H. Mosebach, Industrieanlagen-Betriebsgesellschaft (IABG), Ottobrunn. Thanks are also due to Mrs. M. Malchow for carefully typing the manuscript and Miss G. Jacob for accurately drawing the illustrations.

THEORETICAL ASPECTS OF TARGET CLASSIFICATION:
PHYSICAL OPTICS AND RADON TRANSFORM METHODS

by

K.J. Langenberg
Professor Electromagnetic Theory
University of Kassel
Dept. of Electrical Engineering
Wilhelmshöher Allee 71
D 3500 Kassel, FRG

AD-P005649

SUMMARY

Target classification is set up as a multidimensional inverse scattering problem for electromagnetic waves. The target is considered to be of compact support residing in a medium with constant wave speed. The scattered field produced by a prescribed incident field is represented by its equivalent sources in terms of Huygens' principle; for the sake of simplicity, inversion of this representation is outlined for a scalar quantity, say a scalar potential. It is illustrated that the introduction of the physical optics or weak scatterer approximation linearizes the inverse problem resulting immediately in an inversion formula for the characteristic or singular function of the scatterer if the scattered field is measured as function of frequency - or as broadband transients - on a closed surface sufficiently remote from the target in an either bistatic or monostatic experimental arrangement. When interpreted in the time domain the resulting far-field algorithms turn out to be of the backprojection type inversion of the Radon transform as it is a basic tool in computerized tomography. To get rid of the far-field approximation the wavefield backpropagation principle is utilized to define a generalized holographic field, which is explicitly related to the minimal energy components of the equivalent sources according to the Porter-Bojarski integral equation; integration with regard to frequency yields a unique explicit solution for the geometry of the target if and only if the physical optics or weak scatterer approximation holds. In the time domain the resulting solution of the multidimensional inverse scattering problem can be intuitively interpreted as time domain backpropagation of transient scattered wavefields, which turns out to be a generalization of Radon transform methods to diffractive waves instead of projective rays. As such, the Synthetic Aperture Radar can be theoretically derived within a tomographic framework. Additionally, this gives rise to either bistatic or monostatic Fourier domain processing of transient data even in the near-field.

1. INTRODUCTION

We define the following electromagnetic scattering problem (Fig. 1): a source volume Q transmits

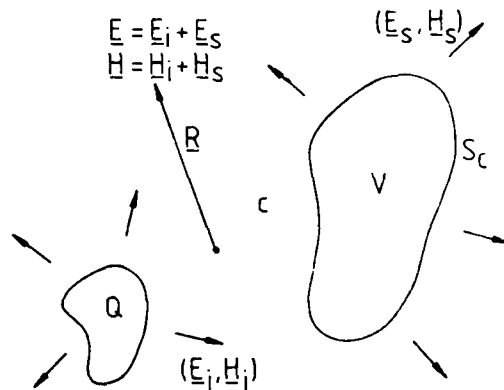


Fig. 1: Scattering problem

an electromagnetic (incident) field (E_i, H_i) , which is scattered by a target of compact support with surface S_c , both residing in free space with (vacuum) wave speed $c = (\epsilon_0 \mu_0)^{-1/2}$. The total field (E, H) at some spatial point R is then composed of the sum of the incident field and the scattered field (E_s, H_s) . In the time domain $E(R, t)$ and $H(R, t)$ have to satisfy time dependent Maxwell equations with initial conditions and appropriate boundary conditions. Introducing a Fourier transform with respect to t according to

$$F(\omega) = \int_{-\infty}^{+\infty} f(t) e^{j\omega t} dt = F_t^*(f(t)) \quad (1)$$

leads to spectral quantities $\underline{E}(\underline{R}, \omega)$ and $\underline{H}(\underline{R}, \omega)$, which satisfy time harmonic Maxwell equations with

the initial condition replaced by a radiation condition; notice that we have chosen the positive sign in the exponential, which yields the complex conjugate of the conventional Fourier transform for real valued time functions; this is indicated by the asterisk in operator notation.

In the spectral domain, a solution - for instance for $E(\underline{R}, \omega)$ - can be given in terms of the following integral representation for the incident and the scattered field [1,2]:

$$\underline{E}(\underline{R}, \omega) = \iiint_Q [j\omega\mu_0 \underline{J}(\underline{R}', \omega) G(\underline{R} - \underline{R}', \omega) + \frac{\rho(\underline{R}', \omega)}{\epsilon_0} \nabla' G] d^3\underline{R}' + \iint_{S_C} \left\{ j\omega\mu_0 [\underline{n}' \times \underline{H}(\underline{R}', \omega)] G(\underline{R} - \underline{R}', \omega) + [\underline{n}' \cdot \underline{E}(\underline{R}', \omega)] \nabla' G + [\underline{n}' \cdot \underline{E}(\underline{R}', \omega)] \nabla' G \right\} dS' \quad (2)$$

where $\underline{J}(\underline{R}', \omega)$ denotes the electric current and $\rho(\underline{R}', \omega)$ the electric charge density in the source volume Q , \underline{n}' is the outward - source point - normal on S_C ; $G(\underline{R} - \underline{R}', \omega)$ represents the three-dimensional free space Green's function

$$G(\underline{R} - \underline{R}', \omega) = \frac{e^{jk|\underline{R} - \underline{R}'|}}{4\pi|\underline{R} - \underline{R}'|} \quad (3)$$

with the wave number $k = \omega/c$.

Usually, equ. (2) is made the basis for the solution of the direct scattering problem where the equivalent surface sources $\underline{n}' \times \underline{H}$, $\underline{n}' \cdot \underline{E}$ on the scatterer have to be determined in advance applying some appropriate boundary condition to $\underline{E}(\underline{R}, \omega)$ [2,3]. With regard to the inverse, i.e. target classification problem, equ. (2) has "simply" to be inverted to determine the localized equivalent sources provided $\underline{E}(\underline{R}, \omega)$ is considered as data and $\underline{E}_i(\underline{R}, \omega)$ is known a priori. This inversion will be outlined in the following, where, for the sake of simplicity, we concentrate upon the scalar counterpart of equ. (2).

It has been emphasized that polarization effects play an important role in target classification [4,5]; they can only be accounted for by the full vector treatment of electromagnetic scattering and inverse scattering. We anticipate that our scalar discussion can be most probably extended not only to the complete electromagnetic vector problem but also to the tensor problem of elastodynamic waves.

Suppose, the electromagnetic field is decomposed into a scalar potential ϕ and a vector potential \underline{A} . In the spectral domain, $\phi(\underline{R}, \omega)$ satisfies the following wave equation

$$(\Delta + k^2)\phi(\underline{R}, \omega) = -q(\underline{R}, \omega) \quad (4)$$

where the source term $q(\underline{R}, \omega)$ is - for instance - proportional to the electric charge density in Q .

With the aid of Green's theorem, we immediately obtain a solution of equ. (4) in terms of an integral representation, which is the scalar counterpart to equ. (2) (compare Fig. 2) as soon as the arbitrary surface S

$$\phi(\underline{R}, \omega) = \iiint_Q q(\underline{R}', \omega) G(\underline{R} - \underline{R}', \omega) d^3\underline{R}' + \iint_S \left[\phi(\underline{R}', \omega) \frac{\partial G}{\partial n'} - G(\underline{R} - \underline{R}', \omega) \frac{\partial \phi}{\partial n'} \right] dS' \quad (5)$$

surrounding S_C is smoothly adjusted to S_C .

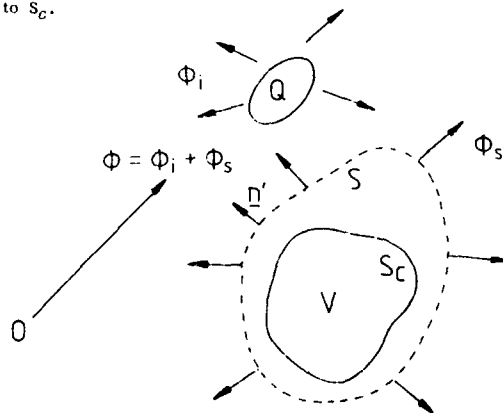


Fig. 2: Scalar Huygens' principle

2. HUYGENS' PRINCIPLE, EQUIVALENT SOURCES, PHYSICAL OPTICS AND WEAK SCATTERER APPROXIMATION

From equ. (5) we immediately learn two things, which are important for the inverse problem:

- Suppose, S characterizes a measurement surface S_M , where the quantities ϕ and $\partial\phi/\partial n'$ are known from experiment; then, equ. (5) tells us that the total potential outside S_M can be computed with the aid of a surface integral, any additional measurement point outside S_M yields redundant information. Therefore, our data space is essentially twodimensional, whereas our scatterer is at least threedimensional (in terms of the equivalent sources - see below - it is even fourdimensional). A remedy consists in the increase of the dimension of the data, varying experimental parameters, which can be conveniently controlled: these could be the angle of incidence of a plane wave, say, modelling the incident field or - more important for radar purposes - spectral frequency. Here, we will concentrate upon the latter procedure.
- Applying equ. (5) to a point interior of S , Green's theorem only tells us that

$$\iiint_V q(\underline{R}', \omega) G(\underline{R} - \underline{R}', \omega) d^3 \underline{R}' = - \oint_S \left[\phi(\underline{R}', \omega) \frac{\partial G}{\partial n'} - G(\underline{R} - \underline{R}', \omega) \frac{\partial \phi}{\partial n'} \right] dS' \quad (6)$$

As has been pointed out by Bojarski [6], equ. (5) cannot be considered explicitly useful for target classification.

In order to invert equ. (5) it is appropriate to transform the surface integral into a volume integral for arbitrary scatterers, be they either perfect ("perfectly conducting") or penetrable, i.e. allowing for wave propagation inside S_c . This can be done defining the characteristic and singular function of the scatterer first. The characteristic function denotes the support of the scatterer according to

$$\Gamma(\underline{R}) = \begin{cases} 1 & \text{for } \underline{R} \in V \\ 0 & \text{for } \underline{R} \notin V \end{cases} \quad (7)$$

and the singular function has been introduced by Bleistein [7] in terms of

$$\int_{-\infty}^{+\infty} \int_{-\infty}^{+\infty} \int_{-\infty}^{+\infty} \gamma(\underline{R}) \phi(\underline{R}) d^3 \underline{R} = \oint_{S_c} \phi(\underline{R}) d^3 \underline{R} \quad (8)$$

to characterize S_c explicitly.

Let us choose the Dirichlet boundary condition $\phi(\underline{R}', \omega) \equiv 0$ on S_c to describe a perfect scatterer. We then obtain the following equivalent volume source representation for the scattered field

$$\phi_S(\underline{R}, \omega) = \int_{-\infty}^{+\infty} \int_{-\infty}^{+\infty} \int_{-\infty}^{+\infty} q_C^D(\underline{R}', \omega) G(\underline{R} - \underline{R}', \omega) d^3 \underline{R}' \quad (9)$$

with

$$q_C^D(\underline{R}, \omega) = - \gamma(\underline{R}) \underline{n} \cdot \nabla \phi \quad (10)$$

where the upper index "D" stands for Dirichlet.

The case of the penetrable scatterer can be obtained transforming the surface integral in (5) for $S = S_c$ into a volume integral for points \underline{R} outside S_c applying Green's theorem, which yields

$$\phi_S(\underline{R}, \omega) = - \iiint_V G(\underline{R} - \underline{R}', \omega) (\Delta' + k^2) \phi(\underline{R}', \omega) d^3 \underline{R}' \quad (11)$$

Very often, a penetrable scatterer is characterized by a variable wave speed $c(\underline{R})$ inside V , which can be modelled by the following wave equation

$$\Delta \phi + k^2(\underline{R}) \phi = 0 \quad \underline{R} \in V \quad (12)$$

From (12) we obtain

$$\Delta \phi + k^2 \phi = - [k^2(\underline{R}) - k^2] \phi \quad (13)$$

and hence

$$\phi_S(\underline{R}, \omega) = \int_{-\infty}^{+\infty} \int_{-\infty}^{+\infty} \int_{-\infty}^{+\infty} q_C(\underline{R}', \omega) G(\underline{R} - \underline{R}', \omega) d^3 \underline{R}' \quad (14)$$

with the equivalent volume source

$$q_C(\underline{R}, \omega) = \Gamma(\underline{R}) [k^2(\underline{R}) - k^2] \phi \quad (15)$$

Therefore, the subsequent integral representation

$$\phi(\underline{R}, \omega) = \phi_i + \int_{-\infty}^{+\infty} \int_{-\infty}^{+\infty} \int_{-\infty}^{+\infty} q_C(\underline{R}', \omega) G(\underline{R} - \underline{R}', \omega) d^3 \underline{R}' \quad (16)$$

can be made the starting point for further investigations: the equivalent volume source is either given by (10) or (15), and we emphasize that a variety of more complex surface or volume sources - electromagnetic currents and charges as well as elastodynamic forces - can be modelled in a similar manner (sometimes only approximately, as it is already the case for the scalar Neumann problem).

In contrast to the prescribed sources accounting for the incident field the equivalent sources are field-dependent, which makes both the direct and the inverse scattering problem non-linear with regard to the scattering geometry: if only a single scattering "pixel" is added to V_C , the whole equivalent source distribution changes.

One might be tempted to solve the non-linear inverse problem by deconvolving equ. (16); in cartesian coordinates (x,y,z), equ. (16) is a three-dimensional convolution equation, and, applying a three-dimensional spatial Fourier transform according to $\underline{K} = (K_x, K_y, K_z)$ denotes the vector of corresponding Fourier variables -

$$\tilde{\phi}(\underline{K}, \omega) = \int_{-\infty}^{+\infty} \int_{-\infty}^{+\infty} \int_{-\infty}^{+\infty} \phi(\underline{R}, \omega) e^{-j\underline{K} \cdot \underline{R}} d^3 \underline{R} \quad (17)$$

we would obtain

$$\tilde{\phi}_S(\underline{K}, \omega) = \tilde{q}_C(\underline{K}, \omega) \tilde{G}(\underline{K}, \omega) \quad (18)$$

Considering $\tilde{\phi}_S$ as (Fourier transformed) data, we could divide by \tilde{G} to obtain the spatial Fourier spectrum of the equivalent sources. Unfortunately, this procedure is not possible for two reasons:

- $\phi(\underline{R}, \omega)$ is only known on S_M or outside S_M (with the aid of Huygens' integral); there is no way to compute it inside S_M , and, hence, $\tilde{\phi}_S$ is missing the most important spectral components.
- Computation of $\tilde{G}(\underline{K}, \omega)$ yields for any spatial dimension

$$\tilde{G}(\underline{K}, \omega) = \text{pf} \frac{1}{K^2 - k^2} \quad (19)$$

with

$$K = \sqrt{K_x^2 + K_y^2 + K_z^2} \quad (20)$$

where "pf" stands for pseudo-function; loosely interpreted, \tilde{G} is singular on the so-called Ewald-sphere $K = k$ preventing simple deconvolution.

The remaining alternatives to solve the multidimensional inverse scattering problem rely on approximations for the equivalent sources, which essentially result in a linearization with regard to the scattering object; the physical optics and weak scatterer assumption are physically intuitive procedures to achieve this linearization.

The case of the penetrable scatterer can be linearized provided the surface S_C encloses a weak scattering volume, which means that it is present as an equivalent source but not as a scatterer, i.e. in (15) we set the total field ϕ inside the scatterer equal to the incident field ϕ_i , which is certainly valid if the difference $|k^2(\underline{R}) - k^2|$ is not too large. Usually, the weak scatterer approximation is associated with the name of Born, i.e. we write instead of (15)

$$q_C^{\text{Born}}(\underline{R}, \omega) = \Gamma(\underline{R}) [k^2(\underline{R}) - k^2] \phi_i(\underline{R}, \omega) \quad (21)$$

Assuming plane wave incidence according to

$$\phi_i(\underline{R}, \omega) = F(\omega) e^{j\underline{k}_i \cdot \underline{R}} \quad (22)$$

where $F(\omega)$ denotes the frequency spectrum of the incident wave, we conclude that a prescribed characteristic function is transformed into an equivalent volume source (within the Born approximation) simply by multiplication with a phase factor, which is completely determined by the propagation vector \underline{k}_i of the incident plane wave with $|\underline{k}_i| = k$.

For very high frequencies ω , a smooth convex surface of a perfect scatterer can be considered to be composed of locally plane patches, which are "infinitely" large with respect to the pertinent

wavelength. Hence, for the Dirichlet boundary condition we put

$$q_0^{\text{D,PO}}(R, z) = 2j_1(R, z) \quad (23)$$

on every locally plane patch which resides on the illuminated side of the scattering surface, in the "dark" side, the equivalent surface sources are set equal to zero. Therefore, we write instead of (19) within the physical optics limit

$$q_0^{\text{D,PO}}(R, z) = 2j_1(R, z) u(\hat{k}_1 \cdot \mathbf{R}) u^*(\hat{k}_1 \cdot \mathbf{z}) \quad (24)$$

where $u(\hat{k}_1 \cdot \mathbf{R})$ denotes a unit step function accounting for the distinction of illuminated and dark side; \hat{k}_1 is the unit vector in \mathbf{k}_1 direction.

Let us briefly consider an example for an equivalent Dirichlet surface source, which is produced by plane wave incidence along the negative z direction upon an infinitely long circular cylinder of radius a whose cross section resides in the xz plane. Fig. 3 shows the magnitude of $q_0^{\text{D,PO}}(x, z, z)$ for $ka = 10$. Obviously, this result is nicely modelled by equ. (24), which reduces to

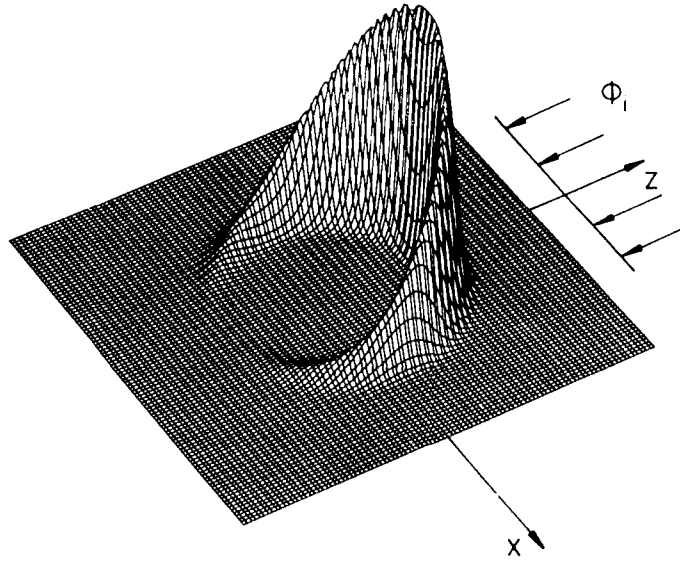


Fig. 3: Equivalent surface sources on a circular cylinder with Dirichlet boundary condition for plane wave incidence ($ka = 10$)

$$q_0^{\text{D,PO}}(x, z, z) = 2jk \sin^2 \theta (r - a) u(z) e^{-jkz} \quad (25)$$

in our special case, where we have introduced polar coordinates (r, θ) in the (x, z) plane according to

$$\begin{aligned} z &= r \sin \theta \\ x &= r \cos \theta \end{aligned} \quad (26)$$

$\delta(r - a)$ denotes a δ -distribution accounting for the (two-dimensional) singular function of the circular cylinder.

3. FAR-FIELD INVERSION VIA \underline{k} SPACE

Introducing the far-field approximation of the Green's function

$$\frac{e^{jk|\underline{R} - \underline{R}'|}}{4\pi|\underline{R} - \underline{R}'|} \approx \frac{e^{jkR}}{4\pi R} e^{-jk\hat{\underline{R}} \cdot \underline{R}'} \quad (27)$$

with the unit-vector $\hat{\underline{R}} = \underline{R}/R$ we obtain instead of (16)

$$\phi_s^{\text{far}}(\underline{R}, \omega) = \frac{e^{jkR}}{4\pi R} H(\underline{k}\hat{R}, \omega) \quad (28)$$

where

$$H(\underline{k}\hat{R}, \omega) = \int_{-\infty}^{+\infty} \int_{-\infty}^{+\infty} \int_{-\infty}^{+\infty} q_C(\underline{R}', \omega) e^{-jk\hat{R} \cdot \underline{R}'} d^3R' \quad (29)$$

denotes the scattering amplitude. Comparing (29) with (17) we conclude

$$H(\underline{k}\hat{R}, \omega) = \tilde{q}_C(\underline{K} = \underline{k}\hat{R}, \omega) \quad (30)$$

which tells us that measurements of the scattering amplitude in various directions \hat{R} provides us with Ewald-sphere information of the equivalent sources, where points on the Ewald-sphere, i.e. in spatial Fourier space, are explicitly related to points in observation space through $\underline{K} = \underline{k}\hat{R}$. This fact can be exploited to derive far-field solutions of the multidimensional inverse scattering problem within the Born or physical optics approximations either in a bistatic or monostatic operational mode.

Here, we want to concentrate upon the bistatic case, because algorithms for monostatic far-field inversion within the physical optics approximation have been reported earlier (compare the famous POFFIS-identity, which stands for Physical Optics Far-Field Inverse Scattering [8,9]). For the Dirichlet scatterer we have

$$\phi_s^{\text{PO}}(\underline{R}, \omega) = -2F(\omega) \int_{-\infty}^{+\infty} \int_{-\infty}^{+\infty} \int_{-\infty}^{+\infty} \gamma(\underline{R}') u(-\hat{k}_i \cdot \underline{R}') \underline{n}' \cdot \underline{v}' e^{jk_i \cdot \underline{R}'} \frac{e^{jk|\underline{R}-\underline{R}'|}}{4\pi|\underline{R}-\underline{R}'|} d^3R' \quad (31)$$

and further

$$\phi_s^{\text{PO, far}}(\underline{R}, \omega) = -2jkF(\omega) \frac{e^{jkR}}{4\pi R} \int_{-\infty}^{+\infty} \int_{-\infty}^{+\infty} \int_{-\infty}^{+\infty} \gamma(\underline{R}') \underline{n}' \cdot \hat{k}_i u(-\hat{k}_i \cdot \underline{R}') e^{-jk(\underline{R}-\hat{k}_i) \cdot \underline{R}'} d^3R' \quad (32)$$

Defining a spatial Fourier-vector through

$$\underline{K} = \underline{k}(\underline{R} - \hat{k}_i) \quad (33)$$

identifies the three-dimensional integral in (32) as a three-dimensional Fourier integral relating far-field data to the Fourier transform of the "Dirichlet singular function"

$$\gamma^D(\underline{R}', \hat{k}_i) = \gamma(\underline{R}') \underline{n}' \cdot \hat{k}_i u(-\hat{k}_i \cdot \underline{R}') \quad (34)$$

in terms of

$$\int_{-\infty}^{+\infty} \int_{-\infty}^{+\infty} \int_{-\infty}^{+\infty} \gamma^D(\underline{R}', \hat{k}_i) e^{-j\underline{K} \cdot \underline{R}'} d^3R' = -2\pi R \frac{\phi_s^{\text{PO, far}}(\underline{K}) e^{-jkR}}{jkF(\omega)} \quad (35)$$

Due to the definition of \underline{K} , a prescribed experimental setup, i.e. choice of \hat{k}_i , \underline{k} and \underline{R} uniquely determines a point in \underline{K} -space; data space and Fourier space are related on a point wise basis. This is the argument to interpret the far-field data $\phi_s^{\text{far}}(\underline{R}, \hat{k}_i, \omega)$ measured in the direction \underline{R} for the direction \hat{k}_i of the incident wave of wavenumber k as a "data point" $\phi_s^{\text{far}}(\underline{K})$ in the Fourier space of the object after the normalization indicated in (35).

Fig. 4 exhibits the relation between object space and Fourier space; obviously, if \hat{k}_i remains fixed, according to (33) the vector \underline{K} reaches all points of the shifted Ewald-sphere $|\underline{K} + \underline{k}_i| = k$ if the receiver rotates around the scatterer recording $\phi_s^{\text{far}}(\underline{R}, \hat{k}_i, \omega)$ for all possible directions \underline{R} . These (normalized) scattering data have to be interpreted as Fourier data $\phi_s^{\text{far}}(\underline{K})$, hence, a single bistatic time harmonic experiment yields spatial Fourier components of the Dirichlet singular function on the Ewald-sphere only. This information can be augmented in a multiple experiment varying the spectral frequency ω ; for $0 < \omega < \infty$ we obtain

$$\gamma^D(\underline{K}, \hat{k}_i) u(-\underline{K} \cdot \hat{k}_i) = -2\pi R \frac{\phi_s^{\text{PO, far}}(\underline{K}) e^{-jkR}}{jkF(\omega)} \quad (36)$$

where the step-function in \underline{K} -space indicates that only "one half" of \underline{K} -space can be swept that way.

Without loss of generality we can assume to find \hat{k}_i in the xz -plane (as well as in the $\underline{K}_x \underline{K}_z$ -plane) according to

$$\hat{k}_i = \underline{k}(-\cos\theta_i, 0, -\sin\theta_i) \quad (37)$$

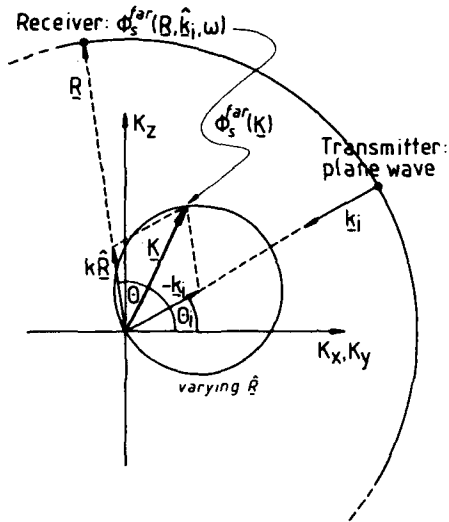


Fig. 4: Object space versus K-space for a bistatic far-field experiment satisfying the physical optics of weak scatterer approximation

We introduce rotated $K_x K_y$ -coordinates instead of K_x and K_y to make

$$-\underline{K} \cdot \hat{k}_i = K_z \quad (38)$$

where the K_z -axis now points into the negative \hat{k}_i -direction; performing a similar rotation of the $x'z'$ -plane with ξ', ζ' to be the new coordinates, the Fourier inversion of the left-hand side of (36) reads

$$\frac{1}{(2\pi)^3} \int_{-\infty}^{+\infty} \int_{-\infty}^{+\infty} \int_{-\infty}^{+\infty} \hat{\gamma}^D(K_x, K_y, K_z, \hat{k}_i) u(K_z) e^{jK_x \xi' + jK_y y' + jK_z \zeta'} dK_x dK_y dK_z \quad (39)$$

$$\frac{1}{(2\pi)^3} \int_{-\infty}^{+\infty} \int_{-\infty}^{+\infty} \hat{\gamma}^D(K_x, K_y, \zeta, \hat{k}_i) * \frac{1}{2} \left[\delta(\zeta) - \frac{1}{\pi} \text{Pf} \frac{1}{j\zeta} \right] e^{jK_x \xi' + jK_y y'} dK_x dK_y$$

where $\hat{\gamma}^D(K_x, K_y, \zeta, \hat{k}_i)$ denotes the twodimensional Fourier transform of $\gamma^D(R, \hat{k}_i)$ with respect to ξ' and y' ; the asterisk in (39) indicates a onedimensional convolution. Interchanging this convolution with the twodimensional inverse Fourier transform and taking the real part yields

$$\gamma^D(R, \hat{k}_i) = -\frac{R}{2\pi^2} \text{Re} \int_{-\infty}^{+\infty} \int_{-\infty}^{+\infty} \int_{-\infty}^{+\infty} \frac{\phi_s^{\text{PO, far}}(K) e^{-jkR}}{jkF(\omega)} e^{j\underline{K} \cdot \underline{R}'} d^3\underline{K} \quad (40)$$

Equ. (40) represents a bistatic far-field inverse scattering identity within the physical optics approximation; obviously, this procedure implies target classification in terms of the magnitude of the equivalent Dirichlet surface sources, which only partly represent the geometry of the scatterer (compare Fig. 3). The situation turns out to be somewhat different for the penetrable scatterer within the weak scatterer approximation; we similarly obtain

$$0(\underline{R}') = -\frac{R}{2\pi^2} \text{Re} \int_{-\infty}^{+\infty} \int_{-\infty}^{+\infty} \int_{-\infty}^{+\infty} \frac{\phi_s^{\text{Born, far}}(K) e^{-jkR}}{k^2 F(\omega)} e^{j\underline{K} \cdot \underline{R}'} d^3\underline{K} \quad (41)$$

where $0(\underline{R})$ denotes the object function, which is directly related to the characteristic function according to

$$0(\underline{R}) = r(\underline{R}) \left[1 - \frac{k^2(\underline{R})}{k^2} \right] \quad (42)$$

The essential difference of the monostatic counterparts to eqs. (40) and (41) is in the definition of the Fourier vector \mathbf{K} ; due to $\mathbf{R} = \mathbf{k}_i$ we then have instead of (33)

$$\mathbf{K} = 2k\hat{\mathbf{R}} \quad (43)$$

Evaluating the corresponding algorithms similarly as above (compare the referenced literature) we find that monostatic far field target classification is in terms of $\theta(\mathbf{R})$ for the penetrable scatterer, and in terms of either $\gamma(\mathbf{R})$ or $\gamma(\mathbf{R})\mathbf{n} \cdot \mathbf{R}$ for the perfect scatterer (Dirichlet and Neumann boundary condition yield the same results). In any case, a closed measurement surface and infinite spectral bandwidth is understood; deviations from these ideal conditions lead to image degradations, which can be intuitively investigated via computer simulations [10]. Alternatively, a certain physical understanding of the occurring phenomena is obtained transforming the far field \mathbf{K} space inverse scattering identities into the time domain. This step formally yields the backprojection algorithm of computerized X-ray tomography as inversion of the Radon transform.

4. RADON TRANSFORM: \mathbf{K} SPACE INVERSION AND FILTERED BACKPROJECTION

For the sake of simplicity we refer to twodimensional problems, i.e. a twodimensional target is defined by its characteristic function $\Gamma(x,z)$. A projection of $\Gamma(x,z)$ along "rays" distinguished by the parameter ξ , whose normal makes an angle θ with the x axis, is obtained through (compare Fig. 5)

$$P_0(\xi) = \int_{-\infty}^{\infty} \int_{-\infty}^{\infty} \Gamma(x,z) \delta(x \cos \theta + z \sin \theta - \xi) dx dz \quad (44)$$

Eqn. (44) is called the Radon transform of $\Gamma(x,z)$.

Computing and evaluating the one-dimensional Fourier transform of $P_0(\xi)$ with respect to ξ according to

$$P_0(K_\xi) = \int_{-\infty}^{\infty} P_0(\xi) e^{-jK_\xi \xi} d\xi \quad (45)$$

leads to the so-called Fourier Slice Theorem [11] of computerized tomography as an inversion of the Radon transform

$$P_0(K_\xi) = \Gamma(K_\xi \cos \theta, K_\xi \sin \theta) \quad (46)$$

which relates (one-dimensionally Fourier transformed) data of observation space to the two-dimensional Fourier transform $\Gamma(K_x, K_z)$ of the characteristic function along a radial line through the origin of \mathbf{K} space (compare Fig. 5); varying θ continuously fills \mathbf{K} space continuously, and, hence, $\Gamma(x,z)$ can be obtained by multidimensional Fourier inversion,

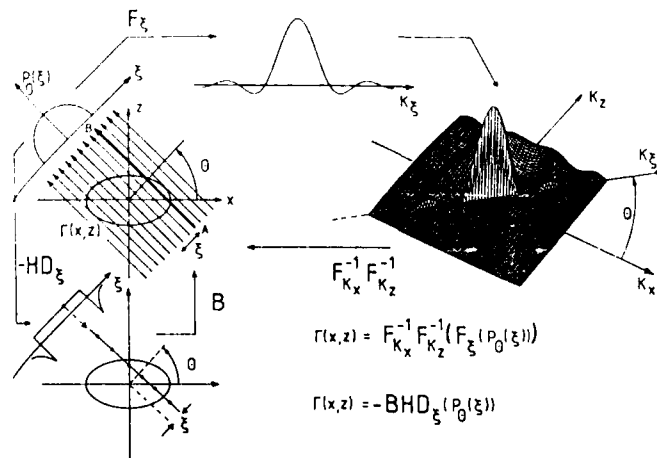


Fig. 5: Illustration of the Fourier Slice Theorem and filtered backprojection

A processing alternative to equ. (46) is obtained via analytical manipulation to yield [11]

$$\Gamma(x,z) = \frac{1}{2\pi} \int_0^\pi Q_\theta(x \cos \theta + z \sin \theta) d\theta \quad (47)$$

with

$$Q_\theta(\xi) = -\mathbf{HD}_\xi [P_\theta(\xi)] \quad (48)$$

where \mathbf{HD}_ξ denotes a filter operation on the data with regard to ξ consisting of a derivative operator followed by a Hilbert transform. According to (47), the filtered data are subsequently backprojected into the target space along lines of constant ξ (compare Fig. 5). Superposition of all backprojections for varying θ yields $\Gamma(x,z)$. For obvious reasons, this data processing procedure is called the filtered backprojection inversion of the Radon transform.

For certain materials projections of the kind (44) can be obtained with X-rays whence the success of computerized tomography in medical imaging and nondestructive testing.

5. FAR-FIELD INVERSION VIA TIME DOMAIN BACKPROJECTION

Similar to the Radon transform inversion, far-field inverse scattering via K-space has its counterpart in filtered backprojection algorithms which operate directly on time domain scattered data. Again, the monostatic case has been treated earlier [9,12,13], therefore, we concentrate upon the bistatic arrangement, and, for the sake of convenience, we choose equ. (41) as starting point. With (37) and

$$\hat{\mathbf{R}} = (\cos\theta\cos\phi, \cos\theta\sin\phi, \sin\theta) \quad (49)$$

we obtain the following Jacobian

$$dK_x dK_y dK_z = \frac{k^2}{2} |\hat{\mathbf{R}} - \hat{\mathbf{k}}_i|^2 dk d\Omega \quad (50)$$

with the spatial angle element

$$d\Omega = \cos\theta d\theta d\phi \quad (51)$$

Insertion into (41) yields

$$0(\underline{\mathbf{R}}') = -\frac{R}{4\pi^2} \operatorname{Re} \int_0^\infty \frac{e^{-jkR}}{F(\omega)} \oint_S^{\text{Born, far}} (\underline{\mathbf{R}}, \hat{\mathbf{k}}_i, \omega) e^{jk(\hat{\mathbf{R}} - \hat{\mathbf{k}}_i) \cdot \underline{\mathbf{R}}'} (\underline{\mathbf{R}}, \hat{\mathbf{k}}_i, \omega) d\omega \quad (52)$$

where the spatial angle integral extends over its full range of 4π . To interpret the k integral as an inverse Fourier integral, we smuggle $\exp(-j\omega t)$ into the integrand, and put $t=0$ immediately afterwards. Due to the step-function $u(\omega)$ the lower integration limit can be chosen as minus infinity. Because $u(t)$ according to

$$u(t) = \frac{1}{2} \delta(t) + \frac{1}{2\pi} \operatorname{pf} \frac{1}{jt} \quad (53)$$

is the inverse transform of $u(\omega)$ (compare equ. (39) and notice the complex conjugate in equ. (11)), we obtain

$$0(\underline{\mathbf{R}}') = -\frac{R}{4\pi c} \oint_S^{\text{I, Born, far}} (\underline{\mathbf{R}}, \hat{\mathbf{k}}_i, t_0) |\underline{\mathbf{R}} - \hat{\mathbf{k}}_i|^2 d\omega \quad (54)$$

with

$$ct_0 = R - (\hat{\mathbf{R}} - \hat{\mathbf{k}}_i) \cdot \underline{\mathbf{R}}' \quad (55)$$

Due to the occurrence of $F(\omega)$ in (52), the time domain data corresponding to the frequency spectrum of the measured data have to be deconvolved with the time dependence of the measured data have to be deconvolved with the time dependence of the incident plane wave whence the upper index "I" in (54), which stands for time domain impulse response.

Equ. (54) represents a time domain bistatic far-field inverse scattering identity within the Born approximation; its expressive interpretation is given in Fig. 6 for the example of a spherical Born scatterer whose far-field impulse response can be computed straightforwardly [10]: a time domain data point observed in the direction $\hat{\mathbf{R}}$ for a time instant t_0 is distributed, i.e. backprojected, to a plane perpendicular to $\hat{\mathbf{R}} - \hat{\mathbf{k}}_i$, where the scalar product $\underline{\mathbf{R}}' \cdot (\hat{\mathbf{R}} - \hat{\mathbf{k}}_i)$ is a constant relating points $\underline{\mathbf{R}}'$ in object space with t_0 through (55). As such, time domain far-field target classification within the physical optics or weak scatterer approximation is closely related to the backprojection operator (47) as an inversion scheme of the Radon transform.

AD-A185 125

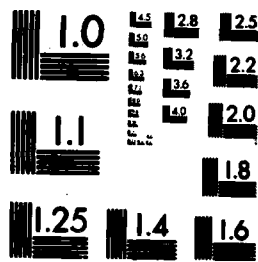
THEORETICAL ASPECTS OF TARGET CLASSIFICATION LECTURE
SERIES OF THE ELECTR. (U) ADVISORY GROUP FOR AEROSPACE
RESEARCH AND DEVELOPMENT NEUILLY.. JUN 87 AGARD-LS-152

2/3

UNCLASSIFIED

F/G 17/11

NL



MICROCOPY RESOLUTION TEST CHART
NATIONAL BUREAU OF STANDARDS-1963-A

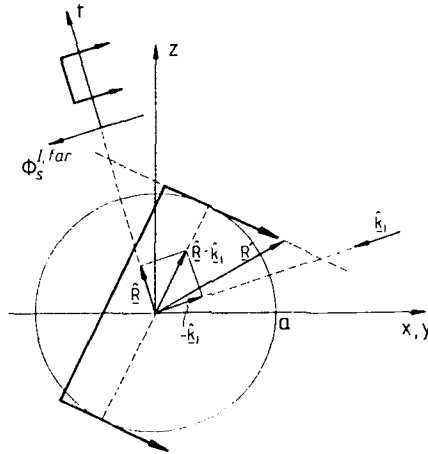


Fig. 6: Time domain backprojection of the bistatic far-field impulse response of a weak spherical scatterer

A straightforward extension of (54) to non-far-field experimental arrangements, where, for instance, extended planar measurement surfaces have to be accounted for, is heuristically obtained inserting t_0 according to

$$ct_0 = \hat{k}_i \cdot \underline{R}' + |\underline{R} - \underline{R}'| \quad (56)$$

instead of (55); from (56) equ. (55) can be deduced if far-field conditions hold. The resulting target classification scheme has been made the basis of the Synthetic Aperture Radar (SAR). In the following we give a rigorous evaluation based on the backpropagation principle. It will enable us to clearly state all approximations, which have to be made to end up with the heuristic SAR scheme. We stay with the bistatic case and the penetrable scatterer; in [10], the monostatic case is treated in detail, and the perfect scatterer can be approached along the same guidelines with our equivalent volume source formulation.

6. BACKPROPAGATION PRINCIPLE, PORTER-BOJARSKI INTEGRAL EQUATION

We return to the formulation of wave scattering in terms of Huygens' principle, which, as we already mentioned, is not explicitly useful to tackle the inverse problem. Therefore, we follow the ideas of Porter [14] and Bojarski [15], and define a so-called generalized holographic field $X_H(\underline{R}, \omega)$ inside the (measurement) surface S (compare Fig. 2) according to the principle of backpropagation

$$X_H(\underline{R}, \omega) = - \oint_S \left[\phi(\underline{R}', \omega) \frac{\partial G^*}{\partial n'} - G^*(\underline{R} - \underline{R}', \omega) \frac{\partial \phi}{\partial n'} \right] dS' \quad (57)$$

here, G^* denotes the complex conjugate of the three-dimensional free space Green's function, which accounts for incoming spherical waves travelling towards the measurement surface with amplitudes according to the known values (and normal derivatives) on S ; we are going to "meet" the outgoing scattered field if we compute X_H inside S from ϕ and $\partial \phi / \partial n'$ via G^* .

As a target classification scheme, equ. (57) has been investigated as generalized holography [16] and within the context of exact inverse scattering [15,17]; it allows to derive a relationship between backpropagated fields and their original equivalent sources, the so-called Porter-Bojarski integral equation [6,14].

Applying Green's theorem to the interior of the surface S_M transforms equ. (57) into

$$X_H(\underline{R}, \omega) = \phi(\underline{R}, \omega) - \int_{-a}^{+a} \int_{-a}^{+a} \int_{-a}^{+a} q_C(\underline{R}', \omega) G_i(\underline{R} - \underline{R}', \omega) d^3 \underline{R}' \quad (58)$$

Inserting (16) we obtain

$$X_H(\underline{R}, \omega) = \phi_i + 2j \int_{-a}^{+a} \int_{-a}^{+a} \int_{-a}^{+a} q_C(\underline{R}', \omega) G_i(\underline{R} - \underline{R}', \omega) d^3 \underline{R}' \quad (59)$$

where G_i denotes the imaginary part of the Green's function. We can eliminate ϕ_i defining

$$\theta_H(\underline{R}, \omega) = X_H(\underline{R}, \omega) - \phi_i \quad (60)$$

which yields

$$\theta_H(\underline{R}, \omega) = - \oint_S \left[\phi_s(\underline{R}', \omega) \frac{\partial G^*}{\partial n'} - G^*(\underline{R} - \underline{R}', \omega) \frac{\partial \phi_s}{\partial n'} \right] dS' \quad (61)$$

and therefore

$$\theta_H(\underline{R}, \omega) = 2j \int_{-\infty}^{+\infty} \int_{-\infty}^{+\infty} \int_{-\infty}^{+\infty} q_c(\underline{R}', \omega) G_i(\underline{R} - \underline{R}', \omega) d^3 \underline{R}' \quad (62)$$

Equ. (62) is an integral equation relating the backpropagated scattered field and its equivalent volume sources; unfortunately, its solution in terms of $q_c(\underline{R}, \omega)$ is non-unique [18]. This can be readily seen applying a three-dimensional spatial Fourier transform

$$\tilde{\theta}_H(\underline{K}, \omega) = 2j \tilde{q}_c(\underline{K}, \omega) \tilde{G}_i(\underline{K}, \omega) \quad (63)$$

Recognizing

$$\tilde{G}_i(\underline{K}, \omega) = \frac{\pi}{2K} \delta(K - k) \quad (64)$$

we obtain

$$\tilde{\theta}_H(\underline{K}, \omega) = j \frac{\pi}{K} \tilde{q}_c(K = k, \theta_K, \phi_K, \omega) \delta(K - k) \quad (65)$$

where θ_K, ϕ_K denote angular coordinates in K -space. Equ. (65) relates the spatial Fourier spectrum of a generalized holographic field - a quantity, which can be computed from measurements - to the Ewald-sphere components of the equivalent sources; obviously, $\tilde{q}_c(\underline{K}, \omega)$ can be arbitrarily changed outside the Ewald-sphere without changing equ. (65), whence the non-uniqueness of the solution of the Porter-Bojarski integral equation (62). Equ. (65) reminds us to equ. (18), where we stated that the scattered field is mainly composed of Ewald-sphere components; here we find, that the backpropagated field is only composed of Ewald-sphere components. In fact, the difference is due to the evanescent or non-radiating source components, which get lost in the backpropagation process [10, 18, 19, 20].

From a physical standpoint, equ. (65) is somewhat similar to the far-field inverse scattering identities, insofar, as scattered fields measured on closed surfaces exhibit specific K -space information about the equivalent sources; we just lost the point-wise correspondence between K -space and observation space: in fact, the backpropagation principle relates all measurement points to all points on the Ewald-sphere. Consequently, as in the previous chapters, we will try to augment K -space coverage via multiple, i.e. broadband or transient experiments. Unfortunately, due to the explicit dependence of $\tilde{q}_c(\underline{K}, \omega)$ upon ω , sweeping k changes the total K -space structure of the equivalent source, which belongs to every single frequency component. To control this dependence, we have to introduce a priori knowledge, which is accessible assuming physical optics or weak scatterer approximations. Therefore, to continue in the derivation of explicit inverse scattering identities, it is a must to introduce linearizing assumptions.

7. INVERSION VIA TIME DOMAIN BACKPROPAGATION

We choose the penetrable scatterer for plane wave incidence within the Born approximation, and rewrite equ. (62)

$$e^{-j\mathbf{k}_i \cdot \underline{R}} \theta_H(\underline{R}, \omega) = -2jk^2 F(\omega) \int_{-\infty}^{+\infty} \int_{-\infty}^{+\infty} \int_{-\infty}^{+\infty} q(\underline{R}') e^{-j\mathbf{k}_i \cdot (\underline{R} - \underline{R}')} G_i(\underline{R} - \underline{R}', \omega) d^3 \underline{R}' \quad (66)$$

Three-dimensional Fourier transformation and integration with respect to \underline{R} yields

$$\frac{j}{\pi} \int_0^{\infty} \frac{1}{k^2 F(\omega)} \tilde{\theta}_H(\underline{K} + \underline{k}_i, \omega) dk = \tilde{\theta}(\underline{K}) I(\underline{K}, \theta_i) \quad (67)$$

with

$$I(\underline{K}, \theta_i) = \int_0^{\infty} \frac{1}{k^2} \delta(|\underline{K} + \underline{k}_i| - k) dk \quad (68)$$

The latter integral can be carried out explicitly with the aid of distributional analysis [10]:

$$I(\underline{K}, \hat{\theta}_i) = \frac{2}{K^2} u(-\underline{K} \cdot \hat{\underline{k}}_i). \quad (69)$$

Therefore

$$\tilde{0}(\underline{K}) u(-\underline{K} \cdot \hat{\underline{k}}_i) = \frac{j}{2\pi} \int_0^{\infty} \frac{K^2}{k^2 F(\omega)} \tilde{\theta}_H(\underline{K} + \underline{k}_i, \omega) dk. \quad (70)$$

The right-hand side of this equation can be manipulated if we recognize that $\tilde{\theta}_H(\underline{K}, \omega)$ satisfies the Fourier transformed homogeneous wave equation

$$(K^2 - k^2) \tilde{\theta}_H(\underline{K}, \omega) = 0. \quad (71)$$

Hence

$$\frac{K^2}{2k} \tilde{\theta}_H(\underline{K} + \underline{k}_i, \omega) = (-\underline{K} \cdot \hat{\underline{k}}_i) \tilde{\theta}_H(\underline{K} + \underline{k}_i, \omega) \quad (72)$$

Insertion into (70) yields in the spatial domain

$$\frac{1}{(2\pi)^3} \int_{-\infty}^{+\infty} \int_{-\infty}^{+\infty} \int_{-\infty}^{+\infty} \tilde{0}(\underline{K}) u(-\underline{K} \cdot \hat{\underline{k}}_i) e^{j\underline{K} \cdot \underline{R}} d^3\underline{K} = -\frac{1}{\pi} \int_0^{\infty} \frac{1}{k^2 F(\omega)} \hat{\underline{k}}_i \cdot \nabla \left[\theta_H(\underline{R}, \omega) e^{-j\underline{k}_i \cdot \underline{R}} \right] dk \quad (73)$$

With the same arguments, which lead from (36) to (40) we find

$$0(\underline{R}) = -\frac{2}{\pi} \text{Re} \int_0^{\infty} \frac{1}{k^2 F(\omega)} \hat{\underline{k}}_i \cdot \nabla \left[\theta_H(\underline{R}, \omega) e^{-j\underline{k}_i \cdot \underline{R}} \right] dk \quad (74)$$

Equ. (74) is an exact inverse scattering identity provided the weak scatterer approximation holds; it can be considered as a generalized filtered backpropagation algorithm.

As previously in our investigations, further manipulation of the k -integral yields a time domain target classification scheme, which represents a generalization of far-field time domain backprojection. Proceeding similarly as in the derivation of equ. (54) we obtain

$$0(\underline{R}) = -2c \hat{\underline{k}}_i \cdot \nabla \theta_H^R(\underline{R}, t = \frac{\underline{k}_i \cdot \underline{R}}{c}) \quad (75)$$

where the upper index "R" stands for "ramp response": instead of deconvolving the time domain generalized holographic field $\theta_H(\underline{R}, t)$ with $k^2 F(\omega)$, we have specially chosen

$$F(\omega) = \text{pf} \frac{1}{\omega^2} \quad (76)$$

which is the spectral Fourier transform of the twosided ramp function

$$f(t) = \frac{|t|}{2} \quad (77)$$

Evaluating the normal derivative of the complex conjugate of the Greer's function in the definition (61) of the generalized holographic field, we obtain

$$\begin{aligned} \theta_H^R(\underline{R}, \omega) = \frac{1}{4\pi} \oint_{S_M} \left[\frac{e^{j\underline{k} \cdot \underline{R}}}{|\underline{R} - \underline{R}'|} - \frac{j\underline{k} \cdot \underline{R}}{|\underline{R} - \underline{R}'|^2} \right] \frac{e^{-j\underline{k} \cdot \underline{R}'}}{|\underline{R} - \underline{R}'|} \frac{n' \cdot (\underline{R} - \underline{R}')}{|\underline{R} - \underline{R}'|^2} \\ + \frac{e^{-j\underline{k} \cdot \underline{R}'}}{|\underline{R} - \underline{R}'|} \frac{n' \cdot (\underline{R} - \underline{R}')}{|\underline{R} - \underline{R}'|^2} \left[\frac{e^{j\underline{k} \cdot \underline{R}}}{|\underline{R} - \underline{R}'|} - \frac{j\underline{k} \cdot \underline{R}}{|\underline{R} - \underline{R}'|^2} \right] dS' \end{aligned} \quad (78)$$

and, hence,

$$\begin{aligned}
 \phi_H^R(\underline{R}, t) &= \frac{1}{4\pi} \oint_{S_M} \left[\frac{\phi_{S, \partial n'}^R(\underline{R}', \theta_i, t + \frac{|\underline{R} - \underline{R}'|}{c})}{|\underline{R} - \underline{R}'|} \right. \\
 &\quad \left. - \frac{\partial \phi_{S, \partial t}^R(\underline{R}', \theta_i, t + \frac{|\underline{R} - \underline{R}'|}{c})}{c|\underline{R} - \underline{R}'|} \right] \frac{n' \cdot (\underline{R} - \underline{R}')}{|\underline{R} - \underline{R}'|^2} \\
 &\quad \left. \right] dS'
 \end{aligned} \tag{79}$$

where, as it is usually understood, the partial derivatives $\partial/\partial n'$ and $\partial/\partial t$ operate on the ramp response scattered field in the time domain before insertion of the retarded time $t + |\underline{R} - \underline{R}'|/c$.

The interpretation of equ. (75) together with (79) is as follows: suppose, a time domain bistatic scattering "experiment" has been made with a weak scatterer, where the incident field is prescribed as plane wave with a twosided ramp function time dependence (which, of course is not available for practical applications): on a closed surface surrounding the scatterer completely, the scattered field, its time derivative and its normal derivative have to be measured as function of time t yielding a three-dimensional triple data field depending on two (primed) spatial variables, say τ_1, τ_2 and the time variable t . Every point in this triple data field for fixed τ_1, τ_2 and varying t_0 has then to be backpropagated, i.e. distributed on a surface given by image points \underline{R} , which satisfy the equation

$$ct_0 = \hat{k}_i \cdot \underline{R} + |\underline{R} - \underline{R}'| \tag{80}$$

where this distribution involves appropriate amplitude normalization. Obviously, equ. (80) is the desired generalization of (55) as proposed in (56) (notice, that the role of \underline{R} and \underline{R}' has been interchanged), whence the interpretation of (75) as a backpropagation instead of a backprojection scheme. The object function $\theta(\underline{R})$ is obtained after coherent superposition of time domain backpropagated data for all points τ_1, τ_2 and subsequent $\hat{k}_i \cdot \nabla$ -operation with regard to \underline{R} .

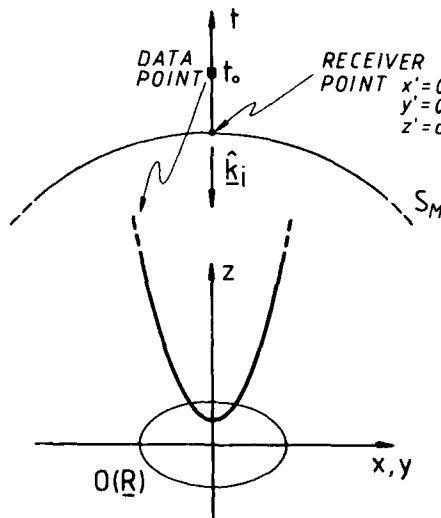


Fig. 7: Illustration of time domain backpropagation in the reflection mode, $\theta = ct_0 = d$

The backpropagation step is illustrated in Fig. 7 for a specific reflection mode experimental arrangement for a receiver point in backscattering direction.

Alternatively to the above time domain backpropagation processing procedure, one could keep the image point \underline{R} fixed and sum up all data points $t_0(\underline{R}, \underline{R}')$ for which equ. (80) holds for varying \underline{R}' .

The inverse scattering algorithm identified as generalized filtered backpropagation in the time domain can be considerably simplified if terms of the order $|\underline{R} - \underline{R}'|^2$ are neglected in the backpropagation integral (61), or (78), respectively. Evaluating the expression

$$\hat{k}_i \cdot v \left[\hat{\epsilon}_H(\underline{R}, \omega) e^{-jk_i \cdot \underline{R}} \right]$$

up to the same order, we obtain after some calculation

$$\begin{aligned} \hat{\epsilon}_H(\underline{R}, \omega) = & \frac{c}{2\pi^2} \operatorname{Re} \int_0^\infty \frac{e^{-jk_i \cdot \underline{R}}}{\omega^2 F(\omega)} d\omega \oint_{S_M} \left[jk \frac{\partial \hat{\epsilon}_S}{\partial n'} e^{-jk|\underline{R}-\underline{R}'|} + \right. \\ & \left. k^2 \hat{\epsilon}_S \frac{e^{-jk|\underline{R}-\underline{R}'|}}{|\underline{R}-\underline{R}'|} - \frac{\hat{n}' \cdot (\underline{R}-\underline{R}')}{|\underline{R}-\underline{R}'|^3} \right] \cdot \\ & \left[1 + \frac{\hat{k}_i \cdot (\underline{R}-\underline{R}')}{|\underline{R}-\underline{R}'|} \right] dS'. \end{aligned} \quad (81)$$

Apparently, equ. (81) can also be interpreted into the time domain; notice, that the ∇ -operation has been - approximately - transformed into jk - and k^2 -filters operating on the double data field $\hat{\epsilon}_S, \hat{\epsilon}_S'$ and $\hat{\epsilon}_S$, simultaneously with the deconvolution filter $\omega^2 F(\omega)$; obviously, these filters partly compensate each other.

Equ. (75) is an exact target classification equation for a bistatic (scalar) Synthetic Aperture Radar; every presently utilized algorithm implicitly relies on additional approximations, whose influence can now be judged against (75). One of the most straightforward approximations is to ignore the occurrence of the normal derivative of the data, which can be hardly measured; in fact, this is correct for planar measurement surfaces S , the corresponding algorithm is given in [10].

Inversion via time domain backpropagation is a generalization of the filtered backprojection Radon transform inversion to diffracted waves, which do not yield simple projections of a target. What we are still missing is the \underline{k} -space processing counterpart; we will briefly comment on that in the following.

B. INVERSION VIA \underline{k} -SPACE

As in conventional computerized tomography let us assume that the measurement surface is a plane (in three spatial dimensions), which coincides with the xy plane of a cartesian coordinate system at some distance $z = d > 0$ from the origin. Therefore, taking the two-dimensional Fourier transform of $\hat{\epsilon}_S$ according to equ. (16) with respect to x and y yields

$$\hat{\epsilon}_S(K_x, K_y, z, \omega) = \frac{1}{2} \int_{-\infty}^{\infty} \hat{q}_c(K_x, K_y, z', \omega) e^{-j|z-z'|\sqrt{k^2 - K_x^2 - K_y^2}} dz' \quad (82)$$

we have $|z-z'| = |d-z'| = d-z'$ on behalf of the bounded support of the scatterer, which is assumed to reside in the half-space $z \leq d$, and therefore

$$\hat{\epsilon}_S(K_x, K_y, d, \omega) = \frac{1}{2} \frac{e^{-jd\sqrt{k^2 - K_x^2 - K_y^2}}}{\sqrt{k^2 - K_x^2 - K_y^2}} \int_{-\infty}^{\infty} \hat{q}_c(K_x, K_y, z', \omega) e^{jz'\sqrt{k^2 - K_x^2 - K_y^2}} dz' \quad (83)$$

The integral in (83) can be considered as the one-dimensional Fourier integral of $\hat{q}_c(K_x, K_y, z, \omega)$ with respect to z' evaluated for the corresponding Fourier variable

$K_z = \sqrt{k^2 - K_x^2 - K_y^2}$, where the positive sign has to be chosen to fulfill the radiation condition of the two-dimensional Fourier transform of the free space Green's function for $z \rightarrow \infty$. Hence

$$\hat{\epsilon}_S(K_x, K_y, d, \omega) = \frac{1}{2} \frac{e^{-jd\sqrt{k^2 - K_x^2 - K_y^2}}}{\sqrt{k^2 - K_x^2 - K_y^2}} \hat{q}_c(K_x, K_y, K_z = \sqrt{k^2 - K_x^2 - K_y^2}, \omega) \quad (84)$$

In order to utilize $\hat{\epsilon}_S(K_x, K_y, d, \omega)$ as input data to a three-dimensional inverse Fourier transform target classification scheme, we have to isolate \hat{q}_c on the right-hand side of equ. (84); the pertinent multiplication with $\exp(-jd\sqrt{k^2 - K_x^2 - K_y^2})$ requires confinement of K_x and K_y to values within the circle $K_x^2 + K_y^2 \leq k^2$, i.e. neglect of the evanescent wave components in our data. We finally obtain

$$\begin{aligned} \bar{q}_c(k_x, k_y, k_z = \sqrt{k^2 - k_x^2 - k_y^2}, \omega) u(k^2 - k_x^2 - k_y^2) \\ \frac{2}{j} \sqrt{k^2 - k_x^2 - k_y^2} e^{-j d \sqrt{k^2 - k_x^2 - k_y^2}} \bar{f}_s(k_x, k_y, d, \omega) u(k^2 - k_x^2 - k_y^2) \end{aligned} \quad (85)$$

Equ. (85) relates three-dimensional Fourier spectra of equivalent sources on one Ewald-hemisphere to two-dimensional Fourier spectra of planar measured wavefields; it is obviously an inverse scattering extension of the Fourier Slice Theorem, whence the terminology Fourier Diffraction Slice Theorem (an extensive reference list is given in [10]). In our context, it is nothing but the Porter-Bojarski equation for planar measurement surfaces, therefore, in order to increase K-space coverage for varying frequency we have to introduce physical optics or weak scatterer approximations.

Apart from being a data processing alternative to time domain backpropagation, equ. (85) can serve as a tool to estimate spatial resolution associated with prescribed experimental parameters, say aperture width, frequency bandwidth and angle of illumination. A certain number of possibilities is discussed in [10], where the interested reader can also find the monostatic counterpart to equ. (85).

REFERENCES

- [1] J.A. Stratton: *Electromagnetic Theory*, McGraw Hill, New York 1941.
- [2] R. Mittra (Ed.): *Computer Techniques for Electromagnetics*, Pergamon Press, Oxford 1973.
- [3] V. Stein, M. Morgan: *Theoretical aspects of target classification: numerical modelling*, These Lecture Series.
- [4] W.-M. Boerner et al. (Eds.): *Inverse Methods in Electromagnetic Imaging*, D. Reidel Publ. Comp., Dordrecht 1985.
- [5] W.-M. Boerner, A. Kostinski: *A critical review of polarimetric theory and its application to high resolution polarimetric radar imaging*, Kleinheubacher Berichte 29 (1986) 189.
- [6] N.N. Bojarski: *A survey of the near-field far-field inverse scattering inverse source integral equation*, IEEE Trans. Ant. Propagat. AP-30 (1982) 975.
- [7] N. Bleistein: *Mathematical Methods for Wave Phenomena*, Academic Press, Orlando 1984.
- [8] N.N. Bojarski: *A survey of the physical optics inverse scattering identity*, IEEE Trans. Ant. Propagat. AP-30 (1982) 980.
- [9] N. Bleistein: *Physical optics far field inverse scattering in the time domain*, J. Acoust. Soc. Am. 60 (1976) 1249.
- [10] K.J. Langenberg: *Applied Inverse Problems*, Report TW 860 144 of the Fraunhofer Institute for Nondestructive Testing, Saarbrücken 1986.
- [11] A. Rosenfeld, A.C. Kak: *Digital Picture Processing*, Academic Press, Orlando 1982.
- [12] W.-M. Boerner, C.-M. Ho, B.-Y. Foo: *Use of Radon's projection theory in electromagnetic inverse scattering*, IEEE Trans. Ant. Propagat. AP 29 (1981) 336.
- [13] J.O. Young: *Radar imaging from ramp response signatures*, IEEE Trans. Ant. Propagat. AP 24 (1976) 276.
- [14] R.P. Porter: *Diffraction limited scalar image formation with holograms of arbitrary shape*, J. Opt. Soc. Am. 60 (1970) 1051.
- [15] N.N. Bojarski: *Exact inverse scattering theory*, Radio Science 16 (1981) 1025.
- [16] R.P. Porter, A.J. Devaney: *Generalized holography and computational solutions to inverse source problems*, J. Opt. Soc. Am. 72 (1982) 1707.
- [17] W.R. Stone: *The inverse medium (or inhomogeneous medium remote probing) problem and a closed-form inverse scattering solution to the medium synthesis problem*, Radio Science 16 (1981) 1029.
- [18] A.J. Devaney, G.C. Sherman: *Nonuniqueness in inverse source and scattering problems*, IEEE Trans. Ant. Propagat. AP 30 (1982) 1034.
- [19] A.J. Devaney: *Nonuniqueness in the inverse scattering problems*, J. Math. Phys. 19 (1978) 1526.
- [20] A.J. Devaney: *Fundamental limitations in inverse source and scattering problems in NDE*, In: *Review of Progress of Quantitative NDE*, Vol. 5 (Eds.: D.O. Thompson, D.E. Chimenti), Plenum Press, New York 1986.

ACKNOWLEDGEMENTS

This work has been financially supported by the Stiftung Volkswagen Werk.

PARAMETRIZATION
IN
SCATTERING MODELS

D.G. Dudley
Director, Electromagnetics Laboratory
ECE, Bldg. 104
The University of Arizona
Tucson, AZ 85721
USA

AD-P005 650

SUMMARY

We discuss parametric modeling in transient wave scattering. We review global modeling based on the body resonances of the scattering object and give two examples. We explore the nature of the incompleteness of global models and introduce the concept of the local model, based on ray-optic methods. We include an example of local modeling. We show that the local model is an order of magnitude more parsimonious and more robust in the presence of noise, compared to the global model. We conclude with a discussion indicating that the local model has a better probability of success in practical target classification because of its performance in a noisy environment.

1. INTRODUCTION

Scattering problems in many areas of applied physics are governed by the wave equation. In the usual situation, we are given the incident wave (input) and the scatterer(s) and attempt, through analytical, experimental, or numerical methods, to produce the scattered waves (output). Such procedures can be carried out in either the time or frequency domains and are categorized under the general heading of "forward problems." In a less usual, but no less important situation, we are given the incident wave (input) and the scattered waves (output) and attempt to find the scatterer(s) that produced the output. In this case, we call the procedures "inverse problems." Unfortunately, there are few inverse problems that can be solved exactly [1]. Recently, however, there has been attention to a class of inverse problems, solved by approximation techniques, with the potential for application to practical target classification. In this situation, we are given the incident wave (input) and the scattered waves (output), and attempt to find parameters that describe the scatterer(s). We call such procedures "parametric inverse" methods [2].

In this paper, we describe the parametric inverse problem and discuss the present state of affairs with regard to its solution and its application to target classification. We begin with a review of basic results from scattering theory. We next introduce a global model that has been the subject of intensive investigation in electromagnetics over the past decade. We include some results with simulated data that point out the capabilities and limitations of global modeling. We next introduce the concept of a local model and include a recent example. Finally, we discuss the possibilities of using global and local modeling in practical target classification. We conclude with a discussion of the present state of affairs in parametric inverse descriptions and suggestions for future work.

2. SCATTERING THEORY

Procedures in parametric inverse problems are based on the following fundamental result from mathematical scattering theory [3]: Given a scattering problem governed by the wave equation with Dirichlet boundary conditions, the scattered response to monochromatic plane wave excitation is, with mild mathematical restrictions, a meromorphic function of complex frequency. This result has been extended to the vector wave equation in electromagnetics [4] for scatterers upon whose surface the tangential electric field vanishes. By the Mittag-Leffler Theorem [5], the meromorphic property allows the scattered response $V(x,y,z,s)$, abbreviated $V(\mathbf{x},s)$, to be written as a sum over the complex body resonances of the scatterer plus an entire function of complex frequency s [2]. The inverse Laplace transform yields $v(\mathbf{x},t)$ in the form of a complex exponential series plus the inverse transform of the entire function, viz:

$$v(\mathbf{x},t) = R_1(\mathbf{x})\exp(s_1 t) + R_2(\mathbf{x})\exp(s_2 t) + \dots + w(\mathbf{x},t) \quad (1)$$

In (1), $v(\mathbf{x},t)$ is any component of the electric or magnetic field, s_n is the n -th complex resonance, and R_n is the residue at the n -th resonance. In addition, if $W(\mathbf{x},s)$ is the entire function, $w(\mathbf{x},t)$ is its inverse transform. Note that the residues are functions of position but the complex resonances are not. This fact is an indication that the complex s -plane locations of the natural resonances of the scattering object are not a function of how the body is illuminated or where the scattered response is measured. Their strengths (the residues), however, vary with position.

The formulation given by (1) is the cornerstone of the Singularity Expansion Method [6], discussed in detail elsewhere in this Lecture Series [7]. Two features are important to note. First, the entire function contribution $w(\mathbf{x},t)$ is time-limited to early

time [8,9]. Therefore, for times greater than the time of disappearance of the entire function, the scattering is given completely by the complex exponential series in (1). Second, whereas the complex series contribution is parametrized by the poles s_n and residues R_n , the entire function contribution is not parametrized at all [10]. Therefore, in any target identification scheme based on (1), there are parameters describing the target (body resonances) available in the complex exponential series. The entire function, however, yields no target information unless it can be further analysed.

3. GLOBAL MODELING

Despite the inadequate target description provided by (1), there has been some success in target classification based on the complex exponential series portion of (1). Since this series contains the body resonances of the scattering object, the technique we shall describe is a form of global modeling. (The distinctions between global and local target descriptions are discussed by Felsen elsewhere in this lecture series [11].) The basic ideas begin with some concepts in electromagnetic system identification [2,12]. Let a plane wave be incident on a scattering system from a given direction. In the absence of the scatterer(s), the time history $f(t)$ of the incident wave is recorded at a reference position $P(x)$. This time history, adjusted so that $t = 0$ corresponds to the initial arrival time of the pulse, is the single input to the system. With the scatterers in place, observations of the components of the vector field are made at p locations. Observation of a given component at a given location comprises one response (scalar) in a sequence of p responses. The time reference of each response is adjusted so that its turn-on time is $t = 0$. The incident pulse $f(t)$ defined above is then subtracted from each response to yield time histories $y^{(j)}(t)$, $j = 1, 2, \dots, p$, corresponding to components of the scattered field at different spatial locations. The p time histories are defined as the multiple output ports of the system. Define the electromagnetic system transfer function $H^{(j)}$ by

$$H^{(j)}(s) = Y^{(j)}(s) / F(s) \quad (2)$$

where $Y^{(j)}(s)$ and $F(s)$ are the Laplace transforms of the multiple outputs and single input, respectively. For a given value of the index j , the system transfer function represents one component of the electric or magnetic field at a given location. The electromagnetic system description in (2) is for a single-input, multiple-output (SIMO) system. For the case of single-input, single-output (SISO), we shall omit the superscripts and write

$$H(s) = Y(s) / F(s) \quad (3)$$

We now show that if we truncate the complex exponential series in (1) after N terms, the series is compatible with electromagnetic system ideas for both the SIMO and SISO cases. We shall concentrate on the SISO case. The extension to SIMO is trivial [2].

Because most analysis is done digitally, we shall consider discrete time formulations. Let $f(k)$ and $y(k)$, $k = 1, 2, \dots$, be the input to and output from, respectively, a SISO linear system. The notation $f(k)$ is the brief form for $f(kT_s)$, where T_s is the sampling interval. We model the system by the difference equation

$$Ay(k) = Bf(k) + e(k) \quad (4)$$

where $e(k)$ is an error term and A and B are polynomial stepping operators with, typically,

$$A = a_0 + a_1q^{-1} + \dots + a_Nq^{-N} \quad (5)$$

and where

$$q^{-1}f(k) = f(k-1) \quad (6)$$

The error term $e(k)$ is included to account for the usual case where the model fails to fit the data exactly. It is well known [13] that the Z-transform of (4) gives a transfer function $H(z)$ of the form $H(z) = Y(z) / F(z)$, plus an error term. A subsequent inverse Z-transform yields

$$h(k) = R_1 \exp(s_1 k T) + \dots + R_N \exp(s_N k T) + e'(k) \quad (7)$$

where $e'(k)$ is an error term obtained from $e(k)$ in the difference equation [13]. Note that the solution to the difference equation is a finite length complex exponential series. We now compare the result in (7) with the result from scattering theory in (1). We can interpret (7) as a discrete time equivalent of (1) provided we lump the tail of the series and the entire function in (1) together as an error term. For the error to be small, both the tail and the entire function must be small. The tail can be made small by limiting the data to a restricted frequency range. In actual experiments, this limitation often happens naturally because of the bandwidth limitations on equipment. In any event, it can be forced by intelligent filtering. We emphasize that for times earlier than the disappearance of the entire function, it is not clear that the entire function contribution is small. Indeed, in early time, it often dominates the scattered signal.

The difference equation model in (4) is called the equation error model [14]. The

SISO electromagnetic system identification problem with equation error model can now be defined as follows: Given data on the single input $f(k)$ and single output $y(k)$, identify the difference equation coefficient sequences $\{a_k\}$ and $\{b_k\}$. Transform [13] the coefficient sequences into the pole sequence $\{s_k\}$ and the residue sequence $\{R_k\}$. Provided that the resonances obtained from the solution to the electromagnetic system identification problem can be interpreted as body resonances of the scatterer, we shall have arrived at a global modeling method for classification of the target.

The most usual method for obtaining an estimation of the pole and residue sequences [13,15] is to adjust the coefficients a_p and b_p in (4) to minimize the Euclidean norm of the error $e(k)$. This procedure is a linear least squares problem that has been quite popular in electromagnetics over the past decade [13,15-17]. Recently, we have been using the minimization of the equation error to produce initial values of the difference equation coefficients [18,19]. We then follow with the minimization of the norm of the error $e_o(k)$ in the following output error model:

$$y(k) = A^{-1}Bf(k) + e_o(k) \quad (8)$$

The estimation of parameters in (8) is a nonlinear least squares problem. We use the VAX/VMS interactive algorithm NLS [20], beginning with initial estimates obtained by solving (4). We shall discuss two examples utilizing simulated data.

4. GLOBAL MODELING EXAMPLES

As a first example of global modeling, consider an electromagnetic plane wave at normal incidence on a lossless dielectric slab (Fig. 1) of thickness d and dielectric constant ϵ_r . The slab is terminated by a perfect conductor at its back face ($z = -d$). Assume that the plane wave polarization is (E_x, H_y) . The details of the solution to this problem are well known [18,19] and will not be repeated here. What are important are the locations in the s -plane of the complex resonances and the two forms of solution for the electric field in Region 1. The complex resonances are located at the s -plane poles of the scattered field, and are given by

$$s_m = T^{-1}[\ln(R) + i\pi(2m + 1)], \quad m = 0, \pm 1, \dots \quad (9)$$

where R is the reflection coefficient at the front face ($z = 0$) under the condition that the slab is infinitely thick, and where

$$T = 2d / v \quad (10)$$

where v is the propagation velocity in the slab. For the two forms of solution, the first is ray-optic and the second is hybrid. For the ray-optic form, we obtain for the electric field in the time domain in Region 1

$$e_{x1}(z,t) = f(t) - Rf(t - 2z/c) - (1 - R^2)[R^0f(t - 2z/c - T) + R^1f(t - 2z/c - 2T) + \dots] \quad (11)$$

where $f(t)$ is the incident pulse and c is the speed of light. The terms on the right side of (11) can be described as follows: The first term is the incoming pulse; the second is the pulse reflected from the front face of the slab ($z = 0$); the remaining terms are successive reflections from the back face of the slab ($z = -d$). A significant feature of this solution form, provided that $f(t) = 0$ for $t < 0$, is that the successive terms in the solution can be truncated and still give the exact solution up to the time of the most recent reflection.

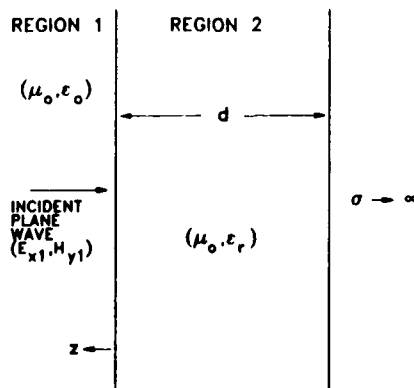


Fig. 1 - Dielectric slab backed by a perfect conductor.

For the hybrid solution form, we obtain

$$e_{x1}(z,t) = f(t) - Rf(t - 2z/c) - (1 - R^2)s(t - 2z/c - T) \quad (12)$$

where $s(t)$ consists of a complex exponential series plus any additional terms that might arise from s -plane singularities contained in the spectrum of the input pulse $f(t)$ [18]. Note that the first two terms in (12) are identical to the ray-optic case in (11). The remaining terms, however, are very different. Whereas each term in (11) represents the onset of a localized event, the terms in the complex exponential series are global. The representation is called "hybrid" because it consists of both local and global terms. To obtain the hybrid representation from the ray-optic, all terms with turn-on times greater than or equal to $2z/c + T$ must be combined and then re-separated in an entirely different form.

We shall now attempt a global target classification of the dielectric slab. All signal processing was done using the algorithm SIG [21]. All system identification was done using NLS [20]. For an input pulse, we choose the double exponential pulse

$$f(t) = Au(t)[\exp(-c_1t) - \exp(-c_2t)] \quad (13)$$

where $u(t)$ is the unit step function and A is a normalization constant selected so that the peak of the signal is unity. We have adjusted the parameters c_1 and c_2 to give a rise time (10 to 90 percent of peak) of 5 ns and a fall time (measured from $t = 0$ to the point where the pulse has decayed to $1/e$) of 30 ns ($c_1 = 7 \times 10^8$, $c_2 = 1.7 \times 10^8$). For slab parameters, we select $d = 10$ m and $\epsilon_r = 4$. We display the raw input data (Fig. 2) and the raw output data (Fig. 3) with 1024 points and a 1 ns sampling interval. We have used the ray-optic form of the solution to generate the output data. Since the information we seek (complex resonances) is contained in the scattered field, we subtract the incident pulse, the first term in (11), from the data. In addition, since information concerning the complex resonances is not available until after the arrival of the first return from the back face ($z = -d$), we subtract the reflection from the front face, the second term in (11). We remark that in practice, it is always possible to subtract the incident pulse. Subtraction of further early returns, in this case the front face reflection, is often impossible because of radiation damping. This is precisely the region where the entire function contribution is present. We emphasize that any such contributions will be modeled as if they were complex exponentials. Because of our ability to subtract these terms in our example, there are only complex resonance contributions in our synthetic data.

In the output data (Fig. 3), note the occurrence of successive events, caused by multiple reflections between the slab front and back faces. This onset of time-successive events is a prominent feature in electromagnetic scattering, where the external body resonances are caused by the mutual constructive and destructive interference of localized phenomena. A 4096 point discrete Fourier transform (DFT) of the output data (Fig. 4) shows the well-known low-pass characteristic of the double exponential pulse and the successive resonances of the slab. To enable identification with a parsimonious model, we low-pass filter (Butterworth, 8-th order) the input and output data at 50 MHz, thereby including seven resonances (seven complex pole pairs) in the pass band. We next decimate the data by 8:1 (down to 128 points) with the resulting input (Fig. 5) and output (Fig. 6) data at 1.25 times the Nyquist rate.

We apply the NLS algorithm to the decimated data, beginning with the initial selection of 24 poles and 24 zeros. After the algorithm converges, we use a model order

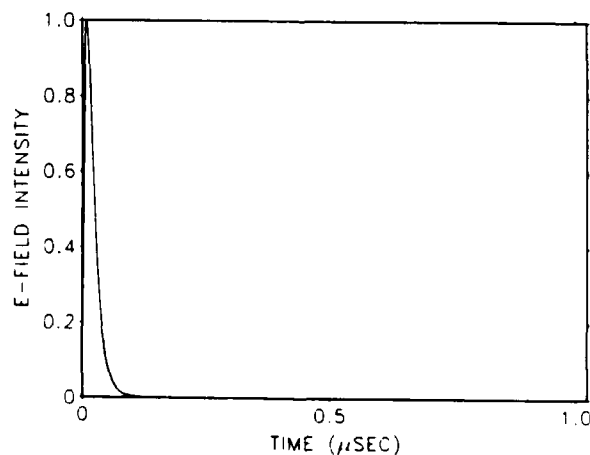


Fig. 2 - Incident field (input); 5 ns rise, 30 ns fall time; 1024 points; 1 ns sampling interval.

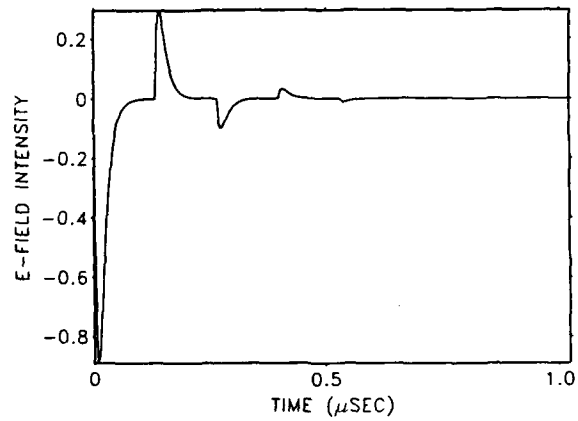


Fig. 3 - Scattered field (output); incident field and front face reflection removed; $d = 10\text{m}$; $\epsilon_r = 4$; 1024 points; 1 ns sampling interval.

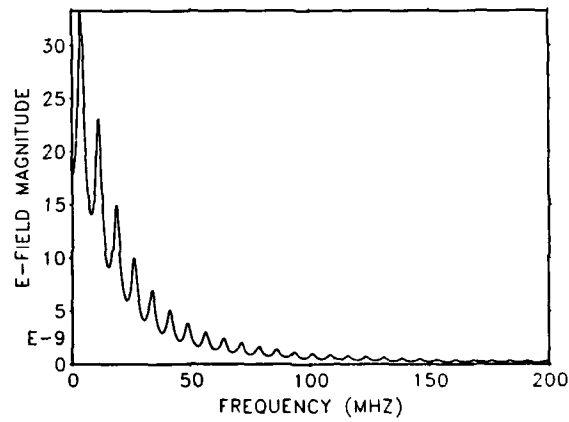


Fig. 4 - Discrete Fourier transform of output, zero-filled to 4096 points, showing low-pass characteristic of input and slab resonances.

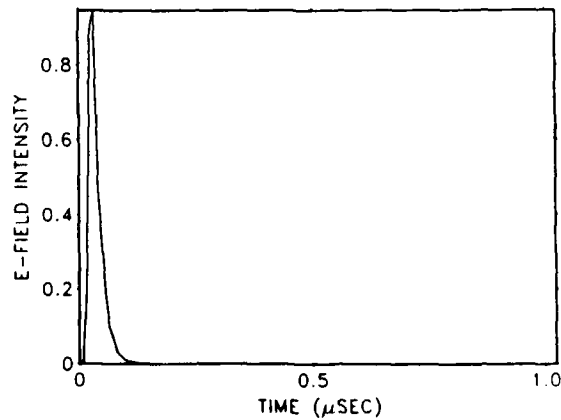


Fig. 5 - Input; low-pass filtered (8-th order Butterworth) at 50 MHz; decimated to 128 points; 8.055118 ns sampling interval.

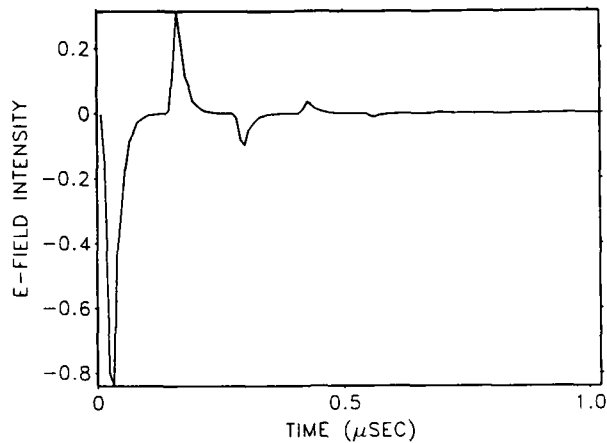


Fig. 6 - Output; low-pass filtered (8-th order Butterworth) at 50 MHz; decimated to 128 points; 8.055118 ns sampling interval.

reduction scheme [20] to eliminate six poles and produce an 18-th order model. We next use a partial fraction decomposition algorithm to compute poles and residues. The algorithm computes s-plane poles from z-plane results by the transformation

$$s = [\ln(z)] / T_s \quad (14)$$

This procedure gives nine pairs of identified poles which in Fig. 7 are compared with the theoretical ones computed from (9). Note that the poles compare closely until we go beyond the cutoff of the Butterworth filter (3.1416×10^8 rad/sec).

We remark that the above identification was done on data where the only noise is the roundoff error in the computer. The SIG package contains a Gaussian noise generator, which we use to add increasing amounts of noise to the output signal. As might be expected, the identification degenerates with increasing noise. We display the 5% noise case (Fig. 8). (By "five-percent," we mean that the noise standard deviation is 0.05 times the peak value.) Note the strong corruption, with successive reflections disappearing into the noise after the third reflection. We again filter at 50 MHz and decimate to 128 points. We begin the identification with a 32-nd order model with 32 zeros and then use the order reduction scheme to reduce the model order to 14. Our identified poles (Fig. 9) show good agreement with theory for the first two pole pairs. The next four pole pairs agree in frequency, but deviate in damping. This result is consistent with the deterioration of the resonances displayed in the DFT (Fig. 10) of the filtered and decimated data.

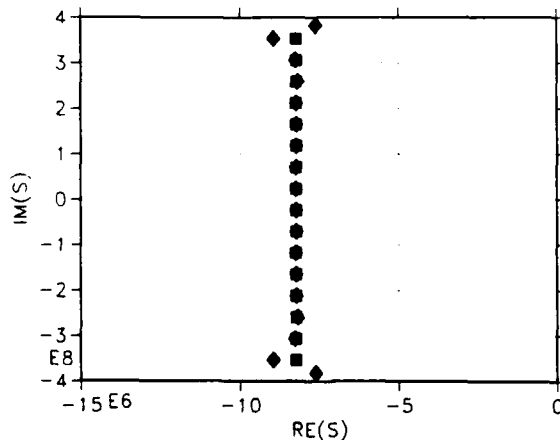


Fig. 7 - Identified poles (diamonds), 18-th order model; theoretical poles (squares).

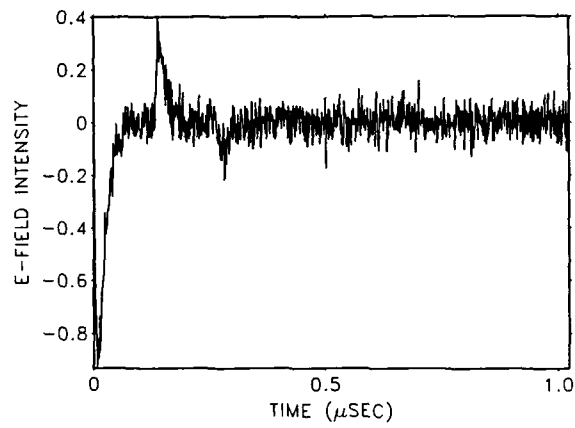


Fig. 8 - Output; 5 percent Gaussian noise; 1024 points; 1 ns sampling interval.

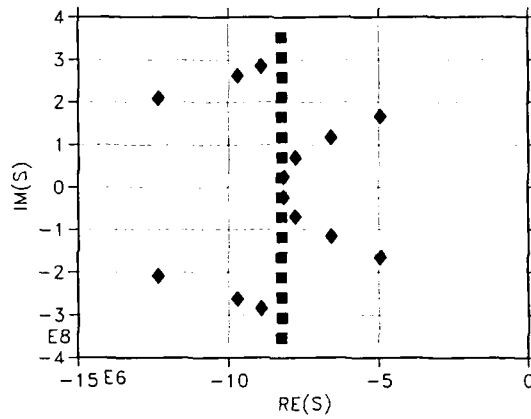


Fig. 9 - Identified poles (diamonds), 18-th order; 5 percent noise; theoretical poles (squares).

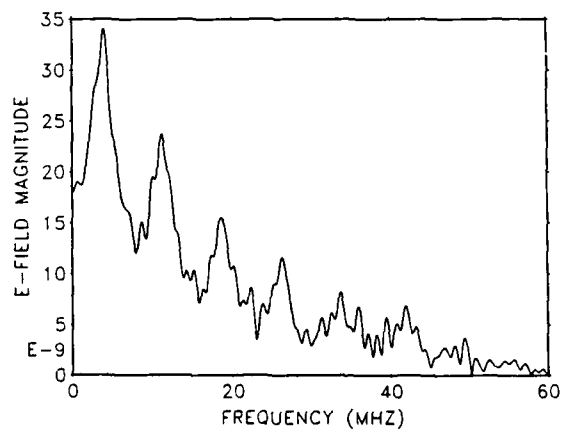


Fig. 10 - DFT of output; 5 percent noise; low-pass filtered (8-th order Butterworth) at 50 MHz; decimated to 128 points; 8.055118 ns sampling interval.

Although the above results give a positive indication of ability to apply a global modeling method to identify complex body resonances in the presence of small amounts of noise, considerable caution must be exercised in interpreting the results. In this example, the scattering has been given completely by the complex exponential series. In the example to follow, however, we must also deal with the presence of the entire function.

As a second example of global modeling [22], consider an acoustic plane wave incident in the $-z$ direction on a rigid sphere (Neumann boundary conditions) of radius $a = 1$ m (Fig. 11). We shall attempt to identify a subset of the complex resonances (Fig. 12). The s -plane locations are well known [23]. For an input signal, we choose $f(t)$ to be zero everywhere, except on the interval $0 < t < \pi/c_1$, where it is given by

$$f(t) = \sin(2\pi f_0 t) \sin^2 c_1 t \quad (15)$$

The input (Fig. 13, with $f_0 = 150$ Hz and $c_1 = 150$ rad/sec) vanishes after $t = 20.9$ msec and has the spectrum of a bandpass filter (Fig. 14). The center frequency corresponds to the $n=3$ pole (153.5 Hz) in the first layer of poles (Fig. 12). A relatively small number of poles either side of the $n=3$ pole are in the passband. We have found that the best results occur when we are required to identify from three to five pole pairs. Wider bandwidths drive up the order of the model required by NLS and make the identification more difficult. The choice of $c_1 = 150$ rad/sec corresponds to having four pole pairs in the passband.

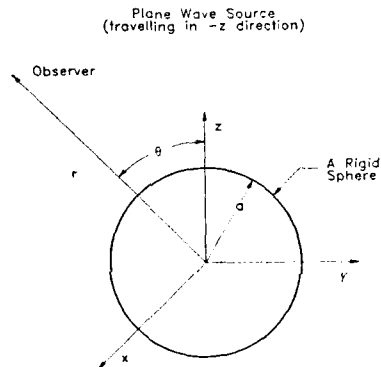


Fig. 11 - Sphere of radius $a = 1$ m illuminated by a $-z$ traveling plane wave.

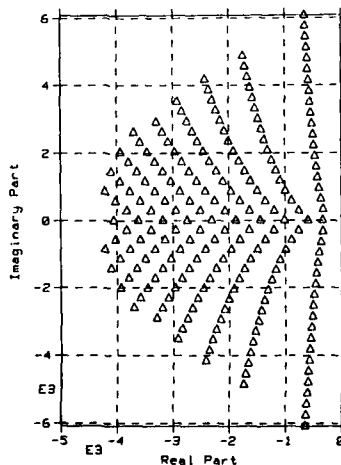


Fig. 12 - Theoretical pole locations in the s -plane for a sphere of unit radius.

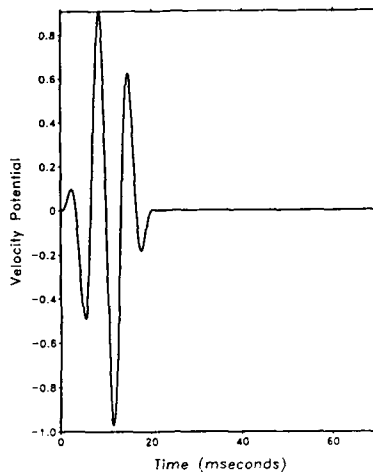


Fig. 13 - Input signal (zero after 20.9 msec).

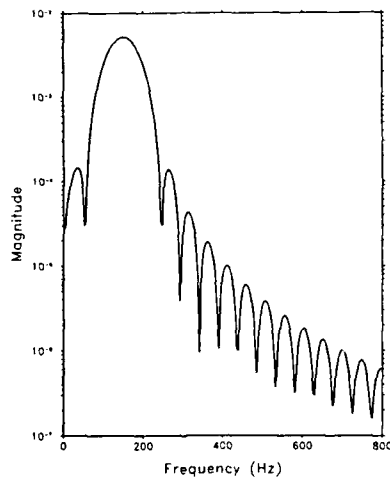


Fig. 14 - Spectrum of input (showing bandpass characteristic).

The scattered field (synthetic output data) was calculated in the frequency domain using the classic Mie series [24] with the spectrum of $f(t)$ as an input. The inverse transform was performed using a Filon method [25]. To determine the essential elements of the synthetic output data needed for accurate identification, we divide the synthetic output into three components: the reflection, the first creeping wave, and the second creeping wave. We display the reflection and the first creeping wave in Fig. 15, and the second creeping wave in Fig. 16. Note the change in scale for the second creeping wave. (It is too small to be visible on the previous figure.) In the figures, the reflection comes first. Its magnitude is much greater than that of the other components; it therefore contains most of the energy in the output. Following the reflection is the first creeping wave, which has made one excursion around the sphere before returning to the observer. As the wave travels around the sphere, it loses energy to radiation and arrives at the observer one-tenth the size of the reflection. Following the first creeping wave is the second creeping wave, which has made an additional excursion around the sphere, arriving at the observer $1/10000$ the size of the reflection. This smallness causes its retrieval from experimental data, even in a controlled

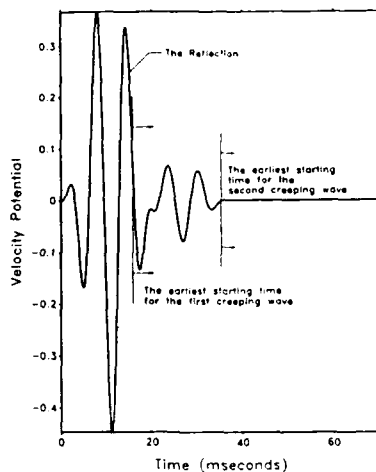


Fig. 15 - Synthetic output showing the reflection and first creeping wave.

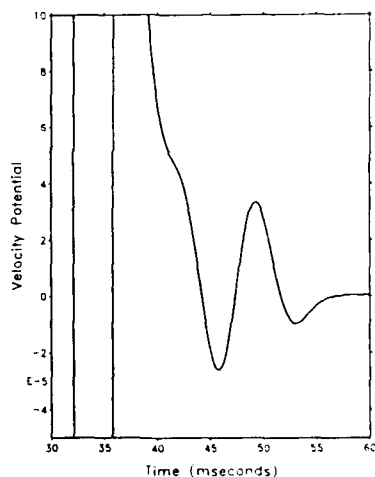


Fig. 16 - Synthetic output (enlarged scale) showing second creeping wave.

environment to be an exercise in frustration. This result is unfortunate because we are able to demonstrate that the second creeping wave is essential to the identification of the resonances.

There are important similarities and differences between the return from the sphere and the slab considered previously. In both cases, the complex resonances are produced from the mutual interaction among local events. In the case of the sphere, however, the radiation damping causes the local events (creeping waves) to disappear into the noise more quickly than in the case of the slab. In addition, the sphere data contains the entire function.

We have found little difficulty in identifying a limited number of pole pairs centered around the pole in center of the passband. To restrict the influence of higher order poles, we filter the input and the output with an 8-th order Butterworth filter. There are approximately four pole pairs in the passband. We next decimate the 1000 points in our data to 100 points thereby eliminating oversampling and reducing the

computational burden. We next use NLS to identify the coefficients in an equation error model. Finally, we obtain the poles and residues by partial fraction expansion.

We show (Fig. 17) the agreement between theoretical (triangles) and identified poles and a function of model order. The first layer of poles and the first two poles on the second layer are shown. Since the poles are in complex conjugate pairs, we display only the upper half plane. We find that the $n=1$ through $n=4$ poles are correctly identified. We note, however, that the order of the identification model must be greater than 24. High order models are required for two reasons. First, the scattered field consists of an infinite number of poles. Through filtering, we attempt to limit the number of poles, but filtering does not correspond to truncation. Second, we have failed to model the entire function, which contains a large percentage of the energy in the total signal. The difference equation model treats the entire function as a part of the complex exponential series thus driving up the order of the model.

We have performed many experiments on identification of sphere resonances. We find that our basic result above is unaltered if we remove the reflection portion of the output signal, provided that we do not destroy the time reference. If we remove the reflection and change the time reference, the identification collapses. A very important computer experimental result is associated with the second creeping wave. Although the second creeping wave is only one part in 10000, compared with the reflection, if we remove it from the output signal, the identification is unsuccessful. This result is an important limitation in complex resonance modeling of objects containing high radiation damping. As a final test, we added small amounts of noise to the data. Because of our earlier tests with the second creeping wave, we expected the noise to defeat the identification as soon as it overwhelmed the second creeping wave. This is in fact what occurred. If we select the variance of the noise such that the ratio of the peak of the spectrum to the average of the spectrum of the white noise is 70 db, we find that the noise is a few times larger than the creeping wave. In this case, the identified poles (Fig. 18) are in error by approximately 25% in attenuation. If we increase the noise to 60 db, the identification is defeated. This result is in agreement with the findings of Ksienski and Willis [26]. They found, using frequency domain methods, that similar amounts of noise defeated pole identification methods for the sphere in the electromagnetic case.

The sensitivity of the identification to small amounts of noise is a crucial defect in any attempt to use the method with real data. We emphasize that the model is incomplete since it ignores the entire function. The entire function occurs in early time where the reflection is the dominant portion of the scattered signal. In the next section, we shall show a local modeling method that models the reflection.

5. LOCAL MODELING

Our initial approach to obtaining a local model for scattering has been to use an asymptotic series solution to the wave equation [27]. Our goal has been to identify the local radius of curvature of a scatterer. In particular we have concentrated on acoustic scattering from the sphere, using the same input-output data as described above. We write the asymptotic series as follows:

$$Y(s) = [d_0 + d_1 s^{-1} + \dots] F(s) \quad (16)$$

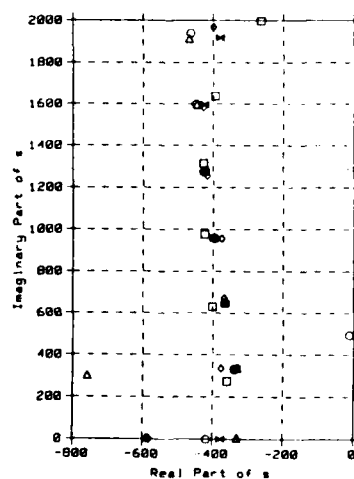


Fig. 17 - Theoretical poles (triangles) compared with identified poles; 20-th order (squares), 24-th order (diamonds), 26-th order (bowties), 28-th order (circles).

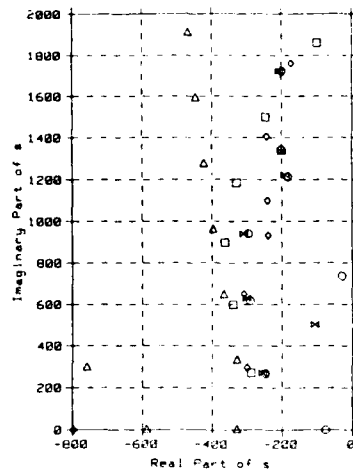


Fig. 18 - Theoretical poles (triangles) compared with identified poles; 20-th order (squares), 24-th order (diamonds), 26-th order (bowties), 29-th order (circles); 70 db signal-to-noise ratio.

where $F(s)$ and $Y(s)$ are the Laplace transforms of the input and output, respectively. The coefficients d_k , $k = 0, 1, \dots$, can be related to the radius a of the sphere. In particular [24],

$$a_0 = 2d_0 \quad (17)$$

$$a_2 = 5c^2 / 4d_2 \quad (18)$$

$$a_3^2 = 25c^3 / 8d_3 \quad (19)$$

where $c = 330$ m/sec. The subscripts on the a 's indicate different estimates of the radius a obtained from the different coefficients in (16). (There is no relationship between d_1 and the radius. For the acoustic sphere with Neumann boundary conditions, d_1 should be equal to unity [22].) Note that the successive terms in (16) imply, in the time domain, successive integrations of the input signal. We therefore adopt the following local model for our radius of curvature identification:

$$y(k) = d_0 f_1(k) + d_1 f_2(k) + \dots + e(k) \quad (20)$$

where k again refers to the kT_s time step and $e(k)$ is an error term. The sequence f_n represents successive integrations of the input, with $f_1 = f(t)$. The identification procedure is as follows: Given the input sequence $f(k)$ and output sequence $y(k)$, identify the coefficients d_n in (20) by minimizing the Euclidean norm of the error $e(k)$; then transform the estimates of the d_n into estimates of the radius by using (17) through (19).

We have done exhaustive tests using our algorithm to identify the radius of the sphere [27]. We include a sample of the results here. We use the same input signal as in the previous example, except that we vary the carrier frequency f_0 from 300 to 1500 Hz. We filter and decimate the input and output data and then plot the results for the radius as a function of f_0 . Actually we normalize the frequency to the radius and plot as a function of ka , where k is the wave number. In the results, when we refer to "model order" we mean the number of terms in the identification equation (20). We plot the results for the first order model in Fig. 19, for the second order model in Fig. 20 and Fig. 21, and for the third order model in Fig. 22 and Fig. 23. Since the radius is to be determined, we require the estimates of the radius to be relatively frequency independent for the identification technique to be practical.

The first order model has two terms (zeroth and first, Fig. 19) which give estimates that improve with increasing ka . (The known radius of the sphere is 1 m.) As previously noted, the first term provides no information on sphere radius, but should be equal to unity. At low ka the estimates are biased low; however, they still provide useful information since they are only 6.5% in error for the zeroth term and 10% in error for the first term.

The second order model has zeroth, first and second terms (Fig. 20 and Fig. 21). We note that the first term estimate of the second order model is identical to the first term estimate of the first order model. Indeed, we have proved [27] that as model order

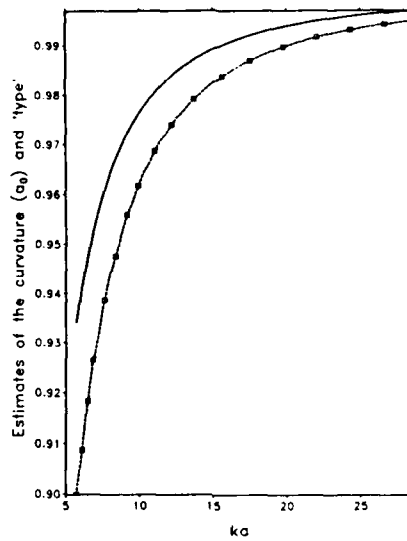


Fig. 19 - Least squares estimates of the zeroth (solid line) and first (dashed line) terms in the first order model versus ka .

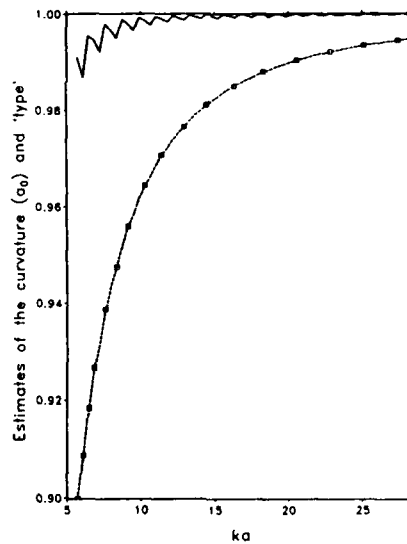


Fig. 20 - Least squares estimates of the zero (solid line) and first (dashed line) terms of the second order model versus ka .

is increased by one, only every other new estimate changes with respect to the previous order estimates. When the new order is odd, the odd terms change; when the new order is even, the even terms change. In this case, the zeroth term is within one percent of the correct value over the entire frequency range. Indeed, at carrier frequencies above $ka = 15$, the estimates are within .1%. The second term, however, gives poor estimates of the radius. The estimate is over 50% in error at low frequencies and 10% at the higher frequencies.

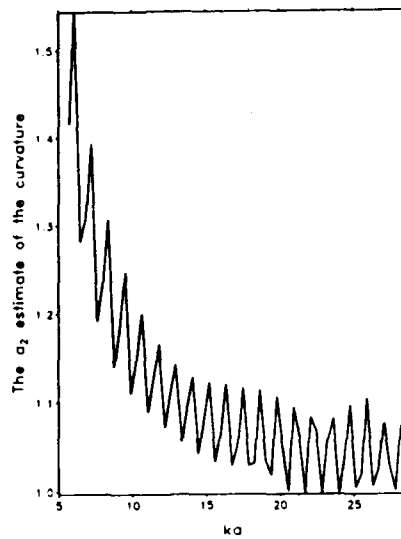


Fig. 21 - Least squares estimate of the second term in the second order model versus ka .

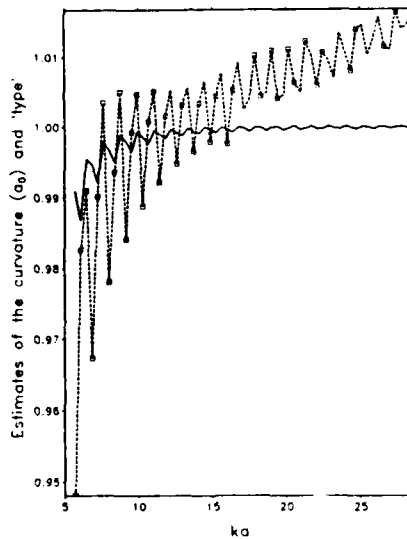


Fig. 22 - Least squares estimates of the zeroth (solid line) and first (dashed line) terms in the third order model versus ka .

For the third order model, the zeroth and second term estimates are the same as the previous model. The first term estimate (Fig. 22) at low frequencies has less bias than the first term in the second order model (5.5% versus 10% error). The estimate, however, no longer strictly improves with frequency. The third term (Fig. 23) fails to accurately estimate the radius. We emphasize that the magnitude of the third coefficient d_3 is 60 db down from the coefficient d_0 for $ka > 20$ (Fig. 24).

We have done detailed noise studies on our local modeling method. Our procedure has been to add noise to 200 pairs of input-output data. We then calculate estimates of the mean and variance of the identified radius. We have found that we can obtain estimates

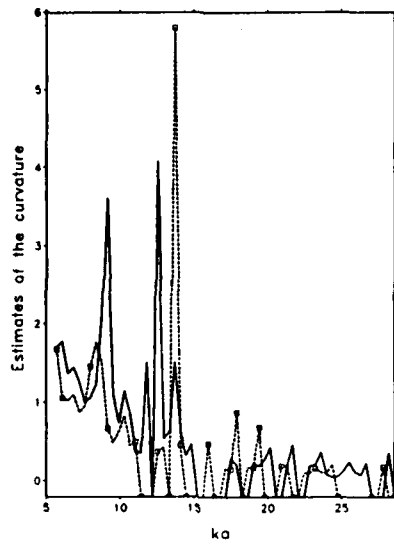


Fig. 23 - Least squares estimates of the second (solid line) and third (dashed line) terms in the third order model versus ka .

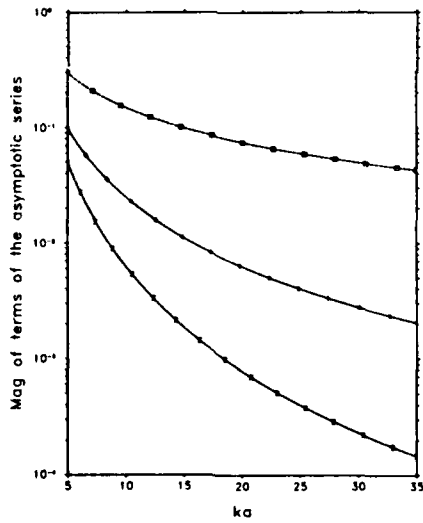


Fig. 24 - Magnitude of the first three terms in the asymptotic series versus ka ; each term normalized to d_0 ; first term marker with squares; second with diamonds; third with hourglasses.

that are within 1.5% of the no-noise case when the signal-to-noise ratio is 45 db. We note that in the global technique described previously, the identification failed completely at 60 db. The details are contained in [27].

6. DISCUSSION

We have shown examples of both global and local identification methods. The local

model has been motivated by the incompleteness of the parametrization in the global model. Indeed, we have shown [22] that the early time portion of the scattered return can be eliminated from consideration in the global model with negligible effect on the identification of the resonances. In the local model, however, we have shown that the early time portion plays a central role in overall target classification since it yields an asymptotic model describing local features.

There are two principal advantages to the local model. First, it is more robust in the presence of noise. Second, since it requires an order-of-magnitude lower model order, it is significantly more parsimonious [14]. Moreover, the estimation of parameters is more efficiently performed since the problem is linear least squares. These considerations lead us to speculate that, whereas the global resonance method is marginal with real data, the local model may prove to be a practical target classifier.

For immediate future work, we propose the investigation of objects with varying curvature. We favor using multiple data sets containing specular returns from different points on the scattering surface. Each data set might then provide an estimate of the local curvature at each point. There has been some work with multiple data sets in SIMO global modeling of the acoustic sphere [28]. The results showed some improvement in the robustness of identification of the resonances, but not enough to make it practical for real noisy data.

Finally, we believe that further efforts in complex resonance modeling should be minimized unless they are coupled with techniques that utilize the local information available in early time. This coupling of the two techniques might then lead to a truly hybrid target classification method.

REFERENCES

- [1] Habashy, T. and R. Mittra, Review of some inverse methods in electromagnetics, *J. Electromagnetic Waves and Applications*, 1987, to appear.
- [2] Dudley, D.G., A state-space formulation of transient electromagnetic scattering, *IEEE Trans. Antennas Propagat.* **AP-33**, 1985, 1127-1130.
- [3] Lax, P.D. and R.S. Phillips, *Scattering Theory*, New York, Academic Press, 1967.
- [4] Marin, L., Natural mode representation of transient scattered fields, *IEEE Trans. Antennas Propagat.* **AP-21**, 1973, 809-818.
- [5] Knopp, K., *Theory of Functions*, New York, Dover, 1947, Part II, Chapt. 2.
- [6] Baum, C.E., On the singularity expansion method for the solution of electromagnetic interaction problems, Air Force Weapons Laboratory, Albuquerque, Interaction Note **88**.
- [7] Morgan M.A. and E. Heyman, Singularity expansion method: target resonances, AGARD, Neuilly sur Seine, France, Lecture Series **152**, 1987.
- [8] Morgan, M.A., Singularity expansion representations of fields and currents in transient scattering, *IEEE Trans. Antennas Propagat.* **AP-32**, 1984, 466-473.
- [9] Pearson, L.W., A note on the representation of scattered fields as a singularity expansion, *IEEE Trans. Antennas Propagat.* **AP-32**, 1984, 520-524.
- [10] Dudley, D.G., Comments on SEM and the parametric inverse problem, *IEEE Trans. Antennas Propagat.* **AP-33**, 1985, 119-120.
- [11] Felsen, L.B., Spectral foundation for rays and modes: wavefronts and resonances, AGARD, Neuilly sur Seine, France, Lecture Series **152**, 1987.
- [12] Dudley, D.G., The parametric inverse problem in transient scattering, in *Review of Progress in Quantitative Nondestructive Evaluation*, D.O. Thompson and D.E. Chimenti (editors), New York, Plenum Press, 1986, 317-326.
- [13] Dudley, D.G., Parametric modeling of transient electromagnetic systems, *Radio Science* **14**, 1979, 387-396.
- [14] Ljung, L. and T. Soderstrom, *Theory and Practice of Recursive Identification*, Massachusetts, MIT Press, 1983, Chapt. 2.
- [15] Dudley, D.G., Parametric identification of transient electromagnetic systems, *Wave Motion* **2**, 1983, 369-384.
- [16] Van Blaricum, M.L. and R. Mittra, A technique for extracting the poles and residues of a system directly from its transient response, *IEEE Trans. Antennas Propagat.* **AP-23**, 1975, 777-781.
- [17] Moffitt, D.L. and R.F. Mains, Detection and discrimination of radar targets, *IEEE Trans. Antennas Propagat.* **AP-23**, 1975, 358-367.

- 71
- [18] Dudley, D.G. and D.M. Goodman, Transient identification and object classification, in Time-Domain Measurements in Electromagnetics, E.K. Miller (editor), New York, Van Nostrand Reinhold, 1986, 456-497.
 - [19] Goodman, D.M. and D.G. Dudley, An output error model and algorithm for electromagnetic system identification, Circuits, Systems and Signal Processing, 1987, in review.
 - [20] Goodman, D.M., NLS: a system identification package for transient signals, Lawrence Livermore National Laboratory Report UCRL-19767, 1983.
 - [21] Lager, D.L. and S.G. Azevedo, User's manual, SIG, a general-purpose signal processing program, Lawrence Livermore National Laboratory Report UCRL-19912, 1983.
 - [22] Weyker, R.R. and D.G. Dudley, Identification of the resonances of an acoustically rigid sphere, IEEE J. Oceanic Engineering, Special Issue on Scattering, 1987, to appear.
 - [23] Uberall, H., G.C. Gaunaurd, and J.D. Murphy, Acoustic surface wave pulse and the ringing of resonances, J. Acoust. Soc. Am. 72, 1982, 1014-1017.
 - [24] Bowman, J.J., T.B.A. Senior, and P.L.E. Uslenghi, Electromagnetic Scattering by Simple Shapes, Amsterdam, North Holland Publishing, 1969, Chapt. 10.
 - [25] Dudley, D.G., Numerical inversion of the Fourier transform: a combination trapezoidal and Filon technique, Lawrence Livermore National Laboratory Report UCRL-51878, 1975.
 - [26] Ksienski, D.A. and T.M. Willis, Numerical methods of noise reduction for frequency domain SEM, Electromagnetics 4, 1984, 393-405.
 - [27] Weyker, R.R. and D.G. Dudley, Asymptotic model-based identification of an acoustically rigid sphere, Wave Motion, 1987, to appear.
 - [28] Weyker, R.R., Resonance and asymptotic series based identification of an acoustically rigid sphere, Doctoral Dissertation, University of Arizona, 1986.

INPUT SIGNAL SHAPING: K-PULSE

Michael A. Morgan, Associate Professor, (Code 62Mo)
 Naval Postgraduate School, Monterey, CA 93943 USA

AD - P005651

SUMMARY

Classification of electromagnetic scatterers by selective mode annihilation is discussed. After providing a brief description of historical background, the conceptual basis of this methodology will be developed, followed by a theoretical explanation of the techniques that are employed. Some particular resonance annihilation schemes that have been implemented and tested, on a preliminary basis, are illustrated. Results from tests using synthetic signals, integral equation computations and experimental transient scattering measurements are featured.

HISTORICAL BACKGROUND

The concept of radar target identification by use of electromagnetic natural resonances was introduced in 1974 by Mains and Moffatt [1]. This idea, in turn, evolved from the earlier work of Baum at the Air Force Weapons Laboratory [2], who developed the formalism known as the Singularity Expansion Method (SEM) for use in the analysis of nuclear EMP vulnerability of strategic systems. Within the context of SEM, the response of a system can be represented as a weighted expansion using complex natural modes. These modes, which are self-sustaining in the absence of any excitation, are only functions of the structural geometry and composition of the scatterer and are independent of the incident excitation. The temporal variation of each mode pair has the form of an exponentially decaying sinusoid. In the Laplace transform domain this is represented by a pair of conjugate poles (natural resonances) in the left half complex plane. The knowledge of a finite subset of these poles for each potentially observable target can thus serve as an *aspect invariant* parameter set for unique identification.

Much of the initial work in utilizing natural resonances for non cooperative target recognition (NCTR) has been in the context of attempting to identify the "dominant" poles in the time domain scattering response of simple targets. These extracted poles are then correlated with a data base of computed natural resonances for candidate targets. Early efforts in this direction were "less than successful" and created much controversy within the electromagnetics basic research community concerning the validity of SEM. A theoretical study by Morgan, [3] and [4], has shown that the validity of the pole series expansion is restricted to the "late-time" portion of the scattering response which occurs *after* the incident field has completed its illumination of the target. As a result of this, the energy content of the usable late-time portion of the scattered signal is often a small percentage of that contained in the complete transient signature.

Early failures in demonstrating aspect-independent pole extractions resulted from attempts to process the entire scattered signal rather than just the undriven late-time portion. A recent endeavor by Van Blaricum [5] to identify poles in measured data, using the late-time signal, have met with success under the condition of relatively high signal to noise ratio (SNR of about 30 dB).

A new class of techniques has arisen for aspect-independent NCTR which is based upon the selective annihilation of resonances in the received scattered signal. These dynamically evolving methods are extensions of the original "K Pulse" concept proposed by Kennaugh [6]. Independent efforts by Morgan [7] and Chen [8] have shown that NCTR which is based upon the annihilation of natural resonances has two primary advantages vis a vis NCTR which utilizes pole extraction:

- (1) Successful identifications using SNR's of 10dB and lower
- (2) Orders of magnitude reduction in signal processing time in comparison to pole extraction methods

NATURAL RESONANCE SCATTERING

Consider the basic radar scattering scenario as depicted in Figure 1, where a time-limited pulse illuminates the radar target. The currents induced on the target reradiate a scattered field in all directions, a small portion of which is intercepted by the receiving antenna. As was shown in a previous paper in this publication, [4], the received echo signal will have the form

$$y(t) = y_E(t) [u(t) - u(t-T_0)] + y_L(t) u(t-T_0) + N(t) \quad (1)$$

Early-Time

Late-Time

Noise and Clutter

The early-time component of this signal is generated by directly driven (physical optics) currents as well as source-free currents which are located in the "wake" of the incident pulse, as it transits the object. The transitions from early to late-time signal

components are specified in Eq.(1) by the explicit use of unit step functions. In particular, the early-time signal will transition into the late time signal after

$$T_0 = T + 2D/c \text{ seconds} \quad (2)$$

where T is the incident pulse width, D is the dimension of the scatterer in the line-of-sight (LOS) direction of the radar and c is the velocity of light. A generic waveform, indicating the early and late-time nature of the received signal, is shown in Figure 2.

The results of [4] indicate that the late-time signal will be composed of a constant coefficient complex exponential series of the form

$$y_L(t) = \operatorname{Re} \left(\sum_{n=1}^{\infty} R_n \exp(s_n t) \right) = \sum_{n=1}^{\infty} A_n \exp(\sigma_n t) \cos(\omega_n t + \phi_n) \quad (3)$$

where the complex "poles" of the scatterer,

$$s_n = \sigma_n + j \omega_n \quad (4)$$

are innate functions of the shape and composition of the object and are independent of the aspect and polarization of the incident field. On the other hand, the complex "residues" of the expansion, $R_n = A_n \exp(j \phi_n)$, are highly dependent upon all properties of both the incident field and the scatterer. This dependence of the residues is such that for an essentially band-limited incident field there will typically be only a small finite subset of significant complex "modes" in the infinite series in Eq.(3). This effect is so strong, in fact, that some modes which are strongly excited at some aspects may vanish at other aspects. The damped cosine series form of the late time response in Eq.(3) results from combining conjugate pairs of terms in the series (ordered as $-n$ and $+n$). Complex values of poles and residues occur in conjugate pairs since the response to a real-valued excitation must also be real-valued.

The third component of the received signal is the "noise and clutter" which may be due to combinations of such pollutants as receiver system noise, antenna noise from external sources (both natural and man-made) and undesirable scatterers with propagation delays that are similar to that of the target. There are many possible sources of this clutter component, including colocated interfering targets, multipath scattering from low flying targets and returns through the antenna sidelobes from significant scatterers. In any case, the $N(t)$ is an undesirable element whose presence will increase the difficulty of implementing NCTR using natural resonance annihilation.

THE RESONANCE ANNIHILATION FILTERING CONCEPT

The resonance annihilation filter (RAF) concept for NCTR is depicted in Figures 3 and 4. As indicated in Figure 3, the output of the m th RAF will be a convolution of its impulse response, $k_m(t)$ with the input signal of Eq.(1),

$$z_m(t) = k_m(t) * \{ y_E(t) [u(t)-u(t-T_0)] + y_L(t) u(t) + N(t) \} \quad (5)$$

The decision process for NCTR is based upon selecting that target whose RAF in Figure 4 exhibits the minimum output signal energy in the "late-time" of $z_m(t)$. This late-time energy is defined as

$$E_m = \int_{T_L}^{\infty} z_m^2(t) dt \quad (6)$$

The late-time startup, T_L , must be large enough to exclude any significant contribution from the convolution with the early-time signal, which is not composed of simple aspect-independent modes. The RAF is designed to cancel a selected subset of the natural modes, which appear in their pure form only in the late-time. One way to guarantee that there will be no contribution to the energy in Eq.(6) from the early-time signal is to use finite impulse response (FIR) digital filters in the design of the RAF's. Such filters are nonrecursive (no feedback paths) and have impulse responses that are identically zero beyond some finite time, T_k , [9]. This would give $T_L > T_0 + T_k$ in Eq.(6).

Three primary design criteria for RAF's are:

- (1) The convolution of the RAF impulse response and the early-time echo signal should decay to an "insignificant" amplitude in as short a time beyond T_0 as is possible. This translates into minimizing the significant duration of the individual impulse responses.
- (2) The ratios of late-time energy for the "matched" target to that of all other targets should be minimized. This minimization should be made over a range of

pertinent aspect angles.

- (3) The RAF should be designed to minimize the transfer of the pollutant, $N(t)$ through the filter.

The reason for the demand in (1) is to allow a maximum usable late-time interval for computing the energy values in Eq.(6). This also assists in optimizing the energy ratios as discussed in the constraint (2). This first criterion will, however, conflict with that of (3) since effective noise filtering requires either signal integration, through recursive filter design (with feedback paths), or by use of extended feed-forward paths in an FIR filter design. In either case, there is a tradeoff of the effective RAF impulse response duration for enhanced noise and clutter suppression.

The whole process is also complicated by the effect on the design of the RAF's when there are uncertainties in the exact pole locations for each target class. This latter sensitivity may be a very real problem where there are several variations on the same type of target due, for instance, to alternate external fuel pod and weapon configurations. With variable wing angle the same target may even present a continuum of natural resonance sets.

It should also be mentioned that the original K-Pulse idea of Kennaugh, [6], accomplished the same objective as the RAF concept, except the transmitted pulse was to be designed to perform the annihilation of the natural resonances. This would require the transmission of one pulse for each candidate target, but otherwise is an equivalent idea to that of RAF.

FILTER EXAMPLES

We are now in a position to consider two initial generic RAF examples. The first of these RAF designs failed to provide consistently lower late-time energies for the matched target in our tests. As will be shown, this failure resulted from attempts to implement an analog signal processing strategy using digital techniques. The second form of RAF is based entirely upon digital signal processing methods and is shown to be successful using synthetic, integral equation and experimental data. Both of these RAF's are conceptually simple and do not rigorously address the constrained optimization problem which was posed in the previous section. They do, however, provide illustrations of the considerations that must be made and the pitfalls that may appear in even the most elementary implementation methods. Current efforts are underway towards developing RAF designs that more completely optimize the NCTR constraints.

The first RAF is based upon the use of differential operators to cancel individual natural modes. It follows from elementary calculus that the exponential modes in Eq.(3) of the form $y_n(t) = R_n \exp(s_n t)$ are each a solution of the appropriate first-order homogeneous differential equation¹

$$L_n \cdot y_n(t) = (d/dt - s_n) y_n(t) = 0 \quad (7)$$

where the operator, L_n , which cancels the n -th mode, is as defined. Using this simple result, it follows that multiple modes can be annihilated by the successive application (in any order) of the corresponding operators. For example, to eliminate the set of modes, $\{y_n(t)\}$ for $n = -N$ to $+N$ excluding $n=0$, requires the use of a $2N$ -order differential operator formed from the operator product of each L_n in the range indicated. The corresponding RAF impulse response, whose convolution the late-time signal in $y(t)$ will eliminate these same $2N$ modes, is simply $k(t) = L \cdot f(t)$, where L is the $2N$ th order operator and $f(t)$ is a smoothing function with continuous derivatives up to and including order $2N$. In such a case, it can be shown by way of either repeated integration by parts or via Parseval's Fourier transform theorem, that

$$k(t) * y(t) = f(t) * L \cdot y(t) \quad (8)$$

To implement this differential operator RAF, one may be tempted to make use of the digital Fast Fourier Transform (FFT), where $y(t)$ is transformed and then multiplied by the complex transfer function of the RAF. The analytical form of this transfer function can be obtained through Fourier transformation of $k(t)$,

$$K(\omega) = \{ (j\omega - s_1) (j\omega - s_1^*) \cdots (j\omega - s_N) (j\omega - s_N^*) \} F(\omega) \quad (9)$$

The $2N$ th order polynomial, which appears within the curly brackets, will tend to provide extreme high frequency noise amplification. The raison d'etre for $f(t)$ is thus seen to be its reduction of this effect through supplying appropriate high-frequency "compensation". This can be viewed in the time domain as a smoothing operation on the noise to reduce the effects of high order differentiations. A Gaussian shaped smoothing function,

$$f(t) = \exp[-a(t-t_0)^2] \quad (10)$$

allows the selection of "a" to provide optimum rolloff of $F(\cdot)$.

The second form of RAF is also based upon cancellation of the natural modes, but through the construction of appropriate "difference equations". Consider the conjugate-pair damped sinusoid representation of the late-time signal in Eq.(3). These individual modes are solutions to a three-point homogeneous difference equation of the form

$$A_n y[(p-1)\Delta t] + y[p\Delta t] + B_n y[(p+1)\Delta t] = 0 \quad (11)$$

where the sampling interval is Δt . The coefficients to cancel the n -th mode-pair are

$$\begin{cases} A_n \\ B_n \end{cases} = -0.5 \exp(\pm \sigma_n \Delta t) / \cos(\omega_n \Delta t) \quad (12)$$

where the + sign gives A_n while B_n is produced by the - sign in the exponential. The 3-point difference equation is easily synthesized using a nonrecursive digital FIR filter (also known as a transversal filter). To cancel N pole-pairs, a cascade of N such filters can be employed. By combining coefficients that multiply the same sample points, a simpler FIR filter can be generated which has a total of $2N$ delays. The difference equation that represents this new filter will have the form, [9],

$$z[p\Delta t] = \sum_{m=-N}^N C_m y[(p-m)\Delta t] \quad (13)$$

Of course, this filter is non-causal and could not be implemented for real-time operation without adding N additional delays in the design. For post-processing of acquired data, as was done in this effort, no such constraint on causality is needed and the filter can be used as is. As will be seen in the next section, this filter has the same type of high-frequency noise amplification as does the analog differential operator based filter. For noisy signals it will thus be necessary to perform additional smoothing on the input signal in the form of a low-pass filter.

RESULTS OF ANNIHILATION FILTERING

The initial tests on both methods were performed using a set of "synthetic" signals whose form in the late-time was that of a sum of damped sinusoids, as in Eq.(3). The early-time signal was set equal to

$$y_E(t) = A \sin^2(1.5\pi t / T_0) \quad (14)$$

where T_0 is the transition-time in Eq.(1). The upper half-plane complex poles and their corresponding residues are shown in Table 1.

Table 1 Synthetic Signal Poles and Residues

n	Poles	Residues	
		Magnitude	Phase
1	-0.10 + j 1.50	10.0	0
2	-0.19 + j 2.85	7.0	/2
3	-0.28 + j 4.20	5.0	0
4	-0.39 + j 5.85	3.0	
5	-0.46 + j 6.90	2.0	/2
6	-0.54 + j 8.10	1.0	0

These values were selected to follow the generic behavior of typical "layered" pole patterns of simple symmetrical objects such as wires and spheres. The constant "A", in the early-time, was selected to provide continuity of the waveform (but not the derivatives) at the transition time, T_0 . The 6 pole-pair synthetic signal is displayed in Figures 5 and 5, where Gaussian distributed random digital noise is added in the second case to provide a 10 dB average power SNR.

The testing of the analog-based RAF proceeded only to the the synthetic data level without noise, since consistently correct NCTR decisions could not be made using this filter type. The particular testing, which was duplicated for the digital FIR RAF with

excellent success, involved processing the synthetic signal using numerous versions of the respective RAF. These various RAF versions included an "exact" 6 pole-pair filter, as well as filters which cancelled the first 1, 2 and 4 pole-pairs of the signal. Additional RAF's included those with all (1,2,4 or 6) poles-pairs shifted in magnitude by 5% or 10%. These RAF's represented alternate "targets". The results of the tests for the analog-based RAF are displayed in Table 2., where the late-time signal energies are tabulated.

Table 2 Analog-Based RAF Late-Time Energy
(Noiseless Case)

	RAF Pole-Pairs			
	1	2	4	6
Exact	1.5E-2	6.04E-5	2.43E-9	6.38E-16
5% Shift	2.5E-2	1.50E-4	3.65E-9	3.29E-16
10% Shift	2.0E-1	1.49E-3	1.50E-8	6.94E-16

In following each vertical column, the "exact" RAF should ideally display the lowest output energy. The result in the last column and second row indicates that for the case of 6 pole-pair filters, the 5% displaced pole-pair RAF yields a smaller signal energy than does the exact RAF. The explanation for this error can be seen by looking at the output waveform for the N=6 exact RAF, as shown in Figure 7. Notice the non-zero late-time output signal for this "exact" case RAF. The reason for this late-time residue is the large high-frequency amplification of small round-off errors. To implement the differential equation approach, the discrete $K(\omega)$ is formed by using the formula in Eq.(8). This is then multiplied by the digital FFT of the sampled $y(t)$, followed by an inverse FFT to obtain the output waveform. Any errors in the FFT (in say the 14th decimal place) are amplified by the high-order (12-th order in this case) all-zero filter characteristic polynomial in $K(\omega)$. The source of this error has been confirmed by extensive tests involving additional cases not shown here. The end result is that an attempt to simulate very high-order analog differentiation using discrete FFT methods is wrought with seemingly insolvable problems brought on by extreme amplification of otherwise insignificant roundoff errors.

Turning now to the digital FIR realization of the RAF, the same test was repeated for both "clean" input data and for the case of a 10dB SNR noisy input signal, as shown in Figure 6. The unit sample response of the digital RAF, which uses the exact 6 pole-pairs, is shown in Figure 8, where the scale has been greatly expanded to show the initial 13 non-zero values. The output of this exact RAF, as shown in Figure 9, displays virtually zero late-time response. A summary of the test results is shown below in Table 3.

Table 3 Digital FIR RAF Late-Time Energy
(Noiseless Synthetic Signal Case)

	RAF Pole-Pairs			
	1	2	4	6
Exact	7.9E-24	2.16E-23	7.32E-23	1.17E-16
5% Shift	1.0E-3	5.95E-5	3.29E-5	9.90E-2
10% Shift	7.0E-3	3.09E-4	3.97E-4	1.55

At the T_c transition, a very large and rapid oscillation occurs. In fact, the level of this oscillation is so large that extensive "clipping" has been employed in the figure so that the late-time level can be seen. The reason for this behavior is the lack of any smoothing function being utilized for this noiseless case. At the T_c transition, the synthetic $y(t)$ has discontinuous derivatives, and these are amplified by the high-frequency asymptotic behavior of $K(\omega)$, which is shown in Figure 10. Since the proper RAF filter "exactly" cancels the matched late-time signal (without noise), there is no noticeable effect except in the vicinity of the discontinuous derivative transition region, having $2N+1$ points.

For the case of 10dB SNR, an additional Gaussian shaped smoothing function was used to reduce the high-frequency content of the additive noise. The output for the exact RAF is shown in Figure 11 and the late-time signal energies are contained in Table 4. Note, that with the smoothing function convolution, the large oscillation near T_c has disappeared. The improvement of performance accompanying the increase of RAF pole-pairs (up to the actual number contained in the processed signal) can be seen by comparing energy ratios in each column in Table 4.

Table 4 Digital FIR RAF Late-Time Energy
(10 dB SNR Synthetic Signal Case)

	RAF Pole-Pairs			
	1	2	4	6
Exact	630.4	2.80E-2	1.13E-4	6.43E-6
5% Shift	773.9	4.20E-2	2.86E-4	5.46E-5
10% Shift	940.9	6.20E-2	7.07E-4	1.99E-4

After validating the concept of digital RAF using synthetic signals, it was decided to progress to a simple electromagnetic scattering case where, both the complex pole values and the scattering response could be obtained to a high accuracy. The thin-wire was chosen because of its amenability to numerical scattering solutions and SEM analysis. Thin-wire scattering is depicted in Figure 12, where a Gaussian-shaped incident pulse, having a 10% pulse duration of 2 Nsec (where the pulse amplitude is greater than 10% of its 1 V/m maximum value), arrives at an angle of incidence, θ_i . The electric field has linear polarization which is parallel to the plane of incidence. The temporal waveform of the transient far-zone scattered field is computed in the the direction θ_s . Numerous combinations of θ_i and θ_s were considered for each of three wire "targets" having lengths, in meters, of 0.9, 1.0 and 1.1. The length to diameter ratio of each target was 100. A single RAF was constructed for each target and was then used for all incident and scattering angles to demonstrate its aspect independence.

A time-domain thin wire integral equation computer program was written, and extensively tested, following the method of Harrington and Sayre, [10]. An example scattered field waveform for the 1 meter thin-wire, with $\theta_i = \theta_s = 90$ degrees is shown in Figure 13. The magnitude of the associated frequency spectrum is displayed in Figure 14, where the resonant peaks are indicative of the presence of individual natural modes whose poles are in the first "layer" which is adjacent to the $j\omega$ axis. For the case of broadside 90 degree incidence, only the symmetric current modes having odd integer mode indices are excited. For other incident angles, the antisymmetric modes were also present. The abrupt spectral rolloff beyond the n=5 mode is due to that of the incident Gaussian shaped waveform.

Resonant filters which canceled the first seven pole pairs for each of the three thin-wires were implemented using the digital FIR design technique. The poles values were extrapolated from parameterized plots in the work of Tesche, [11], and are only accurate to about 3 decimal places. Example RAF outputs are displayed in Figure 15, for the case of 10 dB SNR waveform from the $L = 1$ m wire with $\theta_i = 90$ deg and $\theta_s = 45$ deg. The late-time energy results are summarized in Tables 5 and 6 for the respective cases of no additive noise and 10 dB additive noise. For the sake of brevity, these tables only display the results of RAF operations on the scattered waveforms from the $L = 1$ m wire. Equally good results were obtained in processing the waveforms from the other two wires in that the matched RAF consistently provided the lowest late-time signal energy, independent of bistatic aspects on the target. It should be noted that a more optimal "double-Gaussian" smoothing function was employed with the noisy data to reduce both high and low frequency noise content. This smoothing function is the sum of two collocated Gaussian functions having opposite polarity and different standard deviations. The constraint is that the function has zero area under its curve. The adjustment of the two different standard deviations allows tailoring of the frequency filtering characteristics at both the high and low range. As is apparent, consistently good identifications can be made even with a relatively low fidelity scattered signal in the case of a thin-wire.

Table 5 Digital FIR Late-Time Energy
(Noiseless Thin-Wire I.E. Case)

	90/90	Bistatic θ_i/θ_s (deg)		45/45
		90/45	45/135	
L = 0.9 m	4.24E-15	1.87E-15	1.33E-15	9.35E-16
L = 1.0 m	7.99E-18	3.00E-18	1.90E-18	2.04E-18
L = 1.1 m	1.30E-17	5.38E-18	3.74E-18	2.82E-18

Table 6 Digital FIR Late-Time Energy
(10 dB SNR Thin-Wire I.E. Case)

	90/90	Bistatic θ_i/θ_s (deg)		45/45
		90/45	45/135	
L = 0.9 m	.045	.018	.012	.014
L = 1.0 m	.019	.005	.005	.008
L = 1.1 m	.112	.055	.028	.038

The final evaluation of the RAF concept is through use of experimental broadside back-scattering signatures of copper wires having lengths of 9 cm, 10 cm and 11 cm with a common diameter of .24 cm. These measurements were performed using the Transient Electromagnetic Scattering Laboratory at the Naval Postgraduate School, which is described in a separate article within this publication as well as in a previous paper, [12], [13]. An example scattering signature and its corresponding spectral magnitude (for the L = 10cm wire) are respectively shown in Figures 16 and 17. The scattering responses are due to a double-Gaussian shaped excitation having zero mean. Because of the smoothing that was used in synthesizing the double-Gaussian response from the "raw data", it was not necessary to perform further smoothing. Based upon the spectral behavior of the responses, at most, only three significant pole-pairs are present in the data. These poles were estimated from the data in [11] in order to produce the RAFs. The measured broadside backscattering signatures of each of the three wires was then filtered by each of the three RAFs, with the late-time energy results being shown in Table 7. The consistently low energies provided by the proper RAFs appear as the diagonal values in this table. These results, although hardly comprehensive, are yet another indicator of the potential of this method for target identification.

Table 7 Digital FIR Late-Time Energy
(Measured Thin-Wire Broadside Backscatter)

RAF	Wire Length for Data		
	9 cm	10 cm	11 cm
L = 9 cm	2.53	12.92	53.95
L = 10 cm	15.88	2.89	10.97
L = 11 cm	41.07	17.31	3.79

CONCLUSION

A new class of "K-pulse" based aspect independent NCTR, which makes use of simple digital FIR filters, has been described and initially tested on a very limited basis using synthetic waveforms, integral equation computations and measured data. The original concept, which was based upon analog differential operator methods, was described and then shown to fail because of critical, although small, roundoff errors in the digital implementation.

Future work will involve several important investigations on further refinements and more comprehensive validations of the RAF method. One of the first orders of business will be to conduct a performance comparison with the alternate "E-pulse" method, which has been developed by Chen and others, [8]. This will be a cooperative effort which will seek to uncover the relative virtues of each method and address their possible integration. Another major quest, perhaps tied in with the first, will be in the development of systematic digital design methods to optimize the RAF performance for realistic cases of transient scattering. Such optimization will address several issues, including moderate and low "Q" target signatures, having more rapidly damped natural modes than that of thin-wires. An additional concern is the tradeoff of system bandwidth reduction for reduced decision reliability. This issue will be considered as part of a more general effort which seeks to quantify the expected error probabilities as a function of (1) signal center frequency and bandwidth, (2) SNR and (3) target ensemble. This latter consideration will be highly significant since a target ensemble which has elements whose dominant poles are close to those of other element(s) will be more difficult to consistently identify. This "selectivity" issue also has another aspect, where a single target type may have multiple configurations due to variable wing sweep and "stores", for example. The viability of the resonance annihilation method for real world NCTR may ultimately prove insufficient for stand-alone aspect independent identification. On the other hand, this late-time data set may be highly useful when augmented by aspect-dependent "imaging" methods, which primarily employ the early time signal.

REFERENCES

- [1] R.H. Mains and D.L. Moffatt, "Complex natural resonances of an object in detection and discrimination," TR-3424-1, Ohio State University, Electroscience Laboratory, Columbus, OH, June 1974.
- [2] C.E. Baum, "On the singularity expansion method for the solution of electromagnetic interaction problems," AFWL Interaction Note 88, Dec 11, 1971.
- [3] M.A. Morgan, "Singularity expansion representations for fields and currents in electromagnetic scattering," *IEEE Trans. on Antennas & Propagation*, Vol. AP 32, May 1984, pp. 466-473.
- [4] M.A. Morgan, "Singularity expansion method: Target resonances," *This Publication*

- [5] M.L. Van Blaricum, et al, "Radar target identification and characterization using natural resonance extraction," Final Report on ONR Contract N00014-82-C-0079, September 1984.
- [6] E.M. Kennaugh, "The K pulse concept," *IEEE Trans. on Antennas & Propagation*, Vol. AP-29, March 1981.
- [7] M.A. Morgan and J.B. Dunavin, "Discrimination of Scatterers using natural resonance annihilation," *Abstracts of 1986 National Radio Science Meeting*, Philadelphia, PA, June 1986.
- [8] K.M. Chen, et al, "Radar target discrimination by convolution of radar return with extinction-pulses and single-mode extraction signals," *IEEE Trans. on Antennas & Propagation*, Vol. AP-34, July 1986, pp. 896-904.
- [9] A.V. Oppenheim and R.W. Schaffer, *Digital Signal Processing*, Englewood Cliffs: Prentice-Hall, 1975, Chap. 5.
- [10] E.P. Sayre and R.F. Harrington, "Time-domain radiation and scattering by thin wires," *Applied Sci. Res.*, Vol. 26, pp. 413-444, 1972.
- [9] F.M. Tesche, "On the analysis of scattering and antenna problems using the singularity expansion technique," *IEEE Trans. on Antennas & Propagation*, Vol. AP-21, January 1973, pp. 53-62.
- [12] M.A. Morgan, "Time-domain scattering measurements," *IEEE Antennas & Propagation Newsletter*, Vol. 6, August 1984, pp. 5-9.
- [13] M.A. Morgan, "Experiments: Test Range Facilities", this publication.

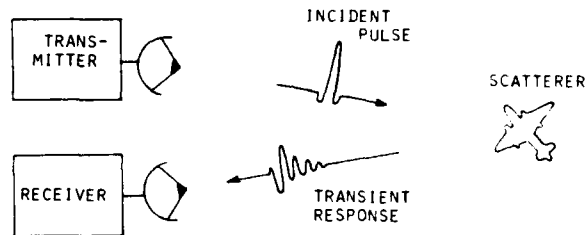


FIGURE 1 TRANSIENT RADAR SCATTERING

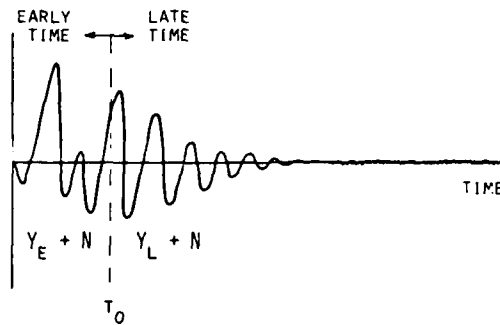


FIGURE 2 TRANSIENT SCATTERING SIGNATURE

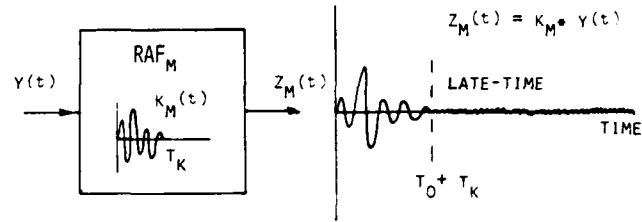


FIGURE 3 RESONANCE ANNIHILATION FILTERING

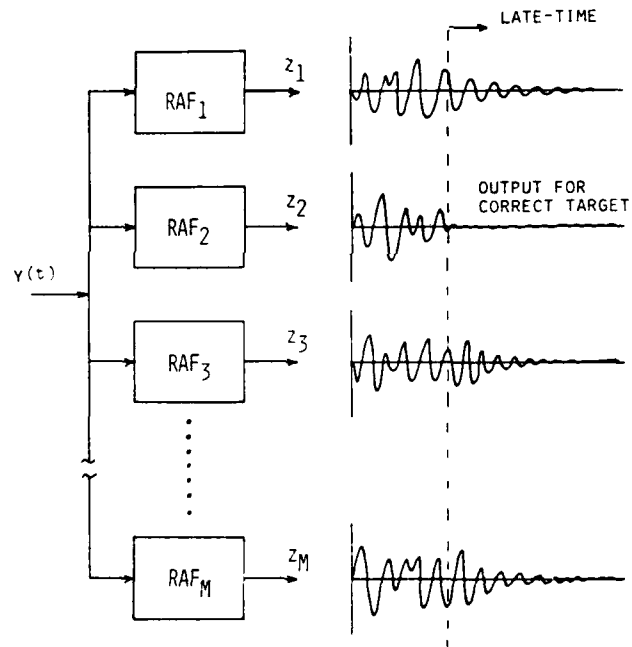


FIGURE 4 RAF IDENTIFICATION PROCESSING

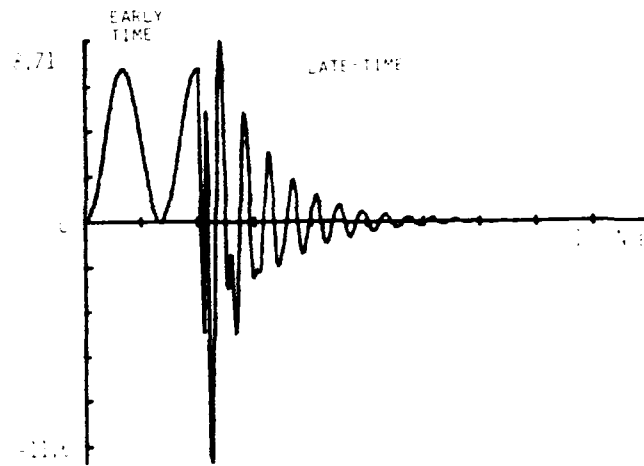


FIGURE 5 6 MODE SYNTHETIC WAVEFORM NO NOISE

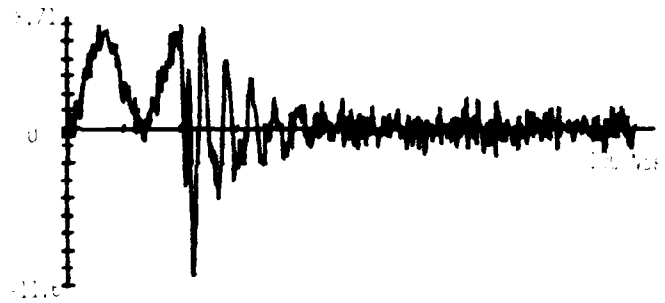


FIGURE 6 6 MODE SYNTHETIC WAVEFORM (10 dB SNR)

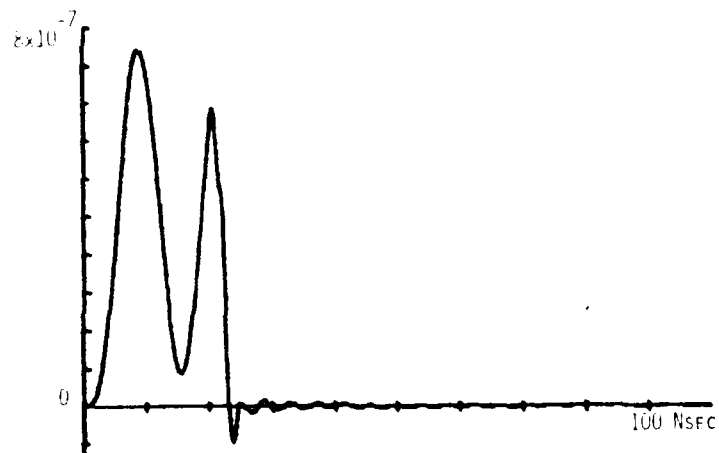


FIGURE 7 OUTPUT OF EXACT 6 MODE ANALOG RAF

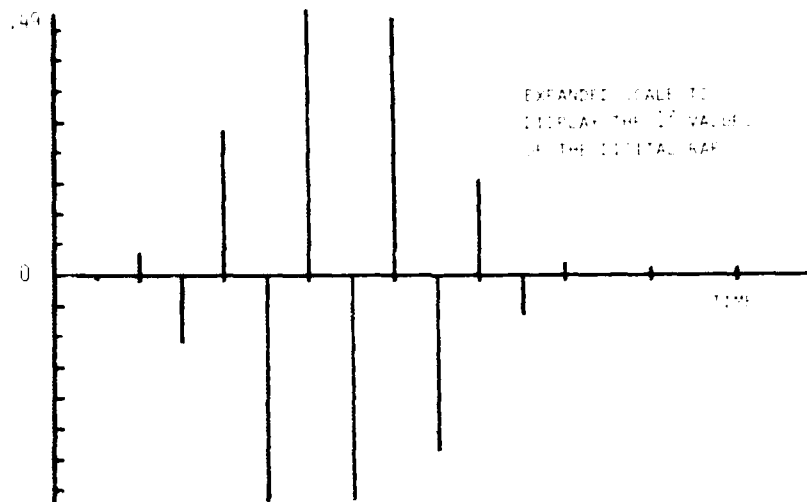


FIGURE 8 UNIT SAMPLE RESPONSE OF DIGITAL 6 MODE RAF

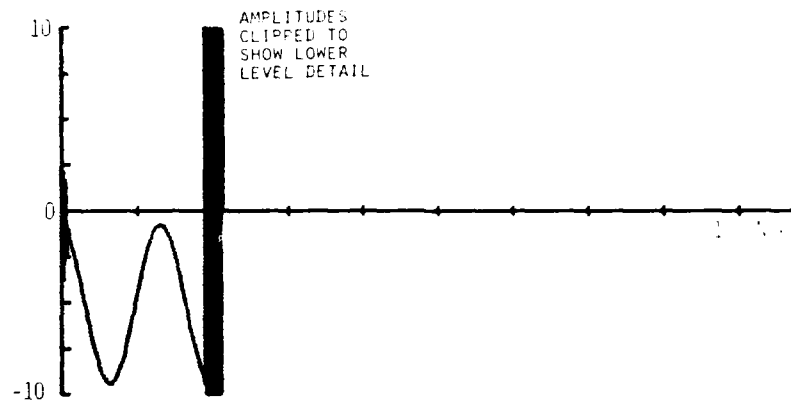


FIGURE 9 OUTPUT OF EXACT 6 MODE DIGITAL RAF (NO NOISE)

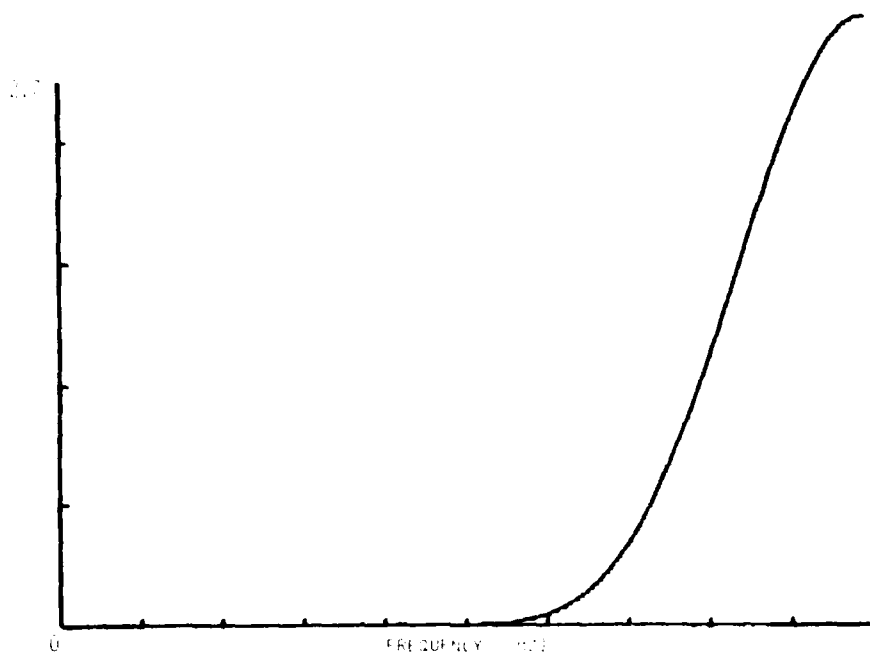


FIGURE 10 SPECTRAL MAGNITUDE OF DIGITAL 6 MODE RAF

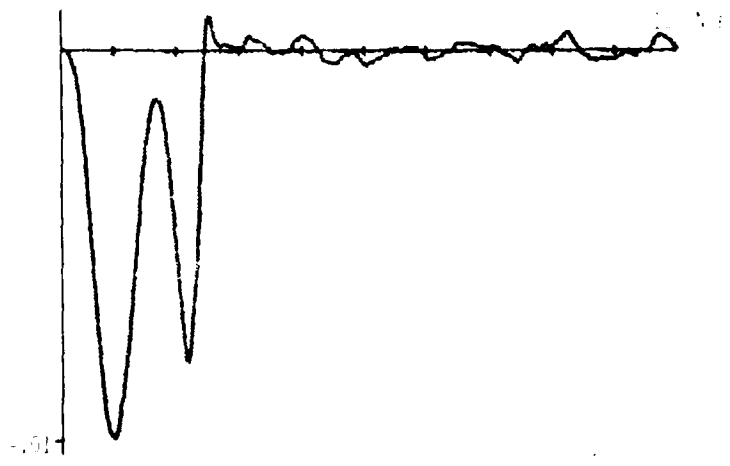


FIGURE 11 OUTPUT OF EXACT 6 MODE DIGITAL RAF (10 dB SNR)

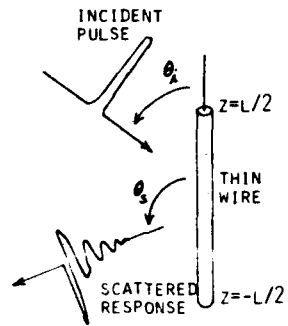
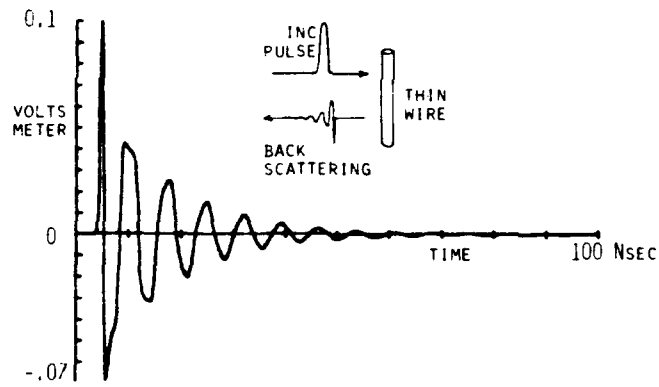
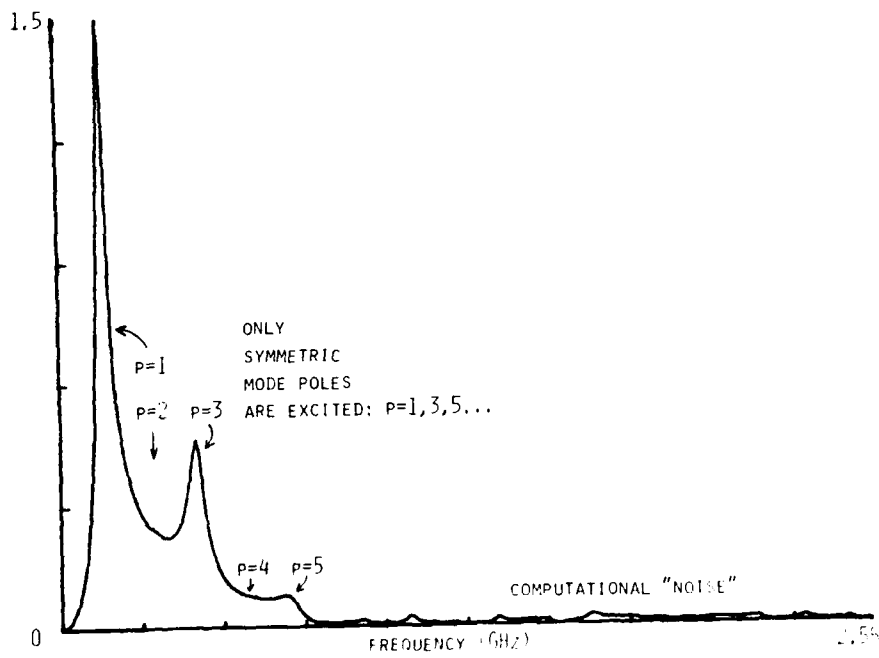


FIGURE 12 THIN-WIRE SCATTERING GEOMETRY

FIGURE 13 THIN WIRE SCATTERED FIELD SIGNATURE $\theta_i = \theta_s = 90^\circ$

FIGURE 14 SCATTERED FIELD SPECTRAL MAGNITUDE $\theta_s = \theta_i = 90^\circ$

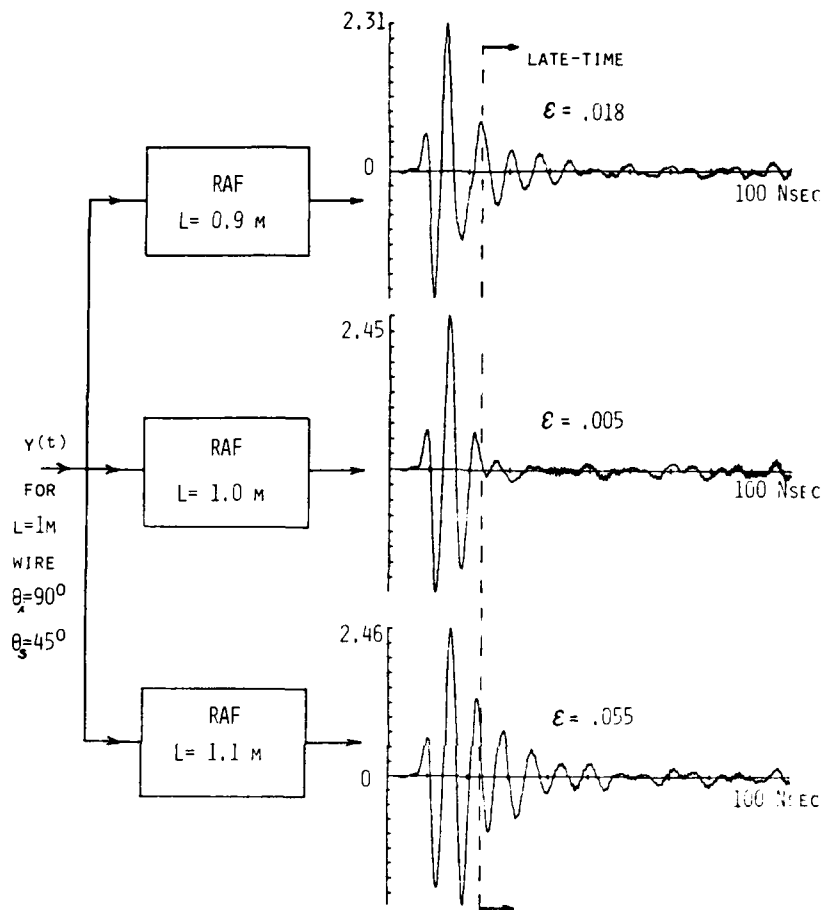


FIGURE 15 RAF OUTPUTS FOR L = 1 M WIRE SCATTERED SIGNAL (10 dB SNR)

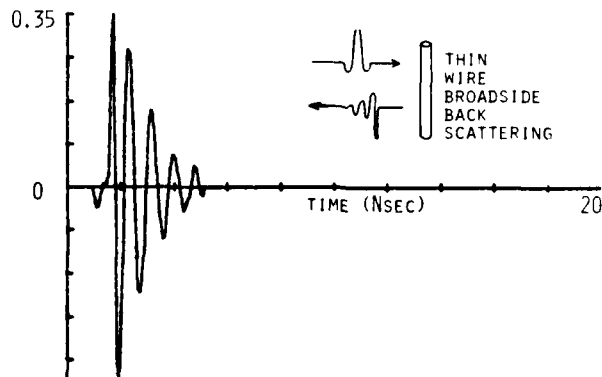


FIGURE 16 MEASURED TRANSIENT SCATTERING RESPONSE OF L = 10 CM WIRE

FIGURE 17 SPECTRAL MAGNITUDE OF MEASURED SCATTERING RESPONSE

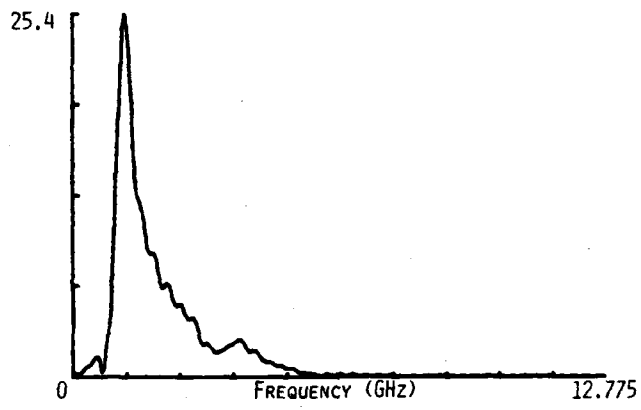


FIGURE 17 SPECTRAL MAGNITUDE OF MEASURED SCATTERING RESPONSE

NUMERICAL MODELING: FINITE METHODS

Michael A. Morgan, Associate Professor, (Code 62Mo)
Naval Postgraduate School, Monterey, CA 93943 USA

AD-8005652

SUMMARY

Recent developments in computational methods for unbounded electromagnetic problems involving antennas and scattering will be considered. Emphasis will be given to the numerical implementations of differential equation based formulations using either finite differences or finite elements, to be referred to as the finite methods. Elementary examples are used as conceptual vehicles for introducing finite element and unimoment techniques. This is followed by a discussion concerning some of the most recent innovations, such as that of the finite element boundary integral method and the field feedback formulation. Current capabilities are demonstrated by considering some of the most important research results utilizing the finite methods.

INTRODUCTION

The numerical computation of electromagnetic interaction with increasingly complex material structures has been a major research topic for over two decades. Surface integral equations have been utilized extensively in the solution of problems involving both metallic structures and layered penetrable materials. Formulations based upon differential equations have been employed for the most generalized inhomogeneous geometries, with numerical solutions effected through the *finite methods* (i.e. finite elements and finite differences) [1]. The numerical implementations of the finite methods usually result in the production of very sparse system matrices while full matrices are generally produced by integral equation formulations. The use of sparse matrix algorithms often result in significant reductions of needed memory and computation time when compared to the case of full matrix inversions, if the same number of unknowns are to be considered. As a result of this, for given computational constraints of time and memory, the finite methods have the potential to solve larger volume electromagnetic problems (in wavelengths) than can be handled by volume integral equations.

Although the finite methods offer numerical efficiency they are, by necessity, formulated as boundary value problems, as will be considered in the next section. As such, the solution of scattering and radiation problems in unbounded spatial regions requires a mechanism for coupling closed region solutions to the exterior space. This procedure must also ensure that the proper radiation conditions are satisfied, since these form the "boundary conditions" at infinity. The *Unimoment Method*, as developed by Mei [2], provided a self-consistent approach to coupling interior and exterior field problems through a separable surface interface. This method was employed by Stovall and Mei [3] and Morgan and Mei [4] to both antenna radiation and scattering problems involving inhomogeneous axisymmetric dielectrics. Further applications of the unimoment method, using finite elements, were made by Morgan [5],[6] to problems involving raindrop scattering and microwave energy deposition in the human head. Some of these results will be considered in the section devoted to the unimoment method.

For many applications the use of a separable surface, as is needed in the unimoment method, results in numerical inefficiencies and other difficulties. To allow the use of more generalized surfaces, which may even be made conformal to the object's outer surface, a new hybrid method was developed by Morgan, Chen, Hill and Barber, [7]. This approach, termed the *Finite Element Boundary Integral* (FEBI) method, combines a finite element interior solution with a surface integral equation on the boundary. The FEBI formulation will be briefly discussed in a subsequent section concerning recent advances. The most recent innovation is that of the *Field Feedback Formulation*, (F^3), which replaces the integral equation on the boundary in the FEBI approach with a discrete feedback relationship between adjacent boundaries, [8]. This methodology will also be developed at a basic level in the section on recent advances.

Additional methods exist for employing finite method solutions in open region problems. One such technique imposes an artificial zero boundary condition at sufficiently large distance from the antenna or scatterer, [9]. The drawbacks of this procedure are (1) the inaccuracy of such an assumption and (2) the large mesh that is needed, with the accompanying large matrix size. Another method employs "infinite elements", where an assumption is made as to the behavior of the exterior field, [10]. To approach an accurate approximation, these infinite elements must lie in the "far-field" of the problem. This means that the finite mesh region must be extended sufficiently far from the scatterer to accomplish this, yielding the same type of inefficiency as the zero boundary method.

THE FINITE METHODS

The finite methods may be classified as the various techniques that provide discrete-wise approximate solutions to continuous boundary value problems, [1]. As such, the finite methods offer a means to approximate the solution of specified differential equations in one or more dimensions, including time. The most common method has been that of finite differences, which obtains discrete approximations to partial derivatives

by differentiating a piecewise polynomial, or other approximating function, which has been "point-matched" to the actual unknown function at the "nodes" of the problem. As a simple example, consider the finite difference approximation of the various derivatives, up to the n -th order, of an unknown function, $f(x)$, in one-dimension. The domain of x is partitioned into generally unequal segments, separated by ordered nodes, x_k , for $k=1,2,\dots$. In the region of x that contains the i -th node, x_i , let $f(x)$ be approximated by an n -th order polynomial,

$$f(x) = a_n x^n + a_{n-1} x^{n-1} + \dots + a_1 x + a_0 \quad (1)$$

The coefficients can be found as linear functions of $n+1$ of the unknown nodal values of $f(x)$. Usually, these particular nodes will be taken to bracket the i -th node. The linear relationship between the coefficients and the nodal values of $f(x)$ is developed by point matching the polynomial in Eq. (1) at the $n+1$ nodes, resulting in the linear system defined by

$$\sum_{p=0}^n x_k^p a_p = f(x_k) \quad \text{for } n+1 \text{ distinct values of } k \quad (2)$$

After inverting this system, the resultant linear functional form for each a_p can be substituted into Eq. (1). The finite difference formulas for each derivative up to the n -th order can then be obtained by analytically differentiating Eq. (1), followed by an evaluation at $x=x_i$. This procedure will yield a formula for each of the derivatives which is a linear function of the $n+1$ nodal values of $f(x)$. For example, if $n=2$, with equal segments, Δx , then a quadratic expression in (1) yields the well-known formula for the second derivative,

$$\frac{d^2 f(x_i)}{dx^2} \approx \frac{f(x_{i+1}) - 2f(x_i) + f(x_{i-1}))}{(\Delta x)^2} \quad (3)$$

The finite difference solution of a boundary-value problem is set up by replacing the analytical derivatives contained in the differential equation by finite difference formulas at each nodal point where the solution function is to be found. Thus, there results a system of linear equations relating the unknown nodal values of the solution function to both the known excitations (drivers) of the differential equation and the known boundary values of the solution function. As will be shown, the finite difference method can be thought of as a very special case of a much more generic technique, called the finite element method (FEM).

The finite element method can be approached in general through the "weighted residual method", [11], which considers the numerical solution of a differential operator equation in an M -dimensional "volume", V_0 , which bounds $r = (r_1, r_2, \dots, r_M)$, where M is usually no more than 4,

$$D(r) \cdot f(r) = g(r) \quad \text{for } r \text{ inside } V_0 \quad (4)$$

$D(r)$ is the differential operator, f is the unknown vector function, g is the known driving vector. Essential boundary data concerning f is known on a surface, S_0 , which encloses V_0 . An example is the scalar Helmholtz equation in 2-D,

$$(\nabla^2 + k_0^2) f(x,y) = g(x,y) \quad (5)$$

To find the approximate numerical solution of this equation we use a basis function expansion to represent f ,

$$f(r) = \sum_{n=1}^N C_n U_n(r) \quad (6)$$

where the set $\{U_n\}$ should, ideally, have the same order of differentiability as does the exact solution and, as N is increased, the approximate expansion should converge in a pointwise sense to $f(r)$. This last condition depends upon how completely the set of basis functions "spans" the subspace of functions occupied by the various solutions to (4). This quality is reflected in the linear independence of the function set.

Upon substituting Eq. (6) into (4), there results,

$$D \cdot f(r) = \sum_{n=1}^N C_n \{D(r) U_n(r)\} = g(r) \quad (7)$$

To solve for the N coefficients, we enforce this equation with respect to a succession of N weighted integrations over V_0 ,

$$\langle w_k(r), D \cdot f(r) \rangle = \sum_{n=1}^N C_n \{ \langle w_k(r), D(r) \cdot U_n(r) \rangle = \langle w_k(r), g(r) \rangle \text{ for } k=1, N \quad (8)$$

with $\langle w(r), v(r) \rangle$ indicating an integration of the dot product of the two indicated vector functions over V . The set $\{w_k(r)\}$ is termed the "weighting functions" or "testing functions". This weighted residual approach has also been termed the "Method of Moments" (MoM), [12], because of the similarity of the weighted inner product integral terms to statistical "moments". The MoM has, for the most part, been applied to integral equations in electromagnetics. The conceptually identical weighted residual approach was originally associated with numerical developments in finite elements, as applied to structural and fluid dynamics problems.

In setting up the $N \times N$ linear system indicated by (8) there are some additional considerations that need to be addressed. One of these concerns the support region of the basis functions: either full range (over all of V) or compact (each being nonzero over only a portion of V). An example of full range basis functions is the set of complex exponentials employed in Fourier series, where the C_n 's are termed the spectra of the expansion. Compact basis functions are more common to finite element applications. Usually these basis functions are selected so that at each node of the discretized problem all basis functions, except one, are zero. At its associated node, where it is nonzero, the basis function will usually be set to unity. In such a case, the compact support basis set conveniently yields C_n 's which represent the solution values of $f(r)$ at the N nodes. Another consideration involves the set of weighting functions. There is obviously an unlimited selection available. Three of the more common types are:

- (1) Point Collocation, which uses a delta function at each ordered node coordinate, r_k , for the associated w_k . The effect of this is to reduce the integration "moments" in Eq.(8) to simple point-matching at the respective nodes, resulting in nothing more than the finite difference method. An advantage of this method is its relative simplicity in generating the matrix elements from (8), since integrations are reduced to enforcing the approximation at the node points. On the other hand, there is no control on the behavior of the solution in-between the nodes, in the sense of solving the differential equation. This usually results in the least accurate solution of these three methods, assuming a similar node density and computer word-length in each case.
- (2) Subdomain Collocation, which employs a set of mutually exclusive constant functions, $w_k(r)=1$, in a defined region around the k -th node. These regions around each node are non-overlapping and usually are directly adjacent to one another, without unfilled space. This approximation is usually more accurate than Point Collocation, but not as accurate as Galerkin's method, when self-adjoint operators are involved.
- (3) Galerkin's Method, which uses the same set of functions for both basis and testing, $w_k(r)=U_k(r)$. For the case of a self-adjoint operator, $D(r)$, it can be shown that the functional defined by $Q(f) = \langle f, D \cdot f \rangle - 2 \langle f, g \rangle$ is stationary about the solution to the original operator equation, in (4), [13]. This variational principle, when enforced upon the basis function expansion in Eq.(6) is termed the "Rayleigh-Ritz Method" and yields the Galerkin's result for the weighted residual approach. This method generally provides the most accurate solution and forms the foundation for most of the FEM work that has been done. Another means of achieving this same result (the Galerkin equations, with $w_k=U_k$) is by way of the classical Euler-Lagrange variational formulation. This has the advantage of reducing the order of differentiation on the basis functions, via-a-vis a direct Galerkin approach, and will be demonstrated in the following section.

An excellent discussion of the error bounds and rates of convergence for these three methods is given by Strang and Fix, [13].

FINITE ELEMENT EXAMPLE

Consider the simple problem of the undriven ($g=0$) Helmholtz equation in Eq.(5) in a rectangular region with "mixed" boundary conditions (BCs), as shown in Figure 1. The rectangular problem space is discretized into a grid of doubly ordered nodes, with triangular finite elements, as per Figure 2. The unknowns are thus the values of $f(x_i, y_j)$ at the nodes where $f(x, y)$ is not given by the BCs.

We will employ piecewise linear "pyramid" basis functions, $U_{i,j}(x, y)$, to represent the solution,

$$f(x, y) = \sum_{i=1}^6 \sum_{j=1}^7 f_{i,j} U_{i,j}(x, y) \quad (9)$$

The support region for $U_{i,j}$ is all elements which share the (i, j) node, as illustrated in Figure 3 for an interior node. In the l -th element, we will locally number the associated 3 nodes, $k=1, 2, 3$, as shown in Figure 4. Within this l -th element, the linear basis function associated with the k -th node is given by the matrix product

$$U_k(x,y) = [x, y, 1] \cdot [L]_k \quad (10)$$

with $[L]_k$ the k-th column of the element coordinate matrix,

$$[L] = D_1^{-1} \begin{bmatrix} (y_2 - y_3) & (y_3 - y_1) & (y_1 - y_2) \\ (x_3 - x_2) & (x_1 - x_3) & (x_2 - x_1) \\ (x_2 y_3 - x_3 y_2) & (x_3 y_1 - x_1 y_3) & (x_1 y_2 - x_2 y_1) \end{bmatrix} \quad (11)$$

where $D_1 = \det [L]$ is twice the area of the triangle.

Employing the Euler-Lagrange formulation, we seek the nodal values in (9) for which the quadratic functional below is stationary,

$$Q(f) = \langle \nabla f, \nabla f \rangle - k_0^2 \langle f, f \rangle \quad (12)$$

Note that this functional has only first order derivatives inside of the \langle, \rangle integrals in x, y . This result follows directly from the classical variational formulation and can be obtained through applying Green's theorem (or multiple integration by parts) to the Galerkin equations. The stationary solution is found by substituting (9) into (12) and then differentiating Q with respect to each of the unknowns, setting the results to zero in each case, resulting in the linear system of equations,

$$\sum_{i=1}^6 \sum_{n=1}^7 f_{i,j} \langle \nabla U_{i,j}, \nabla U_{m,n} \rangle - k_0^2 \langle U_{i,j}, U_{m,n} \rangle = 0 \quad (13)$$

for $i=2$ to 5 and $j=2$ to 7. Note that for a given (i,j) node, only (m,n) nodes sharing at least one common element will provide a nonzero contribution to the moment integrations. Thus, the matrix defined by (13) will usually be quite sparse, with most matrix elements, indicated by the terms in curly brackets, being zero. This feature is produced by all finite methods upon using compact support basis and testing functions.

Denoting the 4 unknowns at the nodes across the j -th horizontal row of the mesh in Figure 2 by the vector,

$$F_j = [f_{2,j}, f_{3,j}, f_{4,j}, f_{5,j}]^T \quad (14)$$

the matrix equation implied by Eq.(13) can be written as a linear matrix-vector relationship between adjacent row vectors,

$$[A]_j \cdot F_{j-1} + [B]_j \cdot F_j + [C]_j \cdot F_{j+1} = P_j \quad (15a)$$

where the "block-matrices" are banded in structure,

$$[A]: \begin{bmatrix} x & x & & & \\ & x & x & 0 & \\ 0 & & x & x & \\ & & & & x \end{bmatrix} \quad [B]: \begin{bmatrix} x & x & & & \\ & x & x & x & 0 \\ 0 & x & x & x & \\ & & & & x & x \end{bmatrix} \quad [C]: \begin{bmatrix} x & & & & \\ & x & x & 0 & \\ 0 & x & x & & \\ & & & & x & x \end{bmatrix} \quad (15b)$$

These nonzero matrix elements, indicated by "x", as well as the elements of the boundary condition vector, P_j , are obtained in terms of the element integrals within the curly brackets in Eq.(13). Within the l -th element, having L -matrix defined by (11), the integrands can be obtained directly from Eq.(10). Denoting the relationship between local (in element l) and global node coordinates by $k=(m,n)$ and $k=(i,j)$, there results

$$U_k U_q = ([L]^k)^T \cdot \begin{bmatrix} x^2 & xy & x \\ xy & y^2 & y \\ x & y & 1 \end{bmatrix} \cdot [L]^q \quad (16)$$

$$\nabla U_k \cdot \nabla U_q = ([L]^k)^T \cdot \begin{bmatrix} 1 & 0 & 0 \\ 0 & 1 & 0 \\ 0 & 0 & 0 \end{bmatrix} \cdot [L]^q \quad (17)$$

with $H_n^{(2)}$ the Hankel function of the 2nd kind. Notice that this is an approximate result due to the truncation of the series at $N+1$ terms. In practice, this series will converge rapidly to the scattered field if $N > k r_2$. To find the unknown scattered field coefficients, a_n and b_n , we first solve the interior region problem for $2N+1$ separate BCs on $r=r_1$. These BCs are composed of the incident field and each of the scattered field modes in the expansion. The numerical solution within the interior, which corresponds to one of these applied BCs, is indicated by \hat{f}_n (circumflex overbar). For example, a BC of $f^n(r_1, \theta)$ produces an interior solution of $\hat{f}_n^n(r, \theta)$ while a BC of $S_n(r_1, \theta)$ produces $\hat{S}_n^n(r, \theta)$ for $r < r_1$. Using the principle of superposition, the numerical solution for the total field inside of the outer boundary will be given by Eqn. (21), but with numerical solutions replacing f^n , C_n and S_n .

To solve for the coefficients, we simply equate the numerical solution to the analytical solution along the circular contour, $r=r_2$, resulting in

$$\sum_{n=0}^N a_n (\hat{C}_n(r_2, \theta) - C_n(r_2, \theta) + b_n (\hat{S}_n(r_2, \theta) - S_n(r_2, \theta))) = f^n(r_2, \theta) - \hat{f}_n^n(r_2, \theta) \quad (22)$$

The equality of the analytical and numerical expressions for the total field at $r=r_2$ is theoretically correct. The unknown scattered field coefficients may be obtained by a weighted residual approach, where $\langle \rangle$ indicates, in this case, an integration on θ from 0 to 2π and the Δ functions below indicate the respective function differences in (22).

$$\sum_{n=0}^N a_n \langle W_m(\theta), (\Delta C_n(\theta)) \rangle + b_n \langle W_m(\theta), (\Delta S_n(\theta)) \rangle = \langle W_m(\theta), \Delta f^n(\theta) \rangle \quad (23)$$

for $m=0$ to $2N$, with $2N+2$ linearly independent weighting functions, W_m . By selecting delta function weights at $2N+2$ nodes along the matching contour, $r=r_2$, Eq.(23) will provide the point-matching form of the solution. A much more accurate method is to enforce (22) in the least-squares sense over the entire circle, including in between the nodes. In this case, this results in the weighting functions being proportional to the complex conjugates of the function differences within the curly brackets. The integrations to evaluate the matrix elements in (23) are performed either numerically, or semi-analytically by using the basis function expansions employed in the interior solution to represent both the difference functions and the weighting functions. In any case, the resultant $2N+1$ square matrix can be inverted to obtain the scattered field coefficients. The scattered field may then be obtained from its expansion and, if desired, the interior field can be found by using the weighted superposition of the stored interior field solutions.

The unimoment method has been employed in several computational efforts. One of the earliest of these involved the finite difference solution for radiation and input impedance of a finite length biconical antenna, loaded by inhomogeneous dielectric [3], as is depicted in Figure 6. Since both the fields and material structure are axisymmetric in form (invariant to the ϕ -coordinate) the solution can be reduced to a single meridian plane, (r, θ) in spherical coordinates. A section of the finite difference mesh is shown in Figure 7. The interior region solution for this antenna problem was formulated using a special case of the Coupled Azimuthal Potential (CAP) formulation, where all fields are represented using two (in this case only one was needed) continuous potential functions which are related to the azimuthal field vector components, [16]. A sample result is shown in Figure 8, which compares the computed and measured input impedance of a plexiglas loaded biconical antenna. The computation was performed at discrete frequencies over a 10:1 range, wherein the bicone height ranged from .16 to 1.6 wavelengths.

As a second example of the unimoment method, consider scattering by inhomogeneous bodies of revolution [4], which employed the tri-regional finite element mesh in the (r, θ) meridional plane, as shown in Figure 9. The CAP formulation was employed to represent the general (non-axisymmetric) fields using two coupled potentials and a Fourier series in the ϕ -coordinate. Independent spherical harmonic expansions were used to represent the scattered field outside of the mesh and the total fields within the spherical "core" region surrounded by the mesh. The sets of coefficients used in these field expansions were found by applying the various expansion modes for the potentials as boundary conditions along the contours $r=a$ and $r=b$. In addition, the various incident fields being considered were applied along $r=b$. A finite element solution for each applied BC was then then evaluated along the inner contours $r=r_1$ and $r=r_2$. The total fields were then assembled from these numerical solutions and equated in the least-squares sense to the original analytical expansions, resulting in a matrix equation for the coefficients. Numerous comparisons to experiments were made for solid and hollow dielectric bodies of various shapes. A typical result is shown in Figure 10, where the bistatic scattering is from a plexiglas body having cylindrical, conical and spherical portions. Note that the vertical scale is not in dB.

Additional research efforts involving the unimoment method include scattering by dielectric cylinders [17] and axisymmetric raindrops [5], as well as scattering by multiple bodies of revolution [18] and even buried objects [19]. In another case, the scattering problem was solved for a complex lossy dielectric model of the human head, in order to evaluate the interior field distribution as a function of frequency, incident aspect and polarization, [6].

The numerical solution within a spherical interior region becomes inefficient, for scattering shapes that occupy only a small portion of the enclosed volume (e.g. thin cylinders and flat discs). Although it is possible to utilize a separable non spherical surface to increase the numerical efficiency of the interior region solution, this will be offset by additional requirements in both generating the special functions that are needed in the exterior expansion and in computing the required *moments* of these functions with the numerical solutions over the interface.

RECENT ADVANCES

A technique to circumvent the need for a separable boundary interface was developed by Morgan, Chen, Hill and Barber [8]. This hybrid Finite Element Boundary Integral (FEBI) method combines a finite element solution of the interior region with the surface integral equation found in the extended boundary condition method. The FEBI procedure allows the use of a surface interface that conforms to the outer boundary of the scattering object, as is shown for the finite element mesh in Figure 11. The finite element solution proceeds in a similar manner to that of the unimoment method, with the incident field and scattered field spherical harmonic expansion modes being applied as BCs at the outer boundary, S_G . Numerical solutions are then found at the surface of the scattering body, S_B , for each of these applied BCs. Since these boundaries at S_G and S_B do not in general conform to a spherical surface, a single spherical harmonic expansion for the scattered fields outside of S_B is not "complete", except outside of a sphere that encloses the scatterer. Thus we can not, in theory, match the numerical solution at S_B to the original analytical expansion, as we did for the unimoment method. To evaluate the expansion coefficients for the boundary field, we use a combined field integral equation, as employed by Waterman in the "extended boundary condition formulation" [20]. This integral equation relates the tangential field just inside of the boundary S_B to that just outside and does not make use of a knowledge of the material structure inside of S_B .

The FEBI method has been shown to work well for T-matrix calculations involving moderately elongated lossy dielectric scatterers. An example computation, with comparison to that performed using the extended boundary condition method, is illustrated in Figure 12. The method tends to have difficulties, however, with attaining convergence of the solution if the surface interface becomes extremely elongated (i.e. length to diameter ratios exceeding about 10). This failure occurs because of the generally *incomplete* nature of the exterior region spherical harmonic expansion which is employed to represent the field over the surface of the scattering body. Such a problem is related to the *Rayleigh hypothesis* [21].

The Field Feedback Formulation (F^3) has been proposed, [8], to mitigate the restrictions inherent in coupling interior and exterior region field solutions, as are found in other techniques. Using F^3 , the interior boundary value problem is initially decoupled from the outside region. The interior problem may then be formulated and computed using the most expedient approach that can accurately accommodate the level of material complexity that is present. The exterior region field is represented in terms of modes generated from surface integrations involving equivalent currents obtained from the interior region solution. These modal fields, which satisfy the radiation conditions, do *not* rely upon the use of separable coordinate surfaces for their completeness. Another primary advantage of this method is its *modular* nature, where forward and feedback transfer matrices can be independently computed.

The F^3 scattering solution method may be easily conceptualized by considering the simple feedback system which is depicted in Figure 13. The input to the forward transfer function, A , is an array composed of boundary nodal values of the field on the outer surface, S_G as was shown in Figure 11. The A -operator represents the finite method solution to attain the tangential field values on the inner surface, S_B , in terms of any specified boundary data on S_G . These numerically derived tangential fields on S_B can then be used to form equivalent electric and magnetic currents (combined to form an array K) that generate the scattered field from the object. In particular, by way of Green's function integrations of these equivalent currents on S_B the scattered field can be found on the outer surface, S_G . These integrations are represented by the feedback operator β . The original boundary array on S_G was composed of the incident field plus an expansion, with unknown coefficients C_n , for the scattered field. By superposition, the numerically generated "feedback" scattered field, will be equal to a known term, given by $\beta \cdot A$ operating on the incident field, plus an expansion of the unknown coefficients with known expansion functions ($\beta \cdot A$ operating on the original scattered field expansion functions on S_G). By closing the loop, and literally making the feedback field equal to the scattered field portion of the original expansion, an equation results that is similar in form to that from the analysis of a simple recursive control system,

$$\Phi^{scat} = \sum_{n=1}^N c_n \Phi_n = [I - \beta \cdot A]^{-1} \cdot \beta \cdot A \cdot \Phi^{inc} \quad (24)$$

where $[I]$ is an identity matrix. The unknown coefficients may be found from this equation through the method of weighted residuals, where both sides are integrated over S_G with respect to a set of N linearly independent weighting functions. Once the coefficients are obtained, then the scattered far field is found through simplified Green's function integrations of the assembled equivalent currents on S_B . These

integrations are denoted by the \square -operator in Figure 13.

A very simple demonstration of the F^3 is scattering by a metallic thin wire. The finite element mesh for this is shown in Figure 14. This is obviously a case where the unimoment method would be quite inefficient, requiring a meridian spherical mesh to enclose the wire. Using the F^3 , the mesh has only a single column of triangular elements, which produces an interior solution global system matrix having a nonzero bandwidth of only 3 matrix elements in this case. The Riccati transform allows ultra-fast inversion of this matrix. Comparisons of the magnitude and phase of current on a 1 wavelength long wire, as computed from the F^3 and Hallen's integral equation, is shown in Figure 15. One source of error in the F^3 computation was the use of linear basis functions in the finite element calculation, which were used to represent the phi component of magnetic field. In the immediate vicinity of the thin-wire this field component is characterized by a rapidly decaying evanescence which is not accurately "trackable" using linear functions. More specialized basis functions would allow a natural convergence of the solution as the wire is made thinner.

CONCLUSION

The objective here has been to consider recent developments in finite method based computational techniques for unbounded electromagnetic field problems. Along the way, a brief tutorial concerning the finite methods was provided. Special consideration was then given to three methods for solving field problems involving scatterers or antennas which use finite method boundary value numerical solutions. The most established of these techniques, the unimoment method, was developed through a simple example, and some representative computational results were given. This was followed by the description of two more recently developed methods which provide the systematic coupling of interior region solutions to the unbounded exterior domain. These formalisms, called the finite element boundary integral method (FEBI) and the Field Feedback Formulation (F^3) permit the use of sparse matrix finite methods for field solutions within complicated scatterers composed of inhomogeneous and anisotropic materials. Furthermore, a minimal volume conformal bounding surface may be employed to enclose the scatterer, which is an advantage over the need for a separable surface mesh in the unimoment method. Convergence problems for non-spherical boundary surfaces, as encountered in the FEBI work, led to the F^3 concept, which circumvents the need for any separable coordinate expansion.

The F^3 casts the scattering problem into a vector matrix equivalent of a simple feedback system, wherein the forward (interior problem) and feedback (radiated field) matrices may be computed independently and then combined to obtain a self consistent scattering solution. A very simple example of thin-wire scattering was considered to demonstrate the technique. The unique power of this method resides in extending the realm of electromagnetic computation to large and quite complex scattering configurations where volume integral equation techniques are numerically *bottlenecked* by their resultant full system matrices. Current work by the author is being directed at demonstrating this potential power in scattering computations involving complex 3-D objects having both metallic and penetrable substructures.

REFERENCES

- [1] K.K. Mei, M.A. Morgan and S.K. Chang, "Finite methods in electromagnetic scattering," in *Electromagnetic Scattering*, P.L.E. Ushlenghi, Ed., New York: Academic Press, 1978.
- [2] K.K. Mei, "Unimoment method of solving antenna and scattering problems," *IEEE Trans. Antennas Propagat.*, vol. AP-22, pp.760-766, Nov. 1974.
- [3] R.E. Stovall and K.K. Mei, "Application of a unimoment technique to a biconical antenna with inhomogeneous dielectric loading," *IEEE Trans. Antennas Propagat.*, vol. AP-23, pp. 335-341, May 1975.
- [4] M.A. Morgan and K.K. Mei, "Finite element computation of scattering by inhomogeneous penetrable bodies of revolution", *IEEE Trans. Antennas Propagat.*, vol. AP-27, pp. 202-214, March 1979.
- [5] M.A. Morgan, "Finite element computation of microwave scattering by raindrops," *Radio Science*, vol. 15, pp.1109-1119, Nov. 1980.
- [6] M.A. Morgan, "Finite element calculation of microwave absorption by the cranial structure," *IEEE Trans. Biomed. Eng.*, vol. BME-28, pp.687-695, Oct. 1981.
- [7] M.A. Morgan, C.H. Chen, S.C. Hill and P.W. Barber, "Finite element - boundary integral formulation for electromagnetic scattering," *J. Wave Motion*, vol. 6, pp. 91-103, Jan. 1984.
- [8] M.A. Morgan and B.E. Welch, "The field feedback formulation for electromagnetic scattering problems," *IEEE Trans. Antennas Propagat.*, Vol. AP-34, December 1986.
- [9] N. Mabaya, P.E. Lagasse and P. Vandenbulcke, "Finite element analysis of optical waveguides," *IEEE Trans. Microwave Theory Tech.*, vol. MTT-29, pp. 600-605, 1981.

- [10] P. Bettess, "Infinite elements," *Int. J. Num. Meth. Eng.*, vol. 11, pp. 53-64, 1977.
- [11] L. Lapidus and G.F. Pinder, *Numerical Solution of Partial Differential Equations in Science and Engineering*, New York: Wiley, pp 49-79, 1982.
- [12] R.F. Harrington, *Field Computation by Moment Methods*, New York: Macmillan, 1968.
- [13] G. Strang and G. Fix, *An Analysis of the Finite Element Method*, Englewood Cliffs: Prentice-Hall, 1973.
- [14] R.P. Tewarson, *Sparse Matrices*, New York: Academic, 1973.
- [15] P.M. Morse and H. Feshbach, *Methods of Theoretical Physics*, Vol. 1, New York: McGraw-Hill, 1953, section 5.1.
- [16] M.A. Morgan, K.K. Mei and S.K. Chang, "Coupled azimuthal potentials for electromagnetic field problems in inhomogeneous axially-symmetric media," *IEEE Trans. Antennas Propagat.*, vol. AP-25, pp. 413-417, May 1977.
- [17] S.K. Chang and K.K. Mei, "Application of the unimoment method to electromagnetic scattering of dielectric cylinders," *IEEE Trans. Antennas Propagat.*, Vol. AP-24, pp.35-42, January 1976.
- [18] J.F. Hunka and K.K. Mei, "Electromagnetic scattering by two bodies of revolution," *Electromagnetics*, vol. 1, no. 3, pp. 329-347, July-Sept. 1981.
- [19] S.K. Chang and K.K. Mei, "Multipole expansion technique for electromagnetic scattering by buried objects," *Electromagnetics*, vol. 1, no. 1, pp. 73-89, Jan.-Mar. 1981.
- [20] P.C. Waterman, "Scattering by dielectric obstacles," *Alta Frequenza*, vol. 38 (Speciale), pp. 348-352, 1969.
- [21] R.F. Miller, "Rayleigh Hypothesis in Scattering Problems," *Electronics Letters*, vol. 5, No. 17, pp. 416-418, 1969.

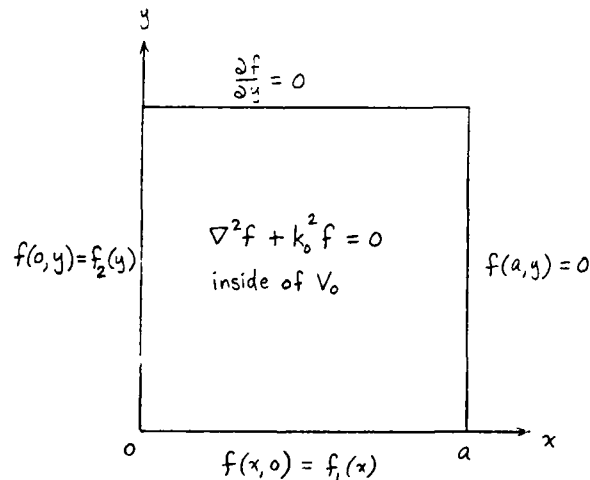


FIGURE 1 HELMHOLTZ EQUATION WITH MIXED BOUNDARY CONDITIONS

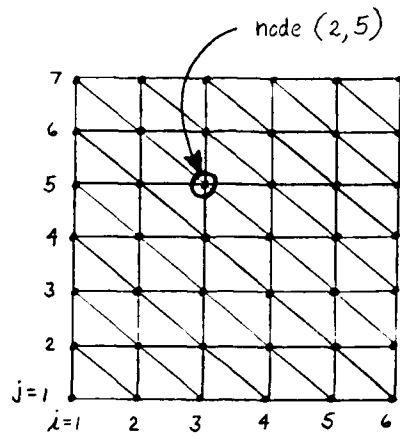


FIGURE 2 RECTANGULAR REGION FINITE ELEMENT MESH

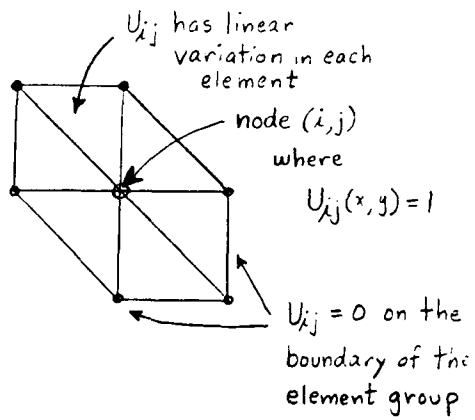


FIGURE 3 NODE WITH SURROUNDING ELEMENT GROUP

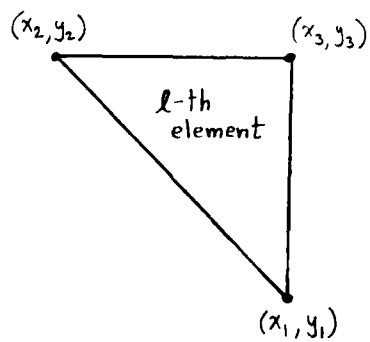


FIGURE 4 LOCAL COORDINATES IN AN ELEMENT

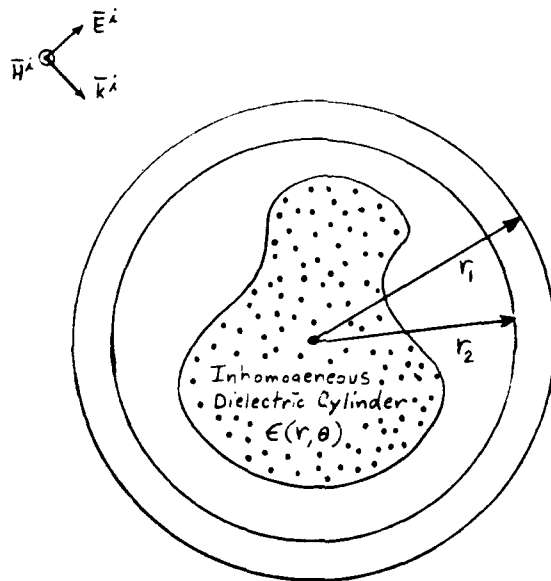


FIGURE 5 UNIMOMENT MATCHING CONTOURS FOR CYLINDRICAL PROBLEM

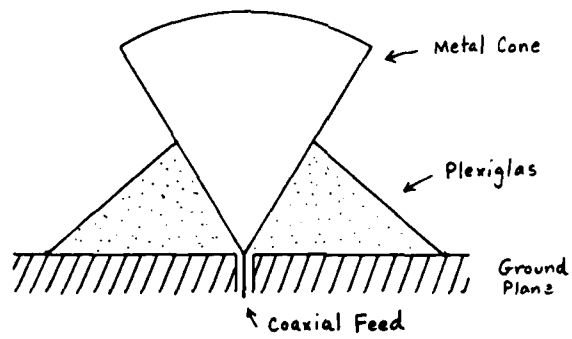


FIGURE 6 EXPERIMENTAL DIELECTRICALLY LOADED BICONICAL ANTENNA

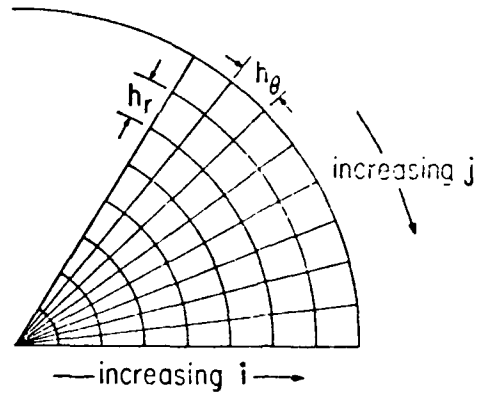


FIGURE 7 FINITE DIFFERENCE MESH FOR THE BICONICAL ANTENNA

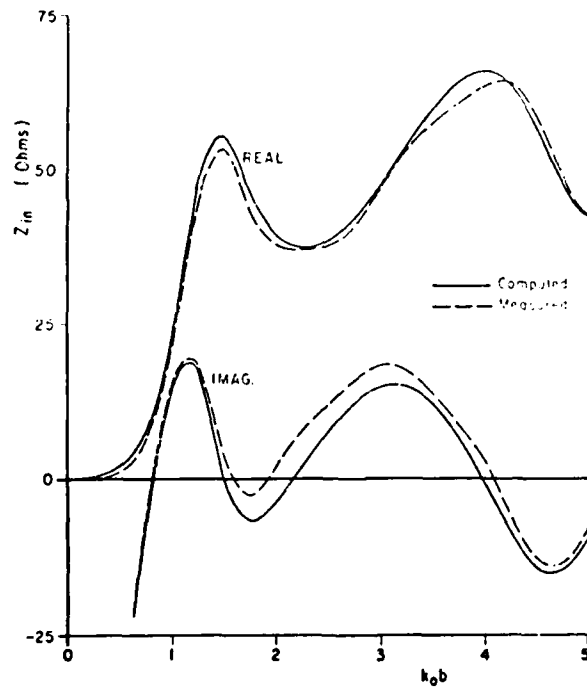


FIGURE 8 COMPARISON OF MEASURED AND COMPUTED INPUT IMPEDANCE

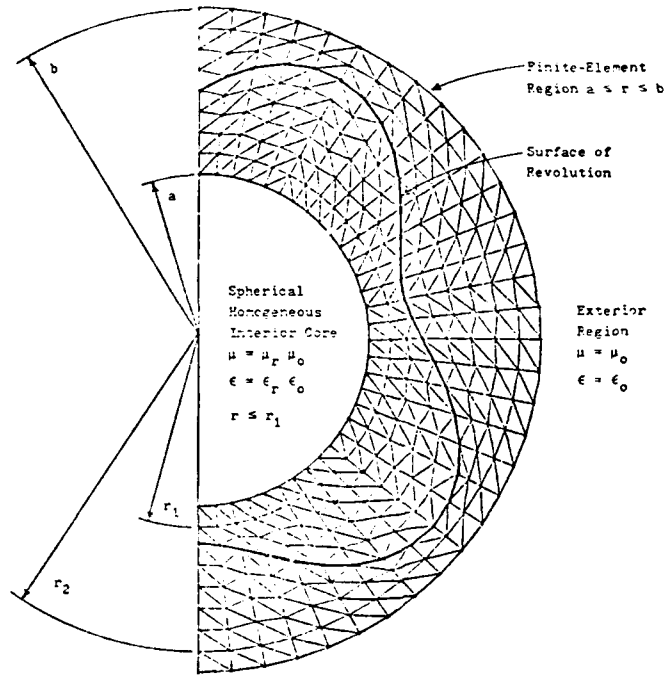


FIGURE 9 SEMI-ANNULAR CONFORMAL FINITE ELEMENT MESH

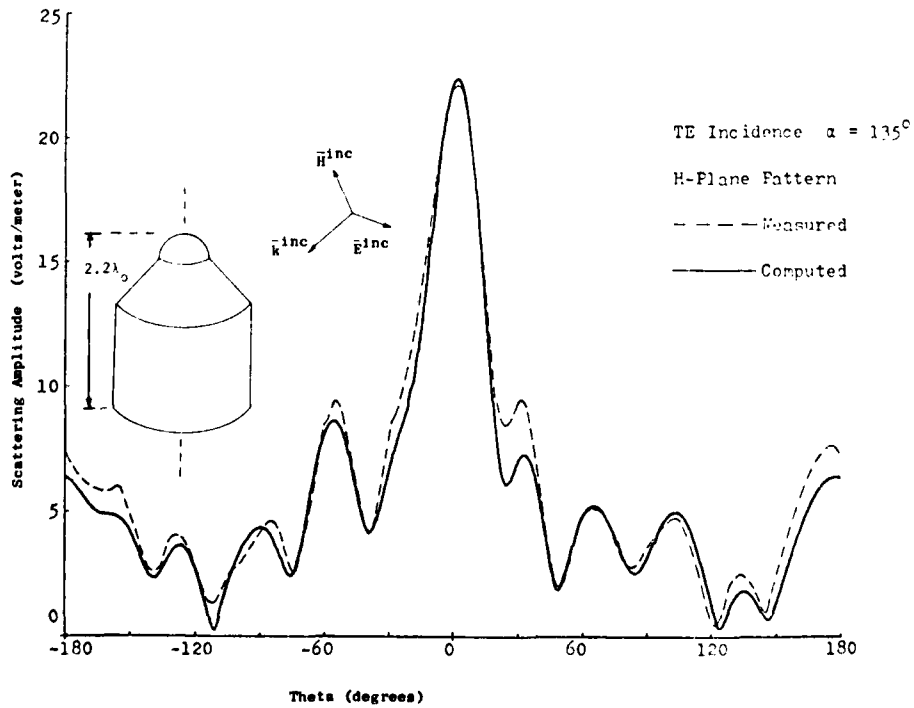


FIGURE 10 SCATTERING AMPLITUDE COMPARISON FOR A PLEXIGLAS OBJECT COMPUTED USING THE UNIMOMENT METHOD

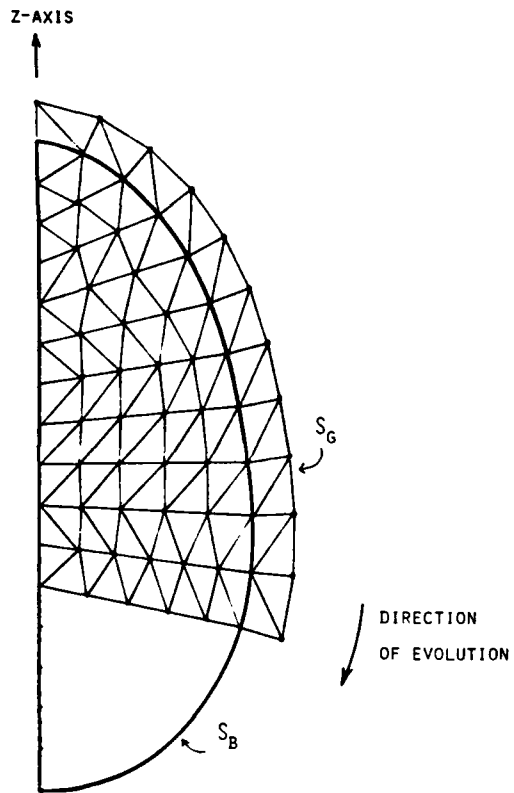


FIGURE 11 SURFACE CONFORMING FINITE ELEMENT MESH

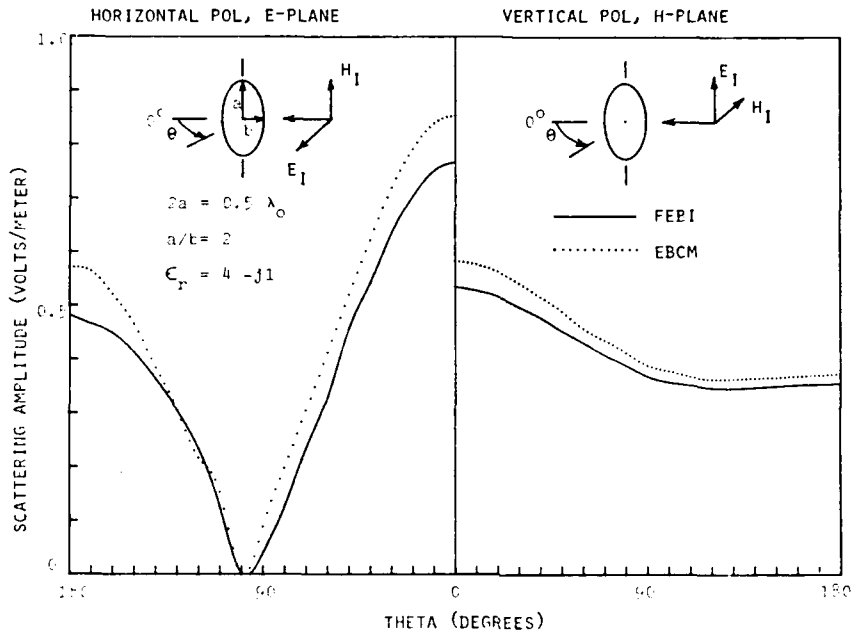


FIGURE 12 SCATTERING AMPLITUDE COMPARISON FOR FEBI COMPUTATION

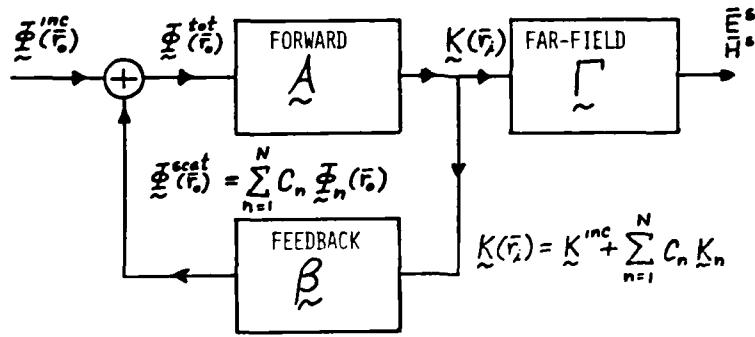


FIGURE 13 FIELD FEEDBACK FORMULATION EQUIVALENT SYSTEM

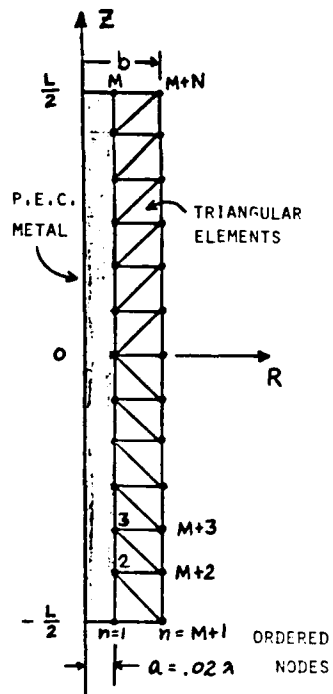


FIGURE 14 FINITE ELEMENT MESH FOR THIN-WIRE SCATTERING USING F^3

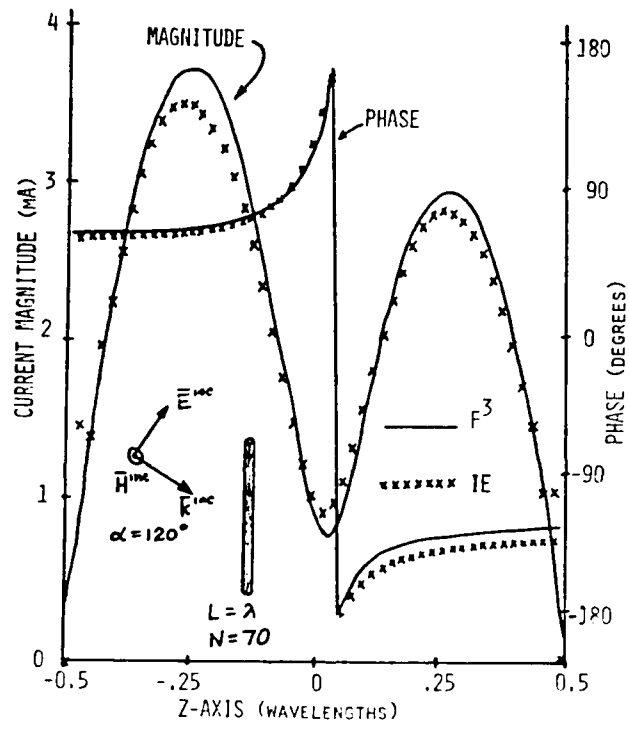


FIGURE 15 INDUCED CURRENT COMPARISON FOR I.E. & F^3 COMPUTATIONS

NUMERICAL MODELING: INTEGRAL EQUATION METHOD

V. Stein

Deutsche Forschungs- und Versuchsanstalt für Luft- und Raumfahrt e.V.
 Institut für Hochfrequenztechnik,
 8031 Oberpfaffenhofen
 Germany

SUMMARY

A review is given to the different expressions for the representation of the electromagnetic fields by integrals over the surface current. The integral equations, which mostly are used for the solution of practical problems, are discussed and the method of moments is outlined, where the use of pulses as basis functions is emphasized. Estimations of the core storage and the computer time are given. Two geometrical models for the scattering structure are discussed in more detail: the surface patch model and the wire-grid model. A list of application examples of the integral equation method with references is given. Two further examples are outlined in detail: computation of the radiation pattern of an antenna mounted on a helicopter and determination of the extreme near field of a cube.

1. INTRODUCTION

A prediction and analysis of target signatures can be made more effective, if electrodynamic models are available, which describe the interaction process between the electromagnetic wave and the structure under test with sufficient accuracy. In the event that the objects are in the design phase, where a lot of structural changes must be provided, the worth of such models will be obvious. Two examples will demonstrate this.

Fig. 1.1 shows two airfoil sections [1]. The question arises, which of the two airfoils has the smaller monostatic cross section for a wave impinging on the broadside or on the trailing edge etc., and which different frequency dependence exists for both configurations. The question can be answered if the current distribution on the airfoil is known so that the scattered far field may be computed.

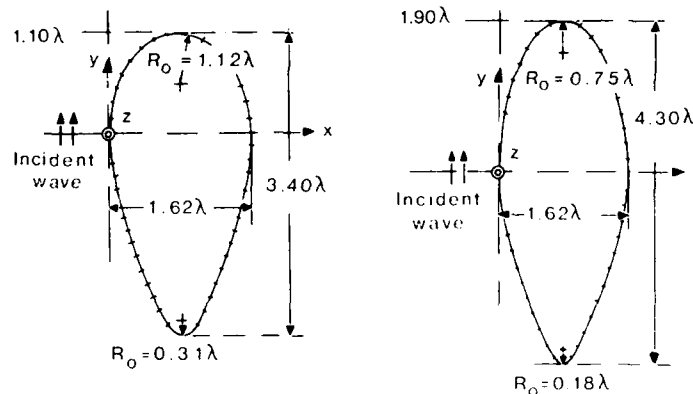


Fig. 1 Optimized design of structures.

Fig. 2 shows an airplane, which is equipped for position finding purposes. Since the phase front of the incoming plane wave is distorted more or less by the airplane structure, depending on the angle of incidence and the frequency, the question arises, where an appropriate place on the plane for the installation of the direction finding antenna may be found. The magnitude of the distortion of the wave front in dependence from frequency, polarization and incidence angle of the wavefront is of great interest. The solution of this problem requires the computation of the scattered near field.

In the past only approximate theoretical or experimental methods were available. While approximate methods can fail in giving sufficient accurate predictions of the scattering process, experimental methods require a high effort especially if changes of the structure must be carried out. Therefore, it is desirable to reduce the number of experimental studies to a few final measurements, which can be defined by the preceding theoretical analysis. This requires from the theory to develop and validate models which are able to predict the interaction of electromagnetic waves with a complicated structure with an accuracy, which is sufficient for practical applications.

The progress in computer techniques permits in an increasing manner the use of theories, which because of their high numerical effort could not be considered, in the past. Among these theories are not only heuristic methods like the physical optics method [2], and the geometrical theory of diffraction [3, 4], but also rigorous methods like the integral equation [3, 5 - 7], and the differential equation method [8, 9]. A survey over the variety of methods, which come into consideration, is given in [10].

AD-P005 653

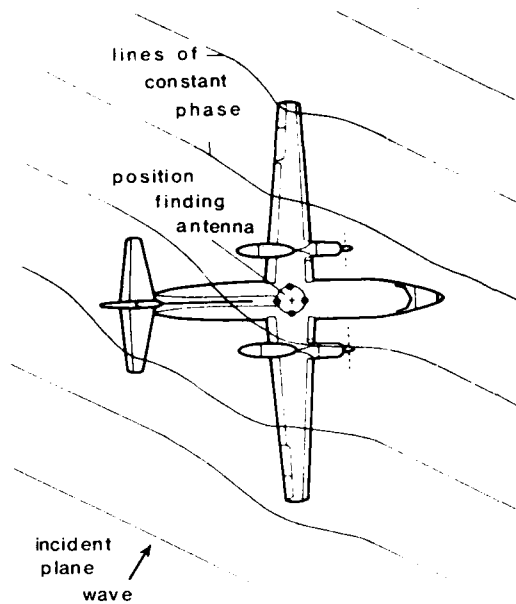


Fig. 2 Phase errors due to the interaction between electromagnetic wave and structure.

The heuristic methods allow the computation of the far field or quasi far field, if the object's dimensions are larger than several wave lengths. The rigorous methods in principle permit a computation also of the near field, since the accuracy is limited only by the computer capacity. The computer effort, however, increases considerably with the dimension of the scatterer, and therefore, limits the size of the structure.

This paper deals with the integral equation method (IEM) and its geometrical and numerical models. First the way is resumed to derive the integral equations for ideal conducting bodies of general and thin-wire structure. The solution of the integral equations for the current with the method of moments is reviewed and an estimation of computer storage and computer time is made. In the following sections the modeling of structures by surface patches and wire-grids is discussed in detail. A list of various application examples (antenna and scattering case), which are treated by the IEM, is presented. Two examples are outlined in detail. One treats the far field of VHF antennas mounted on a helicopter, the other has the objective to determine the extreme near field of a cube.

2. INTEGRAL REPRESENTATIONS OF THE ELECTROMAGNETIC FIELD FOR IDEALLY CONDUCTING STRUCTURES

One is used to represent the total field \vec{E}, \vec{H} at an observer point $P(\vec{r})$ as the sum of the known incident field \vec{E}_e, \vec{H}_e and the scattered field \vec{E}_s, \vec{H}_s :

$$\vec{E}(\vec{r}) = T \vec{E}_e(\vec{r}) + T \vec{E}_s(\vec{r}), \quad (1)$$

$$\vec{H}(\vec{r}) = T \vec{H}_e(\vec{r}) + T \vec{H}_s(\vec{r}). \quad (2)$$

In introducing the factor T one can take into account the nature of the immediate neighbourhood of the observer point. T is given by the formula [5]

$$T = \frac{1}{1 - \mu/4\pi}, \quad (3)$$

where μ is the solid angle, which is enclosed by the surface F of the scatterer at the observer point P , see Fig. 3.

The above general equations include the following familiar special cases:

- The observer point is situated in the volume V and not on the surface of the scatterer. This results in $\mu = 0$ and $T = 1$.
- The observer point is situated on a smooth surface. This results in $\mu = 2\pi$ and $T = 2$.

For the construction of an integral equation it is necessary to represent the scattered field in an integral form. There are several ways in literature [5, 11 - 13] to derive integral representations for the scattered field. For an ideal conducting structure the following expressions are available:

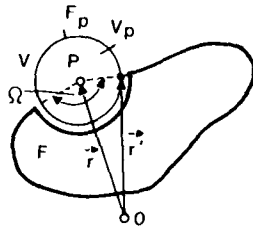


Fig. 3 Geometry for the calculation of the factor T.

$$\begin{aligned} \vec{E}_s(\vec{r}) &= \frac{T}{4\pi j\omega\epsilon} \oint_F (k^2\phi(\vec{r},\vec{r}') \vec{J}_F(\vec{r}') + (\vec{J}_F(\vec{r}') \cdot \nabla)\psi(\vec{r},\vec{r}')) d\vec{r}' = & (4a,b,c) \\ &= \frac{T}{4\pi j\omega\epsilon} \oint_F ((-1-jkR+k^2R^2) \vec{J}_F(\vec{r}') + (3+3jkR-k^2R^2)(\vec{J}_F(\vec{r}') \cdot \vec{e}_R)\vec{e}_R) \frac{e^{-jkR}}{R^3} d\vec{r}' = \\ &= \frac{T}{4\pi j\omega\epsilon} \oint_F (k^2\phi(\vec{r},\vec{r}') \vec{J}_F(\vec{r}') + (\nabla'_F \cdot \vec{J}_F(\vec{r}'))\psi(\vec{r},\vec{r}')) d\vec{r}' , \end{aligned}$$

$$\vec{H}_s(\vec{r}) = \frac{T}{4\pi} \oint_F (\nabla\psi(\vec{r},\vec{r}') \times \vec{J}_F(\vec{r}')) d\vec{r}' = \frac{T}{4\pi} \oint_F (1+jkR)(\vec{J}_F(\vec{r}') \times \vec{e}_R) \frac{e^{-jkR}}{R^2} d\vec{r}' . \quad (5a,b)$$

Denotations:

$\omega = 2\pi f$ = angular frequency,
 f = frequency,
 $k = 2\pi/\lambda$ = wave number of the propagation medium,
 λ = wavelength,
 ϵ = absolute complex dielectric constant of the propagation medium,
 \vec{J}_F = electric surface current,
 F = surface of the scatterer,
 \vec{r} = vector of the observer point,
 \vec{r}' = vector of the integration point on the surface of the scatterer,
 $R = |\vec{r} - \vec{r}'|$ = distance between observer and integration point,
 $\vec{e}_R = \vec{R}/R$ = unit vector, pointing from the integration point toward the observer,
 $\psi = \exp(-jkR)/R$ = scalar Green's function,
 ∇ = Nabla-operator, $\nabla = \vec{e}_x \partial/\partial x + \vec{e}_y \partial/\partial y + \vec{e}_z \partial/\partial z$ for cartesian coordinates,
 $\nabla'_F \cdot \vec{J}_F(\vec{r}') = \partial J_{Fu}/\partial u + \partial J_{Fv}/\partial v$ = surface divergence of the current with surface components J_{Fu} and J_{Fv} .
 The geometrical situation is illustrated in Fig. 4.

The symbol \oint is used to denote the principal value integral over a closed surface excluding an neighbourhood of the singularity. The terms under the integral become singular if the observer point is situated on the surface and the integration point approaches the observer point: $\vec{r}' \rightarrow \vec{r}$.

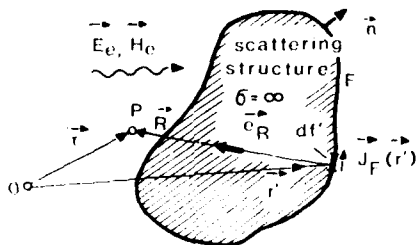


Fig. 4 Geometrical situation for the description of the scattering problem.

Eq. (4b) resp. (5b) may be evaluated directly from Eq. (4a) resp. (5a) by inserting ϕ and ψ and rearranging the terms. Eq. (4c) is equivalent to Eq. (4a) in the case that the surface is a closed one as indicated by the circle in the integral sign. The equations are rigorously valid, if the closed surface has no edges, that is no discontinuity in the surface tangents is allowed to occur. If there are any edges, the field and with it the current distribution must be determined under the constraint that the edge conditions [14, 15] are satisfied. Only in this case an unique solution of the boundary value problem can be evaluated. The edge condition for an infinite thin half-plane is known and is formulated as follows: The current component vertical to the edge, see Fig. 5, is given by

$$J_{Fz} \sim \nu^{1/2} , \quad \text{for } \nu \rightarrow 0 , \quad (6)$$

ν = vertical distance of the current point from the edge. The current component parallel to the edge behaves like

$$J_{F\parallel} \sim \nu^{-1/2} , \quad \text{for } \nu \rightarrow 0 . \quad (7)$$

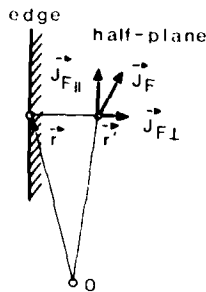


Fig. 5 Geometry for the formulation of the edge condition for a half-plane.

There is a lack in the literature concerning edge conditions for other configuration. For a wedge, however, some informations may be found in [14].

If the surface is not closed it is always limited by edges. For an open surface Eq. (4c) no more satisfies the Maxwell equations, which is the case for Eqs. (4a,b) and Eqs. (5a,b). If, however, the edge conditions are satisfied in the sense that $J_{F\perp} = 0$ on the edge, then also Eq. (4c) is a solution of Maxwell's equations [14]. Therefore, if the edge conditions are not taken into account, it is preferable to use Eqs. (4a,b) and Eqs. (5a,b), which in any case satisfy Maxwell's equations. Regarding the edge conditions all the given equations determine an unique solution also for open surfaces.

If one is interested to compute the field on the surface of the scatterer, specially in the point $\vec{r}' = \vec{r}$ and its neighbourhood, one has to make considerable efforts in treating the singularity. There are two ways to proceed. The first way [16, 17] consists in splitting the surface into a subsurface $F - F_0$ without singularity and a subsurface F_0 with boundary line C_0 , which contains the singularity, see Fig. 6.

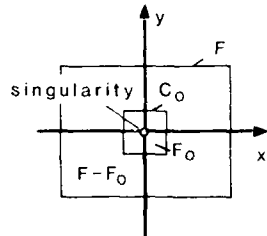


Fig. 6 Rectangular plate with a singularity at the center and with square exclusion area.

The kernel of Eq. (4a) is rearranged in such a way, that the surface integral over F_0 , which contains the singularity, is splitted into two parts by subtracting and adding Green's function for the static case. The first part can be integrated over the surface F_0 . The second surface integral is transduced to a line integral by using Stoke's theorem. The line integral has no singularity problems, since the line doesn't cross the singularity itself.

The second way [17] consists in an expansion of the phase function e^{-jkR} in Eq. (4b) into a potential series with sufficient terms. After integrating, which can be done analytically, the limiting process $\vec{r}' \rightarrow \vec{r}$ is carried out. Both ways are applied in computing the extreme near field of a cube.

Of special interest in numerical modeling are the expressions for the scattered field of a thin circular cylinder. For the derivation of the field equations a series of assumptions usually are made:

- a) there is only a current component J_{Fz} parallel to the axis of the cylinder, with a direction described by the unit vector \vec{e}_s' , see Fig. 7,

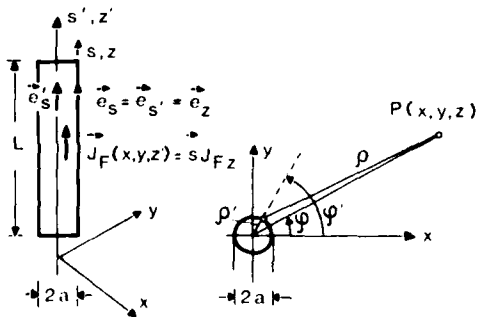


Fig. 7 Geometry of a circular cylinder.

- b) the contribution of the end faces of the cylinder are neglected,
 c) the current is assumed to tend to zero in approach to the end faces.

With assumption c) one satisfies the boundary conditions, so that Eqs. (4a,b) and (4c) can be used.

The evaluation of the integral over the circumference of the cylinder can be done analytically only if the distance

$$R = \sqrt{(x-x')^2 + (y-y')^2 + (s-s')^2} = \sqrt{\rho^2 + \rho'^2 - 2\rho\rho' \cos(\varphi-\varphi') + (s-s')^2} \quad (8)$$

between the observer point (ρ, φ, s) and the integration point (ρ', φ', s') becomes independent from the integration coordinate φ' . This is the case under the following conditions:

- the observer point is far enough from the surface, so that $R^2 \gg \rho^2, \rho'^2$:

$$R \approx \sqrt{\rho^2 + (s-s')^2}, \quad (8a)$$

- the observer point is situated on the axis of the cylinder ($\rho = 0$) and the current is assumed to be concentrated on the shell ($\rho' = a$):

$$R = \sqrt{a^2 + (s-s')^2}, \quad (8b)$$

- the current is concentrated in the axis ($\rho' = 0$), see Fig. 8:

$$R = \sqrt{\rho^2 + (s-s')^2}. \quad (8c)$$

The assumptions cause only minor errors if the cylinder is thin in comparison to its length ($a/L \ll 1$) and to the wavelength ($a/\lambda \ll 1$), a = radius of the cylinder.

The most common formula is given by Eq. (8c). So assumption d) is formulated as follows:

- d) the current is assumed to be concentrated in the axis of the wire and expressed by the line current $I(s')$ with the unit vector \vec{e}_s :

$$\vec{J}_{Fz}(\vec{r}') = \frac{I(s')}{2\pi a} \vec{e}_s. \quad (9)$$

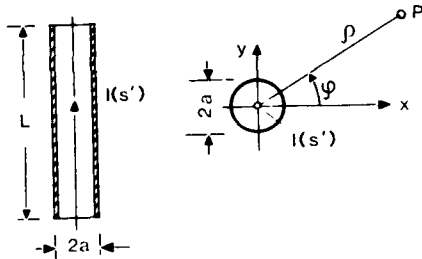


Fig. 8 Introduction of the line current $I(s')$.

With assumption d) it is possible to evaluate the integration over the surface in a trivial manner. A second consequence of assumption d) is, that a coincidence between observer point and integration point is avoided, and therefore, no longer singularity problems must be considered.

Under the assumptions a), b), c) and d) one receives for the scattered field of a thin cylinder of length L :

$$\begin{aligned} \vec{E}_s(\vec{r}) &= \frac{I}{4\pi j\omega\epsilon} \int_L (k^2\phi(\vec{r}, \vec{r}') \vec{e}_s + (\vec{e}_s \cdot \nabla)\nabla\phi(\vec{r}, \vec{r}')) I(s') ds' = \\ &= \frac{I}{4\pi j\omega\epsilon} \int_L \{ (-1-jkR+k^2R^2) \vec{e}_s + (3+3jkR-k^2R^2)(\vec{e}_s \cdot \vec{e}_R)\vec{e}_R \} \frac{e^{-jkR}}{R^3} I(s') ds' = \\ &= \frac{I}{4\pi j\omega\epsilon} \int_L (k^2\phi(\vec{r}, \vec{r}') \vec{e}_s, I(s') + (\nabla' \cdot (\vec{e}_s, I(s')))\nabla\phi(\vec{r}, \vec{r}')) ds', \end{aligned} \quad (10a,b,c)$$

$$\vec{H}_s(\vec{r}) = \frac{I}{4\pi} \int_L (\nabla\phi(\vec{r}, \vec{r}') \times \vec{e}_s) I(s') ds' = \frac{I}{4\pi} \int_L (1+jkR)(\vec{e}_s \times \vec{e}_R) \frac{e^{-jkR}}{R^2} I(s') ds'. \quad (11a,b)$$

Since

$$R = \sqrt{x^2 + y^2 + (s-s')^2} = \sqrt{\rho^2 + (s-s')^2},$$

$$\vec{e}_R = (x \vec{e}_x + y \vec{e}_y + (s-s')\vec{e}_s)/R = (\rho \cos\varphi \vec{e}_x + \rho \sin\varphi \vec{e}_y + (s-s')\vec{e}_s)/R,$$

$$\nabla = \vec{e}_x \frac{\partial}{\partial x} + \vec{e}_y \frac{\partial}{\partial y} + \vec{e}_s \frac{\partial}{\partial s},$$

$$\vec{e}_s \cdot \vec{e}_s = 1, \quad \vec{e}_s \cdot \vec{e}_x = \vec{e}_s \cdot \vec{e}_y = 0,$$

there results for the electric field of a thin cylinder

$$\begin{aligned} \vec{E}_S(\vec{r}) &= \frac{T}{4\pi j\omega\epsilon} \int_L (k^2 \phi(\vec{r}, \vec{r}') \vec{e}_s + \frac{\partial}{\partial s} \nabla \phi(\vec{r}, \vec{r}')) I(s') ds' = & (12a, b, c) \\ &= \frac{T}{4\pi j\omega\epsilon} \int_L \left((-1 - jkR + k^2 R^2) \frac{e^{-jkR}}{R^3} \vec{e}_s + (3 + 3jkR - k^2 R^2)(s-s') \vec{e}_R \frac{e^{-jkR}}{R^4} \right) I(s') ds' = \\ &= \frac{T}{4\pi j\omega\epsilon} \int_L \left(k^2 \phi(\vec{r}, \vec{r}') \vec{e}_s, I(s') + \frac{\partial I(s')}{\partial s'} \nabla \phi(\vec{r}, \vec{r}') \right) ds', \end{aligned}$$

and for the magnetic field

$$\vec{H}_S(\vec{r}) = \frac{T}{4\pi} \rho (-\sin\phi \vec{e}_x + \cos\phi \vec{e}_y) \int_L (1 + jkR) \frac{e^{-jkR}}{R^3} ds'. \quad (13)$$

The latter equation indicates that the thin cylinder has only azimuthal components of the magnetic field.

3. THE INTEGRAL EQUATIONS AND THE METHOD OF MOMENTS

Since the boundary conditions for the total field at the surface of an ideally conducting body are given by

$$\vec{n}(\vec{r}) \times \vec{E}(\vec{r}) = 0, \quad \vec{n}(\vec{r}) \times \vec{H}(\vec{r}) = \vec{J}_F(\vec{r}), \quad \vec{r} \text{ on the surface,} \quad (14)$$

the integral equations for the surface current \vec{J}_F or the line current I can easily be constructed in positioning the observer point on the surface of the scatterer. One receives with the total electric field Eq. (1) and the scattered electric field according Eq. (4a) the Electric Field Integral Equations (EFIE) for general structures:

$$\begin{aligned} \vec{n}(\vec{r}) \times \vec{E}_e(\vec{r}) &= -\vec{n}(\vec{r}) \times \vec{E}_S(\vec{r}) = & (15) \\ &= -\frac{1}{4\pi j\omega\epsilon} \vec{n}(\vec{r}) \times \int_F \left(k^2 \phi(\vec{r}, \vec{r}') \vec{J}_F(\vec{r}') + (\vec{J}_F(\vec{r}') \cdot \nabla) \nabla \phi(\vec{r}, \vec{r}') \right) df'. \end{aligned}$$

The equations (4b,c) lead correspondingly to equivalent integral equations. Because of the Nabla-operator acting on the surface current, the integral equation resulting from Eq. (4c) is denoted as integro differential equation. Using the expression for the total magnetic field Eq. (2) and the scattered magnetic field according Eq. (5b) the Magnetic Field Integral Equation (MFIE) results:

$$\begin{aligned} \vec{J}_F(\vec{r}) &= T \vec{n}(\vec{r}) \times \vec{H}_e(\vec{r}) + T \vec{n}(\vec{r}) \times \vec{H}_S(\vec{r}) = & (16) \\ &= T \vec{n}(\vec{r}) \times \vec{H}_e(\vec{r}) + \frac{T}{4\pi} \vec{n}(\vec{r}) \times \int_F (1 + jkR) (\vec{J}_F(\vec{r}') \times \vec{e}_R) \frac{e^{-jkR}}{R^2} df'. \end{aligned}$$

Equation (5a) again leads to an equivalent formulation of the MFIE.

The equation (15) is an integral equation of the first kind from Fredholm's type with the unknown surface current only inside the integral, whereas the equation (16) is an integral equation of the second kind from the same type with the current outside and inside the integral. Both integral equations in principle can be used for the determination of the surface currents. From the mathematics of integral equations, however, one knows that an integral equation of the second kind in general involves less problems for the solution finding.

Some advantages of the MFIE become obvious in regarding the first term of the right-hand side. If the surface of the scatterer is smooth and convex in the sense that the radius of curvature is large compared to the wavelength, then the factor T becomes 2 and the first term represents the well-known physical optics ansatz for the surface current [2]:

$$\vec{J}_F = 2\vec{n}(\vec{r}) \times \vec{H}_e(\vec{r}).$$

In this case of surface shapes, the integral can be regarded as a correction term for the physical optics current. That is why the MFIE is frequently preferred if the scatterer's surface is smooth. However, the EFIE also can be used for this class of scatterers. In the following we will consider only surfaces for which $T = 2$ is valid.

In applying the boundary conditions to a thin cylinder one usually neglects the effects of azimuthally directed incident fields. Therefore, the boundary condition for the electric field can be readily stated by only regarding the field component in the direction of the axis:

$$\vec{s} \cdot \vec{E}(s) = 0. \quad (17)$$

This leads to the following electric field integral equations:

$$\begin{aligned}
\vec{e}_s \cdot \vec{E}_e(s) &= -\vec{e}_s \cdot \vec{E}_s(s) = & (18a, b, c) \\
&= -\frac{1}{4\pi j\omega\epsilon} \int_L \left(k^2\psi + \frac{\partial^2\psi}{\partial s^2} \right) I(s') ds' = \\
&= -\frac{1}{4\pi j\omega\epsilon} \int_L \left((-1-jkR+k^2R^2) \frac{e^{-jkR}}{R^3} + (3+3jkR-k^2R^2)(s-s')^2 \frac{e^{-jkR}}{R^5} \right) I(s') ds' = \\
&= -\frac{1}{4\pi j\omega\epsilon} \int_L \left(k^2\psi I(s') + \frac{\partial I(s')}{\partial s'} \frac{\partial\psi}{\partial s} \right) ds' .
\end{aligned}$$

Equation (18a) is denoted as integral equation of Pocklington, and equation (18c) is the integro differential equation of Harrington.

The integral equation of Hallén, established for thin cylindrical antennas, is directly related to the integral equation of Pocklington in assuming that the incident field is given by

$$\vec{e}_s \cdot \vec{E}_e(s) = -U_0 \delta(s) ,$$

where U_0 is the excitation voltage over the (infinitesimal small) feeding gap of the antenna. $\delta(s)$ represents the Dirac-function.

If one substitutes in Eq. (18b) $s-s'$ by the relation

$$(s-s')^2 = R^2 - a^2$$

and rearranges the terms one receives the integral equation of Richmond

$$\begin{aligned}
\vec{e}_s \cdot \vec{E}_e(s) &= -\vec{e}_s \cdot \vec{E}_s(s) = & (18d) \\
&= -\frac{1}{4\pi j\omega\epsilon} \int_L \left((1+jkR)(2R^2-3a^2) + k^2a^2R^2 \right) \frac{e^{-jkR}}{R^5} I(s') ds' .
\end{aligned}$$

In reviewing the magnetic field equation (13) for thin cylinders one recognizes that the scattered magnetic field vanishes, if ρ tends to zero. This means, that in the case of zero-thickness there is no magnetic field integral equation. But also for thin cylinders with finite thickness the magnetic field integral equation is fraught with numerical instability problems, so that only the electric field integral equation is applicable.

The integral equations can be transduced to a linear system of equations with the aid of the method of moments [7], which in the following is shortly outlined. For this purpose operators are introduced with which the integral equations can be expressed in a more compact form. The magnetic field integral equation (16) is represented by

$$L_H(\vec{J}_F(\vec{r}')) = -\vec{n}(\vec{r}) \times \vec{H}_e(\vec{r}) , \quad (19)$$

with the operator

$$L_H(\vec{J}_F(\vec{r}')) = -\frac{1}{2} \vec{J}_F(\vec{r}') + \frac{1}{4\pi} \vec{n}(\vec{r}) \times \oint_F (1+jkR) (\vec{J}_F(\vec{r}') \times \vec{e}_R) \frac{e^{-jkR}}{R^2} d\vec{r}' . \quad (19a)$$

These equations will be used in Sec. 4, where the impedance matrix for a structure modeled by surface patches is evaluated.

For the electric field integral equation of a thin cylinder one receives, introducing the scattered field according Eq. (10b)

$$L_E(I) = -\vec{e}_s \cdot \vec{E}_e(s) , \quad (20)$$

with

$$L_E(I) = \frac{1}{4\pi j\omega\epsilon} \vec{e}_s \cdot \int_L \left((-1-jkR+k^2R^2) \vec{e}_s + (3+3jkR-k^2R^2)(\vec{e}_s \cdot \vec{e}_R) \vec{e}_R \right) \frac{e^{-jkR}}{R^3} I(s') ds' . \quad (20a)$$

The equations will be used in Sec. 5 for the representation of the impedance matrix of a wire-grid structure.

In the first case the operator acts on a vector, in the second on a scalar. The more general case, therefore, is described by

$$L(\vec{J}_F(\vec{r}')) = \vec{B}(\vec{r}) , \quad (21)$$

where \vec{B} contains the known incident field. The following procedure can be described by four steps:

- a) Definition of a set of basis functions $\{\vec{F}_n\}$ with coefficients I_n and expansion of the surface current \vec{J}_F according with these basis functions

$$\vec{J}_F(\vec{r}') = \sum_{n=1}^{N^*} I_n \vec{F}_n(\vec{r}') . \quad (22)$$

The coefficients I_n will become the unknowns of the linear system of equations. Since there is a finite number of basis functions an error $\vec{z}(\vec{r})$ arises which is determined by

$$\vec{z}(\vec{r}) = \sum_{n=1}^{N^*} I_n L(\vec{F}_n(\vec{r}')) - \vec{B}(\vec{r}) . \quad (23)$$

- b) Definition of a set of testing or weighting functions $\{\vec{w}_m\}$ and evaluation of the inner products with both sides of Eq. (23):

$$\langle \vec{w}_m, \vec{z} \rangle = \sum_{n=1}^{N^*} I_n \langle \vec{w}_m(\vec{r}), L(\vec{F}_n(\vec{r}')) \rangle = \langle \vec{w}_m(\vec{r}), \vec{B}(\vec{r}) \rangle , \quad m = 1, 2, \dots, M \quad (24)$$

The inner product of two vectors \vec{P} and \vec{Q} is defined by $\langle \vec{P}, \vec{Q} \rangle = \int_F \vec{P} \cdot \vec{Q} \, df$.

F is extended over the common range of definition of the functions \vec{P} and \vec{Q} . The left-hand side of Eq. (24) represents the projection of the error vector in the space of the weighting functions. By forming the moments, the satisfaction of the boundary conditions are enforced in certain points or regions on the scatterer's surface.

- c) Setting the left-hand side of Eq. (24) to zero one receives the following system of equations:

$$LZ_{mn} |x_n| = |y_m| , \quad (25)$$

with

$$Z_{mn} = \langle \vec{w}_m(\vec{r}), L(\vec{F}_n(\vec{r}')) \rangle , \quad (26a)$$

$$y_m = \langle \vec{w}_m(\vec{r}), \vec{B}(\vec{r}) \rangle . \quad (26b)$$

The column vector $|x_n|$ contains the current coefficients I_n , the column vector $|y|$ represents the tangential components of the known fields \vec{E}_e or \vec{H}_e , incident on the scatterer. The incident field may be the field of a plane wave propagating from infinity (scattering case) or the field of the feeding gap of a radiator (antenna case).

The matrix $|Z_{mn}|$ frequently is denoted as generalized impedance matrix. It represents the coupling impedances of the currents of different surface parts. It characterizes the structure independent from aspect angle and polarization of the incident field. The expression impedance matrix was chosen in analogy to the network theory, the unit of the elements is not necessarily the Ohm. In a more general case the elements of the columns may be vectors, the elements of the matrix then are dyads.

The computer effort of the method of moments is concentrated on the computation of the elements of the impedance matrix and the solution of the linear system of equations. In reviewing Eq. (26a) one realizes that for the computation of the matrix elements a twofold integration is necessary, one over the basis functions and the other over the testing functions. In general both integrations are to be evaluated numerically.

The structure of basis and testing functions influences strongly the computer effort. If a basis function is well adapted to the actual current distribution then a comparatively small system of equations is generated since the convergence to the actual current will be fast. On the other side the integration over such basis functions probably can be done only numerically. Using Dirac delta functions as testing functions the first integration in Eq. (26a) just yields the operator, so that only the integration over the basis functions remains. This special case of the moment method is denoted as point-matching method which is also known as collocation method. Physically this means, that the boundary conditions are satisfied not continuously over the total structure but rather in discrete points. The point-matching method is frequently applied in electromagnetics. In the case of thin cylinders the use of pulse functions as basis functions leads to very simple expressions and the use of trigonometric functions even allows an analytical evaluation of the integral. If basis and testing functions are chosen to be equal one has another special case of the method of moments known as Galerkin's method. Galerkin's method with trigonometric functions is applied in literature [18, 19] in treating thin-wire structures. Of special interest is the use of pulse functions as basic functions and the approximation of the operator integral by its mean value, that is, for the integration the pulses are reduced to Dirac delta functions, see the following sections.

In the literature there are numerous examples in combining basis and testing functions to treat scatterers, which are modeled by surface patches or/and wire-grids, with the EFIE or/and MFIE. A survey over the literature and a summary of the different experiences till now would result in an own report, see [20, 21]. The following table 1 presents computer programs, which solve three-dimensional scatter problems. One realizes that the point-matching method with pulses as basis functions are preferred. Pulse functions seem also to have some advantage when one tries to satisfy the edge condition, see [22]. Fig. 9 shows the current distribution of a flat plate when a wave is normally incident. The dashed line shows the current when the edge conditions are satisfied by an edge correction term, while the solid line shows the current represented by pulses alone.

There is a great variety of methods for the solution of large linear systems of equations. A good survey is given in [26]. The methods may be classified into direct and iterative methods:

Name of the computer program	Reference	Model	Basis functions	Testing functions	Field-integral equation
WIRE-GRID BODY PROGRAM	6	wire-grid	pulse	Dirac	EFIE
WF-OSU/NPS1	23	wire-grid	trigonometric	trigonometric	EFIE
H3F-TUD1	24	surface patches and wire-grid	pulse pulse	Dirac Dirac	MFIE and EFIE
NEC	25	surface patches and wire-grid	pulse and trigonometric	Dirac Dirac	MFIE and EFIE
INFE	17	surface patches	pulse	Dirac	MFIE

Abbreviations:

WF-OSU/NPS1: Wire Configuration, Frequency domain, originated at Ohio State University, modified at Naval Postgraduate School, Monterey, California
H3F-TUD1: Hybrid, 3-dimensional, Frequency domain, developed at the Technical University of Denmark
NEC: Numerical Electromagnetics Code
INFE: Integral equation method Near Field Evaluation

Table 1 Some computer programs based on the IEM.

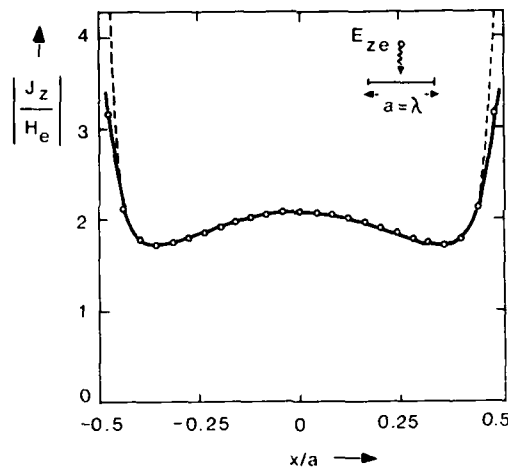


Fig. 9 The behaviour of pulse functions near the edges of a flat plate.

1. Direct solution methods

Gaussian elimination

2. Iterative methods

2.1 Linear iterative methods

Jakobi's iterative method
Seidel's iterative method

2.2 Nonlinear iterative methods

method of steepest descent
conjugate gradient method

The advantage of the direct solution method becomes obvious if the current distribution has to be determined for a variety of aspect angles or/and polarizations of the incident field. Since the matrix elements depend only from the geometrical parameters of the structure and the frequency, the computer effort for the inversion of the matrix has to be done only once per frequency. The currents for the different situations are determined only by multiplying the inverted matrix with the incident field.

A very important point for practical application of the method of moments is the estimation of the computer effort with respect to storage and time. The dimension N of the system of equations and therefore with the number of the complex unknowns to be determined are influenced by the chosen basis and testing functions and the mathematical model of the scatterer. For the estimation of N the following empirical va-

lues can serve, see also the following paragraph:

- a) modeling by surface patches, point-matching method, pulse functions as basis functions:

$$N < 50 \frac{F}{\lambda^2}, \quad (27)$$

if F is the surface of the scatterer,

- b) wire-grid modeling, point-matching method, pulse functions as basis functions:

$$N < 200 \frac{F}{\lambda^2}. \quad (28)$$

From this rough estimation it becomes evident, that the application limits of the integral equation methods are reached if the dimensions of the scatterer will exceed some few wavelengths.

In the following Tables 2 and 3 the computer storage and the number of arithmetic operations for various methods are compared [26].

Method	Core Storage	Method	Number of arithmetic operations		
			Divisions	Multiplications	Additions
Gaussian elimination	N^2+2N	Gaussian elimination +	N	$N^3/3+N^2-N/3$	$N^3/3+N^2/2-5N/6$
Seidel's iterative method	N^2+2N	Seidel's and Jacobi's iterative method ++	N	N^2	N^2-N
Gaussian elimination with complete pivoting	N^2+3N	method of steepest descent ++	1	$2N^2+3N$	$2N^2+4N$
Jacobi's iterative method	N^2+3N	conjugate gradient method ++	2	$2N^2+6N$	$2N^2+6N$
method of steepest descent	N^2+4N+2	+ Gaussian elimination with complete pivoting requires $N^3/3+N^2/2-5N/6$ comparisons in addition to the above arithmetic operations			
conjugate gradient method	N^2+6N+3	++ number of arithmetic operations per iteration			

Table 2 Core storage requirement of various methods for the solution of linear system of equations.

Table 3 Number of arithmetic operations of various solution methods.

4. MODELING OF SMOOTH BODIES BY SURFACE PATCHES

In this section details, see also [24, 27], are given for the application of the MFIE, when the surface of the structure is modeled by patches (solid surface structures). The basis functions are chosen to be pulse functions and the point-matching method is applied. Use is made from the formula (19) with the operator L_H given by Eq. (19a).

The surface of the smooth body is modeled by N^s surface patches with sizes ΔF_q , see Fig. 10. The experience shows that far field problems will be solved with sufficient accuracy if one models a surface of one square wavelengths by at least 20 to 30 patches. This means that the edge length of a surface patch should have an amount of less than about $\lambda/5$ (maximum size of about 0.04 square wavelengths).

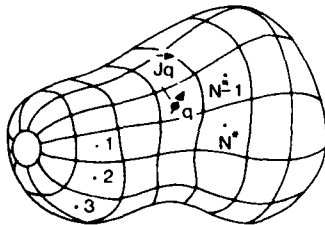


Fig. 10 Modeling of a surface $F(\xi, \eta)$ of a smooth body by N^s surface patches.

In choosing basis functions $S_q(\xi, \eta)$ the surface current is expanded according

$$\vec{J}_F(\xi, \eta) = \sum_{q=1}^{N^s} \vec{J}_q S_q(\xi, \eta). \quad (29)$$

S_q represents a pulse function with amplitude 1 on the surface patch q and 0 on all other surface patches. ξ^q and η are orthogonal coordinates of a local coordinate system (ξ, η, n) , where ξ and η are parallel to the plane of the patch. For the unit vectors of the local coordinate system the following relations hold:

$$\vec{e}_n = \vec{e}_\xi \times \vec{e}_\eta \quad \text{or} \quad \vec{n} = \vec{e}_\xi \times \vec{e}_\eta. \quad (30)$$

\vec{n} is the normal unit vector on the patch, see Fig. 11a.

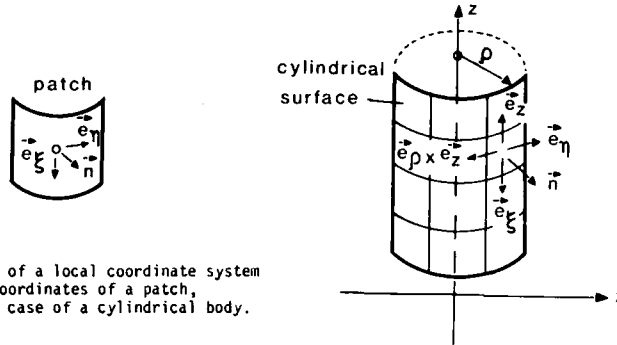


Fig. 11 Definition of a local coordinate system
a) local coordinates of a patch,
b) special case of a cylindrical body.

The orientation of the local coordinate system within the global coordinate system depends on the specific geometry of the scatterer. For a cylindrical body, the axis of which points in the direction of the z -axis of a global cylindrical coordinate system (ρ, φ, z) , the relation between local and global coordinate system can be established by the following equation:

$$\vec{e}_\zeta = \frac{\vec{n} \times (\vec{e}_\rho \times \vec{e}_z)}{|\vec{n} \times (\vec{e}_\rho \times \vec{e}_z)|}, \quad (31)$$

see Fig. 11b.

In this case, where the current coefficients \vec{J}_q are vectors, one receives instead of Eq. (25) the following system of equations

$$[\vec{Z}_{pq}] \cdot [\vec{x}_q] = [\vec{y}_p],$$

where the matrix elements are dyads and the elements of the columns are vectors.

Introducing the current expansion in the operator of Eq. (19) and choosing the point-matching method one explicitly receives the following system of equations:

$$[\langle \delta_p, L_H(S_q) \rangle] \cdot [\vec{J}_q] = - [\langle \delta_p, \vec{n}_p \times \vec{H}_{pe} \rangle]. \quad (32)$$

δ_p denotes a Dirac function, which is infinite in the center of the patch p and zero in all other regions of the structure. In the center of each patch the current is decomposed into two orthogonal components $J_{q\xi}$ and $J_{q\eta}$:

$$\vec{J}_q = J_{q\xi} \vec{e}_{q\xi} + J_{q\eta} \vec{e}_{q\eta}. \quad (33)$$

The vectorial elements of the current column therewith are

$$\vec{x}_q = J_{q\xi} \vec{e}_{q\xi} + J_{q\eta} \vec{e}_{q\eta}. \quad (34)$$

The vectorial elements of the right-hand side are represented by

$$\vec{y}_p = - \langle \delta_p, \vec{n}_p \times \vec{H}_{pe} \rangle = (\vec{e}_{p\eta} \cdot \vec{H}_{pe}) \vec{e}_{p\xi} - (\vec{e}_{p\xi} \cdot \vec{H}_{pe}) \vec{e}_{p\eta}, \quad (35)$$

where $\vec{n}_p = \vec{e}_{p\xi} \times \vec{e}_{p\eta}$ is introduced.

For the determination of the matrix elements \vec{Z}_{pq} the integral of the operator Eq. (19a) must be evaluated. This can be simplified by assuming that the distance R_{pq} between integration point varying on patch q and observer point situated in the center of patch p is given by the distance between the centers of the patches q and p , see Fig. 12. This means, for the integration purpose the pulse functions are reduced to Dirac functions. With these simplifications we get the following analytical expressions for the matrix elements:

$$\vec{Z}_{pp} = - \frac{1}{2} (\vec{e}_{p\xi} \vec{e}_{p\xi} + \vec{e}_{p\eta} \vec{e}_{p\eta}) = - \frac{1}{2} \vec{E}, \quad p = q, \quad (36a)$$

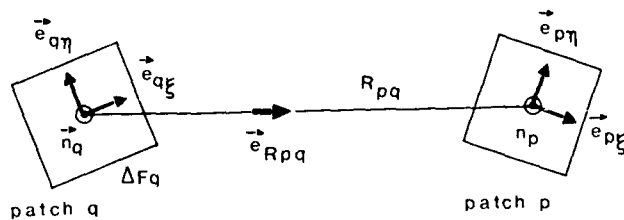


Fig. 12 Geometrical situation of two patches.

$$\begin{aligned} \bar{Z}_{pq} = & \frac{\Delta F_q}{4\pi} \frac{1+jkR_{pq}}{R_{pq}^2} e^{-jkR_{pq}} (\vec{e}_{p\zeta} \cdot (\vec{e}_{q\zeta} \times \vec{e}_{R_{pq}}) \vec{e}_{p\eta} \vec{e}_{q\zeta} + \vec{e}_{p\zeta} \cdot (\vec{e}_{q\eta} \times \vec{e}_{R_{pq}}) \vec{e}_{p\eta} \vec{e}_{q\eta} - \\ & - \vec{e}_{p\eta} \cdot (\vec{e}_{q\zeta} \times \vec{e}_{R_{pq}}) \vec{e}_{p\zeta} \vec{e}_{q\zeta} - \vec{e}_{p\eta} \cdot (\vec{e}_{q\eta} \times \vec{e}_{R_{pq}}) \vec{e}_{p\zeta} \vec{e}_{q\eta}), \quad p \neq q. \end{aligned} \quad (36b)$$

ΔF_q = area of patch q,

$\vec{e}_{R_{pq}}$ = unit vector directed from the center of patch q towards the center of patch p.

For the determination of the elements Z_{pp} of the main diagonal the contribution of the integral in the operator is neglected in order to avoid the singularity. This procedure approximates the principal value of the integral.

Eq. (36b) may be written in the following alternative form:

$$\bar{Z}_{pq} = -\frac{\Delta F_q}{4\pi} \frac{1+jkR_{pq}}{R_{pq}^2} e^{-jkR_{pq}} (\vec{e}_{R_{pq}} \cdot \vec{n}_p - (\vec{e}_{R_{pq}} \cdot \vec{n}_p) \vec{E}).$$

The dimension N (number of complex unknowns) of the linear system of equations to be solved is determined as follows: a patch size of about $\lambda/5$ results in 25 patches for one square wavelength of the scatterer's surface. For each patch 2 complex current coefficients have to be determined. Therefore the dimension of the complex linear system of equations can be estimated by $N = 2N^2 \sim 50 F/\lambda^2$, F representing the surface size of the scatterer.

The following Fig. 13 represents the time t which computers of the type IBM 3081 and CRAY-1 need for the inversion of the complex matrix. The time required by the computer CRAY-1, which is installed at the data center in Oberpfaffenhofen, may be expressed by the formula

$$T = (1.59 N^3 + 70 N^2) 10^{-6} \text{ s},$$

N = number of the complex unknowns. The Gaussian elimination method with complete pivoting was used.

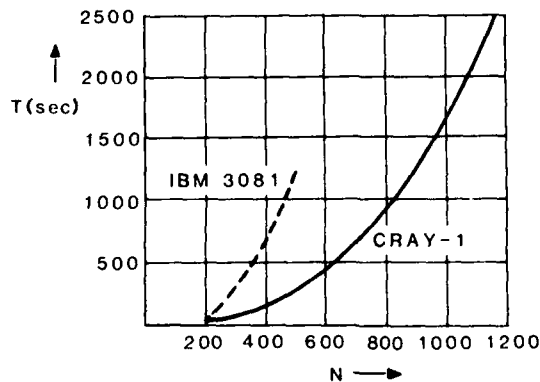


Fig. 13 Computer time for matrix inversion, N = number of complex unknowns (dimension of the complex matrix), N^2 = $N/2$ = number of surface patches.

One can see, that the computer time increases with approximately N^3 . Assuming that a patch has a size of $\lambda^2/25$ then the dimension $N = 1120$ means that the surface of the body to be modeled may have a size of about $22 \lambda^2$. A cube, which is a representative of a three-dimensional scatterer, has then an edge length

of a little less than 2λ . It is to be emphasized, however, that for accurate near field investigations the patch sizes must be chosen to be much smaller as assumed in this section.

5. MODELING OF STRUCTURES BY A WIRE-GRID

The method of wire-grid modeling is based on the fact, that a structure consisting of thin wires (Fig. 14), has the same electromagnetic features as a solid structure, if the mesh width is chosen to be sufficiently small.

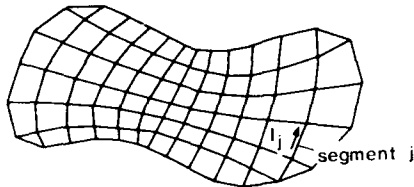


Fig. 14 Modeling of a structure by thin wires.

A good estimation of the mesh width is obtained, if a source is positioned within a structure, which is modeled by a wire-grid with variable mesh width. The field in the exterior of the structure, which should be zero, is then computed in dependence from the mesh width.

For this theoretical experiment a cube with an edge length of 0.4λ has been chosen. In the center of the cube a point source was positioned. The diameter of the wire was 0.003λ , so that the thin cylinder approximation of the EFIE holds. The basis functions are chosen to be pulses, the boundary conditions were satisfied in the center of the wire (Dirac functions as testing functions).

Figure 15 shows the electric field in the exterior in dependence from the mesh width. A mesh width of 0.057λ corresponds to about 600 wire segments. One can assume, that a mesh width of about 0.1λ in modeling a structure could be sufficient for far-field computations. This means, that about 200 wire segments are necessary to model a surface with a size of $\lambda \times \lambda$. Since per segment only one current coefficient has to be determined the dimension of the linear system of equations is given by $N = 200 F/\lambda^2$. Shorter wire segments, 0.05λ or less, may be needed in modeling critical regions of a structure.

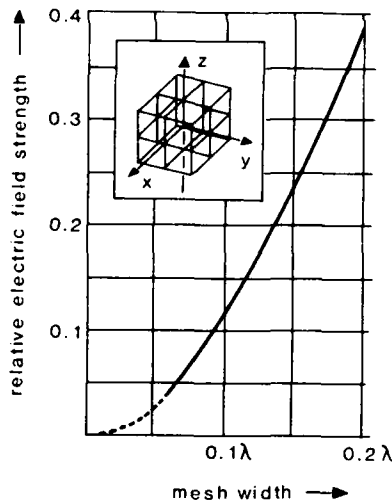


Fig. 15 Influence of the mesh width.

For the solution of this scattering problem the EFIE is applied. Use is made from the formula (20) with the operator L_E given by Eq. (20a). The line current $I(s')$ is expanded in a set of pulse functions $P_j(s')$:

$$I(s') = \sum_{j=1}^N I_j P_j(s') . \quad (37)$$

The pulse functions have the value 1 on wire segment j and zero on all other segments. N is identical with the total number of segments. Using the point-matching method one receives the linear system of equations

$$[Z][x] = [y]$$

in the following form

$$L\langle\delta_i, L_E(\rho_j)\rangle |I|_j = -L\langle\delta_i, \vec{e}_{s_i} \cdot \vec{E}_e\rangle. \quad (38)$$

The elements of the current column now are scalars and given by

$$x_j = I_j, \quad (39)$$

and the elements of the right-hand side result in

$$y_i = -\vec{s}_i \cdot \vec{E}_e. \quad (40)$$

If again the numerical integration in the operator is avoided by reducing the pulses to Dirac functions one gets for the matrix elements immediately

$$Z_{ij} = \frac{\Delta x_j}{4\pi j \omega \epsilon} \frac{e^{-jkR_{ij}}}{R_{ij}^3} ((-1-jkR_{ij} + k^2 R_{ij}^2)(\vec{e}_{s_i} \cdot \vec{e}_{s_j}) + (3+3jkR_{ij} - k^2 R_{ij}^2)(\vec{e}_{s_i} \cdot \vec{e}_{R_{ij}})(\vec{e}_{s_j} \cdot \vec{e}_{R_{ij}})). \quad (41)$$

R_{ij} = distance between the centers of the segments i and j ,

$\vec{e}_{R_{ij}}$ = unit vector directed from segment j toward segment i ,

Δx_j = length of segment j ,

\vec{e}_{s_i} respectively \vec{e}_{s_j} = unit vector parallel to segment i respectively segment j , see Fig. 16.

The main diagonal elements can be formally determined from Eq. (40). The expression cannot become singular since the line current coincides with the axis of the segment and the boundary conditions are satisfied on the surface of the segment.

Since there are analytical expressions for the matrix elements the matrix fill time is very low, as before. This procedure was developed in [24] and provided good results when antennas on satellites were computed.

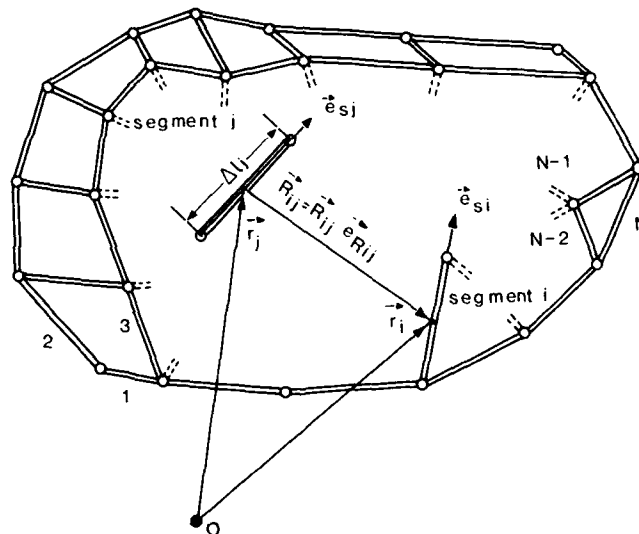


Fig. 16 Geometry of a wire-grid.

6. APPLICATION EXAMPLES

In literature there are numerous examples to demonstrate the field of application of the integral equation method as well in the antenna as in the scattering case. Therefore, the following list, which only can give a survey, cannot be complete, also only those configurations are mentioned, for which either experimental results or results of independent theories are available for comparison. Most of the examples are taken from reference [5]. Where this is not the case the pertinent reference is cited behind the example.

Solid surface structures

- bistatic cross-section (BSCS) of a sphere,
- radiation pattern (RP) and input impedance of a monopole antenna, driven against a sphere,
- BSCS of a spheroid,
- monostatic cross-section (MSCS) of a cone sphere,
- MSCS of a flat-back cone,
- MSCS of a right circular cylinder [5] and [28],
- MSCS of a sphere-cylinder,
- MSCS of a stub-cylinder,
- MSCS of a rectangular box [28],
- mutual impedances between two rectangular dipoles [28],
- MSCS of a thin plate [28],
- MSCS of a thick plate [29],
- MSCS of a cube [29].

Wire-grid structures

- MSCS of a circular disk,
- MSCS of a sphere,
- MSCS of a slotted grid,
- BSCS of a cone sphere,
- scattered field pattern of a OH-6a helicopter model,
- RP of a towel-bar humming antenna on a OH-6a helicopter model,
- MSCS of an aircraft (MiG 19) model [30],
- MSCS of two coplanar, concentric rings,
- MSCS of a planar, log-periodic zig-zag array,
- MSCS of a five-ring, log-periodic array of circular rings,
- MSCS of a straight wire, straight wire with low-impedance terminations, eleven-element array of log-periodically spaced straight dipoles, diamond-band dipole, circular ring with spokes, seven-ring array squirrel cage,
- input impedance of a $2\ 1/2$ -turn loop [6],
- input impedance of a three-element coplanar TEM-line antenna [6],
- RP of a monopole and a circular slot in the base of a cone [6, 33],
- RP of a monopole and a loop on a cube [3],
- RP of a three-element Yagi antenna [3],
- RP of a fifteen-element Yagi antenna [3],
- RP of corner reflectors [3],
- input impedance and current distribution of linear antennas [3, 31],
- input resistance and RP of a pair of dipoles over lossy ground [3],
- input impedance and RP of twelve-element log-periodic dipole antenna [32],
- gain of coupled log-periodic dipole antennas (systems of two, three and five log-periodic antennas) [32],
- gain and RP of log-periodic dipole feeds for reflector antennas [32].

Combination of solid surface structures and wire-grid structures

- antenna on a cylindrical satellite model with experimental boom or solar cells [24],
- cylinder with excited and passive elements, RP [34],
- cone-sphere with loop, RP [34],
- sphere with excited and passive elements, RP [34].

In the following two further examples are presented showing particular features, which are different from the cited examples. In the first example the radiation pattern of a monopole antenna on a helicopter is determined. The theoretical results computed for a wire-grid model, which only can roughly represent the real structure, are compared with in flight-measurements of a real helicopter. The second example deals with the scattered field of a cube. For this geometrically simple structure the numerical model with patches agrees perfectly with the real structure. The extreme near field behaviour is subject of the investigations.

Fig. 17 shows the wire-grid model of a helicopter of the type Bo 105 and Fig. 18 the details of the actual structure with the position of the two $\lambda/4$ -monopoles operating in the VHF-band. The antenna on the right-hand side of the flight direction was driven, the other was terminated. The in flight-measurement [35] of the radiation pattern in the horizontal plane for a frequency of 117,6 MHz is represented in Fig. 19 by the dashed line. The flight direction is defined by $\psi = 0^\circ$. For the computation of the radiation pattern the computer program WF-OSU NPS 1 was used. It could be shown that the immediate neighbourhood of the antennas, that is the shape of the top side and the drive for the blades, must carefully be modeled while the farer parts of the helicopter, especially the lower part could be approximated only roughly or even completely neglected. The actual thickness of the shaft of the drive was taken into account. In principle a monopole array, consisting of a driven and two parasitic excited monopoles, a thin and thick one, over a finite plane, was analyzed. The theoretical results are illustrated in Fig. 19 by the solid line.

The cube of the second example had an edge length of λ . The incident field is oriented parallel to the z-axis. Each side of the cube was modeled by 25 to 49 patches, that is, the patches had a dimension of $0.2\ \lambda$ to $0.14\ \lambda$, see Fig. 20. In using the point-matching method with pulses for the current one follows exactly the details of Sec. 4 for the determination of the surface current. The computation of the extreme near field, however, is indicated in Sec. 2, see [17].

The computed copolar component in amplitude and phase of the current on the front side (side II) is compared with measurements in Fig. 21. The copolar tangential electric field component is depicted together with measurements in Fig. 22. For various distances from the surface this component has to vanish if one reaches the surface. In this way an internal accuracy test of the integral equation method may be performed. The measurements were carried out at a wavelength of $\lambda = 30$ cm. Amplitudes and phases are re-

10-16

lative values.

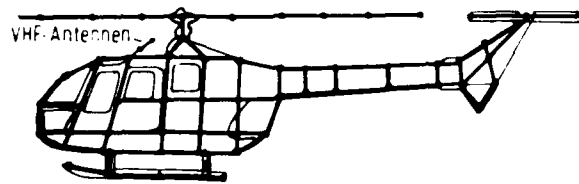


Figure 17 Wire-grid model of a Bo 105-helicopter.

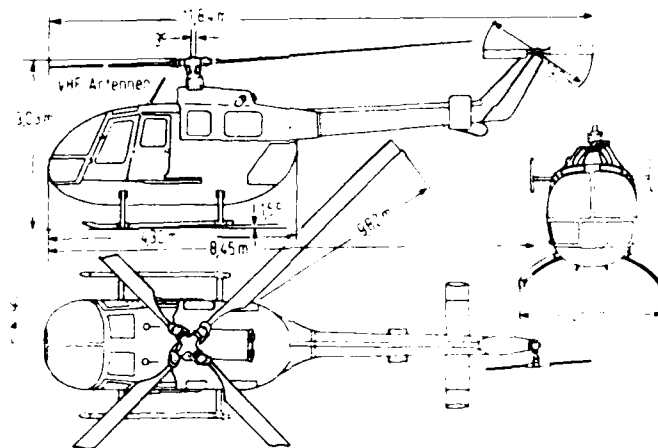


Figure 18 Position of the VHF-antennas on the helicopter.

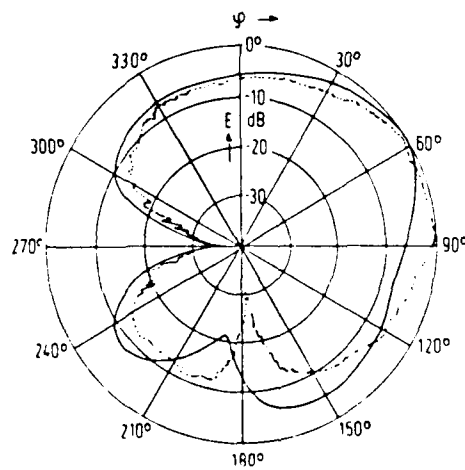


Fig. 19 Comparison between in flight-measurements (dashed line) and results of the IEM (solid line), frequency 117.6 MHz.

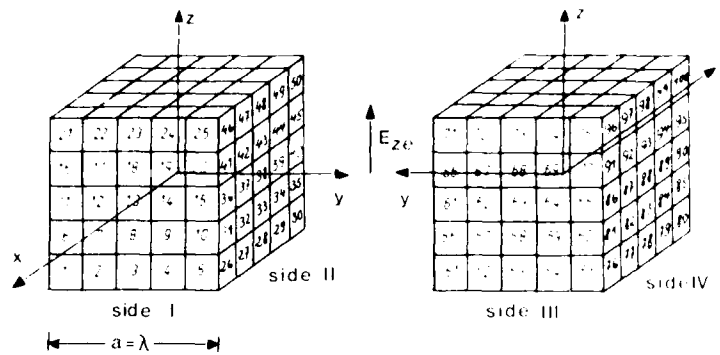


Fig. 20 Modeling of a cube by surface patches.

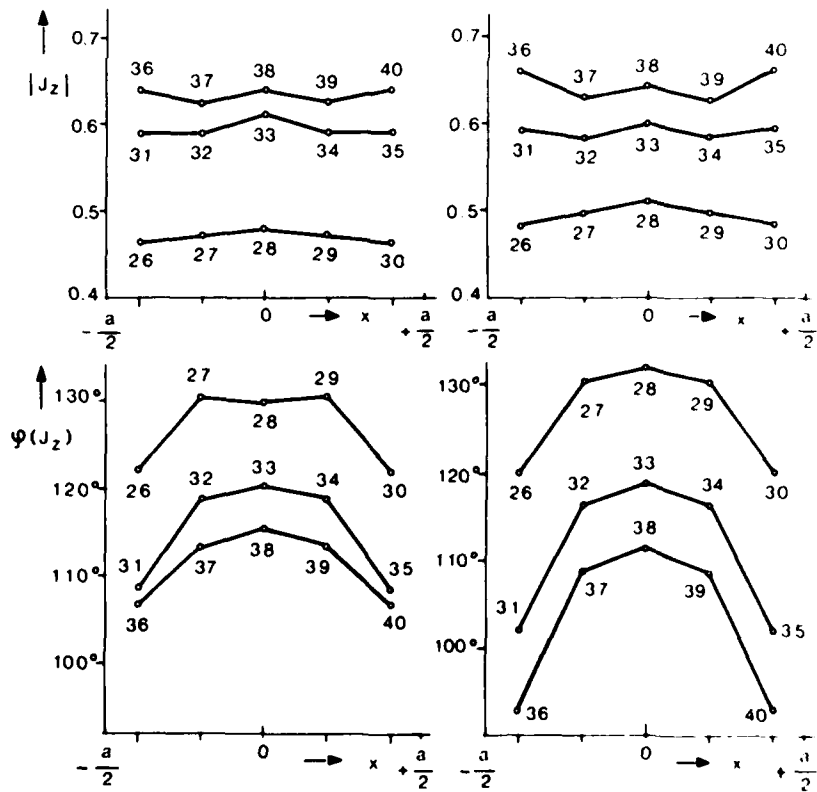


Fig. 21 Comparison of experimental (left side) and theoretical (right side) results for amplitude and phase of the current distribution on the front side (side II) of the cube.

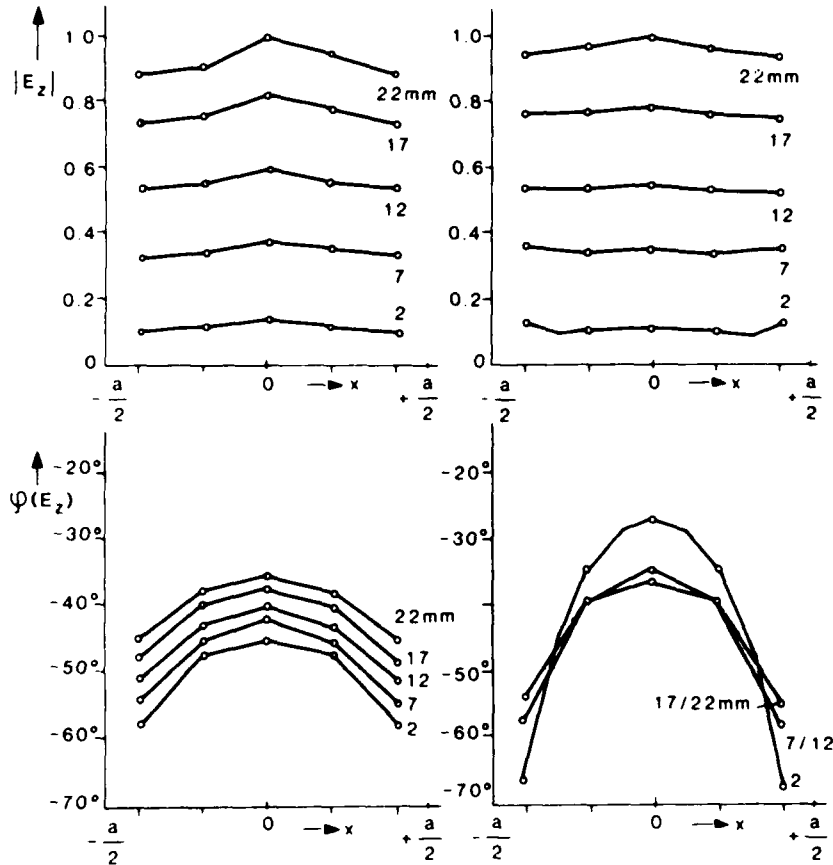


Fig. 22 Comparison of experimental (left side) and theoretical (right side) results for amplitude and phase of the tangential electric field component with the distance from the cube as parameter.

7. CONCLUSION

The objective of the paper has been to consider the range of application of the integral equation method under practical viewpoints. A brief review of the electromagnetic field integral representations, the resulting integral equations and their solution with the aid of the method of moments was provided. A survey of computer programs was given, which were used to solve practical problems within the own research work. From the great variety to choose basis and testing functions only pulses and Dirac functions were considered and applied on structures, which are modeled either by patches or wire-grids. For these cases estimations for the minimum number of unknowns are made and therewith the core storage and the number of arithmetic operations for the solution of the integral equations can be determined. Since the number of structures, which are treated by the integral equation method, is very high, only a survey, which cannot be complete, with citing of the references was given. Two application examples are outlined in more details: the radiation pattern of a VLF antenna on a helicopter modeled by wire grids and the extreme near field of a cube modeled by patches which forms the preliminary step to compute the phase lines of an incident field disturbed by an airplane structure.

The integral equation method seems to be suited to compute the scattered near and far field of a variety of application oriented structures under economic viewpoints if the dimensions of the structure are comparable to the wavelength, even in the case that symmetry properties will be used, the size of the structures will be limited to a few wavelengths. The aim for further work is to make more internal accuracy checks in a systematic manner by studying the convergence of the results, in dependence from the size of patches or wire segments, or by investigating the near field properties.

8. REFERENCES

- [1] F.K. Oshiro, Ch.W. Su, "A Source Distribution Technique for the Solution of General Electromagnetic Scattering Problems", Northrop Corporation Norair Division, Hawthorne, California 90250, NOR-65-271, Oct. 1965.
- [2] V. Stein, "Physical Optics Method: Prediction of Radar Signatures", AGARD Lecture Series No. 152 on: "Theoretical Aspects of Target Classification", Rom, Neubiberg, Noresund, 1987.
- [3] A. Schroth, V. Stein, "Moderne numerische Verfahren zur Lösung von Antennen- und Streuproblemen", München: R. Oldenbourg Verlag, 1985.
- [4] J.B. Keller, "Diffraction by an Aperture", *J. Appl. Phys.*, Vol. 28, No. 4, Apr. 1957, pp. 426-444.
- [5] A.J. Poggio, E.K. Miller, "Integral Equation Solutions of Three-Dimensional Scattering Problems", Chapter 4 in "Computer Techniques for Electromagnetics", Oxford, New York, Toronto, Sydney, Braunschweig: Pergamon Press, 1973, edited by R. Mittra.
- [6] G.A. Thiele, "Wire Antennas", Chapter 2 in "Computer Techniques for Electromagnetics", Oxford, New York, Toronto, Sydney, Braunschweig, Pergamon Press, 1973, edited by R. Mittra.
- [7] R.F. Harrington, "Field Computation by Moment Methods", New York: The Mcmillan Company, 1968.
- [8] K.K. Mei, M.A. Morgan, S.K. Chang, "Finite Methods in Electromagnetic Scattering", Chapter 10 in "Electromagnetic Scattering", New York, San Francisco, London: Academic Press, 1978, edited by P.L.E. Ushlenghi.
- [9] M. Morgan, "Numerical Modeling: Finite Methods", AGARD Lecture Series No. 152 on: "Theoretical Aspects of Target Classification", Rom, Neubiberg, Noresund, 1987.
- [10] E.F. Knott, "A Progression of High-Frequency RCS Prediction Techniques", *Proceedings of the IEEE*, Vol. 73, No. 2, Febr. 1985, pp. 252-264.
- [11] J.A. Stratton, "Electromagnetic Theory", New York, London: McGraw-Hill Book Company, 1941, pp. 464-470.
- [12] S. Silver, "Microwave Antenna Theory and Design", New York, Toronto, London: McGraw-Hill Book Company, 1949, pp. 80-80.
- [13] V. Stein, "Die Integraldarstellungen des elektromagnetischen Felds", DFVLR, Institut für Hochfrequenztechnik, 18 551-d5/7, 1985.
- [14] H. Moll, A.W. Maue, K. Westpfahl, "Theorie der Beugung", in "Handbuch der Physik", S. Flügge (editor), Berlin, Göttingen, Heidelberg: Springer Verlag, 1961, S. 252-258, 311.
- [15] D.S. Jones, "The Theory of Electromagnetism", New York: Pergamon, 1964, pp. 566-569.
- [16] D.B. Miron, "The Singular Integral Problem in Surfaces", *IEEE Transactions on Antennas and Propagation*, Vol. AP-31, No. 5, May 1983, pp. 507-509.
- [17] C. Kemptner, "Nahfeldberechnungen bei komplizierten Körpern mittels der Integralgleichungsmethode", Institut für Hochfrequenztechnik, DFVLR, Oberpfaffenhofen, to be published 1987.
- [18] J.H. Richmond, "Computer Analysis of Three-Dimensional Wire Antennas", The Ohio State University, Electro Science Laboratory, Technical Report 2708-4, 1969.
- [19] J.H. Richmond, "Radiation and Scattering by Thin-Wire Structures in the Complex Frequency Domain", The Ohio State University, Electro Science Laboratory, Report 2902-10, NASA CR-2396, 1974.
- [20] T.K. Sarkar, "An Note on the Choice of Weighting Functions in the Method of Moments", *IEEE Transactions on Antennas and Propagation*, Vol. AP-33, No. 4, April 1985, pp. 436-441.
- [21] T.K. Sarkar, A.R. Djordjevic, E. Arvas, "On the Choice of Expansion and Weighting Functions in the Numerical Solution of Operator Equations", *IEEE Transactions on Antennas and Propagation*, Vol. AP-33, No. 9, Sept. 1985, pp. 988-996.
- [22] D.R. Wilton, S. Govind, "Incorporation of Edge Conditions in Moment Method Solutions", *IEEE Transactions on Antennas and Propagation*, Vol. AP-25, No. 6, Nov. 1977, pp. 845-850.
- [23] J.W. McCormack, "ASAP, Antennas-Scatterers Analysis Program, a General Purpose User-Oriented Computer Program for Analysis of Thin-Wire Structures in the Presence of Finite Ground", Naval Postgraduate School, Monterey, Calif., Report No. NPS-52 AP-74122, AD/A-004-227, Dec. 1974.
- [24] N.C. Albertsen, J.E. Hansen, N. Eilskov Jensen, "Computation of Spacecraft Antenna Radiation Patterns", Laboratory of Electromagnetic Theory, The Technical University of Denmark, Lyngby, Report R 108, June 1972.
- [25] G.J. Burke, A.J. Poggio, "Numerical Electromagnetics Code (NEC) - Method of Moments", Lawrence Livermore Laboratory, NOSC TD 116, Vol. 1 and Vol. 2, Jan. 1981.
- [26] T.K. Sarkar, K.R. Siarkiewicz, F.R. Stratton, "Survey of Numerical Methods for Solution of Large Systems of Linear Equations for Electromagnetic Field Problems", *IEEE Transactions on Antennas and Propagation*, Vol. AP-29, No. 6, Nov. 1981, pp. 847-856.

- [27] N.C. Albertsen, "Study of VHF Antennas on Large Satellites", TICRA A/S, Lyngby, Denmark, Report S-19-02, April 1974.
- [28] J.J.H. Wang, Ch. J. Drane, "Numerical Analysis of Arbitrarily Shaped Bodies Modeled by Surface Patches", IEEE Transactions on Microwave Theory and Techniques, Vol. MTT-30, No. 8, Aug. 1982, pp. 1167-1173.
- [29] L.L. Tsai, D.G. Dudley, D.R. Wilton, "Electromagnetic Scattering by a Three-dimensional Conducting Rectangular Box", Journal of Applied Physics, Vol. 45, No. 10, Oct. 1974, pp. 4393-4400.
- [30] Y.T. Lin, "EM Modeling of Aircraft at Low Frequencies", IEEE Transactions on Antennas and Propagation, Vol. AP-23, no. 1, Jan. 1975, pp. 53-56.
- [31] R.F. Harrington, J.R. Mautz, "Straight Wires with Arbitrary Excitation and Loading", IEEE Transactions on Antennas and Propagation, Vol. AP-15, No. 4, July 1967, pp. 505-515.
- [32] W.A. Inbriale, "Application of the Method of Moments", Chapter 2 in "Numerical and Asymptotic Techniques in Electromagnetics", Berlin, Heidelberg, New York: Springer Verlag, 1975, edited by R. Mittra.
- [33] W.L. Stutzmann, G.A. Thiele, "Antenna Theory and Design", New York, Chichester, Brisbane, Toronto: John Wiley and Sons, 1981, pp. 309-365.
- [34] J.F. Shaeffer, L.N. Medgyesi-Mitschang, "Radiation from Wire Antennas Attached to Bodies of Revolution: The Junction Problem", IEEE Transactions on Antennas and Propagation, Vol. AP-29, No. 3, May 1981, pp. 479-487.
- [35] H. Bothe, "Flugvermessung der Strahlungsdiagramme von 4 Bordantennen des Hubschraubers Bo 105", DFVLR, Institut für Flugführung, IB 153-76/10, 1976.

9. ACKNOWLEDGEMENT

The author wishes to thank his colleagues E. Kemptner for developing the computer program INFE and for carrying out the near field computations for the cube and K.-H. Dreher for the precise near field and current measurements. Thanks are also due to Mrs. M. Malchow for carefully typing the manuscript and Miss G. Jacob for accurately drawing the illustrations.

EXPERIMENTS: TEST RANGE FACILITIES (PART 1)

Michael A. Morgan, Associate Professor, (Code 62Mo)
Naval Postgraduate School, Monterey, CA 93943 USA

AD-P005 654

SUMMARY

A brief overview of some of the transient electromagnetic scattering ranges at U.S. universities and research facilities will be given. This will be followed by a detailed discussion of the Transient Electromagnetic Scattering Laboratory which is located at the Naval Postgraduate School. Particular attention is given to the role of this facility in studies of natural resonance target classification studies. Detailed consideration will be given to the measurement concepts of transient scattering, with examples presented to illustrate the procedures and requisite signal processing that is involved.

INTRODUCTION

Transient electromagnetic scattering measurements offer a viable and often advantageous alternative to the more conventional continuous wave (CW) approach. As a result of recent advances in short-pulse technology, impulse generators having very broad instantaneous bandwidths, as high as several thousand to one, are available. Transient measurements also provide response waveforms that can be directly interpreted as to cause and effect. In fact, the fundamental methodology behind transient scattering measurements can be considered as an extension of that which is utilized in time domain reflectometry (TDR). The TDR method has been extensively employed for measuring dispersion and imperfections on guided wave structures, [1].

In the historical context, transient scattering ranges are relatively recent innovations when compared to their CW counterparts. This is not surprising, since electromagnetic analysis and design has historically tended to be heavily biased towards frequency domain approaches. The development of fast pulse sources and sampling oscilloscopes in the 1960's provided the technical foundation for direct transient scattering measurements. One of the earliest facilities to use this new technology began operation at Sperry Research Center in the late 1960's, [2]. This was a ground plane range which supported theoretical efforts in radar target imaging through synthesized "ramp-responses of scatterers. More recently developed transient scattering ranges, which are currently in operation, include facilities at Michigan State University [3], Naval Surface Weapons Center [4] and the Naval Postgraduate School (NPS). The first two of these are ground plane ranges which can be used for bistatic scattering measurements on symmetric targets. The NPS range is a "free-field" configuration, where scatterers are suspended in free space without a ground plane. The relative merits of both types of scattering range will be discussed in the following section.

Another class of transient electromagnetic facility came into existence in the early 1970's: Electromagnetic Pulse (EMP) ranges. Such facilities came about because of revelations regarding EMP vulnerability of electronic systems, as were observed during many of the initial atmospheric thermonuclear weapon tests in the Pacific. EMP ranges were developed to support both basic research and to assess the vulnerability of various tactical and strategic electronic systems. These installations came in two varieties: full-scale and scale-model. Two of the most notable scale model EMP ranges are those at the Lawrence National Laboratory [5], and at the Naval Oceans Systems Center. The LNL facility, which has been operational since the early 1970's, has provided extensive measurements of EMP induced currents on scale models of tactical and strategic weapon systems. The NOSC range, on the other hand, has been used to assess the EMP responses of in situ mounted antennas on scale model ships. The measurement of scattered far fields is usually not of primary concern in EMP ranges and they are often not even configured to support such measurements.

Transient scattering ranges have, for the most part, evolved from the need to support basic research in resonant region noncooperative radar target recognition (NCTR). Of course, broad band stepped-frequency CW ranges are also employed in this type of research, one of the most notable being the state of the art "compact range" at Ohio State University, [6]. The approaches to resonant region NCTR can be broadly classed into two categories: inverse scattering and natural resonance identification. The first of these seeks to provide direct evaluation of the scatterer's geometry and composition by approximate application of fundamental inverse scattering theory embodied in, for instance, the integral transform relationships of Bojarski [7] and Kennaugh and Cossgriff [8]. In applying these principles it becomes necessary, in the general case of 3-D inverse scattering, to have available wide bandwidth scattering data from numerous aspects on the target. Conversely, natural resonance based NCTR requires only single aspect scattering data since the target's resonances are, in principle, functions only of its innate structural and material properties. The resulting tradeoff for natural resonant NCTR is that the identified complex poles must be correlated with a comprehensive data base that includes these parameters for all candidate targets. Although this may appear as a major disadvantage, consider that for the case of inverse scattering, an "image" of the target must also be correlated, but with other images using either human observers and/or automated image recognition algorithms.

TRANSIENT ELECTROMAGNETIC SCATTERING LABORATORY

The transient electromagnetic scattering laboratory (TESL) became operational at NPS in early 1980, [9], with the initial establishment of an outside ground plane range, as is depicted in Figure 1. Bisected targets were placed upon the 12 meter square aluminum ground-plane. An omnidirectional quasi-TEM incident field was provided by a 7 meter long vertical monopole antenna, which was driven with an impulse generator. An imaged pyramidal TEM horn functioned as the bistatic receiving antenna. The instrumentation was housed below the ground-plane structure. This type of configuration offered simple bistatic measurement flexibility along with a usable 5 octave bandwidth from 100 to 3200 MHz.

The ground-plane TESL was originally constructed to support inverse scattering research based upon multiple aspect ramp responses. This concept, which was originally based upon the physical optics approximation, as proposed in 1958 by Kennough and Cosgriff [8], was suggested for radar target imaging in 1965 by Mains and Moffatt [10]. The idea was later extended by Bennett [11] to an exact theoretical formulation using the magnetic field integral equation. The use of resonance region frequencies allows imaging of the complete target, even beyond the shadow boundary. It thus becomes possible, in principle, to look around to the back of an object as perceived by the normal high frequency optical perspective. Very impressive work by Young [12], used stepped frequency CW measurements to synthesize ramp responses for forming target images. The NPS effort in this regard was also quite successful and incorporated Bennett's iterated integral equation method to enhance image fidelity, with particular improvement noted beyond the shadow boundary [13]. A major limitation of ramp response methods is the need for multiple aspect data to provide images of general 3 D objects. From a practical radar standpoint, this is a serious penalty and would require either cooperative or naturally rotating targets, and/or a multistatic radar system. This limitation motivated the investigation of an alternate methodology, based upon aspect invariant natural resonances. The requisite experimental capabilities for this new area of research brought about the construction of a unique "free field" configuration, as will be discussed shortly.

The conceptual basis of natural resonance NCTR is derived from the results of the singularity expansion method (SEM) which was originated by Baum [14] for use in both explaining and predicting EMP interactions with electromagnetic systems. The aspect independent virtue of SEM is embodied in the innate complex natural frequencies of material structures, which appear as fixed parameters in analytical SEM expressions for both induced current and scattered field responses, [15]. The accurate estimation of these natural resonance frequencies, using experimental data, requires relatively high signal to noise ratios vis-a-vis that needed for ramp response imaging. This enhanced data requirement for natural resonance estimation is a result of three fundamental facts:

- (1) The ramp response is obtained by twice integrating the impulse scattering response, thus providing an effective low pass filter to eliminate much of the inherent noise and other broad band signal pollutants. This type of filtering would be unacceptable for use with natural resonance processing because of the suppression of higher frequency (and innately weaker) resonances.
- (2) The ramp response is obtained by use of the "early time" scattering, as opposed to the "late-time" signal being employed for natural resonance identification. In most cases the early time signal component, which is due to directly driven induced currents, contains most of the total signal energy. On the other hand, the late time field is due to inertia driven natural modes which reradiate the remnants of the energy that had been previously injected into the system by the incident field.
- (3) The process of estimating the natural resonances in a given late time scattered signal is highly sensitive to pollutants. This sensitivity results from the nonlinear relationship between the natural resonance signal parameters (system poles) and the signal time-history. Numerical experiments indicate that even with the most advanced signal processing strategies, accurate extraction of complex natural resonance frequencies requires SNR's of 15 to 30 dB, [16].

Although the accurate estimation of natural resonances requires high SNR's, alternate methods of identifying radar targets based upon annihilating the known poles in the system appear to be much less demanding on signal fidelity. However, any natural resonance NCTR method will still need to rely upon an accurate *a priori* knowledge of the observable poles of targets which are expected to be observed. This requisite pole library will need to be obtained, at least in part, by extracting complex resonances from experimental data. As supercomputer run electromagnetic scattering software becomes increasingly sophisticated in handling the complexities of realistic radar targets, this situation may change.

The free field TESL became operational at NPS in 1983, [17], and incorporates a shielded anechoic enclosure, as is depicted in Figure 2. Inside chamber dimensions are 6.2 meters long by 3.1 meters square. Because targets are suspended within the chamber, there is no restriction to symmetric objects, as is the case for a ground-plane range (where the target must be bisected along the plane of symmetry). Also, the free field configuration poses no polarization restriction on the incident field. For the ground plane range, the incident E-field will be linearly polarized and normal to the metal plane.

The metallic shielding in the chamber reduced the effects of outside interference to the point that it became negligible compared to either "thermal noise" provided by the receiver system (sampling head front-end) or antenna noise generated by ambient radiation of the absorbing material on the inside of the chamber. This minimal noise configuration allowed the introduction of a unique wide band, but relatively low power, pulse generator. This pulse generator is composed of a very fast (25 psec rise time) step generator followed by a highly stable 1 watt peak GaAs FET linear amplifier, having an effective bandwidth of 1 to 7 GHz, [18]. Several alternate pulse generators had been utilized (or tested and rejected) over the years. The main drawback of many of these generators is their lack of pulse stability, or repeatability. This is of extreme importance in sampling measurements where the data waveforms are produced by the superposition of shifted time samples from repeated observations, each due to a separate pulse excitation of the system. Any change in the pulse shape or amplitude as the sampling measurement proceeds appears as equivalent signal pollution. Such "pulse-noise" is quite common to gas-discharge pulse generators, which often have very impressive power and bandwidth specifications, but are otherwise unusable for natural resonance experiments.

Returning to the depiction in Figure 2, the pulse amplifier and the sampling head for the digital processing oscilloscope (DPO) are each directly connected to coaxially fed double-ridged horn antennas, for nearly monostatic (3 degree angle separation) transmission and reception from the source wall of the chamber. These horns provide an effective bandwidth of 1 to 12 GHz and are linearly polarized in the boresight direction. An example of a suspended scale model aircraft target, in front of the back-wall, is shown in Figure 3. The back wall is composed of 46 cm long pyramids while the source wall is covered by 21 cm pyramids. The walls, floor and ceiling are covered by 21 cm longitudinal wedged material, which acts to channel energy towards the back wall, with minimal reflections. A very low density foam target support is used in lieu of the polyethylene support shown. The rotational position of the target is computer controlled to high resolution by a stepping motor.

SIGNAL ACQUISITION AND PROCESSING

The operation of the free field scattering range can be readily understood by referring to the system representation shown in Figure 4. Various frequency domain transfer functions represent the physical interactions embodied in the scattering process as they affect the measured scattered field waveform. For example, the pulse generator output, $X(f)$, drives the transmitting antenna, whose field is then incident upon the scatterer, $H_S(f)$, and the the absorber in the chamber (clutter scatterers), $H_C(f)$. In addition, energy is directly coupled into the physically adjacent receiving antenna, as is symbolized by $H_A(f)$. The purpose of the measurement is to ascertain the transient field response of the target to some specified excitation function. The pertinent scattering characteristics of the target are embodied in its transfer function, $H_T(f)$, which gives the frequency domain scattered field response at the receiving antenna due to the incident field at the scatterer. Direct scattering of the incident field by the chamber is symbolized by $H_C(f)$, with multipath and multiple scattering between the target and the chamber walls represented by the two-way interaction arrow from H_C to H_S . The thermal noise and interference, which either arrive through the receiving antenna (antenna noise) or are innate to the DPO (receiver system noise), are lumped together as $N(t)$.

We will only have direct measurement access to $Y(f)$, via $y(t)$. A multiple measurement technique will allow us to eliminate (in theory) the effects of the antenna transfer functions, antenna coupling and direct clutter pollution of the received signal, $Y(f)$. We will even be able to obtain the target response to some specified incident waveform, whose spectral content does not extend beyond that of the actual incident field. As a vehicle for understanding this data acquisition and front-end signal processing, we will follow the measurement of scattering from a 8.095 cm diameter aluminum sphere, which we will refer to as the target. There are three fundamental measurements to be made:

- (1) No target present (termed the background measurement)
- (2) Desired target present (termed the target measurement)
- (3) Canonical target present (termed the calibration measurement)

Without any target present, the received signal spectrum will be given by

$$Y_1(f) = H_R(f) H_T(f) X(f) (H_A(f) + H_C(f)) + N_1(f) \quad (1)$$

With the desired target present, this quantity becomes

$$Y_2(f) = H_R(f) H_T(f) X(f) (H_A(f) + H_C(f) + H_S^T(f) + H_{SC}^T(f)) + N_2(f) \quad (2)$$

where the superscript "T" indicates that the target is present while the interaction between the target and the chamber, which includes multipath and multiple scattering is

denoted by H_{SC} . Note that the measured random noise, $N_2(f)$, is assumed to differ from that acquired from the independent background measurement, as it should.

With the "canonical" target present, the received signal spectrum is given by

$$Y_3(f) = H_R(f) H_T(f) X(f) \{ H_A(f) + H_C(f) + H_S^C(f) + H_{SC}^C(f) \} + N_3(f) \quad (3)$$

The purpose of this calibration measurement is to eliminate the effects of the antenna transfer functions by comparing Y_3 to a computation of $H_S^C(f)$. Thus, the canonical target should be amenable to an accurate and efficient computer algorithm. A 20.32 cm diameter aluminum sphere is used for the canonical target.

The three basic measurements are made directly in the time domain and are stored as digital time-series for 2^N equispaced points ranging from 64 to a maximum of 1024. Example 512 point time-series for the background, target and calibration measurements are shown respectively in Figures 5 through 7. These measurements are each composed of 500 ensemble averaged (time overlaid) sampled waveforms. This is done to reduce the noise background and improve the SNR by approximately 500 times over that of a single sampled signal. As part of this extensive ensemble averaging, an adapt-squares "drift compensation" algorithm is employed to compensate for slow shifts of the temporal range being sampled. This relatively small drift occurs over the long time periods taken for each measurement (typically several minutes).

Notice the large response beginning at about 16 Nsec in these measurements. This is due to scattering from the back-wall, whose pyramid tips are roughly 2.5 m behind the target support. In addition, the contribution that appears in the beginning of the background measurement is the remnant of the very large antenna coupling which began approximately 24 Nsec prior to the start of this time window. To eliminate the clutter returns and antenna coupling that are common to the three measurements we simply subtract the background measurement from both the target and calibration measurements. The corresponding time-series of these subtracted waveforms are shown in Figures 8 and 9, where the elimination of the common clutter and antenna coupling provides such enhanced scattering signatures. A Fast Fourier Transform (FFT) is then applied to each of these subtracted time-series. Using our previous frequency domain nomenclature, the subtracted scattering signals have respective spectra given by

$$Y_4(f) = Y_2(f) - Y_1(f) = H_R(f) H_T(f) X(f) \{ H_S^T(f) + H_{SC}^T(f) \} + N_2(f) - N_1(f) \quad (4)$$

$$Y_5(f) = Y_3(f) - Y_1(f) = H_R(f) H_T(f) X(f) \{ H_S^C(f) + H_{SC}^C(f) \} + N_3(f) - N_1(f) \quad (5)$$

The magnitude of $Y_5(f)$ is illustrated in Figure 10, where the system bandwidth of about 1 to 7 GHz becomes apparent.

To further process the acquired data, in order to eliminate the antenna transfer function effects and to provide the target response to a specified incident waveform, the canonical target transfer function is computed using a Mie series solution [19]. This computation provides the frequency domain scattered field at the location of the receiving antenna, including the effects of: (1) finite distance, without far field approximations in the Hankel functions, and (2) the slight bistatic angle between the transmitting and receiving antennas. The desired incident field waveshape is somewhat arbitrary, being constrained only in its significant bandwidth, which can not be expected to extend beyond that of the measurement system (1 to 7 GHz). One such waveform is the Gaussian amplitude modulated cosine (GAMC) of the form

$$x_0(t) = A_0 \exp[-\alpha(t-t_0)^2] \cos(2\pi f_0 t) \quad (6)$$

where the center frequency, f_0 , and significant bandwidth (via α) can be adjusted independently. An example of the GAMC waveform is shown in Figure 11, while the magnitude of the computed scattered electric field for the 20.32 cm diameter sphere (canonical target) is provided in Figure 12, being represented by

$$Y_6(f) = X_0(f) H_S^C(f) \quad (7)$$

The next processing step involves forming an optimal deconvolution estimator for the target's frequency domain response,

$$\hat{X}_0(f) H_S^T(f) = \frac{Y_4(f) Y_5^*(f)}{Y_5(f) Y_5^*(f) + C} Y_6(f) \quad (8)$$

This form of estimator can be shown to provide the best fidelity, in the least squares sense, for the deconvolved target response [20]. The "smoothing parameter", C , is

selected so that the significant spectral content of the deconvolved response in Eq. (8) is approximately equal to that of the measurement system, as is shown in the spectral magnitude plot of Figure 13. Notice that when $C=0$, the ratio in Eq. (8) becomes simply Y_4/Y_5 , which could be termed "naive deconvolution". In such a case, signal pollution in $Y_5(t)$, which has spectral components at frequencies where the unpolluted signal has low spectral content will yield a very large amplified effect on the resultant spectral ratio. This noise enhancement is thus tempered by establishing a minimum baseline for the denominator through the addition of a positive C .

The inverse FFT of the spectrum in Figure 13 is shown as the time-series in Figure 14, which represents the estimated transient scattering response of the spherical target due to an incident field having the GAMC waveform in Eq. (6). This deconvolved measured response can be compared to the computed target response, which is shown in Figure 15. This computation is provided by performing an inverse FFT on a Mie series based spectral response, obtained using the same algorithms as was employed to compute Y_6 for the canonical sphere target. Notice that the computed transient response is essentially composed of a main specular return, from the front face of the sphere, followed by a first order (single circumnavigation) "creeping-wave" return. The deconvolved experimental return has this same initial waveform, but is followed by a small "error" signal which continues out to the end of the 20 Nsec time window. Part of this error is due to unfiltered measurement noise which is collocated in frequency with the scattered field waveform. This noise remnant is further augmented by specular side-wall multipath returns which are delayed by about 3 Nsec from the direct return, when the target is positioned at 3.5 meters from the antennas. For the near grazing angle incidence on these corrugated walls, independent experiments indicate an approximate 12 dB reflection coefficient which, if doubled to 24 dB for two-way multipath from the target, roughly corresponds to the magnitude that is observed in the multipath signal component. The additional error contribution, near the end of the time record, is due to the uncanceled back-wall echo of the forward scattering from the target.

To indicate the level of fidelity of the measurement deconvolution, a comparison is shown, in Figure 16, of the first 5 Nsec of the measured target response to that which is computed. The RMS error is of the order of only a few percent. The FFT magnitude for this time-windowed measured target response is compared to the computed spectral magnitude in Figure 17. Note the comparison of this "clean" spectrum with that in Figure 14, which is polluted by the noise and other error sources that appear outside of the temporal support region of the scattered signal. This dramatic improvement of the measured spectrum results from both frequency and time filtering. The same type of range-gate filtering can even be used to improve the spectral measurements of CW ranges. In such cases, an inverse FFT is used on stepped-frequency measurements, with the resultant time-response being range-gated around the target to eliminate clutter. This range-gated signal is then transformed back to the frequency domain. Another common method in CW ranges is to use a pulsed CW waveform and physical range-gating of the return signal, [6].

A second scattering measurement that illustrates the accuracy of the TESL is that of broadside backscatter from a thin copper wire, of length 10 cm and 0.24 cm diameter. The measurement of the background was subtracted from that of the thin wire and canonical sphere, as before, and the spectral estimator was formed using Eq. (8). The resultant spectral estimator of the thin-wire scattering response to the GAMC waveform is then inverse FFTed to yield the time-series in Figure 18. Notice the small multipath contribution occurring near the end of the decaying wire response (approximately 3 Nsec from the initially large direct return) as well as the uncanceled back-wall echo of the target's forward scattering. To check the accuracy of the scattering measurement deconvolution, a comparison is made in Figure 19 to a time-domain computation of the wire scattering using the time domain E-field integral equation approach of Sayre and Harrington, [21]. The apparent slight difference in the fundamental natural resonance frequency may be due to the thin-wire approximation employed in the computation, which ignores the current path length on the finite end caps of the wire. This effective lengthening of non-ideal thin-wires is analogous to the "end effect" in predicting resonant frequencies in antenna theory, [22]. In FFTing the 10 Nsec windowed transient responses in Figure 19, we obtain the spectral responses, whose magnitudes are compared in Figure 20. As was the case with the sphere scattering example, the RMS error level is only a few percent.

It should be noted that numerous additional measurements have been made using much more complex scattering objects than just simple spheres and wires. In fact, there exists a library of metalized scale model tactical aircraft. The measured scattering responses of these are being used in studies of natural resonance NCTR.

CONCLUSION

After providing some historical perspective on transient scattering measurements, the unique free-field range at the Naval Postgraduate School was described. This description included both the physical configuration and a comprehensive system measurement model, which is based upon linear system theory. Two particularly significant attributes of the range are its free-field configuration and its employment of a solid-state amplified step generator transmission source. Using the scattering measurement from a simple target as an example, the acquisition and signal processing methodology of the range was considered. Direct time-domain interpretations were given for noise and clutter pollutants of the measured signal. Special emphasis was placed

upon both the need for highly stable pulse sources, when used with sampling measurements, and the limitations imposed by the finite practical bandwidth of the range. Additionally, the respective effects of spectral and temporal signal filtering on improving time and frequency domain data was considered in the example.

Although the indicated fidelity of the scattering measurements for the sphere and wire targets were quite good when compared to computations, there is room for improvement. The primary role of this facility is to support natural resonance target identification efforts. As such, there is a continuing quest to improve both the SNR and the frequency bandwidth of the measurements. Both of these improvements translate into better target discrimination capability. A simple way to extend the effective bandwidth of any scale model range is to employ a succession of alternately scaled replicas of the targets, as was done in using the NPS TESL and an alternate stepped frequency range in the effort described in [16]. This technique will be employed in the future, as needed. On the other hand, to physically increase the range bandwidth to its full potential of 1 to 12 GHz (as limited by the antennas and the sampling configuration) two new methods are planned. These methods are intended to circumvent the current limitations in the power-bandwidth product of stable (meaning solid-state) pulse generators. One such method is to extend the bandwidth of the amplified step-generator by adding an additional higher frequency amplifier in parallel with the current 1 - 7 GHz amplifier. This can be done using a power splitter and a recombiner network. A more novel method is also planned for enhancing the SNR and bandwidth: using a broadband random noise source as the generator and employing a coherently triggered dual-channel sampling scheme to provide cross-correlation measurements of the transmitted and received noise signals. This cross-correlation provides an effective dynamic matched-filtering whose output is the smoothed impulse response of the scattering system.

A final consideration for the future improvement of the measurement fidelity is the multipath signal interference, as was observed in the example measurements. To reduce this effect directly requires either a significant reduction in the reflection coefficient around the specular regions of the chamber and/or the construction of a new, and larger, anechoic chamber. Because of the small cross-sectional dimensions of the chamber, the specular region is illuminated at near grazing incidence, thus providing enhanced reflection, even from otherwise excellent absorbing material. The enlargement of the chamber's cross-sectional dimensions is not possible because of physical space limitations. Also, there is currently no larger space available to rebuild a larger chamber. So, alas, there remains the possibility of a *software fix*. Such an approach will rely upon an accurate estimate of the frequency behavior of the specular region scattering matrix elements. Since the multipath angle is only a few degrees from direct backscattering, and the target is, at most, only a few wavelengths in dimension (at the highest frequency), the multipath return can be approximated as a delayed and frequency filtered (dispersive) version of the direct return. Such a model will permit the extraction of some of the multipath interference. The accuracy and practicality of such a technique have yet to be tested.

REFERENCES

- [1] "Time-Domain Reflectometry," Hewlett Packard Application Note No. 62, 1964.
- [2] J.D. DeLorenzo, "A range for measuring the impulse response of scattering objects," 1967 NEREM Record, Vol. 9, pp. 80-81, Nov. 1967.
- [3] K.M. Chen, et al, "Radar target discrimination by convolution of radar return with extinction-pulses and single mode extraction signals," *IEEE Tran. on Antennas & Propagation*, Vol. AP 34, July 1986, pp. 896-904.
- [4] B.Z. Hollmann, E.D. Ball, "Experimental time-domain determination of complex resonances of simple objects," NSWC Report TR 80-414, Dec. 1981.
- [5] R.M. Bevenssee, F.J. Dadrack, E.K. Miller, J.T. Okada, "Validation and calibration of the LLL transient electromagnetic measurement facility," Report UCRL-52225, March 1977.
- [6] E.K. Walton, J.D. Young, "The Ohio State University compact radar cross-section measurement range," *IEEE Trans. Antennas Propagat.*, Vol. AP-32, pp. 1218-1223, Nov. 1984.
- [7] N.N. Bojarski, "A survey of the physical optics inverse scattering identity," *IEEE Trans. Antennas Propagat.*, Vol. AP 30, pp. 980-990, Sept. 1982.
- [8] E.M. Kennaugh and R.L. Cosgriff, "The use of impulse response in electromagnetic scattering problems," *Proceedings 1958 IRE National Convention Record*, Part I, pp. 72-77.
- [9] C.W. Hammond, "The development of a bistatic electromagnetic scattering laboratory," M.S. Thesis, Electrical Engineering Department, Naval Postgraduate School, Dec. 1980.
- [10] R.H. Mains and D.L. Moffatt, "Complex natural resonances of an object in detection and discrimination," TR-3424-1, Ohio State University, Electroscience Laboratory, Columbus, OH, June 1974.

- [11] C.L. Bennett, "Time-domain inverse scattering," *IEEE Trans. Antennas Propagat.*, Vol. AP-29, pp. 213-220, March 1981.
- [12] J.D. Young, "Radar imaging from ramp response signatures," *IEEE Trans. Antennas & Propagation*, vol. 24, pp. 276-282, May 1976.
- [13] M. Morag, "Radar target imaging by time-domain inverse scattering," M.S. Thesis, Electrical Engineering Department, Naval Postgraduate School, March 1981.
- [14] C.E. Baum, "On the singularity expansion method for the solution of electromagnetic interaction problems," Air Force Weapons Laboratory Interaction Notes, No. 88, Dec. 1971.
- [15] M.A. Morgan, "Singularity expansion representations of fields and currents in transient scattering," *IEEE Trans. Antennas & Propagation*, vol. 32, pp. 466-473, May 1984.
- [16] J.R. Auton, T.L. Larry and M.L. VanBlaricum, "Radar target identification and characterization using natural resonance extraction," Final Report on ONR Contract N00014-82-C-0079, September 1984.
- [17] M.A. Morgan, "Time-domain scattering measurements," *IEEE Antennas & Propagation Newsletter*, Vol. 6, August 1984, pp. 5-9.
- [18] B.W. McDaniel, "Calibration and evaluation of a free-field scattering range using wideband pulse amplification," M.S. Thesis, Electrical and Computer Engineering Dept., Naval Postgraduate School, Dec. 1985.
- [19] R.F. Harrington, *Time-Harmonic Electromagnetic Fields*, New York: McGraw-Hill, 1961.
- [20] S.M. Riad, "Impulse response evaluation using frequency domain optimal compensation deconvolution," 23rd Midwest Symposium on Circuits and Systems, August 1981, University of Toledo.
- [21] E.P. Sayre and R.F. Harrington, "Time-domain radiation and scattering by thin-wires," *Applied Sci. Res.*, Vol. 26, pp. 413-444, 1972.
- [22] E.C. Jordan, K.G. Balmain, *Electromagnetic Waves and Radiating Systems*, Englewood Cliffs: Prentice-Hall, 1968, p. 394.

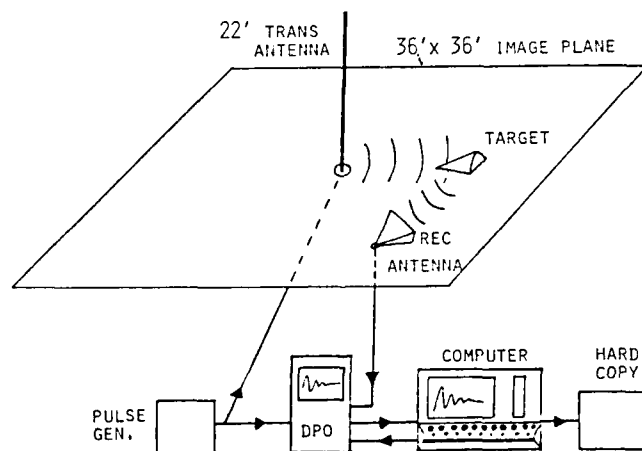


FIGURE 1 ORIGINAL NPS GROUND-PLANE SCATTERING RANGE

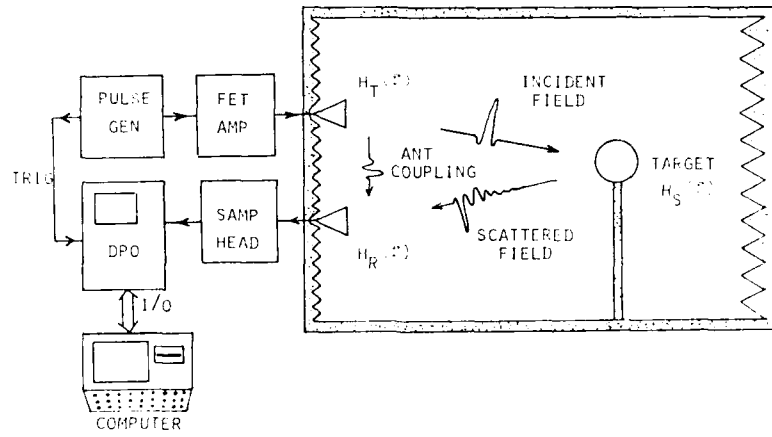


FIGURE 2 NPS FREE FIELD SCATTERING RANGE CONFIGURATION

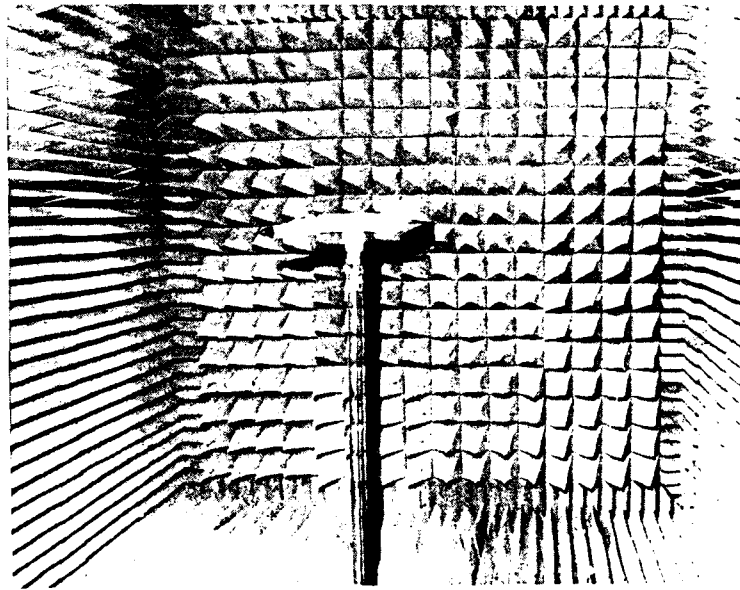


FIGURE 3 SUSPENDED TARGET AND BACK WALL

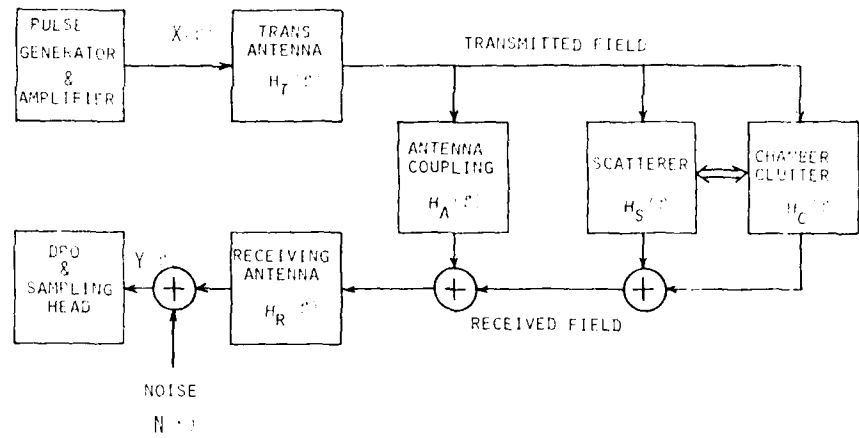


FIGURE 4 FREE-FIELD RANGE SYSTEM REPRESENTATION

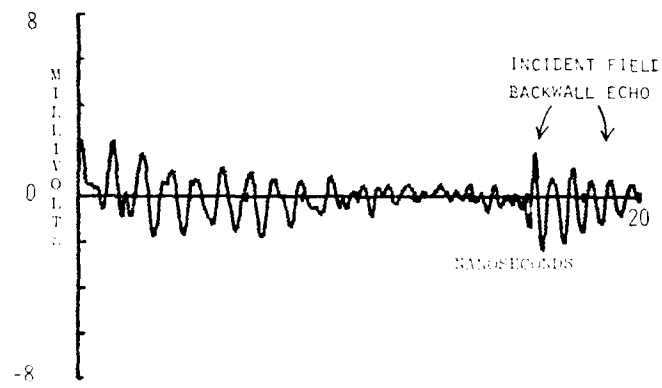


FIGURE 5 512 POINT BACKGROUND SCATTERING MEASUREMENT

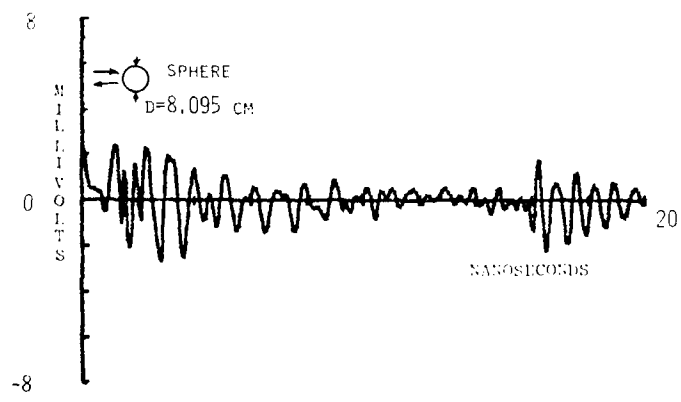


FIGURE 6 512 POINT TARGET SPHERE SCATTERING MEASUREMENT

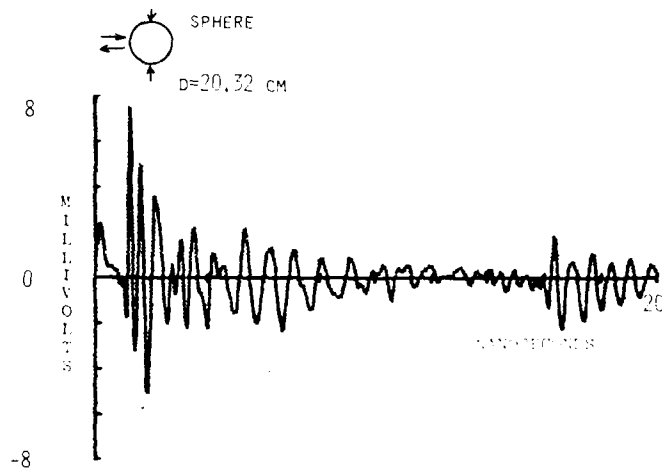


FIGURE 7 512 POINT CALIBRATION SPHERE SCATTERING MEASUREMENT

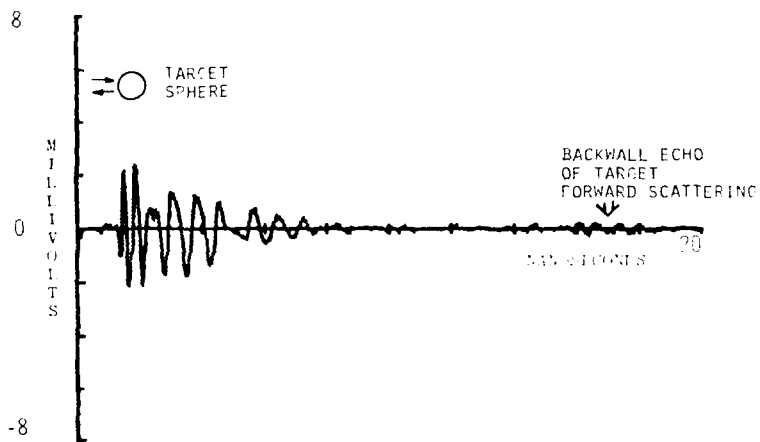


FIGURE 8 TARGET SPHERE SCATTERING MINUS BACKGROUND

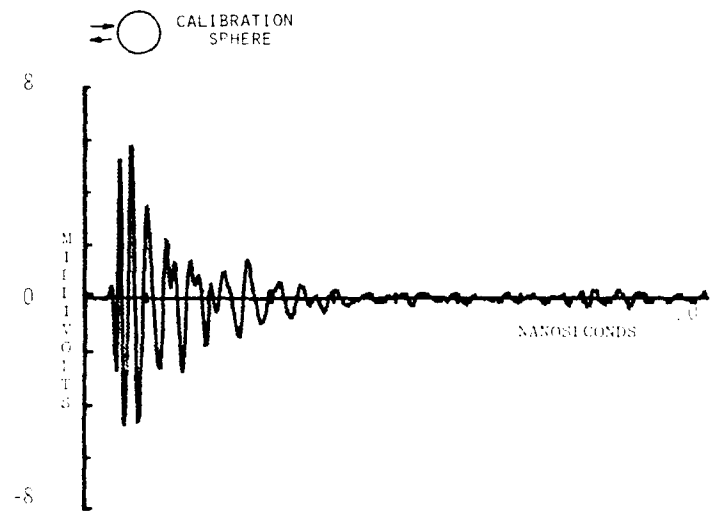


FIGURE 9 CALIBRATION SPHERE SCATTERING MINUS BACKGROUND

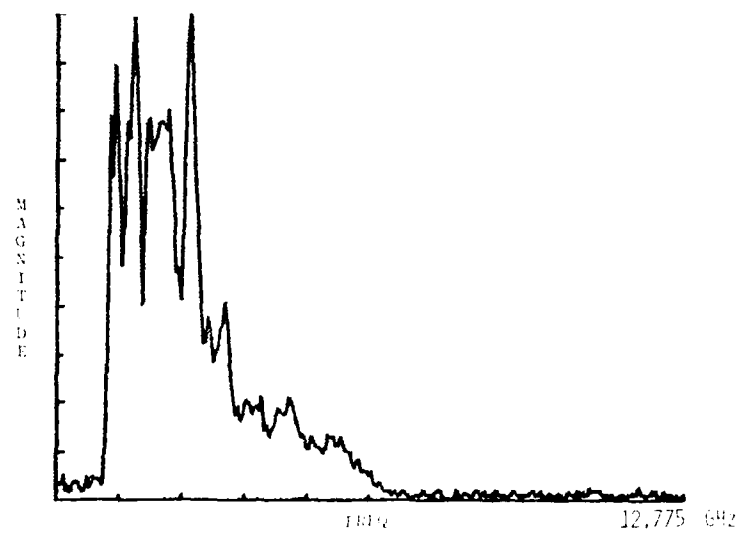


FIGURE 10 SPECTRAL MAGNITUDE OF FIGURE 9 TIME SERIES

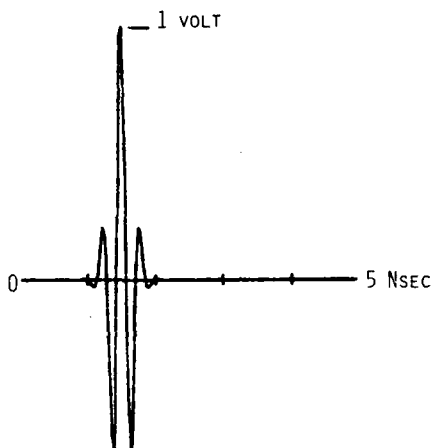


FIGURE 11 GAUSSIAN AMPLITUDE MODULATED COSINE WAVEFORM

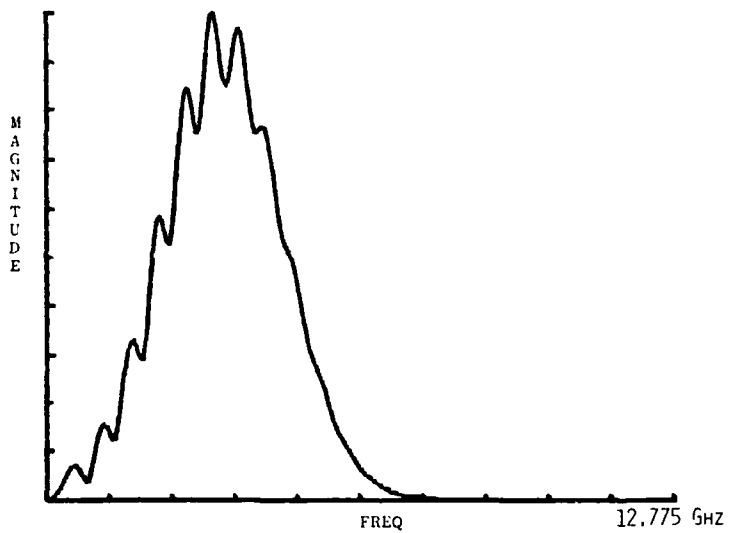


FIGURE 12 COMPUTED SPECTRUM FOR CALIBRATION SPHERE SCATTERING

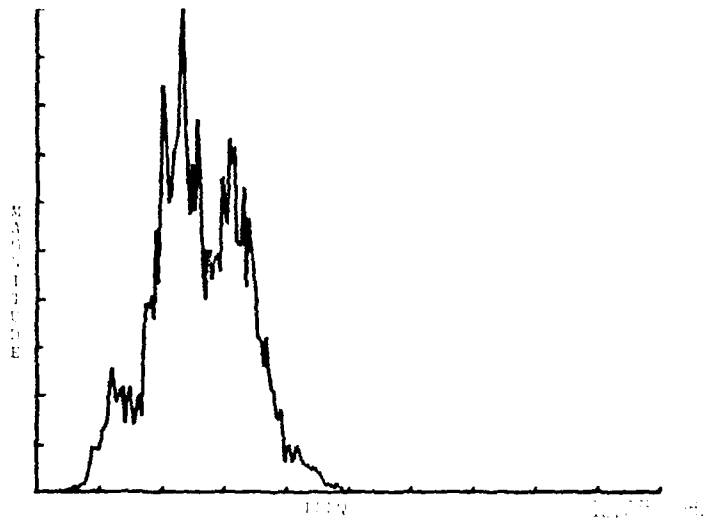


FIGURE 13 SPECTRAL ESTIMATION OF MEASURED TARGET SCATTERING

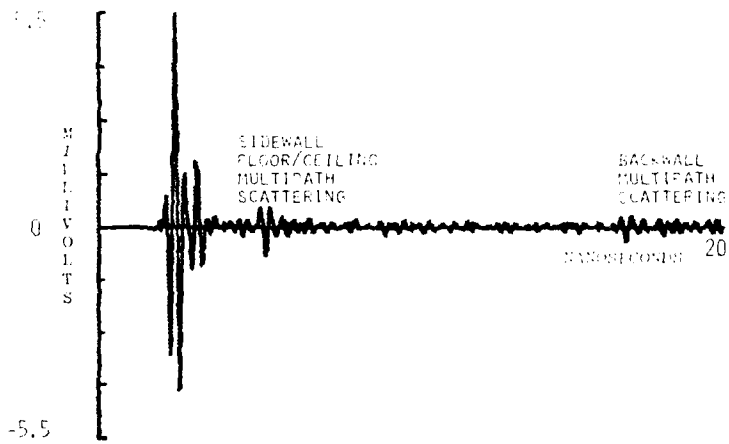


FIGURE 14 TIME SERIES FOR ESTIMATED TARGET SPHERE SCATTERING

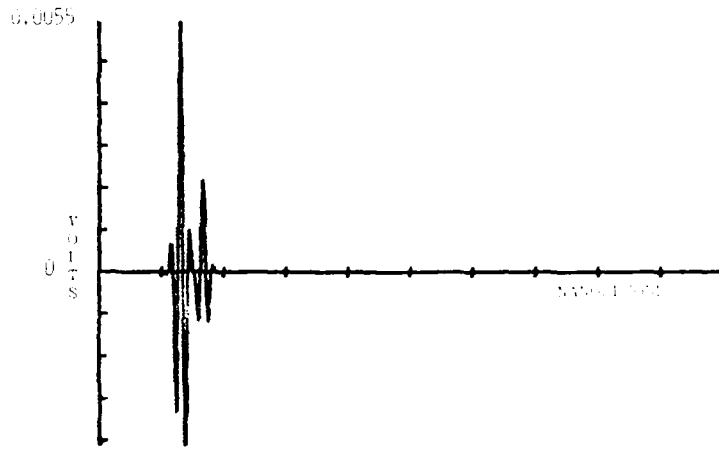


FIGURE 15 MIE SERIES COMPUTED TARGET SCATTERING TIME SERIES

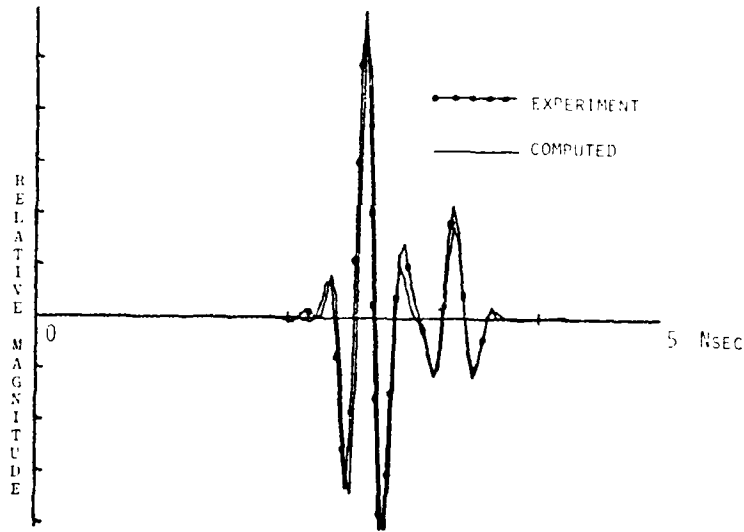


FIGURE 16 COMPARISON OF SPHERE MEASUREMENT WITH COMPUTATION

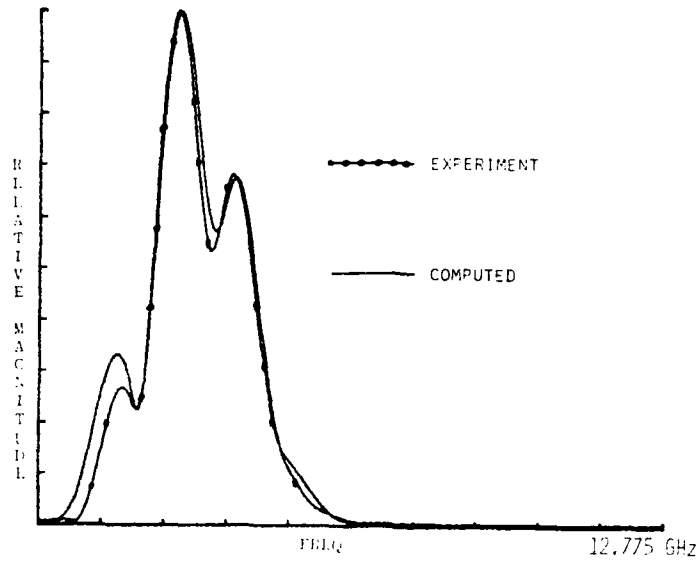


FIGURE 17 SPECTRAL MAGNITUDE COMPARISON FOR SPHERE SCATTERING

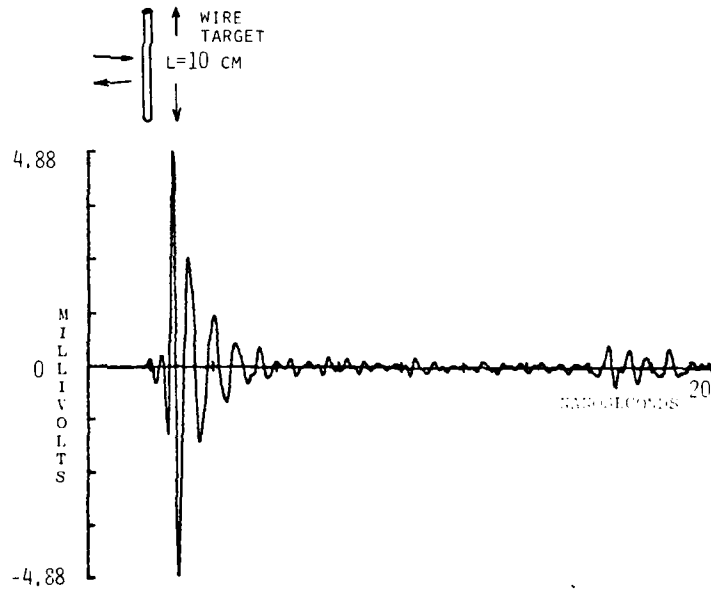


FIGURE 18 MEASURED THIN-WIRE TIME-SERIES ESTIMATOR

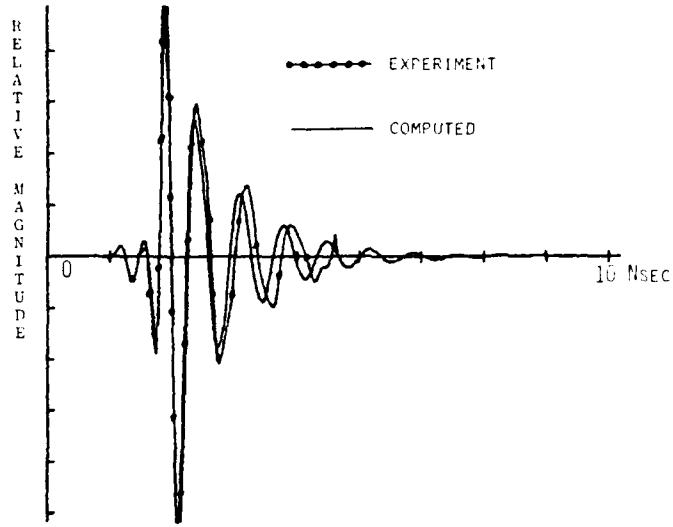


FIGURE 19 COMPARISON OF THIN WIRE MEASUREMENT WITH COMPUTATION

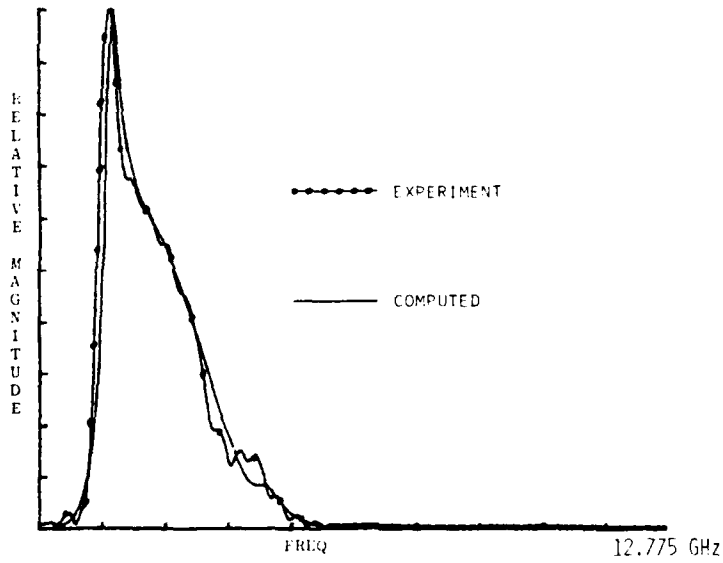


FIGURE 20 SPECTRAL MAGNITUDE COMPARISON FOR THIN WIRE SCATTERING

AD-P005655

EXPERIMENTS:
TEST RANGE FACILITIES
(PART 2)

D.G. Dudley
Director, Electromagnetics Laboratory
ECE, Bldg. 104
The University of Arizona
Tucson, AZ 85721
USA

SUMMARY

We give a description of the electromagnetic transient range facility (EMTRF) at the Lawrence Livermore National Laboratory (LLNL). We discuss the range design and show the instrumentation for both time domain and broadband frequency domain measurements. We give two examples of experiments on the range: Scattering from a conducting plate and transmission through an aperture in a screen.

1. LLNL RANGE HISTORY

The electromagnetic transient range facility (EMTRF) at the Lawrence Livermore National Laboratory (LLNL) was initially constructed in 1968. Since that time, the range has been used for a variety of transient measurements and has undergone a series of improvements and updates [1]. Many scientists, engineers, and technicians have contributed to this range to the degree where the EMTRF can now be considered one of the premier facilities of its kind presently operational.

The range is located indoors and consists of a conducting ground plane (8.5 m x 8.5 m). Initially the transmitting antenna was a long vertical wire fed at its base with a coaxial transmission line located beneath the ground plane. In 1975, the vertical wire was replaced by a monocone with a 377 ohm input impedance. This design was followed by a 120 degree sector monocone (Fig. 1) with a 50 ohm input impedance offering a better match to the pulser. This monocone was constructed with a sheet brass conical section at the apex joined to a conical copper screen and secured to the ceiling with resistively loaded wires.

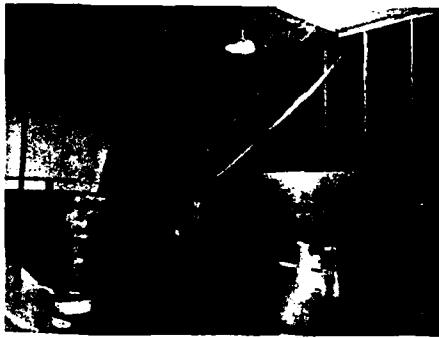


Fig. 1 - Monocone antenna, prior to 1984-1985 range upgrade.

Although the 50 ohm monocone performed adequately in many applications for nearly a decade, there were some serious limitations. Unwanted scattering occurred from the surface of the antenna, the junction with the ceiling, and various obstacles located in the room. These effects combined to limit seriously the signal-to-noise ratio provided by the system. Such limitations are particularly damaging in any attempt to observe late time returns from objects exhibiting a high degree of radiation damping.

In the period 1984 to 1986, the range was subjected to an thorough upgrade aimed at increasing the signal-to-noise ratio and increasing the bandwidth [1]. The result was a new monocone (Fig. 2), the EMP Engineering Research Omnidirectional radiator (EMPEROR). The EMPEROR consists of a solid aluminum section at the apex. The remainder, up to a height of 3 m, is 0.050 in. sheet aluminum attached to a girded framework. The monocone is supported from the ceiling. At the floor is a floating connection allowing flex as the ceiling expands and contracts in response to changes in the environment. The design



Fig. 2 - EMPEROR monocone antenna.

was completed by adding absorber suspended around the cone perimeter (Fig. 3). In addition, a vertical wall of absorber was also placed behind the test area.

The effects of the range upgrade have been demonstrated [1] by comparing the vertical electric field in the absence of any test object (Fig. 4). The field is measured with a small vertical D-dot sensor protruding up through the ground plane. The pulser is an Omni-Wave R-100. Both monocones provide an increase in signal by approximately a factor of three over the long wire. The improvement of the noise level of the new monocone over the old monocone is apparent in the plot. The effect of the absorber is also dramatically displayed on a time scale from zero to 100 ns (Fig. 5). Note that the quieting effect of the absorber is approximately 12 db. This improvement is very important in any attempt to do measurements on the range where observation of small late time phenomena is required.

2. RANGE INSTRUMENTATION

The LLNL range is capable of operating in either the transient or the broadband frequency mode. We shall describe both methods of operation.

In the transient mode (Fig. 6), a repetitive pulser drives the monocone. Typically, the pulser delivers 1 Kv peak at a 250 Hz repetition rate. The pulse has a rise time of less than 0.2 ns and a 3 db width of less than 0.15 ns. The spectrum is flat within ± 2 db from 1 MHz to 1 GHz. The transmitted signal from the monocone is typically received with a D-dot sensor and routed through a delay line to a sampling oscilloscope. The scope is triggered by a tap from the pulser. On-site storage and display is provided by an LSI-11/02 computer. Provisions are made to store the data on floppy disk for transfer to a VAX-11/780, where signal processing is accomplished with the algorithm SIG [2].



Fig. 3 - EMPEROR monocone antenna with absorber; note test object between monocone and vertical absorber.

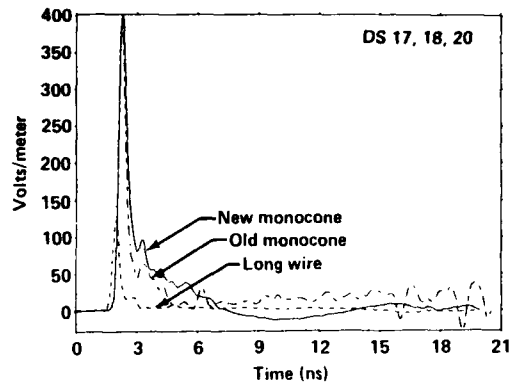


Fig. 4 - Free field time histories of the long vertical wire, the old monocone, and the new monocone.

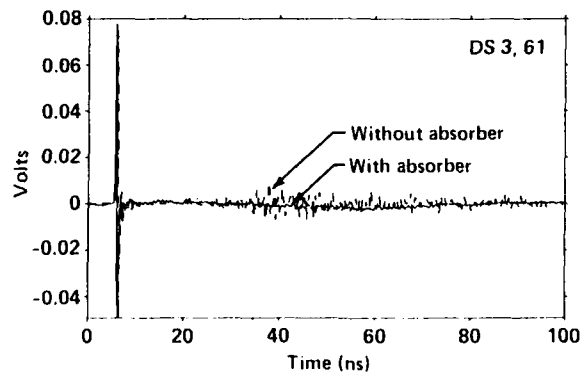


Fig. 5 - Effect of absorber on late time signal.

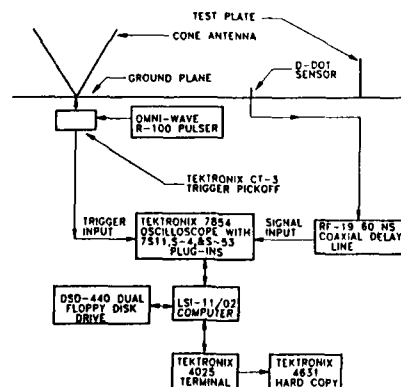


Fig. 6 - Range instrumentation, transient mode.

In the broadband frequency mode [3] (Fig. 7), a frequency synthesized source and a network analyser are used to provide frequency domain data from 0.1 to 18 GHz. Data is typically taken at 401 equi-spaced points so that the frequency resolution is 45 MHz. Should a finer resolution be required, the total frequency range can be subdivided and 401 points taken on each interval. Again, on-site computation is provided by the LSI-11 system, with storage and handover to the VAX.

3. EXAMPLE, PLATE SCATTERING, TRANSIENT MODE

As an example of use of the LLNL range in the transient mode, we have done exhaustive tests [4] involving scattering from a conducting rectangular plate. For the experiments described herein, we have used the sampling oscilloscope to average 100 repetitions of the signal.

A thin rectangular aluminum plate, 30 cm high and 60 cm wide, is mounted perpendicular to the ground plane orthogonal to the direction of propagation from the monocone (Fig. 8). The probe measuring backscatter is positioned 1.49 m from the monocone and 0.914 m from the plate. Data is taken with the probe positioned at five different angles relative to the plate: 0, 45, 90, 135, and 180 degrees (Fig. 9). The distance between the probe and the center of the plate is held constant at 0.914 m.

To obtain a measure of the incident field, as described elsewhere [5] in this lecture series, data is first taken in the absence of the plate. Next the plate is mounted and the data-taking process repeated to obtain the total field. Since the D-dot probe differentiates the data, both data sets are measurements of the time derivative of the vertical electric field. There are 512 points per record at a sampling interval of 3.906×10^{-11} seconds. For each of the five aspect angles, the incident and total

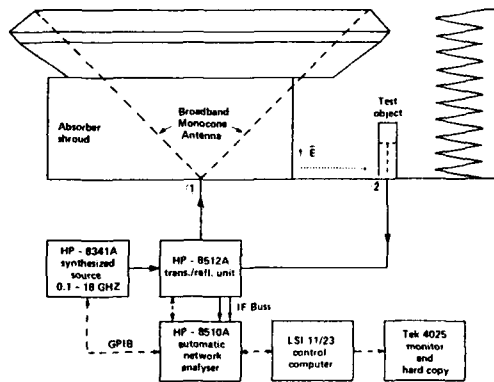


Fig. 7 - Range instrumentation, broadband frequency mode.

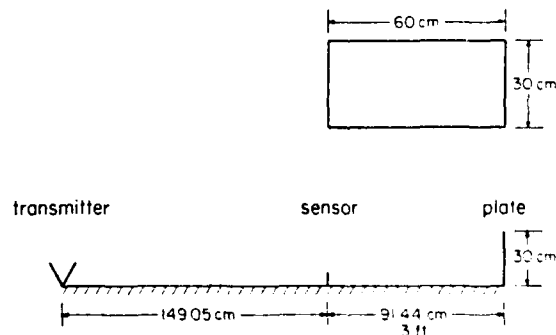


Fig. 8 - Transient range set-up, showing plate dimensions and separation distances.

AD-A185 125

THEORETICAL ASPECTS OF TARGET CLASSIFICATION LECTURE
SERIES OF THE ELECTR. (U) ADVISORY GROUP FOR AEROSPACE
RESEARCH AND DEVELOPMENT NEUILLY.. JUN 87 AGARD-15-152

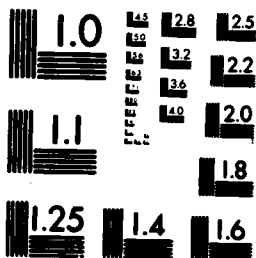
3/8

UNCLASSIFIED

F/G 17/11

NL

END
1987



MICROCOPY RESOLUTION TEST CHART
NATIONAL BUREAU OF STANDARDS-1963-A

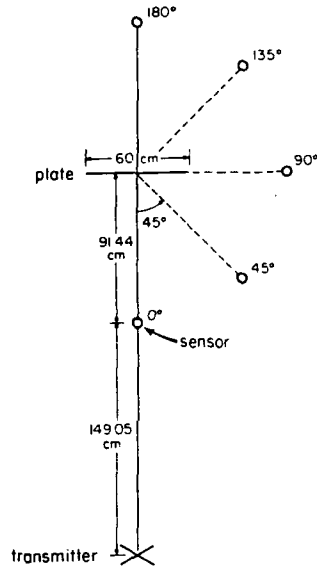


Fig. 9 - Measurement diagram with receiving probe at five locations.

fields are registered. Then the incident field is subtracted from the total field to obtain the scattered field. We process each incident and scattered field using the algorithm SIG [2]. Herein, we describe only the 45 degree case.

We begin with the raw input field (Fig. 10) and total field (Fig. 11). We produce the scattered field as described above. Next, we filter the data at 2 MHz with a tenth order Butterworth filter. (The frequency 2 MHz approaches the upper limits of the pulser bandwidth.) To eliminate low frequency noise, we highpass filter both the input and output data at 100 MHz with a sixth order Butterworth filter. We then decimate the data to 90 points to eliminate oversampling. We display the final input data (Fig. 12) and its spectrum (Fig. 13) and the output data (Fig. 14) and its spectrum (Fig. 15). We have used these results to obtain estimates of the complex resonances of the plate by

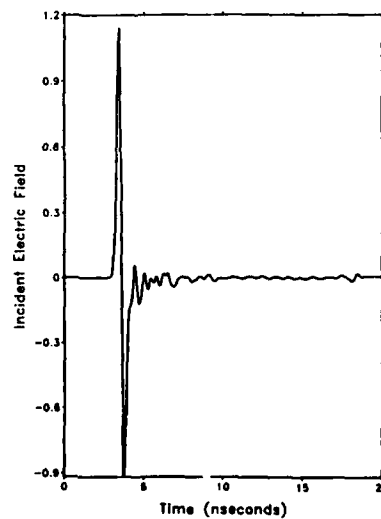


Fig. 10 - Raw input field with probe at 45 degree probe position.

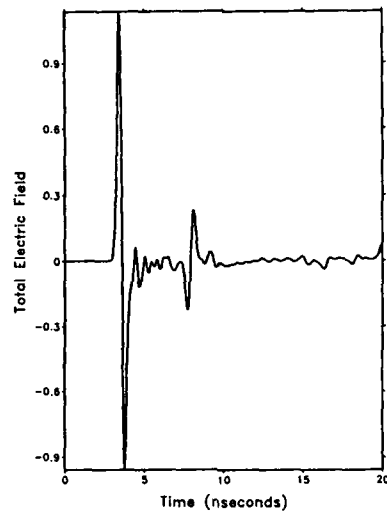


Fig. 11 - Total field at 45 degree probe position.

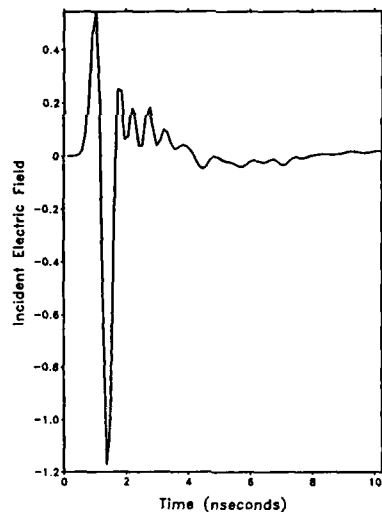


Fig. 12 - Input pulse, bandpass filtered to 0.1 to 2 GHz, decimated to 90 points.

methods discussed elsewhere in this lecture series [5]. Using the algorithm NLS [6], we have attempted to identify the complex resonances of the plate for all five observation angles. Here, we include only representative results at 45 degrees (Fig. 16). We compare results with 18th, 23rd, 25th, and 27th order models with theoretical results obtained by Pearson [7]. Note that for the pole closest to the real axis, the identification is accurate for all model orders. For all other poles, the identification fails.

The upgrade of the LLNL range has made a significant contribution to our efforts to identify the principal resonance of the rectangular conducting plate. Prior to the upgrade, our attempts had been unsuccessful. After upgrade, however, the decrease in

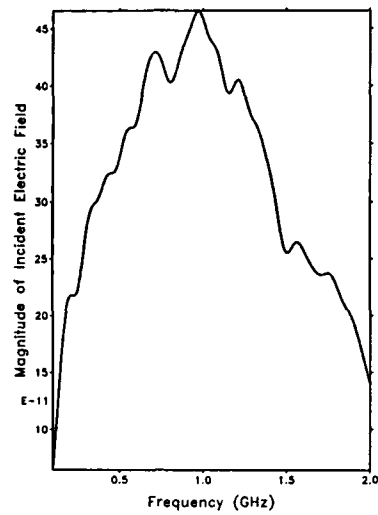


Fig. 13 - Input pulse spectrum.

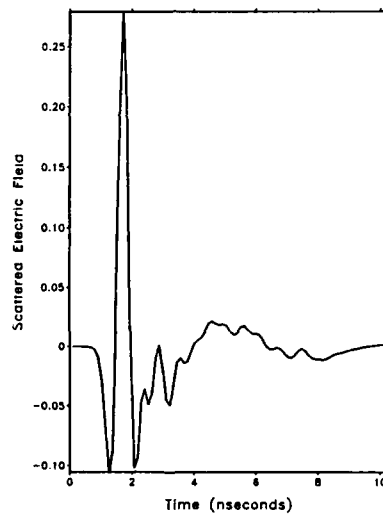


Fig. 14 - Output pulse, bandpass filtered to 0.1 to 2 GHz, decimated to 90 points.

the noise has allowed later time scattering to appear in the data. This improvement is essential because of the strong radiation damping produced by the plate.

4. EXAMPLE - APERTURE COUPLING, BROADBAND FREQUENCY MODE

As a second example, we include aperture coupling through a conducting screen (Fig. 17), a case considered by King and Hudson [3]. A metal wall is mounted perpendicular to the range ground plane with a 5 cm length rectangular aperture at bottom center. A D-dot sensor is located at $d = 5$ cm from the slot. All data taken is with the range instrumented in the broadband frequency mode as described above. We

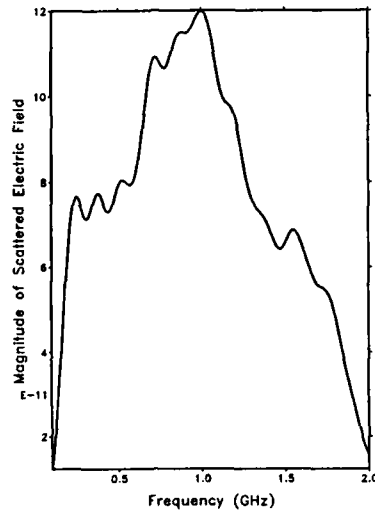


Fig. 15 - Output pulse spectrum.

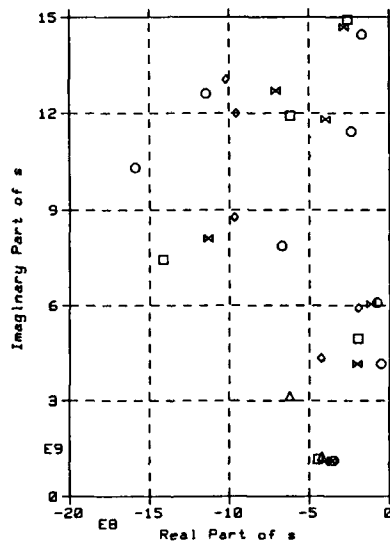


Fig. 16 - Theoretical poles (triangles) compared with identified poles of various model orders; 18th order (squares); 23rd order (diamonds); 25th order (bowties); 27th order (circles).

display (Fig. 18) the transfer function of different slots, all with the same length (5 cm), but with various heights (1,2,4,8 mm). Clearly in evidence are the primary resonances of each and the first secondary resonances at approximately three times primary. The transfer function is simply the ratio of the response of the D-dot sensor when located behind the aperture to the response at the aperture in the absence of the wall. The data clearly shows the utility of the range in making broadband electromagnetic measurements. We comment that our included data is only a sample of a large group of exhaustive measurements that have been taken by LLNL scientists. The interested reader is referred to R.J. Ring or H.G. Hudson at LLNL for details.

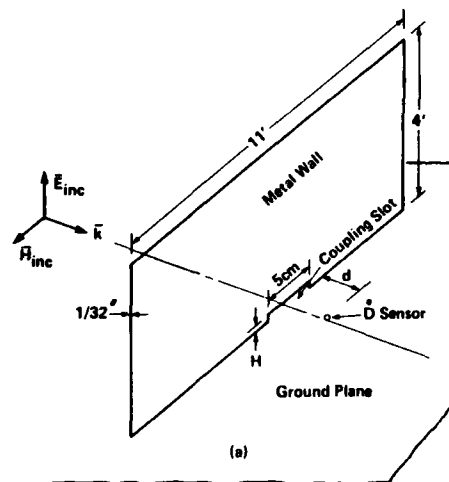


Fig. 17 - Metal wall with coupling slot, LLNL range.

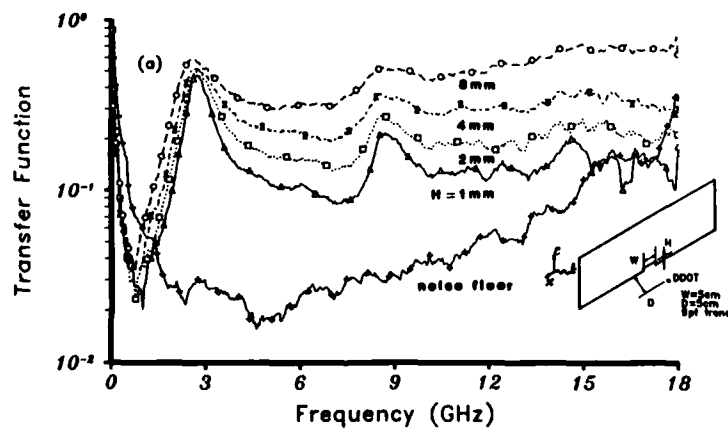


Fig. 18 - Transfer function, various apertures in metal wall, LLNL range.

5. ACKNOWLEDGMENTS

The plate scattering results reported herein are representative of work done by the author and D.B. Wright during a period when D.B. Wright was a Summer Student at Lawrence Livermore National Laboratory. The author wishes to thank R.J. King, H.G. Hudson, and D.K. Gnade for their assistance. Many Lawrence Livermore workers have contributed to the initial design of and subsequent improvements to the EMTRF. Although the author has been a frequent user of the facility, he has played only a minor role in the range evolution. The sources quoted in the references are representative of the LLNL workers, but they are not exhaustive. The author wishes to thank R.J. King for his permission to extract freely from this body of work in preparation of this lecture.

REFERENCES

- [1] King, R.J., Kunz, K.S., Hudson, H.G., Boberg, R.E., Pennock, S.T., and Gnade, D.K., Upgrade of the EM transient range monocone antenna, Lawrence Livermore National

Laboratory Report UCID-20438, 1985.

- [2] Lager, D.L. and S.G. Azevedo: SIG, a general-purpose signal processing program, Lawrence Livermore National Laboratory Report UCID-19912-Rev.1, 1985.
- [3] King, R.J. and H.G. Hudson, Experimental data for EM coupling through slots, Lawrence Livermore National Laboratory Report UCID-20842, 1986.
- [4] Dudley, D.G. and D.B. Wright, Scattering by a conducting rectangular plate, University of Arizona, Engineering Experiment Station Report (in preparation).
- [5] Dudley, D.G., Parametrization in scattering models, AGARD, Neuilly sur Seine, France, Lecture Series 152, 1987.
- [6] Goodman, D.M., NLS, a system identification package for transient signals, Lawrence Livermore National Laboratory Report UCRL-19767, 1983.
- [7] Pearson, L.W., The singularity expansion representation of the transient coupling through a rectangular aperture, University of Illinois, Doctoral Dissertation, 1976.

SELECTIVE BIBLIOGRAPHY

This bibliography with Abstracts has been prepared to support AGARD Lecture Series No. 152 by the Scientific and Technical Information Branch of the US National Aeronautics and Space Administration, Washington, D.C., in consultation with the Lecture Series Director, Professor L.B. Feisen, Polytechnic University, Farmingdale, New York.

UTTL: Radar target discrimination by convolution of radar return with extinction-pulses and single-mode extraction signals
AUTH: A/CHEN, K. M.; B/NYOULIST, D. P.; C/ROTHWELL, E. J.; D/DRACHMAN, B.; E/WEBB, L. L. PAA: D/(Michigan State University, East Lansing); E/(Northrop Corp., Aircraft Div., Hawthorne, CA) IEEE Transactions on Antennas and Propagation (ISSN 0018-926X), vol. AP-34, July 1986, p. 896-904.

ABS: A new method of radar target discrimination and identification is presented. This new method is based on the natural frequencies of the target. It consists of synthesizing aspect-independent discriminant signals, called extinction-pulses (E-pulses) and single-mode extraction signals which, when convolved numerically with the late-time transient response of an expected target, lead to zero or single-mode responses. When the synthesized, discriminant signals for an expected target are convolved with the radar return from a different target, the resulting signal will be significantly different from the expected zero or single-mode responses, thus, the differing targets can be discriminated. Theoretical synthesis of discriminant signals from known target natural frequencies and experimental synthesis of them for a complex target from its measured pulse response are presented. The scheme has been tested with measured responses of various targets in the laboratory. 86/07/00 86A46637

UTTL: A fast shape descriptor
AUTH: A/WA, J.; B/WU, C. K.; C/LU, X. R. PAA: C/(Northwest Telecommunication Engineering Institute, Xian, People's Republic of China) Computer Vision, Graphics, and Image Processing (ISSN 0734-189X), vol. 34, June 1986, p. 282-291.

ABS: A fast normalized shape descriptor for digital pattern-recognition and classification applications is developed and demonstrated. The descriptor employs the rapid transformation of Reitboeck and Brody (1968), preceded by a distance transform to assure invariance to rotation. The performance of the descriptor is compared experimentally with that of a normalized Fourier descriptor (Wallace and Wintz, 1980) in problems involving two-dimensional aircraft images. The new descriptor is found to be faster than and just as accurate as the Fourier descriptor, and to require significantly less memory storage capacity. 86/06/00 86A46377

UTTL: Modified GTD for generating complex resonances for flat strips and disks
AUTH: A/SHIRAI, H.; B/FELSEN, L. B. PAA: B/(New York, Polytechnic University, Farmingdale) IEEE Transactions on Antennas and Propagation (ISSN 0018-926X), vol. AP-34, June 1986, p. 779-790.

ABS: The complex resonance frequencies of a scatterer are important elements in target classification and identification. In the singularity expansion method (SEM), the resonances are defined by a homogeneous integral equation whose numerical solution is feasible in the low, but not in the high, frequency range. At high frequencies, the geometrical theory of diffraction (GTD) provides an attractive numerical alternative and, furthermore, incorporates an interpretation of the resonance generation process in terms of multiple wavefront (ray) transversals. Except for extremely simple scatterer configurations, the (damped) complex resonances are known to occupy an entire half of the complex frequency plane. Dominant and higher order creeping wave GTD applied to cylinders and spheres does indeed yield resonances arranged along a sequence of 'layers' in that entire half-plane, but multiple edge diffracted GTD applied to flat strips and disks furnishes only a single (dominant) layer. By drawing analogies with higher order creeping waves on a smooth object, the conventional edge diffracted GTD field is here augmented by higher order ray fields undergoing higher order 'slope diffraction'. Each of these higher order ray fields can be made to satisfy its own resonance equation, which is now found to provide the missing layers, with remarkably accurate values for the resonances when compared, where available, with those calculated numerically by the moment and T-matrix methods. The success of higher order ray diffraction in predicting the complex resonance structure suggests that this mechanism may play a corrective role also in other edge dominated scattering phenomena. 86/06/00 86A44268

UTTL: A combinatorial approach for classification of patterns with missing information and random orientation
AUTH: A/FLICK, T. E.; B/JONES, L. K. PAA: A/(U.S. Navy, Naval Research Laboratory, Washington, DC); B/(Catholic University of America, Washington, DC) IEEE Transactions on Pattern Analysis and Machine Intelligence (ISSN 0162-8828), vol. PAMI-8, July 1986, p. 482-490. Navy-supported research.

ABS: A maximum likelihood approach is developed for a pattern recognition problem where the patterns are described by configurations of simple easily

recognized parts called primitives. The approach is capable of dealing with three types of noise: measurement noise in the location and shape of observed primitives, undetected or missing primitives (leakage), and the unexpected appearance of extra primitives (false alarms). The approach is called combinatorial because the likelihood function dictates that observed primitives must be assigned to known primitives in all possible combinations. Due to the complexity of the likelihood function, practical classifiers must be based on likelihood function approximations. Several are proposed, and most of these are simple enough to be used in a gradient search strategy for recognizing distorted patterns with random orientations. Examples are included to show the characteristics of combinatorial classifier performance. 86/07/00 86A42173

UTTL: Maximum likelihood classification of synthetic aperture radar imagery
 AUTH: A/FROST, V. S.; B/VUROVSKY, L. S. PAA: B/(University of Kansas Center for Research, Inc., Lawrence) CORP.: Kansas Univ. Center for Research, Inc., Lawrence. Computer Vision, Graphics, and Image Processing (ISSN 0734-189X), vol. 32, Dec. 1985, p. 291-313.

ABS: Classification of synthetic aperture radar (SAR) images has important applications in geology, agriculture, and the military. A statistical model for SAR images is reviewed and a maximum likelihood classification algorithm developed for the classification of agricultural fields based on the model. It is first assumed that the target feature information is known a priori. The performance of the algorithm is then evaluated in terms of the probability of incorrect classification. A technique is also presented to extract the needed feature information from a SAR image; then both the feature extraction and the maximum likelihood classification algorithms are tested on a SEASAT-A SAR image. 85/12/00 86A42016

UTTL: A two-dimensional near-infrared tracking system
 AUTH: A/WALTON, D. P.; B/LIPOMA, P. C. PAA: B/(Lockheed Engineering and Management Services Co., Inc., Houston, TX) CORP.: Lockheed Engineering and Management Services Co., Inc., Houston, Tex. IN: Space Tech; Proceedings of the Conference and Exposition, Anaheim, CA, September 23-25, 1985 (A86-40501 19-12). Dearborn, MI, Society of Manufacturing Engineers, 1985, p. 3-31 to 3-34.

ABS: Video tracking systems face the problem of

discriminating between a target in space and the earth in the background. The visual tracking system described in this paper uses the near-infrared to take advantage of differences in spectral reflectance between the target and the earth in the background to enhance amplitude differences, simplifying the detection process. The real-time visual tracking system is microprocessor controlled, light weight, and low-power. 85/00/00 86A40506

UTTL: Determination of the phase characteristics of reflections from targets in multiple-frequency radar systems in the case of multipath signal propagation
 AUTH: A/VORDBEV, V. I.; B/KLIMOV, A. V. Radiotekhnika (ISSN 0033-8486), Feb. 1986, p. 19-22. In Russian. The paper examines the applicability of a multiple-frequency radar method (US patent No. 3,725,917) to the recognition of targets under conditions of multipath signal propagation. It is shown that the multipath conditions cause a significant deterioration in the efficiency of this method. In particular, the presence of additional Doppler shifts in the partial signals hampers the determination of the difference in phase shifts due to the target. The multipath effect can be weakened by frequency or spatial filtering. 86/02/00 86A36538

UTTL: Polarization weighting functions as a useful tool in clutter suppression, target classification and EM-wave-simulation
 AUTH: A/WANIELIK, G. PAA: A/(Telefunken AG, Forschungsinstitut, Ulm, West Germany). IN: 1985 International Geoscience and Remote Sensing Symposium (IGARSS '85), Amherst, MA, October 7-9, 1985, Digest, Volume 1 (A86-33501 15-42). New York, Institute of Electrical and Electronics Engineers, Inc., 1985, p. 527-532.

ABS: Real valued polarization weighting functions (PWF) whose magnitudes depend on the plane wave state of polarization are used in selected antenna polarizations on the Poincarisphere for deep clutter suppression. PWF's can be used for modeling the histogram of a stochastic electromagnetic wave (EMW) and as the probability of the state of polarization. Clutter adaptive realizations of the PWF can be done with a switched structure of two PWF tables where one is always in the update phase. PWF clutter suppression requires a priori knowledge of the clutter processes. Also discussed are PWF applications in radar target classification. 85/00/00 86A33575

UTTL: Advanced models of targets and disturbances and related radar signal processors

AUTH: A/FARINA, A.; B/RUSSO, A.; C/STUDER, F. A. PAA: C/(Selenia S.p.A., Rome, Italy) IN: International Radar Conference, Arlington, VA, May 6-9, 1985, Record (A86-32576 14-32). New York, Institute of Electrical and Electronics Engineers, Inc., 1985, p. 151-158.

ABS: The first part of the paper provides flexible and reliable stochastic models for the radar signals scattered by target and clutter sources. The models make it possible to consider any shape of autocorrelation function between consecutive pulse echoes and any probability density function for their in-phase and quadrature components. The second part of the paper revises the theory of detecting targets, with any type of probability density and autocorrelation function, embedded in a disturbance having any type of probability density and autocorrelation function. In the third part of the paper, the theory is applied to the cases in which target and/or disturbance may have a log-normal probability density for the amplitudes. Several processing schemes are suggested and corresponding detection performances are evaluated. Finally, adaptive implementation schematics are suggested for some of the processors presented. 85/00/00 86A32602

UTTL: Multi-sensor multi-platform track association using kinematics and attributes

AUTH: A/BDWMAN, C. L.; B/GROSS, M. PAA: B/(VERAC, Inc., San Diego, CA) IN: NAECN 1985; Proceedings of the National Aerospace and Electronics Conference, Dayton, OH, May 20-24, 1985; Volume 1 (A86-28326 12-04). New York, Institute of Electrical and Electronics Engineers, 1985, p. 204-208.

ABS: In a multisensor multiplatform data integration system, the Multi-Sensor Integration (MSI) software correlates the kinematic and classification information from individual sensors and the a priori sensor detection and false alarm statistics to generate track ID and kinematic state estimates. The E-3 and similar platforms then use the MSI track files plus the relative platform position-velocity information to perform Interrelated Surveillance Integration (ISI). The features of the system and the MSI and the ISI algorithms are described. 85/00/00 86A28254

UTTL: K-pulse for a thin circular loop

AUTH: A/KIM, H. T.; B/WANG, N.; C/MOFFATT, D. L. PAA: C/(Ohio State University, Columbus) IEEE Transactions on Antennas and Propagation (ISSN 0018-926X), vol. AP-33, Dec. 1985, p. 1403-1407. Research supported by the Ohio State University Research Foundation.

ABS: Based on the pole-elimination concept, a time-limited input waveform, the K-pulse, is obtained for a thin conducting circular loop. The resultant response waveforms are also found to be time-limited (TL). Therefore, by employing the K-pulse input waveform, the resonant ringing associated with the circular loop has been eliminated. The concept and procedure for deriving the K-pulse are discussed. 85/12/00 86A21288

UTTL: Efficient way for implementing error correcting codes in identification systems

AUTH: A/ARAZI, B.; B/HSEH, J. PAA: B/(Louisiana State University, Baton Rouge, LA) IN: SOUTHEASTCON '84; Proceedings of the Conference, Louisville, KY, April 8-11, 1984 (A86-20501 07-31). New York, Institute of Electrical and Electronics Engineers, 1984, p. 433-437.

ABS: The identity of a certain party X is commonly established by receiving from it an n-bit signal which only X and the receiver are supposed to have. This demonstrates a case where the purpose of transmitting n bits is not for increasing the knowledge of the receiver by n units of information, but for proving to the receiver that the transmitter has that information. Various considerations regarding the implementation of error correcting codes in such "reversed" schemes are discussed in this paper. The specific case of implementing efficiently an error correction scheme in an IFF (Identification Friend Foe) system, is treated in detail. 84/00/00 86A20523

UTTL: Air targeting of the third kind - Airborne vehicles

AUTH: A/GILMORE, J. F. PAA: A/(Georgia Institute of Technology, Atlanta) IN: Applications of digital image processing VII; Proceedings of the Meeting, San Diego, CA, August 21-24, 1984 (A86-19603 07-35). Bellingham, WA, SPIE - The International Society for Optical Engineering, 1984, p. 330-340.

ABS: The majority of research in the area of image analysis over the last several years has centered on ground-based object and region analysis. Recent events have stirred an interest in the detection and

- Classification of aircraft in flight. This paper surveys the six algorithms which have been successful applied to the problem of aircraft classification. Each algorithm is analyzed in terms of relative strengths and weaknesses. Summary results of the filter operators, aircraft types, evaluation imagery, problems addressed, and algorithm assumptions are presented for each approach considered. 84/00/00 86A19617
- UTTL: Model based segmentation of FLIR images
 AUTH: A/BHANU, B.; B/HOLBEN, R. D. PAA: A/(Utah, University, Salt Lake City); B/(Ford Aerospace and Communications Corp., Newport Beach, CA) IN: Applications of digital image processing VII: Proceedings of the Meeting, San Diego, CA, August 21-24, 1984 (A86-19603 07-35). Bellingham, WA, SPIE - The International Society for Optical Engineering, 1984, p. 10-18.
- ABS: Gray scale is used in combination with the edge information present in the image in an effort to obtain more precise segmentation of the target than that obtainable by using gray scale or edge information alone. A model of FLIR images based on gray scale and edge information is incorporated in a gradient relaxation technique which explicitly maximizes a criterion function based on the inconsistency and ambiguity of classification of pixels with respect to their neighbors. Four variations of the basic relaxation technique providing automatic selection of threshold to segment FLIR images are considered and compared. 84/00/00 86A19604
- UTTL: Statistical theory of extended radar targets
 AUTH: A/OSTROVITSIANDOV, R. V.; B/BASALOV, F. A. (Statisticheskaya teoriya radiolokatsii protiazhenykh tseliei, Moscow, Izdatel'stvo Radio i Svyaz', 1982) Dedham, MA, Artech House, 1985, 382 p. Translation. Previously cited in issue 21, p. 3124, Accession no. A83 45024. 85/00/00 86A16217
- UTTL: A context dependent automatic target recognition system
 AUTH: A/KIM, J. H.; B/PAYTON, D. W.; C/OLIN, K. E.; D/TSENG, D. Y. PAA: D/(Hughes Artificial Intelligence Center, Calabasas, CA) IN: Applications of artificial intelligence; Proceedings of the Meeting, Arlington, VA, May 3, 4, 1984 (A86-15278 04-63). Bellingham, WA, SPIE - The International Society for Optical Engineering, 1984, p. 2-7.
- ABS: This paper describes a new approach to automatic target recognizer (ATR) development utilizing artificial intelligent techniques. The ATR system exploits contextual information in its detection and classification processes to provide a high degree of robustness and adaptability. In the system, knowledge about domain objects and their contextual relationships is encoded in frames, separating it from low level image processing algorithms. This knowledge-based system demonstrates an improvement over the conventional statistical approach through the exploitation of diverse forms of knowledge in its decision-making process. 84/00/00 86A15279
- UTTL: Wavefronts and resonances for analysis of transient scattering
 AUTH: A/EISEN, L. B. PAA: A/(New York, Polytechnic Institute, Farmingdale) (Journées Internationales sur les Antennes, Nice, France, Nov. 13-15, 1984) Annales des Telecommunications (ISSN 0003-4347), vol. 40, July-Aug. 1985, p. 396-401.
- ABS: It is shown that a hybrid scheme, combining relevant waveforms and resonances self-consistently within a single framework, can optimize the analysis of the scattered field for all observation times. The role of wavefronts, resonances, and entire functions in the formulation of transient scattering is illustrated on the example of a strip obstacle. The transient fields, constructed by Fourier inversion of the GTD solution, are valid for early time behavior. Numerical comparisons have established the usefulness of the wavefronts and the hybrid format for dealing with the early-time response, in contrast to the less convenient SEM format. 85/08/00 86A14182
- UTTL: Improvement of image fidelity in microwave imaging through diversity techniques
 AUTH: A/GNISS, H.; B/MAGURA, K. PAA: B/(Forschungsgesellschaft fuer angewandte Naturwissenschaften, Forschungsinstitut fuer Hochfrequenzphysik, Wachtberg-Werthhoven, West Germany) IN: Inverse methods in electromagnetic imaging; Proceedings of the NATO Advanced Research Workshop, Bad Windsheim, West Germany, September 18-24, 1983 Part 2 (A85-48926 24-70). Dordrecht, D. Reidel Publishing Co., 1985, p. 1245-1254.
- ABS: This paper discusses some problems concerning the recognition of man-made targets from microwave imagery. Thereby, of special interest is the dependence of the image fidelity on the lateral resolution, on the target orientation, and on the depolarization properties of the target. An

improvement of the image fidelity is obtained through incoherent superposition of independent partial images using aspect and polarization diversity. 85/00/00 85A48985

UTTL: Radar target discrimination using the extinction-pulse technique

AUTH: A/ROTHWELL, E.; B/NYQUIST, D. P.; C/CHEN, K.-M.; D/DRACHMAN, B. PAA: D/(Michigan State University, East Lansing) IEEE Transactions on Antennas and Propagation (ISSN 0018-926X), vol. AP-33, Sept. 1985, p. 929-937.

ABS: An aspect independent radar target discrimination scheme based on the natural frequencies of the target is considered. An extinction-pulse waveform upon excitation of a particular conducting target results in the elimination of specified natural modal contents of the scattered field. Excitation of a dissimilar target produces a noticeably different late-time response. Construction of appropriate extinction-pulse waveforms is discussed, as well as the effects of random noise on their application to thin cylinder targets. Also presented is experimental verification of this discrimination concept using simplified aircraft models. 85/09/00 85A48251

UTTL: Statistically optimum methods of combining multiple sensor data for automatic target acquisition

AUTH: A/ALLEN, J. B. PAA: A/(Texas Instruments, Inc., Dallas) IN: NAECON 1984; Proceedings of the National Aerospace and Electronics Conference, Dayton, OH, May 21-25, 1984, Volume 1 (A85-44976 21-01), New York, IEEE, 1984, p. 237-244.

ABS: Statistically optimum methods of taking data from a multiple sensor suite and making target detection and recognition decisions are described. The decision is optimized with respect to a minimum risk criterion. The data from each sensor is properly weighed according to the reliability of the sensor. The weighed data is then used to make decisions which result in a minimum risk or probability of error. A specific example of a millimeter wave radar, a FLIR, and a Day TV sensor suite is taken. 84/00/00 85A45010

UTTL: Latency dependence of colour-based target vs nontarget discrimination by the saccadic system

AUTH: A/DOTTES, F. P.; B/VAN GIBBERGEN, J. A. M.; C/EGGERMONT, J. J. PAA: C/(Nijmegen, Katholieke Universiteit Nijmegen, Netherlands) Vision Research (ISSN 0042-6989), vol. 25, no. 6, 1985, p. 849 862.

Research supported by the Nederlandse Organisatie voor Zuiver-Wetenschappelijk Onderzoek.

First saccade responses to sudden presentations of a target/nontarget stimulus consisting of green and red spots of light have been investigated. This paradigm, which avoids certain ambiguities present in earlier experiments with identical double stimuli, leads to remarkably similar conclusions. It is found, again, that the saccadic system had short-latency compromising responses (averaging response mode) when the stimulus pair had a modest direction difference. When the direction difference was enlarged, first saccades were either directed near the green or the red spot (bistable response mode). In a second series of experiments different instructions, emphasizing either speed or accuracy of response, have been given to investigate the relation between saccade accuracy and latency. It appears that, independent of instruction, there is a fixed relation between saccade metrics and latency. The only way to avoid errors, such as averaging responses, is to delay the saccade. Hypothetical mechanisms underlying this relation are discussed against recent neurophysiological studies. 85/00/00 85A39960

UTTL: A wavefront interpretation of the singularity expansion method

AUTH: A/HEVMAN, E.; B/FELSEN, L. B. PAA: A/(Tel Aviv University, Tel Aviv, Israel); B/(New York, Polytechnic Institute, Farmingdale, NY) IEEE Transactions on Antennas and Propagation (ISSN 0018-926X), vol. AP-33, July 1985, p. 706-718.

ABS: Fel'sen (1984) has shown that transient fields scattered by an object may be synthesized in terms of progressing waves (wavefronts) or oscillatory waves (resonances). The present paper is concerned with multiple interaction and resonance phenomena in a broad sense, taking into account the employment of ray terminology to identify wave transport and interaction trajectories. Along those trajectories, the time harmonic field may be expressed by the ray approximation and is then subject to the rules and constraints of the geometrical theory of diffraction (GTD). However, the field may be expressed more generally by a 'better' wave function, for example a ray integral spanning a spectrum of local plane waves whose stationary phase approximation yields GTD but which, when kept intact, is uniformly valid in transition regions where GTD fails. Attention is given to the singularity expansion method (SEM) formulation, and the ray formulation, the flow graph representation, and the illustration of the presented concepts with the aid of an example. 85/07/00 85A39352

- UTTL: Design of the SPRT for radar target detection
 AUTH: A/CORSINI, G.; B/DALLE MESE, E.; C/VERRAZZANI, L.;
 D/MARCHETTI, G. PAA: C/(Pisa, Università, Pisa,
 Italy) IEE Proceedings, Part F - Communications,
 Radar and Signal Processing (ISSN 0143-7070), vol.
 132, pt. F, no. 3, June 1985, p. 139-148.
- ABS: Sequential techniques for signal detection are
 becoming increasingly important in radar applications.
 In this paper attention is focused on the sequential
 probability ratio test (SPRT), used for radar target
 detection. This test was proposed and analyzed for the
 first time by Wald (1947), who developed a method to
 approximately determine the performance of the SPRT.
 Unfortunately, this method is not valid in radar
 applications, so an exact analysis of the SPRT is
 required. An exact analysis of the SPRT is presented
 for the following cases: coherent detection,
 incoherent detection with nonfluctuating target, and
 incoherent detection with a Swerling-II-type
 fluctuating target. The results are summarized in a
 set of graphs which are useful for both design and
 analysis purposes. 85/06/00 85A38212
- UTTL: Bearing estimation of radar targets using the
 SPRT statistic
 AUTH: A/CORSINI, G.; B/DALLE MESE, E.; C/VERRAZZANI, L.;
 D/MARCHETTI, G. PAA: C/(Pisa, Università, Pisa,
 Italy) IEE Proceedings, Part F - Communications,
 Radar and Signal Processing (ISSN 0143-7070), vol.
 132, pt. F, no. 3, June 1985, p. 133-138.
- ABS: The paper is devoted to the problem of estimating the
 angular position of targets detected by using the
 sequential-probability ratio test. An estimation
 algorithm, which uses the final value of the
 cumulative variable of the detection test, has been
 analyzed by assuming a scanning step equal to one half
 the -3-dB antenna mainbeam aperture. The estimation
 algorithm is carried out by a decision-directed
 estimator. Its performance has been evaluated by
 numerical computation; the estimate is affected by a
 negligible bias error, and the error standard
 deviation is lower than one fifth of the antenna
 aperture. 85/06/00 85A38211
- UTTL: NATCS - Navigation Aided Target Control System
 for multiple drone applications
 AUTH: A/MORGAN, D. G. PAA: A/(Vega Precision Laboratories,
 Vienna, VA) IN: PLANS '84 - Position Location and
 Navigation Symposium, San Diego, CA, November 26-29,
 1984, Record (AB5-37801 17-17), New York, Institute of
 Electrical and Electronics Engineers, Inc., 1984, p.
 16-24.
- ABS: Modern military target drone scenarios require control
 systems that communicate rapidly with multiple high
 speed drones, provide position location and are cost
 and space effective. This paper describes a system for
 communicating with multiple target drones using
 existing TACAN and/or IFF transponder RF links.
 Demonstration flight test data and additional system
 capabilities such as ship location and over the
 horizon command control are also described. 84/00/00
 85A37803
- UTTL: Novel ways for tracking rays
 AUTH: A/FELSEN, L. B. PAA: A/(New York, Polytechnic
 Institute, Farmingdale, NY) Optical Society of
 America, Journal, A: Optics and Image Science (ISSN
 0740-3232), vol. 2, June 1985, p. 954-963
- ABS: Rays no longer just represent the trajectories
 traversed by a beam of light but they describe the
 general transport properties of high-frequency fields.
 Viewed within the framework of wave spectra, ray
 fields are localized spectral objects synthesized by
 constructive spectral interference. The spectral flesh
 within these objects can be trimmed to the bare bones
 for the simplest type of ray field, a local plane
 wave, but must be augmented in ray transition regions
 near caustics, shadow boundaries, diffraction centers,
 etc., where more-intricate wave phenomena occur. Thus
 ray tracing along ray paths generally involves a
 succession of bare-bones and fleshed-out (uniformized)
 spectral entities that can furnish in a highly
 effective manner the amplitude and the phase of the
 high-frequency field in a complex environment.
 Relevant spectral concepts are discussed, including
 those for complex rays that describe evanescent fields
 and Gaussian beams and those leading to collective
 treatment of multiple reflected or diffracted
 contributions. 85/06/00 85A37058
- UTTL: Radar signal processing
 AUTH: A/HAYKIN, S. PAA: A/(McMaster University, Hamilton,
 Ontario, Canada) IEEE ASSP Magazine (ISSN
 0740-7467), vol. 2, April 1985, p. 2-18. Research
 supported by the Natural Sciences and Engineering
 Research Council of Canada.
- ABS: The role of clutter in radar signal processing is
 considered with particular reference to an air-traffic
 environment. The characteristics of clutter are
 described, and the use of conventional moving-target
 indication filters to reduce the effects of clutter is
 considered. Adaptive clutter suppression schemes are
 addressed, and the adaptive detection of a moving
 target in the presence of clutter of unknown

- statistics is discussed. The use of a parametric spectrum estimation procedure as the basis of clutter classification is described. 85/04/00 85A34443
- UTTL: Calculation of the temporal scattering characteristics of radar targets
 AUTH: A/KIRMAOV, V. I. Radiotekhnika (ISSN 0033-8486), no. 3, March 1985, p. 16-19. In Russian.
 ABS: A simple method for calculating the temporal scattering characteristics of radar targets is proposed which involves the calculation of the ramp function in the framework of the physical-optics approximation. The proposed method can be used to compile a catalog of target profile functions with the aim of target identification. In addition, the computed profile functions can be used as input data for simulating algorithms for the reconstruction of three-dimensional images of targets (e.g., tomography-based algorithms). Numerical results are compared with experimental data for the 1.08-10.8 GHz range. 85/03/00 85A34170
- UTTL: Statistical training of a FLIR target detection algorithm
 AUTH: A/PANDYA, N.; B/LIN, Y.-K. J. PAA: B/(Harris Corp., Government Communications Systems Div., Melbourne, FL) IN: SOUTHEASTCON '83; Proceedings of the Region 3 Conference and Exhibit, Orlando, FL, April 11-13, 1983 (AB5-28101 11-33). New York, Institute of Electrical and Electronics Engineers, Inc., 1983, p. 547-550.
 ABS: The statistical training of a Forward-Looking Infrared (FLIR) target segmentation and classification algorithm is discussed. After statistically training an adaptive thresholding algorithm for FLIR segmentation on 30 images, one common parameter set for evaluating the FLIR images was derived. The adaptive thresholding technique, along with the parameter set, provides segmentation results of 83.32 percent. A set of 19 features was extracted for classification following segmentation. The 'common set of parameters' method is found to be reasonably successful in target detection. Several classifiers were trained and evaluated using the 'resubstitution' and the 'holdout' methods. On the average, 70 percent classification and 80 percent detection rates were achieved for the classification with 0.32 false alarms per image for 2355 target candidates belonging to nine classes. 83/00/00 85A28121
- UTTL: Target detection in digitized imagery using texture operators
 AUTH: A/TRIVEDI, M. M.; B/HARLOW, C. A.; C/CONNERS, R. W.; D/GOH, S. PAA: D/(Louisiana State University, Baton Rouge, LA) IN: SOUTHEASTCON '83; Proceedings of the Region 3 Conference and Exhibit, Orlando, FL, April 11-13, 1983 (AB5-28101 11-33). New York, Institute of Electrical and Electronics Engineers, Inc., 1983, p. 308-312
 ABS: In this paper, detection of targets in high resolution digitized aerial images is viewed as a special kind of segmentation task where the scene has to be segmented into target and background classes. Such a formulation necessitates utilization of a robust technique which can detect targets in a variety of backgrounds. The feasibility of using texture operators based on concurrence matrices is investigated. A statistical measurement selection technique that selects measures which are minimally sensitive to background and a statistical hypothesis test for classification is devised. Experiments on two sets of data were conducted. Results of the study indicate that texture measures can be successfully utilized for the characterization of targets. 83/00/00 85A28109
- UTTL: A progression of high-frequency RCS prediction techniques
 AUTH: A/KNOTT, E. F. PAA: A/(Georgia Institute of Technology, Atlanta, GA) IEEE, Proceedings (ISSN 0018-9219), vol. 73, Feb. 1985, p. 252-264.
 ABS: Attention is given to the unique features and advantages of the various methods that have been devised over the years to predict the radar cross section (RCS) of large, complex detection targets. The method of moments is unsuitable for routine large body computations, and geometric optics yields erroneous results for flat and singly curved surfaces. The theories of Keller (1957) and Ufimtsev (1957) have poor diffraction coefficients in the transition regions of shadow and reflection boundaries. In the Kouyoumjian and Pathak (1974) theory, the scattering direction is constrained to lie on the Keller cone, while a method of equivalent currents, although permitting the scattering direction to be arbitrary, yields nonphysical equivalent currents. It is noted that the methods discussed do not address the problem posed by the surface traveling wave of long, smooth bodies. 85/02/00 85A27830

UTTL: Kalman filter technique in detection and estimation of radar signals

AUTH: A/BEKIR, N.; B/BEKIR, E. PAA: B/(California State University, Northridge, CA) IN: International Radar Symposium, Bangalore, India, October 9-12, 1983. Proceedings (A85-24826 10-32), Bangalore, India, Institution of Electronics and Telecommunication Engineers, 1983, p. 244-249.

ABS: When detecting and tracking targets in realistic physical and electromagnetic environments, extraneous disturbance signals other than the target being tracked may lead to degradation of detection and tracking performance (sometimes resulting in losing the track altogether). Many different approaches have been taken to improve detection and/or tracking performance, among which the Kalman filter as an optimal estimator. In this paper, a Kalman-filter algorithm is used for detecting a moving target immersed in noise and estimating its parameters. The algorithm is not complex and can be considered as a nice approach for detection and estimation problems. Simulation results showed that the filter gave accurate and highly reliable estimates. 83/00/00 85A24864

UTTL: Contrast sensitivity performance assessment of HUD display systems

AUTH: A/GINSBURG, A. P.; B/MARTIN, W. L.; C/SELF, H. PAA: C/(USAF, Aerospace Medical Research Laboratory, Wright-Patterson AFB, OH) IN: Symposium on Aviation Psychology, 2nd, Columbus, OH, April 25-28, 1983. Proceedings (A85-21551 08-53), Columbus, OH, Ohio State University, 1984, p. 473-480.

ABS: The contrast losses of three head-up displays (HUD) having either reflective or refractive optical systems were determined from contrast sensitivity measurements under laboratory and field conditions. Contrast sensitivity losses resulting from the HUD optics due to transmittance, glare and reflections were translated into detection range losses using previously collected field trial data that related differences in detection range of Air Force pilots to differences in their contrast sensitivity. Agreements in detection range loss penalties using this direct approach and traditional approaches are good. In general, these three quite different HUDs produce similar losses in detection range. 84/00/00 85A21593

UTTL: Pole and residue extraction from measured data in the frequency domain using multiple data sets

AUTH: A/KSIENSKI, D. A. PAA: A/(Michigan, University, Ann Arbor, MI) Radio Science (ISSN 0048-6604), vol. 20, Jan.-Feb. 1985, p. 13-19.

ABS: When the singularity expansion method is applied to measured data, the accuracy of the results is often severely limited by the noise and clutter present in the measurement. An effective method of reducing these contaminations is repeating and averaging the measurements. The effectiveness of this approach is related to the number of measurements which are combined. The present paper develops a method which expands the set of measurements which may be combined from the set of identical measurements to the set of all measurements made on the target. The measurements are combined using an optimal weighting scheme to provide a superior estimate for a specified pole. An algorithm is described which increases the accuracy of the estimated pole locations and accurately computes the residues associated with these new pole locations. The algorithm is used to extract a single pole and residue, and additional poles and residues may be obtained through iterative application of the algorithm. 85/02/00 85A21127

UTTL: Detection of multiscatterer targets in K-distributed clutter

AUTH: A/FANIE, R. L. PAA: A/(AVCO Corp., AVCO Systems Div., Wilmington, MA) IEEE Transactions on Antennas and Propagation (ISSN 0018-926X), vol. AP-32, Dec. 1984, p. 1358-1363.

ABS: Results are obtained for the probability of detecting a target consisting of N correlated, equal-amplitude glints immersed in K-distributed clutter. The results indicate that large-resolution-cell sea and land clutter measurements at small grazing angles are well-fit by the K-distribution. It is shown that at short wavelengths real targets cannot be represented as a single complex phasor but may require two to five phasors, each representing a different glint on the target. 84/12/00 85A19288

UTTL: Target identification by means of radar

AUTH: A/DALLE MESE, E.; B/MANCIANTI, M.; C/VERRAZZANI, L. PAA: C/(Pisa, University, Pisa, Italy); D/(Newcastle, University, Newcastle, New South Wales, Australia) Microwave Journal (ISSN 0026-2897), vol. 27, Dec. 1984, p. 85, 86, 88 (7ff.).

ABS: Great practical relevance has the problem of target classification and identification by means of radar. A classification procedure consists basically of two

main steps, including the acquisition of the information useful for classifying the target from raw data (feature extraction), and a suitable processing of the information obtained in the first step (pattern recognition) to perform the association between the received signal and the unknown object. The work of the international radar community on the subject of target classification has been focused mainly on the solution of the problems related to the first step. The present overview is concerned with the classification techniques which utilize the properties of the target frequency response. Classification techniques which use a spatially coherent processing of the received echoes, and classification techniques which use the properties of the target scattering matrix. Classification techniques which use a near millimeter wave (Nmmw) radar system operating in the imaging mode are also discussed. 84/12/00 85A18144

AUTH A/SAWTELLE, S. C.; B/JENNEMINE, R. J. PAA B/LUSAF, Wright Aeronautical Laboratories, Wright-Patterson AFB, OH) IN Digital Avionics Systems Conference, 6th, Baltimore, MD, December 3-6, 1984. Proceedings (AB5-17801 06 01) New York, American Institute of Aeronautics and Astronautics, 1984. p. 60-64.

ABS The Imaging Sensor Autoprocessor (ISA) development effort has as its goal the augmentation of target recognition system operators' abilities and the optimization of their information handling capability. The target recognition algorithms under development for multiscenario environments are intended for VHSIC implementation. The ISA must be capable of greater than 90 percent target detection and classification. Two systems are under competitive development, and will be ready for testing by 1986.

RPT# AIAA PAPER 84 2617 84/00/00 85A17811

AUTH A/DELHOUE, C.; B/COULOMBEIX, C.; C/LE CHEVALIER, F. PAA C/ONERA, Châtillon sous Bagneux, Hauts-de-Seine, France) (International Symposium on Noise and Clutter Rejection in Radar, Tokyo, Japan, Oct 22-24, 1984) ONERA, TP. no 1984-133, 1984. 7 p.

ABS Detection of targets by passive airborne millimetric sensors is limited by clutter. Replica matched filter performance can be improved by an adaptive whitening filter calculated by autoregressive modeling of clutter. The theoretical signal to noise ratio gain is calculated. The procedure is simulated for clutter.

synthesized by ARMA models and the influence of clutter spectrum, receiver noise, and replica bad knowledge is examined.

RPT# ONERA, TP NO. 1984-133 84/00/00 85A15849

AUTH UTTL: Detection of weak third harmonic backscatter from nonlinear metal targets

A/HONG, J. Y.; B/POWERS, E. J. PAA: B/Texas, University, Austin, TX) IN: EASCON '83; Proceedings of the Sixteenth Annual Electronics and Aerospace Conference and Exposition, Washington, DC, September 19-21, 1983 (AB5-14426 04-32). New York, Institute of Electrical and Electronics Engineers, 1983. p. 169-175.

ABS This paper will discuss how one can obtain the third-order characteristics of a metallic target even when the strength of the third-harmonic frequency component is far below that of the external noise or intentional jamming signal. The key idea lies in the fact that the digital third-order cross-trispectrum used to detect the third harmonic is primarily sensitive to the phase coherence between the transmitted fundamental and relatively weak backscattered third harmonic, rather than on the amplitude of the third harmonic. The feasibility of using digital cross-trispectral analysis to detect weak (S/N ratios of about -20 db) third harmonics will be demonstrated with the aid of simulation experiments.

83/00/00 85A14446

AUTH A retrospective detection algorithm for extraction of weak targets in clutter and interference environments

A/PRENGAMAN, R. J.; B/THURBER, R. E.; C/BATH, W. G. PAA C/Johns Hopkins University, Laurel, MD) IN: EASCON '83; Proceedings of the Sixteenth Annual Electronics and Aerospace Conference and Exposition, Washington, DC, September 19-21, 1983 (AB5-14426 04-32) New York, Institute of Electrical and Electronics Engineers, 1983. p. 153-157.

ABS A retrospective processing concept for controlling the false alarm rate of target tracking radar is discussed. The system architecture has memory allotted to previous images for comparisons with updated images, thereby raising the possibilities of eliminating spurious images from i.e., clutter, and of plotting target trajectories. Consequently, the radar is run at an enhanced false alarm rate because clutter is filtered out. The system includes retrospective correlations using a bearing/range link structure, update of a velocity profile mask, and decision output based on the mask update. Decisions are generated

- after an assessment of reasonableness. The system was developed as a means of avoiding clutter in over-ocean surveillance operations. 83/00/00 85A14444
- AUTH** UTTL Aircraft identification based on pattern recognition of FM emission spectra
A/RASHBA, S. F. PAA A/(Bradley University, Peoria, IL) IN: Modeling and simulation, Volume 14, Proceedings of the Fourteenth Annual Pittsburgh Conference, Pittsburgh, PA, April 21, 22, 1983. Parts 1-2 (AB5-11076 01-66). Research Triangle Park, NC, Instrument Society of America, 1983, p. 277-286
- ABS** The purpose of this paper is to present a method for identifying aircraft type. Radar returns from propeller blades are analyzed for signature features. Two new algorithms for identification are presented. (1) The m/N algorithm which requires that m-out-of-N features match a known 'catalogued' pattern; and (2) the beta-recursion algorithm which estimates an aircraft-identifying parameter. Curves of probability of error are given for both algorithms. The m/N algorithm provides probabilities of error in the range 0.1 to 0.001 for low signal-to-noise conditions, 0.001 to 0.000001 for medium conditions, and 10 to the -6th to 10 to the -10th for high signal-to-noise conditions. The beta-recursion algorithm provides probability of error in the range of 0.25 to 0.017 depending on signal-to-noise conditions and the amount of data available. 83/00/00 85A11078
- AUTH** UTTL Parametric studies of space infrared sensors
A/SPIRD, I. J. PAA A/(Aerospace Corp., Los Angeles, CA) IN: Advanced infrared sensor technology, Proceedings of the Meeting, Geneva, Switzerland, April 18, 19, 1983 (AB5-10576 01-35). Bellingham, WA, SPIE - The International Society for Optical Engineering, 1983, p. 182-186
- ABS** The equations used for system infrared calculations are presented. These equations are then rearranged into the forms useful for developing space infrared systems. Curves and nomograms are presented that exhibit the relationships between many parameters such as detector sizes, diameter of the optics, focal lengths of the optics, ground footprint, normalized detectivity, angular resolution, target intensity, and quantum efficiency. 83/00/00 85A10594
- AUTH** UTTL Optical proximity sensor using multiple cones of light for measuring surface shape
A/FURHMAN, M.; B/KANADE, T. PAA B/(Carnegie-Mellon University, Pittsburgh, PA) Optical Engineering (ISSN 0091-3286), vol. 23, Sept.-Oct. 1984, p. 546-553. Research supported by the Carnegie-Mellon University and U.S. Navy.
- ABS** A new compact multilight source proximity sensor has been developed. The sensor is based on the principle of active illumination and triangulation; each time the light is pulsed, the coordinates of the resulting spot of light on a surface is calculated. This model permits the necessary number of light sources and their appropriate orientations to be calculated in order to achieve a specified accuracy when measuring distance and orientation. Two prototype proximity sensors have been built, one with a precision of 0.07 mm and 1.5 deg over a range of 40-50 mm, and the other with a range of 5 cm. These prototypes acquire data at a rate exceeding 1000 points/sec. Previous multilight source proximity sensors are also discussed. 84/10/00 85A10030
- AUTH** UTTL Medium PRF pulse Doppler radar processor for dense target environments
A/FROST, E. L.; B/LAWRENCE, L. CORP: Department of the Air Force, Washington, D.C.
- ABS** This patent is a modification to the ABC range correlators used in medium PRF radars. It extends the functioning of the range correlators to not only derive target unambiguous range while suppressing detections of clutter discretizes but also to reduce the occurrence of false target reports (range ghosts) and blanking of true targets that would otherwise occur when the radar is operated in dense target environments. The specific point of novelty in this design is the operation of two sets of correlators, designated ABC and A'B'C', each with a different M of N detection criterion.
AD-D012344 US-PATENT-4,584,579
US PATENT-APPL-SN-547609 US-PATENT-CLASS-343-17.1
86/04/22 86N32613
- AUTH** UTTL Radial distortion in the reproduction of three-dimensional targets at close range
A/KUPFER, G. CORP: Bonn Univ. (West Germany).
- ABS** Radial distortion in the reproduction of 3D targets in close range photogrammetry is studied based on Seidel series where distortion is a function of radial distance. Radial distortion depends on object remoteness and camera focusing. Distortion is programmed for MOR-S program (and adjustment program).

Test field photographs are used to determine the test field coordinates. 85/00/00 86N29187

UTTL: A mathematical model for calculating non-detection probability of a random four target AUTH: A/ABDEL-FADEEL, S. I., CORP. Naval Postgraduate School, Monterey, Calif.
ABS: The primary objective of this thesis was to build a mathematical model to predict the probability of a target moving according to a two-dimensional random four model avoiding detection (i.e., surviving) to some specified time. This model assumes that there is a stationary searcher having a 'cookie-cutter' sensor located in the center of the search area. A Monte-Carlo simulation computer program was used to generate the non-detection probabilities. The output of this program was used to construct the required mathematical model. The model predicts, and simulation supports, that as the mean segment length of the random four becomes small with respect to the square root of the area size, the probability of non-detection approaches that previously obtained for a diffusing target. In the opposite extreme, the probability of non-detection approaches the general form of Koopman's random search formula.
RPT#: AD-A165019 85/12/00 86N27955

UTTL: Development of a testbed for multisensor distributed decision algorithms AUTH: A/SCHON, M. A., CORP. Naval Postgraduate School, Monterey, Calif.
ABS: Distributed decision problems arise when two or more sensors viewing the same phenomenon must work cooperatively to draw inferences about the observed situation. Typical examples are in target detection and target classification. Such problems are characterized by distributed processors of information and communication between processors over a limited bandwidth data link. This thesis presents some statistical distributed decision algorithms and describes the implementation of one of them on a set of loosely coupled multiprocessor clusters which simulate the distributed environment characterizing multisensor decision problems.
RPT#: AD-A164487 AD-E900539 85/12/00 86N26601

UTTL: Particle beam tracker for an accelerating target AUTH: A/JAMERSON, L. C., CORP. Air Force Inst. of Tech., Wright-Patterson AFB, Ohio. CSS: (School of Engineering.)

ABS: The purpose is to use a PI(Proportional plus INTEGRAL) controller to point the centroid of a particle beam at an intended target. Multiple Model Adaptive Estimator is used to estimate the centroid of a one-dimensional Gaussian shaped source of photo-electron events. Merge Method of filter pruning is used to limit the size of this filter. A standard Kalman filter is used to estimate the position of the target where the target is initially modelled as a first-order Gauss-Markov position process and later as a first-order Gauss-Markov acceleration process. A PI controller is designed using LOG methods, and true states are replaced by their best estimates by invoking the principle of assumed certainty equivalence. With a target position model within the software, a parameter sensitivity analysis is performed as well as a robustness study where unmodelled constant and sinusoidal disturbances are added to the system. With a target acceleration model within the software, a robustness study is carried out where target parameters are varied within the truth model without telling the filter. In an attempt to recover full state feedback robustness qualities, Loop Transmission Recovery tuning is attempted.
RPT#: AD-A163945 AFIT/GE/ENG/85D-22 85/12/00 86N26182

UTTL: Automatic feature extraction/algorithm testing AUTH: A/FERRIS, N. A., CORP. Autometric Corp., Inc., Rome, N.Y.
ABS: Feature extraction results using an Improved Texture Clustering Algorithm were compared to photo interpreters' manual segmentation/classification results. The clustering algorithm segments digital images via texture and edge attributes. The probability of detecting a target or feature is increased if the number of segments is reduced; therefore, the algorithm merges segments via edge thresholds. Evaluation showed general agreement, but the edge attributes would apply more to target detection than to feature classification.
RPT#: AD-A164325 ETL-0410 85/11/00 86N26038

UTTL: Analysis of a distributed decision algorithm AUTH: A/HAHN, S. C., CORP. Naval Postgraduate School, Monterey, Calif.
ABS: Distributed decision problems arise whenever two or more sensors and their associated computers must work cooperatively to make a decision about a commonly

so the system is largely independent of object/sensor orientation.

RPT#: BAE-BT-11140 80/11/00 86N20459

UTTL: Exact performance analysis of the censored mean-level detector in a multiple-target environment

AUTH: A/RITCEY, J. A. CORP: California Univ., San Diego, La Jolla, CSS: (Dept. of Electrical Engineering and Computer Sciences.)

ABS: The censored mean-level detector (CMLD) is an alternative to the mean-level detector that achieves robust detection performance in a multiple-target environment by censoring several of the largest samples of the maximum-likelihood estimate of the background noise level. Here we derive exact expressions for the probability of detection of the CMLD in a multiple-target environment when a fixed number of Swerling II targets are present. The primary target is modelled by Swerling case II, and only single-pulse processing is analyzed. Optimization of the CMLD parameters is considered, and a comparison to other detectors is presented. 85/07/15 86N19496

RPT#: AD-A160349 AFOSR-85-0752TR

UTTL: Performance of resonant radar target identification algorithms using intra-class weighting functions

AUTH: A/MUSTAFA, A. CORP: Ohio State Univ., Columbus.

ABS: The use of calibrated resonant-region radar cross section (RCS) measurements of targets for the classification of large aircraft is discussed. Errors in the RCS estimate of full scale aircraft flying over an ocean, introduced by the ionospheric variability and the sea conditions were studied. The Weighted Target Representative (WTR) classification algorithm was developed, implemented, tested and compared with the nearest neighbor (NN) algorithm. The WTR algorithm has a low sensitivity to the uncertainty in the aspect angle of the unknown target returns. In addition, this algorithm was based on the development of a new catalog of representative data which reduces the storage requirements and increases the computational efficiency of the classification system compared to the NN algorithm. Experiments were designed to study and evaluate the characteristics of the WTR- and the NN-algorithms. Investigate the Classifiability of targets and study the relative behavior of the number of misclassifications as a function of the target backscatter features. The classification results and statistics were shown in the form of performance curves, performance tables and confusion tables 85/00/00 86N19490

UTTL: Acoustic research report

AUTH: A/UEBERALL, H. CORP: Catholic Univ. of America, Washington, D.C. CSS: (Dept. of Physics.)

ABS: A recent investigation has shown that the spectrum of the resonance frequencies of plates can be obtained by ultrasonic pulse techniques. By physically analyzing the distortion of the reflected wave trains, a method was developed through which the parameters of the plate resonances, and hence the physical constants of the plate material, can be determined by ultrasonic means. The physical origin of the plate resonances was elucidated, and it was shown how the observed ringing of ultrasonic resonances is caused by multiple internal reflections in the plate. A series of backscattering experiments employing wavetrains with carrier frequency on or off a resonance was interpreted this way, with perfect agreement between theory and experiment.

RPT#: AD-A159900 85/07/17 86N19128

UTTL: The Smoke Transmission and Reflection Threshold (START) model; the Oldbroek (Netherlands) 2 trials, May 1981

AUTH: A/VALETON, J. M. CORP: Institute for Perception RVO-TNO, Soesterberg (Netherlands). CSS: (Vision Research Group.)

ABS: The contrast reduction caused by the effects of smoke and the natural atmosphere are analyzed. The minimum requirement for a smoke screen to make a target invisible is described in terms of a transmission threshold or a reflection threshold. The dependence of these thresholds on environmental parameters is described with the Smoke Transmission And Reflection Threshold model. A target is visible when the actual transmission is greater than the transmission threshold, or when the actual smoke reflection is below the reflection threshold. The transmission and reflection thresholds depend on distances in the field, inherent target contrast, visual range, and type of smoke. Prediction of the occurrence of holes, the perceptual quality of the smoke screen, and the reduction in effectiveness of weapons is discussed.

RPT#: IZF-1984-22 TDCX-79979 85/01/00 86N18187

UTTL: Time characteristics of scattering by radar targets

AUTH: A/KIRMA5OV, V. I. CORP: Joint Publications Research Service, Arlington, Va.

ABS: A simple method for calculating the temporal scattering characteristics of radar targets is proposed which involves the calculation of the ramp function in the framework of the physical-optics

observed event. Typical examples are in target detection and classification. The problem is usually characterized by a limited bandwidth of the communication link between the sensors. This thesis develops and evaluates an algorithm for distributed decision and compares it to a non-distributed or centralized form of the algorithm. Analysis of the algorithm is carried out for some low-dimensional cases. Computer simulations were carried out for higher dimensional cases. The simulation work was done in FORTRAN under CMS on an IBM 370/3033 computer.

RPT#: AD-A164181 85/12/00 86N25159

UTTL: NCTR using a polarization-agile coherent radar system
 AUTH: A/WALTON, E. K.; B/MOFFATT, D. L.; C/GARBER, F. D.; D/KAMIS, A.; E/LAI, C. Y. CORP: Ohio State Univ., Columbus, CSS: (Electroscience Lab.)

ABS: This report describes the results of the first year of a research project performed by the Ohio State University ElectroScience Laboratory (OSU/ESL) for the Naval Weapons Center (NWC). The goal of this project is to explore the use of the polarization properties of the signal scattered from a radar target for the purpose of radar target identification. Various radar target identification algorithms were applied to the case of a full polarization coherent radar system, and were tested using a specific data base and noise model. The data base used to test the performance of the radar target identification algorithms developed here is a unique set of measurements made on scale models of aircraft. Measurements were made using the OSU/ESL Compact Radar Measurement Range. The range was operated in a broad-band (1-12 GHz) mode and the full polarization matrix was measured. Calibrated values (amplitude and phase) of the RCS for the three polarization states were thus available. The polarization states are listed below.

RPT#: AD-A16528 ESL-716559-2 86/01/00 86N24882

UTTL: Space-frequency sampling criteria for electromagnetic scattering of a finite object
 AUTH: A/FDK, F. Y. S. CORP: Ohio State Univ., Columbus, CSS: (Electroscience Lab.)

ABS: This investigation concerns the sampling criteria in the wave number space for generating the spatial impulse response of a finite target. The impulse response of a finite target is important for target identification and imaging. The other purpose of this report is in the management of large amounts of data for potential application in the presentation of scattered field data and construction of such images.

For clarity, monostatic impulse responses of up to two dimensions are considered. A proper choice of canonical confinement for the target in space can greatly reduce the number of samples required to sufficiently characterize the target's spatial impulse response. One dimensional impulse responses generated using two basic types of confinement: 1) isotropic and 2) parallelepiped, are compared. The two approaches show competitive reconstructed results. Though a sampling lattice may be more efficient in the sense of a reduced number of measurement points, it may be less effective when digital processing is involved. Specifically, the time consuming interpolation step is required to put data presented in other types of sampling lattice into the cubic type. Two dimensional impulse responses reconstructed from cubic sampled data are compared with those using Mensa et al. method. Two dimensional impulse responses obtained also indicate good potentials for image reconstruction via the spatial impulse response.

RPT#: AD-A162553 ESL-714190-11 85/08/00 86N21737

UTTL: Effects of waveguide modes on the scattering of a finite tubular cylinder
 AUTH: A/CHUNG, G. P. CORP: Naval Postgraduate School, Monterey, Calif.

ABS: This thesis is a study of the back scattering of finite tubular cylinders with circular cross-sections and very thin conducting walls. Measurements of several scaled tubular cylinders were taken and the experimental results were compared to theoretical data and to previous results, respectively. This research is part of an ongoing project to investigate the resonant scattering characteristics of targets. The results are expected to find applications in target identification.

RPT#: AD-A161500 85/09/00 86N21729

UTTL: Models for a target recognition system in missiles using a computer and sensor device
 AUTH: A/PUZEY, N. J. CORP: British Aerospace Dynamics Group, Bristol (England), CSS: (Human Factors and Vision Research Dept.)

ABS: Shape recognition models are discussed and recommendations for the design of a computer guidance system for missiles are made. A model to account for shape discrimination by the Octopus visual system is the most heuristic in forming the basis of an automatic target acquisition system. A system based on a recognition template of hexagonal cell sensors is proposed; this can identify the same aspect of an object along the three axes of symmetry of the hexagon

approximation. The proposed method can be used to compile a catalog of target profile functions with the aim of target identification. In addition, the computed profile functions can be used as input data for simulating algorithms for the reconstruction of three-dimensional images of targets (e.g., tomography-based algorithms). Numerical results are compared with experimental data for the 1.08 to 10.8 GHz range. 85/10/24 86N15512

UTTL: Hierarchical relaxation methods for multispectral pixel classification as applied to target identification

AUTH: A/COHEN, E. A., JR. CORP: Naval Surface Weapons Center, Silver Spring, Md.

ABS: This report provides insights into the approaches toward image modeling as applied to target detection. The approach is that of examining the energy in prescribed wave-bands which emanate from a target and correlating the emissions. Typically, one might be looking at two or three infrared bands, possibly together with several visual bands. The target is segmented, using both first and second order modeling, into a set of interesting components and these components are correlated so as to enhance the classification process. A Markov-type model is used to provide an a priori assessment of the spatial relationships among critical parts of the target, and a stochastic model using the output of an initial probabilistic labeling is invoked. The tradeoff between this stochastic model and the Markov model is then optimized to yield a best labeling for identification purposes. In an identification of friend or foe (IFF) context, this methodology could be of interest, for it provides the ingredients for such a higher level of understanding.

RPT#: AD-A158694 NSWC/TR-84-54 85/02/01 86N14575

UTTL: Exact detection probability and fluctuation loss for a partially correlated Rayleigh target

AUTH: A/KANTER, I. CORP: Kanter (Irving), Lexington, Mass.

ABS: Theoretical methods are well known for the determination of the probability of detection for fluctuating and non-fluctuating targets when N pulses of signal pulse noise are integrated incoherently. Previously, correlation of the pulses has been considered to be complete or nonexistent during the integration time. This analysis extends the detection theory to include detection of the sum of N partially correlated pulses. A Rayleigh target whose in-phase and quadrature components have exponential correlation is used as the model. The fluctuation loss for a

Gauss-Markov signal is determined as a function of number of pulses integrated, the correlation between pulses, and the specified detection and false alarm probabilities. This exact loss is compared to Barton's approximation.

RPT#: AD-A159457 AD-E950749 AMSMI/RE-CR-85-3 85/07/00 86N14490

UTTL: Quasi-optic study of dielectric radomes and lenses

AUTH: A/FELSEN, L. B. CORP: Polytechnic Inst. of New York, Farmingdale, CSS: (Microwave Research Inst.)

ABS: The results from this study confirm the utility of complex ray tracing (via ordinary complex rays, collective complex rays or hybrid forms) for Gaussian beam type fields transmitted through tapered or curved two-dimensional shell radomes. The numerical algorithm, which avoids the need for integrations over an equivalent aperture when passing from the near zone to the far zone, can be simplified substantially for a range of applications by recourse to paraxial approximations. These conclusions are expected to remain valid also for more general three-dimensional configurations. Although non-Gaussian aperture distributions are not well modeled by complex ray fields per se, recent studies indicate that general aperture fields can be expressed as discrete superpositions of Gaussian fields. This makes the results for single Gaussians reported here directly relevant for the tracking, via obstacles and interfaces, of this more general class of incident fields.

RPT#: AD-A158441 POLY-MRI-1444-85 ARD-18887.7-EL 85/08/01 86N14481

UTTL: Adaptive detection in nonstationary

interference: Part 1 and part 2

AUTH: A/KELLY, E. J. CORP: Massachusetts Inst. of Techn., Lexington.

ABS: In this report, which consists of two parts, the problem of radar target detection in a background of nonstationary external interference is considered. The object of the analysis is to treat this problem from the point of view of statistical decision theory, and to derive a signal processing algorithm which accepts the totality of inputs on which final decision is to be based, and performs both interference suppression and target detection. It is assumed that the radar is provided with multiple RF input channels and that target-free samples, from range gates other than one in which a target is being sought, can be used for the estimation of the interference statistics. In Part 1 a

general formulation is given and a likelihood ratio detection rule is derived.

RPT#: AD-A158810 TR-724 ESD-TR-85-197 85/06/25 86N13993

UTTL: Target tracking based scene analysis
AUTH: A/KAZOR, N. CORP. Maryland Univ., College Park.
CSS: (Center for Automation Research.)
ABS: Target Tracking and Scene Analysis are two research areas in Computer Vision which, in the past, have been dealt with as separate problems. Most target tracking systems have the relatively modest goal of detecting and identifying moving objects and tracking them, using prediction and correlation techniques, as long as they move unobscured across the field of view. Most of these systems have been developed with a set of stringent real time constraints which, given current hardware technology, constrains them to employ a set of computationally simple algorithms. Most scene analysis/segmentation systems analyze a given scene based on the static properties of objects such as shape/structure and texture, where the class of objects are generally predefined. These systems tend to be slow whenever the scene is complex, containing many objects. There are advantages to combining the two problems into one. This paper is based on such an idea is concerned with the design of an Intelligent Target Tracking System (ITTS). This experimental system tracks targets based not only on models for targets (shape, motion, etc.), but also on models of the environment through which the targets navigate and of the sensing system(s) employed to acquire the time-varying images on which the analysis is based. The ITTS is composed of a number of processes which can be divided into three processing stages: target recognition, segmentation of time-varying images, and scene model generation.

RPT#: AD-A158629 CAR-TR-88 CS-TR-1437 84/08/00 86N13910

UTTL: Second Colloquium on the Scattering of Ultrasonic Waves.
AUTH: A/UBERALL, H. CORP. Catholic Univ. of America, Washington, D.C. CSS: (Dept. of Physics.) Colloq. held at Paris, 4-7 Dec. 1984
ABS: Contents: L'acoustique des faisceaux bornes; Scattering from fluid and elastic layers; Acoustic scattering from elastic cylinders and spheres; Surface waves (Watson transform) and transmitted waves; Helical surface waves on cylinders and cylindrical cavities; Resonance scattering theory; Spherical and cylindrical cavities and inclusions; Scattering from inhomogeneities; Scattering of short and long sound pulses; Connection with the singularity expansion

method; and Inverse scattering and acoustic spectroscopy.

RPT#: AD-A156298 85/01/29 85N35697

UTTL: Selectivity of weight compensator of passive interference to unknown velocities of detectable targets
AUTH: A/KISELEV, A. Z. CORP: Joint Publications Research Service, Arlington, Va.
ABS: Attention is given to a compensator for the detection of targets with unknown velocities. A weight vector is obtained which describes the matching of the compensator with the range of expected target velocities, and the selectivity features of this compensator are investigated. It is shown that, for a larger number of processed pulses, the compensator selects only targets whose Doppler frequencies are close to half the repetition frequency of the radar signals. 84/11/23 85N33317

UTTL: A modified Fresnel scattering model for the parameterization of Fresnel returns, part 2.3A
AUTH: A/GAGE, K. S.; B/ECKLUND, W. L.; C/BALSLEY, B. B. CORP: National Oceanic and Atmospheric Administration, Boulder, Colo. CSS: (Aeronomy Lab.)
ABS: A modified Fresnel scatter model is presented and the revised model is compared with observations from the Poker Flat, Alaska, radar, the SQUAY radar and the Jimcamarca radar. The modifications to the original model have been made to better account for the pulse width dependence and height dependence of backscattered power observed at vertical incidence at lower VHF. Vertical profiles of backscattered power calculated using the revised model and routine radiophone data show good agreement with observed backscattered power profiles. Relative comparisons of backscattered power using climatological data for the model agree fairly well with observed backscattered power profiles from Poker Flat, Jimcamarca, and SQUAY. 84/12/00 85N32483

UTTL: Broadside scattering of a tubular cylinder for evaluation of target identification
AUTH: A/HAKLAY, B. CORP: Naval Postgraduate School, Monterey, Calif.
ABS: The concept of target identification through its backscattering cross section, in the resonance region was investigated. Measurements from the broadside aspect angle of several scaled tubular cylinders have been used for this purpose. The experimental results and theoretical approximation for some of the

cylinders are presented. That data will serve as the baseline for further investigation in this project. Detection by radar is done by detecting the backscattered electromagnetic signal returned from a target. The backscattered signal originates from the surface currents excited on the object when it is irradiated by an incident electromagnetic wave. Different targets have different outer surface that cause different surface currents to flow on the target when identical incident waves are irradiating the targets.

RPT#: AD-A155739 AD-F300619 95/03/00 85N32248

UTTL: Head-on scattering of a tubular cylinder of finite length for radar target identification purposes

AUTH: A/GELLER, D. CORP: Naval Postgraduate School, Monterey, Calif.

ABS: This thesis studies the head-on backscattering of a finite tubular cylinder with a circular cross-section and a very thin conducting wall. At this aspect angle, the backscattered fields depend only on the first Fourier component of the circumferential variations of the psi-current. Measurements of several scaled tubular cylinders were taken and the experimental results were compared to theoretical data available. This thesis is part of an ongoing project of target identification through the investigation of the cross section of a target over a broad frequency band.

RPT#: AD-A155608 85/03/00 85N32246

UTTL: Radar target identification through electromagnetic scattering studies

AUTH: A/LDLIC, M. CORP: Naval Postgraduate School, Monterey, Calif.

ABS: Radar target identification using electromagnetic scattering is discussed. Frequencies being used are those corresponding to wavelengths from half the target size to one-tenth the target dimensions. The frequency domain calibration of the free field radar range at the Naval Postgraduate School is performed and validated on several perfectly conducting metallic spheres. Measurements of the radar cross section and the phase of the return on several finite length, thin walled, right circular cylinders were done.

RPT#: AD-A154596 84/12/00 85N32220

UTTL: The measurement of aircraft windshield haze and its effect on visual performance

A/TASK, H. L.; B/GENCO, L. V. CORP: Aerospace Medical Research Labs., Wright-Patterson AFB, Ohio.

ABS: A new method of measuring haze in installed aircraft transparencies is developed and explained. Using data obtained with the new method, equations were derived to help predict target detection performance as it is affected by windshield haze, windshield transmissivity, ambient illumination, mean target luminance, target contrast and target size. The equations may be applied to many transparency types and configurations. Graphs are provided to show the effects of another of typical visibility conditions. No similar relationships were found for older methods of measuring haze.

RPT#: AD-A154949 AFAMRL-TR-R5-016 85/02/00 85N32114

UTTL: Angular tracking error in A phase comparison monopulse tracking radar: A critical review and extension of the phase front distortion approach

AUTH: A/BUMRDONGPOL, S. CORP: Naval Postgraduate School, Monterey, Calif.

ABS: This thesis studies the inherent angular errors of a phase comparison monopulse system used for tracking a complex target. The phase compensation equation is utilized in justifying Howard's hypothesis on the relationship between the phase front distortion of the scattered wave from a complex target and angular tracking errors, in extending this hypothesis to closer ranges to the target, and in determining the limitations of this hypothesis. Through the phase compensation equation, global errors are demonstrated. A local error bound is also determined for the tracking of a two element target. These new results are not predicted by Howard's hypothesis.

RPT#: AD-A152628 84/12/00 85N28205

UTTL: Digital methods of the optimum processing of radar signals

AUTH: A/SAMSONENKO, S. V. CORP: Air Force Systems Command, Wright-Patterson AFB, Ohio. CSS: (Foreign Technology Div.)

ABS: In book questions of use/application of digital computers for optimum processing of radar signals are examined. Primary attention is given to the detection of signals from the targets, hidden by interferences, and to the determination of the target coordinates. Is described the work of the simplest diagrams of working/treatment, their operating principle, and also work of some nodes of digital computers. Subsequently are given the more complicated cases, special theory

and algorithms of working/treatment. Shows how it is realized the synthesis of the structures of machines and their algorithms on the base of the theory of statistical solutions. The necessary information according to the theory of statistical solutions is given on the course of presentation. Book is intended for cadets of military colleges, students of military academies, military engineers and can be used by civil/ civilian specialists, who work in the region of radar.

RPT#: AD-A152469 AD-E440273 FTD-ID(RS)IT-0667-84 85/02/07
85N28202

UTTL: A mathematical model for calculating detection probability of a diffusion target
AUTH: A/SISLOGLU, M. CORP: Naval Postgraduate School, Monterey, Calif.
ABS: The primary objective of this thesis is to derive a mathematical model to predict the detection probability of a target which moves randomly, according to a two-dimensional diffusion model. This model assumes that there is a stationary searcher which has a cookie cutter sensor with radius R. In order to construct this model, a Monte Carlo simulation program is used to generate detection probabilities. It is demonstrated that this model can be used asymptotically to predict an upper bound detection probability of an equivalent random tour target.

RPT#: AD-A152026 84/09/00 85N27601

UTTL: Low-resolution target classification from a staring infrared sensor
AUTH: A/TILLEY, J. N. CORP: Air Force Inst. of Tech., Wright-Patterson AFB, Ohio. CSS: (School of Engineering.)
ABS: A unique method to extract and classify aircraft targets from low-resolution staring infrared data is presented which uses sequences of sensor frames to obtain target signature samples. The classifier is based on a target feature description consisting of x and y energy projections of the target. The target information is first extracted from sensor data through sampling windows consisting of contiguous rows and columns of detectors in the path of the expected target. The samples are then reduced to remove degradations from noise and sensor optics. The classifier assumes that approximate target position and velocity are available from a target detection and track subsystem. Tests were performed using a software sensor simulation that includes optical blur and sensor motion models. The classifier is shown through

simulation to successfully extract and classify various transport and fighter class aircraft with sensor footprint resolution of 11 to 45 meters.
RPT#: AD-A151690 AFIT/GE/ENG/84D-67 84/12/00 85N26358

UTTL: An investigation into generalised matched filter techniques
AUTH: A/ANDERSON, J. S.: B/SIMS, P. F. CORP: British Aerospace Dynamics Group, Bristol (England). CSS: (Optics Research Dept.)

ABS: A method of constructing an optical correlation system for detection of targets independent of range is described. Digital simulations show good correlation between targets that differ by a scale factor of two, and thus the need for multiple matched filters for different target ranges is reduced. An optical element to perform the logarithmic transform required in the modified optical correlation system is outlined. The method is only effective if the targets are aligned properly.
RPT#: BAE-BR-12971 82/06/00 85N26348

UTTL: Optical flow-patterns of image velocity and their potential use in guidance and image interpretation
AUTH: A/STANLEY, P. A. CORP: British Aerospace Dynamics Group, Bristol (England). CSS: (Human Factors Dept.)
ABS: Optical flow, i.e., the pattern of image velocities created when an observer/sensor moves through the environment is introduced. The temporal optical array of a moving point of observation contains sufficient information (in conjunction with a scaling factor) to extract the ranges of objects in the environment. The applicability of such information to missile guidance is considered. Although the utility of optical flow concepts strongly depends on missile attitude, sensor angle and accuracy of object tracking, a further analysis of specific cases and potential algorithms is worthwhile. It is shown that dynamic images are a source of considerable information of value of an automatic interpretation system. The optical flow fields of solid objects moving relative to an observer/sensor have characteristics useful in frame-to-frame edge tracking, edge to object assignment and target background separation.
RPT#: BAE-BT-12091 81/08/00 85N26347

UTTL: Optical implementation of the synthetic discriminant function

AUTH: A/BUTLER, S.; B/RIGGINS, J. CORP: Air Force Armament Lab., Eglin AFB, Fla.

ABS: Much attention is focused on the use of coherent optical pattern recognition (OPR) using matched spatial filters for robotics and intelligent systems. The OPR problem consists of three aspects -- information input, information processing, and information output. This paper discusses the information processing aspect which consists of choosing a filter to provide robust correlation with high efficiency. The filter should ideally be invariant to image shift, rotation and scale, provide a reasonable signal-to-noise (S/N) ratio and allow high throughput efficiency. The physical implementation of a spatial matched filter involves many choices. These include the use of conventional holograms or computer-generated holograms (CGH) and utilizing absorption or phase materials. Conventional holograms inherently modify the reference image by non-uniform emphasis of spatial frequencies. Proper use of film nonlinearity provides improved filter performance by emphasizing frequency ranges crucial to target discrimination. In the case of a CGH, the emphasis of the reference magnitude and phase can be controlled independently of the continuous tone or binary writing processes. This paper describes computer simulation and optical implementation of a geometrical shape and a Synthetic Discriminant Function (SDF) matched filter. The authors chose the binary Alilebach-Keegan (AK) CGH algorithm to produce actual filters. The performances of these filters were measured to verify the simulation results. This paper provides a brief summary of the matched filter theory, the SDF, CGH algorithms, Phase-Only-Filtering, simulation procedures, and results.

RPT#: AD-A149562 AFATL-TR-84-103 84/10/21 85N19817

UTTL: A methodology for the determination of rotary wing aircraft vulnerabilities in air-to-air combat simulation

AUTH: A/TRAVIS, K. L. CORP: Army Military Personnel Center, Alexandria, Va.

ABS: This research effort proposes a methodology to calculate an aircraft's vulnerability in an air-to-air engagement. The primal processes of such an engagement--detection, acquisition, missile launch, missile intercept and probability of kill--are modeled using an electro-optical device as the source of target detection. The resultant probability of kill is depicted as a function range or a given aspect angle. This constitutes an enhancement over the traditional

kill/no kill representation in that the entire distribution may be obtained for the selected engagement angle. Since little historical or actual test data is available for comparison, evaluation requirements for such a conceptual methodology is discussed. A recalibration process is recommended which will allow the refinement of the model as tests are conducted and observed data becomes available. Applications of the methodology results are recommended for the areas of research and development and pilot tactical training. A pilot decision logic based upon the results of executing the methodology is proposed.

RPT#: AD-A148984 AD-E301513 84/11/23 85N18984

UTTL: Proceedings of the Second Annual Symposium on Mathematical Pattern Recognition and Image Analysis Program

AUTH: A/GUSEMAN, L. F., JR. CORP: Texas A&M Univ., College Station, CSS: (Dept. of Mathematics.) Symp. held in Houston, Tex., 6-8 Jun. 1984

ANN: Several papers addressing image analysis and pattern recognition techniques for satellite imagery are presented. Texture classification, image rectification and registration, spatial parameter estimation, and surface fitting are discussed. For individual titles see N85-16252 through N85-16267.

RPT#: E85-10056 NASA-CR-171819 NAS 1.26:171819 84/00/00 85N16251

UTTL: Distributed sensor networks

AUTH: A/LACROSS, R. T. CORP: Massachusetts Inst. of Tech., Cambridge.

ABS: The Distributed Sensor Networks (DSN) program is aimed at developing and extending target surveillance and tracking technology in systems that employ multiple spatially distributed sensors and processing resources. Such a system would be made up of sensors, data bases, and processors distributed throughout an area and interconnected by an appropriate digital data communication system. The detection, tracking and classification of low-flying aircraft has been selected to develop and evaluate DSN concepts in the light of a specific system problem. A DSN test bed has been developed and is being used to test and demonstrate DSN techniques and technology. The sensors presently in use are small arrays of microphones. The overall concept calls for a mix of sensor types. Visible TV sensors are scheduled for integration into the test bed in the near future.

RPT#: AD-A146209 ESD-TR-84-002 83/09/30 85N12286

UTTL: On aircraft antennas and basic scattering studies
AUTH: A/RUDDUCK, R. C.; B/MARHEFKA, R. J.; C/BURNSIDE, W. D. CRP: Ohio State Univ., Columbus. CSS: (ElectroScience Lab.)
ABS: This report summarizes the work accomplished in each of two areas. The on-aircraft studies involved the GTD (Geometrical Theory of Diffraction) analysis of a strip scatterer in the near field of an antenna. In addition, a method for determining the aperture distribution of a linear array through near field measurements has been developed. The basic scattering studies portion attempts to provide an understanding of ray optical solutions and UTD (Uniform GTD) in particular for the analysis of scattering from basic shapes. Specific examples of scattering from plate models, composite cone frustrums and the near zone effects of a basic aircraft model are presented.
RPT#: AD-A146017 ESL-713303-4 NADC-84081-30 84/07/01
85N12282

REPORT DOCUMENTATION PAGE

1. Recipient's Reference	2. Originator's Reference	3. Further Reference	4. Security Classification of Document						
	AGARD-LS-152	ISBN 92-835-1553-6	UNCLASSIFIED						
5. Originator	Advisory Group for Aerospace Research and Development North Atlantic Treaty Organization 7 rue Ancelle, 92200 Neuilly sur Seine, France								
6. Title	THEORETICAL ASPECTS OF TARGET CLASSIFICATION								
7. Presented at									
8. Author(s)/Editor(s)	Various		9. Date June 1987						
10. Author's/Editor's Address	Various		11. Pages 224						
12. Distribution Statement	This document is distributed in accordance with AGARD policies and regulations, which are outlined on the Outside Back Covers of all AGARD publications.								
13. Keywords/Descriptors	<table> <tr> <td>Target intelligence</td> <td>Classifications</td> </tr> <tr> <td>Radar echoes</td> <td>Signal processing</td> </tr> <tr> <td>Signatures</td> <td>Mathematical models</td> </tr> </table>			Target intelligence	Classifications	Radar echoes	Signal processing	Signatures	Mathematical models
Target intelligence	Classifications								
Radar echoes	Signal processing								
Signatures	Mathematical models								
14. Abstract	<p>Target classification is essential for tactical decision-making. With the present availability of short pulse and sophisticated data processing techniques, target scattering can be observed over long time intervals providing continuous coverage from high to low frequencies in the signal spectrum. Utilisation of early and late time information, as well as dependence in aspects, requires the blending of techniques that have heretofore been considered piecemeal.</p> <p>This Lecture Series will present various analytical methods, and their numerical implement, for generating and classifying target signatures under transient and steady state illumination, with emphasis on classification schemes that facilitate extraction of unknown target features in the inverse problem of identification. Included also are numerical modelling, experimental results obtained under controlled and realistic conditions, and description of measurement range facilities.</p>								

<p>AGARD Lecture Series No.152 Advisory Group for Aerospace Research and Development, NATO THEORETICAL ASPECTS OF TARGET CLASSIFICATION Published June 1987 224 pages</p> <p>Target classification is essential for tactical decision-making. With the present availability of short pulse and sophisticated data processing techniques, target scattering can be observed over long time intervals providing continuous coverage from high to low frequencies in the signal spectrum. Utilisation of early and late time information, as well as dependence in aspects, requires the blending of techniques that have heretofore been considered piecemeal.</p> <p>P.T.O</p>	<p>AGARD-LS-152</p> <p>Target intelligence Radar echoes Signatures Classifications Mathematical models</p>	<p>AGARD Lecture Series No.152 Advisory Group for Aerospace Research and Development, NATO THEORETICAL ASPECTS OF TARGET CLASSIFICATION Published June 1987 224 pages</p> <p>Target classification is essential for tactical decision-making. With the present availability of short pulse and sophisticated data processing techniques, target scattering can be observed over long time intervals providing continuous coverage from high to low frequencies in the signal spectrum. Utilisation of early and late time information, as well as dependence in aspects, requires the blending of techniques that have heretofore been considered piecemeal.</p> <p>P.T.O</p>	<p>AGARD-LS-152</p> <p>Target intelligence Radar echoes Signatures Classifications Signal processing Mathematical models</p>
<p>AGARD Lecture Series No.152 Advisory Group for Aerospace Research and Development, NATO THEORETICAL ASPECTS OF TARGET CLASSIFICATION Published June 1987 224 pages</p> <p>Target classification is essential for tactical decision-making. With the present availability of short pulse and sophisticated data processing techniques, target scattering can be observed over long time intervals providing continuous coverage from high to low frequencies in the signal spectrum. Utilisation of early and late time information, as well as dependence in aspects, requires the blending of techniques that have heretofore been considered piecemeal.</p> <p>P.T.O</p>	<p>AGARD-LS-152</p> <p>Target intelligence Radar echoes Signatures Classifications Signal processing Mathematical models</p>	<p>AGARD Lecture Series No.152 Advisory Group for Aerospace Research and Development, NATO THEORETICAL ASPECTS OF TARGET CLASSIFICATION Published June 1987 224 pages</p> <p>Target classification is essential for tactical decision-making. With the present availability of short pulse and sophisticated data processing techniques, target scattering can be observed over long time intervals providing continuous coverage from high to low frequencies in the signal spectrum. Utilisation of early and late time information, as well as dependence in aspects, requires the blending of techniques that have heretofore been considered piecemeal.</p> <p>P.T.O</p>	<p>AGARD-LS-152</p> <p>Target intelligence Radar echoes Signatures Classifications Signal processing Mathematical models</p>

<p>This Lecture Series will present various analytical methods, and their numerical implementation, for generating and classifying target signatures under transient and steady state illumination, with emphasis on classification schemes that facilitate extraction of unknown target features in the inverse problem of identification. Included also are numerical modelling, experimental results obtained under controlled and realistic conditions, and description of measurements range facilities.</p> <p>The material in this publication was assembled to support a Lecture Series under the Sponsorship of the Electromagnetic Wave Propagation Panel and the Consultant and Exchange Programme of AGARD presented on 29-30 June 1987 in Rome, Italy, 2-3 July in Neuberg, Germany and 6-7 July 1987 in Noresund, Norway.</p> <p>ISBN 92-835-1553-6</p>	<p>This Lecture Series will present various analytical methods, and their numerical implementation, for generating and classifying target signatures under transient and steady state illumination, with emphasis on classification schemes that facilitate extraction of unknown target features in the inverse problem of identification. Included also are numerical modelling, experimental results obtained under controlled and realistic conditions, and description of measurements range facilities.</p> <p>The material in this publication was assembled to support a Lecture Series under the Sponsorship of the Electromagnetic Wave Propagation Panel and the Consultant and Exchange Programme of AGARD presented on 29-30 June 1987 in Rome, Italy, 2-3 July in Neuberg, Germany and 6-7 July 1987 in Noresund, Norway.</p> <p>ISBN 92-835-1553-6</p>
<p>This Lecture Series will present various analytical methods, and their numerical implementation, for generating and classifying target signatures under transient and steady state illumination, with emphasis on classification schemes that facilitate extraction of unknown target features in the inverse problem of identification. Included also are numerical modelling, experimental results obtained under controlled and realistic conditions, and description of measurements range facilities.</p> <p>The material in this publication was assembled to support a Lecture Series under the Sponsorship of the Electromagnetic Wave Propagation Panel and the Consultant and Exchange Programme of AGARD presented on 29-30 June 1987 in Rome, Italy, 2-3 July in Neuberg, Germany and 6-7 July 1987 in Noresund, Norway.</p> <p>ISBN 92-835-1553-6</p>	<p>This Lecture Series will present various analytical methods, and their numerical implementation, for generating and classifying target signatures under transient and steady state illumination, with emphasis on classification schemes that facilitate extraction of unknown target features in the inverse problem of identification. Included also are numerical modelling, experimental results obtained under controlled and realistic conditions, and description of measurements range facilities.</p> <p>The material in this publication was assembled to support a Lecture Series under the Sponsorship of the Electromagnetic Wave Propagation Panel and the Consultant and Exchange Programme of AGARD presented on 29-30 June 1987 in Rome, Italy, 2-3 July in Neuberg, Germany and 6-7 July 1987 in Noresund, Norway.</p> <p>ISBN 92-835-1553-6</p>

END

DATE
FILMED

12 87